Create accurate numerical models of complex spatio-temporal dynamical systems with holistic discretisation

for the degree of Doctor of Philosophy

Tony MacKenzie, BIT, BSc(Hons)

November 2005

Abstract

This dissertation focuses on the further development of creating accurate numerical models of complex dynamical systems using the holistic discretisation technique [Roberts, Appl. Num. Model., 37:371–396, 2001]. I extend the application from second to fourth order systems and from only one spatial dimension in all previous work to two dimensions ($2D$). We see that the holistic technique provides useful and accurate numerical discretisations on coarse grids. We explore techniques to model the evolution of spatial patterns governed by PDEs such as the Kuramoto–Sivashinsky equation and the real-valued Ginzburg–Landau equation. We aim towards the simulation of fluid flow and convection in three spatial dimensions. I show that significant steps have been taken in this dissertation towards achieving this aim.

Holistic discretisation is based upon centre manifold theory [Carr, Applications of centre manifold theory, 1981] so we are assured that the numerical discretisation accurately models the dynamical system and may be constructed systematically. To apply centre manifold theory the domain is divided into elements and using a homotopy in the coupling parameter γ, subgrid scale fields are constructed consisting of actual solutions of the governing partial differential equation(PDE). These subgrid scale fields interact through the introduction of artificial internal boundary conditions. View the

centre manifold (*macroscale*) as the union of all states of the collection of subgrid fields (*microscale*) over the physical domain.

Here we explore how to extend holistic discretisation to the fourth order Kuramoto–Sivashinsky PDE. I show that the holistic models give impressive accuracy for reproducing the steady states and time dependent phenomena of the Kuramoto–Sivashinsky equation on coarse grids. The holistic method based on local dynamics compares favourably to the global methods of approximate inertial manifolds. The excellent performance of the holistic models shown here is strong evidence in support of the holistic discretisation technique.

For shear dispersion in a $2D$ channel a one-dimensional numerical approximation is generated directly from the two-dimensional advection-diffusion dynamics. We find that a low order holistic model contains the shear dispersion term of the Taylor model [Taylor, IMA J. Appl. Math., 225:473–477, 1954]. This new approach does not require the assumption of large x scales, formerly absolutely crucial in deriving the Taylor model.

I develop holistic discretisation for two spatial dimensions by applying the technique to the real-valued Ginzburg–Landau equation as a representative example of second order PDEs. The techniques will apply quite generally to second order reaction–diffusion equations in $2D$. This is the first study implementing holistic discretisation in more than one spatial dimension.

The previous applications of holistic discretisation have developed algebraic forms of the subgrid field and its evolution. I develop an algorithm for numerical construction of the subgrid field and its evolution for $1D$ and $2D$ PDEs and explore various alternatives. This new development greatly extends

the class of problems that may be discretised by the holistic technique. This is a vital step for the application of the holistic technique to higher spatial dimensions and towards discretising the Navier–Stokes equations.

Certification of dissertation

The work contained in this dissertation is the bonafide work of the author; the work has not been previously submitted for an award; and to the best of my knowledge and belief, the dissertation contains no material previously published or written by another person except where due acknowledgement and reference is made in the dissertation to that work.

Signed: Date:

Acknowledgements

This dissertation was prepared while on an Australian Postgraduate Award. I also acknowledge the receipt of a University of Southern Queensland postgraduate research scholarship for the first 12 months of my candidature. I also acknowledge the support of Queensland Treasury Corporation.

I would like to express my sincere thanks to the following people:

- My supervisor, Professor Tony Roberts for his guiding hand, invaluable expertise and the stimulus for this dissertation. I thank Tony for his commitment to this project and his perseverance. Tony's mentoring through my candidature has added value far beyond the scope of this dissertation and the legacy of his unique approach to applied mathematics is embedded in my day to day professional life.

- Dr Chris Harman my associate supervisor for his direction, suggestions and proof reading of this dissertation.

- Dr Dmitry Strunin and Dr Sergey Suslov for their comments, suggestions and valued mentoring throughout this learning experience.

- Dr Mark Thompson, Dr Glen Lochhead, Tanya and my mum for their constant support through the final stages of writing this dissertation.

Contents

Chapter 1

Introduction

The focus of this dissertation is on the further development of the application of dynamical systems theory to constructing numerical discretisations of PDEs. In particular we concentrate on the holistic discretisation technique introduced by Roberts [54]. We focus on extending the application to higher order systems and higher spatial dimensions and show that it provides useful and accurate numerical discretisations. In particular, we explore techniques to model the evolution of spatial patterns governed by PDEs such as the Kuramoto–Sivashinsky equation (2.1) and the real-valued Ginzburg–Landau equation (6.1).

We are aiming towards the simulation of fluid flow and convection with one aim to apply holistic discretisation to the Navier–Stokes equations in three spatial dimensions. This is not achieved in the scope of this dissertation. However, we show in this dissertation that significant steps have been taken in the direction of achieving this aim. The key results of this dissertation are:

- The holistic discretisation technique is extended to fourth order systems, namely the Kuramoto–Sivashinsky equation (2.1) (Chapter 2) which has analogies to the Navier–Stokes equations and exhibits complex spatio-temporal dynamics [8, 23]. Earlier versions of §2.1–2.3 are published in [34].

- The holistic models give impressive accuracy for reproducing the steady states and time dependent phenomena of the Kuramoto–Sivashinsky equation on coarse grids (Chapters 3 and 4). The holistic method based on local dynamics compares favourably to the global methods of approximate inertial manifolds.

- For shear dispersion in a $2D$ channel, a one-dimensional numerical approximation is generated directly from the two-dimensional advection-diffusion dynamics, and the shear dispersion term is generated in the holistic model (Chapter 5). This new approach does not require the assumption of large x scales, formerly absolutely crucial in deriving Taylor's model (5.2). All of the results of Chapter 5 are published in [35].

- We develop holistic discretisation for two spatial dimensions by applying it to the real-valued Ginzburg–Landau equation (RGL) (7.1). The RGL is used as a representative example of second order PDEs and so we argue that the techniques will apply quite generally to second order reaction–diffusion equations in $2D$ (Chapter 7). This is the first study towards using holistic discretisation of PDEs in more than one spatial dimension. Earlier versions of §7.1–7.2 are published in [36].

- The previous applications of holistic discretisation have developed algebraic forms of the subgrid field and its evolution. I present an algorithm for numerical construction of the subgrid field and its evolution for $1D$ and $2D$ PDEs based on the algorithm introduced by Roberts in [52] (Chapter 8). This new development removes the restriction for analytic subgrid fields and greatly extends the class of problems that may be discretised by the holistic technique. This is a vital step for application to problems of higher spatial dimensions.

Numerical discretisation is a transformation of an infinite dimensional PDE to a finite dimensional model for evolution of grid values or local average values. This is an example of low-dimensional modelling. We use centre manifold theory [4, 5, 7] to create the low-dimensional models as it appears to be more powerful.

Holistic discretisation [54, 46, 53, 34, 36, 35, 55] is based upon centre manifold theory so we are assured that the numerical discretisation accurately models the dynamical system and may be constructed systematically. The use of centre manifold theory for this modelling was initiated by Coullet & Spiegel [7] and Carr & Muncaster [4, 5] and has been employed in a wide variety of applications: elasticity [49], heat or mass transfer [39, 66], hydrodynamics [41, 17], thin film flow [50, 57] and many others reviewed in [51].

To apply the centre manifold theory we divide the domain into elements and using a homotopy we couple the elements using the coupling parameter γ and construct subgrid scale fields consisting of actual solutions of the governing PDE [54, 46, 34]. These subgrid scale fields interact through the

introduction of artificial internal boundary conditions (IBCs). We view the centre manifold (*macroscale*) as the union of all states of the collection of subgrid fields (*microscale*) over the physical domain. When $\gamma = 0$ the elements are isolated from each other and exponentially quickly in time the solution becomes independently constant within each element [36]. When $\gamma = 1$ there is sufficient continuity to regain the dynamics of the original PDE. This parameter γ is the coupling parameter and controls the flow of information between elements. The application of the holistic technique is explained in detail for discretising the Kuramoto–Sivashinsky equation (2.1) in §2.1–2.3.

The original work of Roberts [54] in discretising Burgers' equation

$$u_t + \alpha u u_x = u_{xx} - \beta u^3 \,, \tag{1.1}$$

provides the motivation for this study. Consider the nonlinear advection term uu_x. If we directly discretise this term we obtain the approximation

$$uu_x = \frac{u_j(u_{j+1} - u_{j-1})}{2h} + \mathcal{O}(h^2) \,. \tag{1.2}$$

However, if we rewrite the advection term as $\frac{1}{2}(u^2)_x$ and discretise we obtain the approximation

$$uu_x = \frac{1}{2}\left(u^2\right)_x = \frac{u_{j+1}^2 - u_{j-1}^2}{4h} + \mathcal{O}(h^2) \,. \tag{1.3}$$

Fornberg [16] suggests and others [13] have implemented a $1:2$ mix of the above two approximations to improve the stability of the discretisation. However, Roberts [54] argues that the discretisation should depend upon how the nonlinearity interacts with the dynamics of other terms.

We use centre manifold theory to construct approximations based upon the principle of capturing an exponentially attractive manifold of solutions.

Inertial manifolds capture long-term, low dimensional dynamics [63] and in general good approximations to inertial manifolds may be constructed [27]. Construction of the approximate to an inertial manifold is based upon nonlinear Galerkin methods [47, 13, 37, 15, 14, 1, 25]. However, although the nonlinear Galerkin method improves convergence [26], because of its *global* nature its application is not useful for dynamical systems with spatially varying coefficients and does not provide a theoretical framework for handling boundary conditions in general. In contrast, the holistic method is based upon the *local* dynamics of finite elements and allows for a more robust application. The local nature of holistic discretisation is seen in all the applications developed throughout. However, both approximate inertial manifolds and the holistic method aim to capture the long-term behaviour of the original PDE.

The numerical models constructed with holistic discretisation have a dual justification [46]. Traditional finite difference models are constructed requiring the approximation to be consistent with the original PDE as the grid spacing h tends to 0. In contrast, the holistic technique uses finite h and through the application of centre manifold theory models the dynamics in an expansion in the nonlinearity and inter-element coupling. However, we also aim to construct holistic discretisations that are consistent with the original PDE, as shown in §2.5, §5.4.1, §7.3.2 and §8.3. Therefore, the numerical discretisations derived by this method are supported by centre manifold asymptotics in the nonlinearity and inter-element coupling for finite grid size h, as well as justified by its consistency in grid size h.

Holistic discretisation is a multiscale modelling approach. It provides macroscopic evolution on a grid (the numerical discretisation) by solving

microscopic subgrid problems. Kevrekidis, Gear and others [19, 20, 6] are working on new methods for solving large-scale equation-free problems using microscale simulations. Holistic discretisation provides a direct link between the microscale and macroscale dynamics [55] and as such has an important role to play in the field of multiscale modelling for large-scale equation-free simulations. This is subject of collaborative research between Prof. Roberts at the University of Southern Queensland, AUSTRALIA and Prof. Kevrekidis at Princeton University, USA. However, this does not form part of the scope of this dissertation.

1.1 The scope of the dissertation

We begin exploration of the holistic discretisation technique by extending its application to the fourth order Kuramoto–Sivashinsky equation (2.1) in §2.1–2.3. The Kuramoto–Sivashinsky equation [60, 30] is a model of instabilities on interfaces and flame fronts and phase turbulence in chemical oscillations. It has received considerable attention as a model of complex dynamics [24, 44, 8, 23]. We study the Kuramoto–Sivashinsky equation here because it is analogous to the Navier–Stokes equations of fluid dynamics [23] on two levels; the energy source and dissipation terms of both dynamical systems are analogous and it exhibits the complexities of weak turbulence or spatio-temporal chaos [8].

We construct the holistic discretisation of the Kuramoto–Sivashinsky equation by a natural extension of the IBCs of [54, 46] to fourth order. We investigate both a local (2.4–2.5) and non-local (2.7–2.8) form of the IBCs. Both forms of the IBCs result in the dual justification property of the holis-

tic models as shown in §2.5, but through superior performance observed in numerical experiments in Chapters 3 and 4 the non-local IBCs are preferred. We list various holistic models in §2.3.2 for both the non-local and local IBCs.

In Chapters 3 and 4 we investigate the numerical performance of the low order holistic models. We compare predicted steady states and dynamics near steady states by comparing bifurcation diagrams. We also investigate the performance near Hopf bifurcations leading to period doubling sequences and the spatio-temporal patterns at large values of the nonlinearity. We find excellent performance for the holistic models on coarse grids and compare this performance to that of the approximate inertial manifold methods from [25, 29, 59] by comparing bifurcation diagrams. This excellent performance is vital evidence that the holistic technique is a useful and accurate method of creating numerical discretisations.

In Chapter 5 we use the holistic technique to derive a one-dimensional numerical model directly from the two-dimensional advection-diffusion dynamics of shear dispersion of a pollutant or other tracer along a river, channel or pipe. We bypass the Taylor model (5.2) [62] and derive a one-dimensional numerical model from the original dynamics without ever assuming large x scales, an assumption formerly absolutely crucial in deriving Taylor's model (5.2). In §5.4 we find that the shear dispersion term appears with a low order holistic approximation (5.15).

For the shear dispersion problem centre manifold theory also provides the necessary tools to accurately develop approximations near a boundary [53] and in §5.5 we see how the analysis is applied near a physical inlet and outlet boundary. Both Dirichlet and Neumann boundary conditions are considered

and the evolution of the grid values near the boundaries listed in §5.5.1.

In Chapter 6 we explore the application of the holistic technique to discretising the real-valued Ginzburg–Landau equation (RGL) (6.1). This serves as a test case for discretising reaction-diffusion equations before extension to a two dimensional version in Chapter 7. This is the first study for application of the holistic method to PDEs of two spatial dimension and enables discretisation of general spatial problems. Numerical results do not show the same excellent performance seen in Chapters 3 and 4 for the holistic models of the Kuramoto–Sivashinsky equation. However, we see the holistic method is extended to PDEs of two spatial dimensions and the holistic models of the RGL serve as a reference for the numerical construction of the subgrid field detailed in Chapter 8.

In Chapter 8 an algorithm for the numerical construction of the subgrid field and its evolution is presented. The algorithm is based on the algorithm of Roberts [52] and is best implemented using the computer algebra system REDUCE [22] to solve the mixed discrete/symbolic system of equations. The algorithm of §8.4.1 formulates the iteration scheme with an entirely discrete linear operator and employs LU factorisation to solve for updates to the subgrid field and its evolution. In §8.2 Richardson extrapolation is used to increase the order of accuracy of the numerical construction of the subgrid problem.

The numerically constructed holistic models are compared to the analytic models for the one-dimensional RGL (6.1) and the Kuramoto–Sivashinsky equation (2.1). In §8.3 we find that low resolutions for the subgrid scale problem give performance that is indiscernible from the analytic holistic models

for coarse macroscale problems over a large range of the nonlinearity. Higher order holistic models for the two dimensional RGL (7.1) are now possible using the numerical construction of the subgrid field as detailed in §8.5.

The holistic discretisation technique is still in its early stages of application and development. The work of this dissertation is largely proof of principle that the method is extended to higher order systems and higher spatial dimensions. The excellent numerical results seen in Chapter 3 and 4 for the holistic models of the Kuramoto–Sivashinsky equation (2.1) support the claim that the holistic method is an accurate and useful technique for creating numerical discretisations of dynamical systems. Much work still remains for a complete three dimensional application of the holistic method for discretising dynamical systems of fluid flow and convection but the algorithm for numerical construction of the subgrid field detailed in Chapter 8 will play a vital role toward a more general application.

Chapter 2

Discretise the Kuramoto–Sivashinsky equation using the holistic technique

Contents

We continue exploring holistic discretisation by modelling the dynamics of solutions $u(x,t)$, to the Kuramoto–Sivashinsky equation

$$\frac{\partial u}{\partial t} + 4\frac{\partial^4 u}{\partial x^4} + \alpha\left(u\frac{\partial u}{\partial x} + \frac{\partial^2 u}{\partial x^2}\right) = 0\,. \tag{2.1}$$

Earlier versions of §2.1–2.3 are published in [34].

In this form (2.1), with 2π periodic boundary conditions, α is a bifurcation parameter that depends upon the size of the typical pattern [59]. This model equation includes the mechanisms of linear negative diffusion αu_{xx}, high-order dissipation $4u_{xxxx}$, and nonlinear advection/steepening $\alpha u u_x$. We discretise the Kuramoto–Sivashinsky equation by the holistic method introduced by Roberts [54]. The system has strong dissipative dynamics arising from the fourth order dissipation in the governing PDE (2.1). Many modes of this system decay rapidly because of this strong dissipation. Thus the dynamics are dominated by a relatively few large scale modes.

The Kuramoto–Sivashinsky equation was introduced by Sivashinsky [60] as a model of instabilities on interfaces and flame fronts, and Kuramoto [30] as a model of phase turbulence in chemical oscillations. It has since received considerable attention as a model of complex dynamics [24, 44, 8, 23].

We study the Kuramoto–Sivashinsky equation here for several reasons. Firstly, it is fourth order and therefore, following the application to Burgers' equation [54] provides a test case for the application of the holistic method to higher order dissipative PDEs. Secondly, the Kuramoto–Sivashinsky equation is analogous to the Navier–Stokes equations of fluid dynamics. Holmes et al. [23] argue that these analogies exist on two levels; the energy source and dissipation terms of both dynamical systems and the reflection and translational symmetries of the Kuramoto–Sivashinsky equation and the spanwise symmetries of the Navier-Stokes equations in the boundary layer. This analogy between symmetries suggests that the Fourier series and corresponding modal interactions are comparable for these two problems. Thirdly, the Kuramoto–Sivashinsky equation exhibits the complexities of weak turbulence or spatio-temporal chaos [8]. This complex time dependent behaviour supplies a searching test of the performance of the holistic models.

Centre manifold theory, for example, [4, 51] provides the basis for the holistic models as introduced in [54] for Burgers' equation and detailed in §2.2. We divide the physical domain into finite width elements and solve the governing PDE (2.1) with inter-element coupling introduced via artificial internal boundary conditions (IBCs). Since the Kuramoto–Sivashinsky equation is fourth order we require additional IBCs to [54] used to discretise Burgers' equation. Here we extend the IBCs to require higher order continuity across the the element boundaries.

The extension of the holistic method to the fourth order Kuramoto–Sivashinsky equation is achieved by the natural extension of the IBCs presented in [46], to IBCs presented in §2.1. In §2.1 we discuss two different IBCs for

discretising the Kuramoto–Sivashinsky equation, the local IBCs (2.4–2.5) and the non-local IBCs (2.7–2.8).

A low order analysis of the Kuramoto–Sivashinsky equation (2.1) with the non-local IBCs (2.7–2.8) in §2.3 (2.25) favours the discretisation

$$\begin{aligned}\frac{du_j}{dt} &+ \frac{4u_{j+2}-16u_{j+1}+24u_j-16u_{j-1}+4u_{j-2}}{h^4}\\ &+\alpha\left(u_j\frac{u_{j+1}-u_{j-1}}{4h}+\frac{u_{j+1}^2-u_{j-1}^2}{4h}-\frac{u_{j+2}u_{j+1}-u_{j-2}u_{j-1}}{12h}\right)\\ &+\alpha\left(\frac{-u_{j+2}+16u_{j+1}-30u_j+16u_{j-1}-u_{j-2}}{12h^2}\right)\approx 0\,,\end{aligned}\tag{2.2}$$

where the u_j are grid values spaced h apart. Examination of the first and third line of the holistic model (2.2) shows that the holistic method generates conventional centered finite difference approximations for the linear terms $4u_{xxxx}$ and αu_{xx}. However, the second line details a nonstandard approximation for the nonlinear term $\alpha u u_x$. The approximation for the nonlinear term is a $1:2:-1$ mix of (1.2), (1.3) and the non-trivial

$$\alpha u u_x\big|_{x_j} \approx \alpha\frac{u_{j+2}u_{j+1}-u_{j-2}u_{j-1}}{6h}\,.\tag{2.3}$$

The holistic model is not constructed by discretising the Kuramoto–Sivashinsky equation (2.1) term by term, rather the subgrid scale dynamics of (2.1) together with the inter-element coupling generate the holistic model (2.2).

The discretisation (2.2) is a low-order approximation. Centre manifold theory provides systematic refinements. Analysis to higher orders in nonlinearity or inter-element interaction, discussed in §2.3.2, gives further refinement to the discretisation. The higher order terms come from resolving more subgrid scale interactions.

In §2.2 we explore how the extension of the holistic method for constructing accurate and stable approximations, such as (2.2), is extended to

the Kuramoto–Sivashinsky equation. In §2.3.1 the symbolic equations to be satisfied by the holistic approximation are presented. A computer algebra program (Appendix A.1.2) solves the equations and is based on the algorithm introduced in [52]. In particular, in §2.3.2 holistic approximations constructed using the local IBCs (2.4–2.5) and the non-local IBCs (2.7–2.8) are presented.

In §2.4, we view the subgrid fields of various holistic models at some particular steady states. An accurate field is compared to subgrid fields of various holistic models and to a Lagrangian interpolant for a 2nd order centered difference approximation. §2.4 is not intended to be an in-depth numerical study of the holistic models, rather suggestive examples of the subgrid field of the holistic models in several relevant cases.

Finally, in §2.5 we investigate how retaining terms to higher order in the coupling parameter leads to higher order consistency between the equivalent PDEs of the holistic models, such as (2.2), and the Kuramoto–Sivashinsky equation. This is the second part of the dual justification discussed in §1, that is, the discretisation is also consistent with the original PDE as the grid spacing $h \to 0$.

2.1 Apply a homotopy in the inter-element coupling parameter

Here we explore in detail how the inter-element coupling described in [54] for discretising Burgers' equation (1.1) is extended to discretise the Kuramoto–Sivashinsky equation (2.1).

Consider implementing the method of lines by discretising in space and integrating in time as a set of ordinary differential equations. Establish the spatial discretisation by dividing the domain into m elements of equal and finite width h and introducing an equi-spaced grid of collocation points, $x_j = jh$, at the centre of each element, see Figure 2.1. The vertical blue lines form the element boundaries, which for the jth element are located at $x_{j\pm1/2} = (j \pm 1/2)h$. In principle, elements may be of unequal size. However, to simplify the analysis, herein all elements will be of equal width h. We express the field for the jth element by $u = v_j(x, t)$.

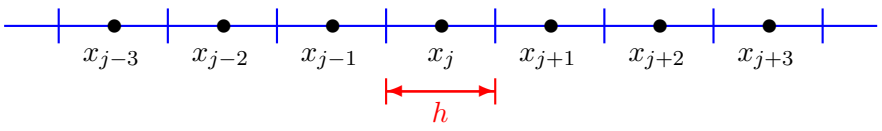

Figure 2.1: An example of the $1D$ grid with regular elements of width h. The jth element is centered about the grid point x_j.

We introduce a homotopy in the inter-element coupling parameter γ: when $\gamma = 0$ the elements are effectively isolated from each other, providing the basis for the application of centre manifold theory; whereas when evaluated at $\gamma = 1$, the elements are fully coupled together and hence the discretised model applies to the original PDE.

The inter-element coupling parameter γ controls the flow of information between neighbouring elements. The application of centre manifold theory constructs solutions as power series expansions in γ. When $\mathcal{O}(\gamma^2)$ terms are neglected in the holistic model, the field in the jth element will involve information about the fields in the $j \pm 1$ elements. Similarly, when $\mathcal{O}(\gamma^3)$ terms

are neglected in the approximation, the field in the jth element will involve information about the fields in the $j \pm 1$ and $j \pm 2$ elements. Consequently, the order of γ terms retained in the holistic model controls the stencil width of the discretisation.

Homotopies have been used successfully in other numerical methods. For example, Liao [32], proposed a homotopy in his general boundary element method which allows the choice of auxiliary linear operators whose fundamental solutions are well known. In our application the homotopy is only in the IBCs. The dynamics in each element are governed by the dynamics of the Kuramoto–Sivashinsky equation (2.1).

This homotopy is applied by introducing artificial internal boundary conditions. There are different possible ways to implement these IBCs and here we discuss two possibilities: the local IBCs (2.4–2.5); and the non-local IBCs (2.7–2.8). To date, theory does not explain which IBCs should perform better. However, numerical experiments with holistic approximations produced by the local IBCs and non-local IBCs, compared in Chapter 3, demonstrate superior performance for the holistic approximations constructed with the non-local IBCs.

2.1.1 The local IBCs

Firstly, we consider local IBCs. At the element boundaries $x = x_{j+1/2}$, introduce the following IBCs:

$$\begin{bmatrix} \frac{\partial v_{j+1}}{\partial x} - \frac{\partial v_j}{\partial x} \\ \frac{\partial^3 v_{j+1}}{\partial x^3} - \frac{\partial^3 v_j}{\partial x^3} \end{bmatrix} = \begin{bmatrix} 0 \\ 0 \end{bmatrix}, \tag{2.4}$$

$$h\left(\frac{1-\gamma}{2}\right)\begin{bmatrix} \frac{\partial v_{j+1}}{\partial x}+\frac{\partial v_j}{\partial x} \\ \frac{\partial^3 v_{j+1}}{\partial x^3}+\frac{\partial^3 v_j}{\partial x^3} \end{bmatrix} = \gamma\mathcal{A}\begin{bmatrix} v_{j+1}-v_j \\ \frac{\partial^2 v_{j+1}}{\partial x^2}-\frac{\partial^2 v_j}{\partial x^2} \end{bmatrix}, \tag{2.5}$$

where $\mathcal{A}$ is given by (2.6). These boundary conditions divide the domain into the set of elements shown in Figure 2.1, with the jth element centered upon x_j and of width $\Delta x = h$.

These IBCs are an extension to fourth order of the local IBCs introduced by Roberts [54] for Burgers' equation. When $\gamma = 0$ the right hand side of (2.5) disappears, implying first and third derivatives of the field v_j are zero at the boundary. Thus, the elements are effectively insulated from each other and so an equilibrium solution of the Kuramoto–Sivashinsky equation in each element is particularly simple, namely $v_j(x,t) = \text{const}$. We use this simple class of solutions as the basis for analysing the $\gamma \neq 0$ case when the elements are coupled together. We are particularly interested in the approximation at $\gamma = 1$ when the PDE (2.1) is effectively restored over the whole domain because (2.4–2.5) then ensures continuity of the field u and its first three derivatives between adjacent elements.

The introduction of the near identity operator

$$\mathcal{A} = 1 + h^2\frac{\partial_x^2}{12} - h^4\frac{\partial_x^4}{720} + h^6\frac{\partial_x^6}{30240} + \cdots = \frac{h\partial_x}{2}\coth\left(\frac{h\partial_x}{2}\right), \tag{2.6}$$

as discussed in [54, §4] ensures holistic models of higher orders in the coupling parameter γ are consistent with (2.1) to higher orders in h. The relationship between the order of the approximation and the equivalent PDE is explored in more detail in §2.5.

2.1.2 The non-local IBCs

The second method to form the elements is to introduce the following non-local IBCs

$$\delta_x v_j(x,t) = \gamma \delta v_{j\pm1/2}(x,t) \quad \text{at } x = x_{j\pm1/2}\,, \tag{2.7}$$

$$\delta_x^3 v_j(x,t) = \gamma^2 \delta^3 v_{j\pm1/2}(x,t) \quad \text{at } x = x_{j\pm1/2}\,, \tag{2.8}$$

which are an extension to the non-local IBCs proposed by Roberts [46] for Burgers' equation.

The non-local IBCs are written in terms of the centered difference operators δ and δ_x. Note the distinction between δ and δ_x. The operator δ_x denotes a centered difference in x only, with step h. For example

$$\delta_x v_j(x,t) = v_j(x+h/2,t) - v_j(x-h/2,t)\,. \tag{2.9}$$

The operator δ denotes a centered difference applied to the grid index j with step 1. For example, as in the right-hand sides of (2.7–2.8)

$$\delta v_{j+1/2}(x_{j+1/2},t) = v_{j+1}(x_{j+1},t) - v_j(x_j,t)\,. \tag{2.10}$$

The field $v_j(x,t)$ is not restricted to the jth element. It extends analytically to at least $x_{j\pm2}$, to allow the application of the non-local IBCs (2.8) which involve the third differences.

The physical interpretation of these non-local IBCs is not as obvious as for the local IBCs (2.4–2.5). When evaluated at $\gamma = 0$, (2.7) ensures that the first differences in x of the field v_j centered about the element boundaries $x_{j\pm1/2}$ are zero. Similarly, (2.8) ensures that the third differences in x of the field v_j centered about the element boundaries are zero. These isolate each element from its neighbours as there is then no coupling between elements. In

each element $v_j(x,t) = \text{const}$ is an equilibrium. It is dynamically attractive provided the instability controlled by α/h^2 is not too large compared with the dissipation of order $1/h^4$. As stated above for the local IBCs, this simple class of solutions provide the basis for analysing the $\gamma \neq 0$ case when the elements are coupled together.

When evaluated at $\gamma = 1$ the non-local IBCs (2.7), in the jth field give

$$\begin{aligned} v_j(x_{j+1},t) - v_j(x_j,t) &= v_{j+1}(x_{j+1},t) - v_j(x_j,t)\,, \\ v_j(x_j,t) - v_j(x_{j-1},t) &= v_j(x_j,t) - v_{j-1}(x_{j-1},t)\,. \end{aligned} \tag{2.11}$$

That is, at $\gamma = 1$, the non-local IBCs require the first difference in x of the field v_j centered about the element boundaries to be equal to the first difference in adjacent fields evaluated at their midpoints. Equations (2.11) simplify to

$$\begin{aligned} v_j(x_{j+1},t) &= v_{j+1}(x_{j+1},t)\,, \\ v_j(x_{j-1},t) &= v_{j-1}(x_{j-1},t)\,. \end{aligned} \tag{2.12}$$

Similarly, (2.8) evaluated at $\gamma = 1$ in the jth, gives

$$\begin{aligned} &v_j(x_{j+2},t) - 3v_j(x_{j+1},t) + 3v_j(x_j,t) - v_j(x_{j-1},t) \\ &\quad = v_{j+2}(x_{j+2},t) - 3v_{j+1}(x_{j+1},t) + 3v_j(x_j,t) - v_{j-1}(x_{j-1},t)\,, \\ &v_j(x_{j+1},t) - 3v_j(x_j,t) + 3v_j(x_{j-1},t) - v_j(x_{j-2},t) \\ &\quad = v_{j+1}(x_{j+1},t) - 3v_j(x_j,t) + 3v_{j-1}(x_{j-1},t) - v_{j-2}(x_{j-2},t)\,. \end{aligned} \tag{2.13}$$

Using (2.12), it follows that (2.13) simplies to

$$\begin{aligned} v_{j+2}(x_{j+2},t) &= v_j(x_{j+2},t)\,, \\ v_{j-2}(x_{j-2},t) &= v_j(x_{j-2},t)\,. \end{aligned} \tag{2.14}$$

Therefore, the non-local IBCs evaluated at $\gamma = 1$ requires that the field $v_j(x,t)$ when extrapolated to $x_{j\pm1}$ and $x_{j\pm2}$ is to equal the grid point value of the subgrid field of that element, $v_{j\pm1}$ and $v_{j\pm2}$ respectively. This is sufficient continuity to ensure that the holistic model is relevant to the original PDE.

Figure 2.2 is a schematic representation of non-local boundary conditions evaluated at $\gamma = 1$. We restrict our plot of the fields $v_j(x,t)$ and $v_{j\pm1}(x,t)$ to the domain $[x_{j-1}, x_{j+1}]$ for this illustration so as not to clutter this diagram with five fields. At x_{j+1} we see the fields $v_j(x,t)$ and $v_{j\pm1}(x,t)$ are equal. Similarly, these fields are equal at x_j and x_{j-1}. Note that the field $v_{j-1}(x,t)$ extends to at least x_{j+1} and the field $v_{j+1}(x,t)$ extends to at least x_{j-1}.

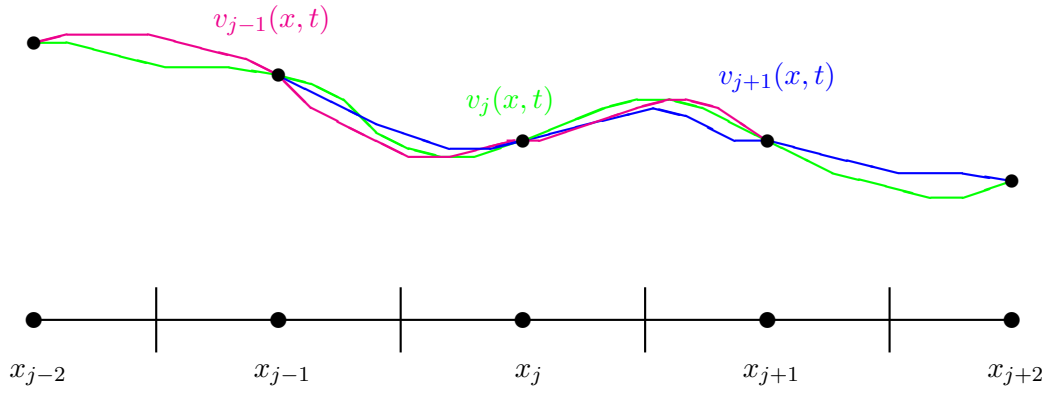

Figure 2.2: Schematic diagram of the fields $v_j(x,t)$, $v_{j+1}(x,t)$ and $v_{j-1}(x,t)$ for the non-local IBCs with $\gamma = 1$

These non-local IBCs ensure that holistic models of higher orders in γ are consistent with (2.1) to high orders in h. This relationship is explained in more detail in §2.5. Additional representations of the non-local IBCs are presented and discussed in [46, 53].

2.2 Centre manifold theory provides the basis for the analysis

The following application of centre manifold theory to rigorously develop the above ideas is based upon the linear dynamics of the Kuramoto–Sivashinsky equation (2.1) and closely follows the justification given by Roberts [54] for Burgers' equation.

The holistic method is supported by the existence, relevance and approximation theorems [5] of centre manifold theory. We consider each here in turn, to give theoretical support to the application of the holistic technique to discretising the Kuramoto–Sivashinsky equation.

2.2.1 There exists a centre manifold

Adjoin to the Kuramoto–Sivashinsky equation (2.1) the dynamically trivial equations

$$\frac{\partial\gamma}{\partial t}=\frac{\partial\alpha}{\partial t}=0, \tag{2.15}$$

and consider the dynamics in the extended state space $(u(x),\gamma,\alpha)$. This method is commonly used to unfold bifurcations [4, §1.5].

The analysis is based around the fixed point $u=$ constant and $\gamma=\alpha=0$, within each element. Linearizing the PDE about each fixed point $u=\text{constant}+u'(x,t)$ gives

$$\frac{\partial u'}{\partial t}=-\frac{\partial^4 u'}{\partial x^4}\,,\quad\text{such that}\quad \left.\frac{\partial u'}{\partial x}\right|_{x=x_{j\pm1/2}}=\left.\frac{\partial^3 u'}{\partial x^3}\right|_{x=x_{j\pm1/2}}=0\,,$$

when the local IBCs (2.4–2.5) are used and

$$\frac{\partial u'}{\partial t}=-\frac{\partial^4 u'}{\partial x^4}\,,\quad\text{such that}\quad \delta_x u'(x,t)\big|_{x=x_{j\pm1/2}}=\delta_x^3 u'(x,t)\Big|_{x=x_{j\pm1/2}}=0\,,$$

when the non-local IBCs (2.7–2.8) are implemented. These are the hyper-diffusion equation with isolating boundary conditions. The nth linear eigenmode associated with each element is

$$\alpha = \gamma = 0\,, \quad u' \propto e^{\lambda_n t} \cos\left[\frac{n\pi}{h}(x - x_{j-1/2})\right]\,, \tag{2.16}$$

for both the local IBCs (2.4–2.5) and the non-local IBCs (2.7–2.8), where $n = 0, 1, \ldots$ and the eigenvalue $\lambda_n = -n^4\pi^4/h^4$. There are also the trivial modes $\gamma = \text{const}$ and $\alpha = \text{const}$. Therefore, in a domain of m elements there are $m + 2$ zero eigenvalues. There is a zero eigenvalue associated with each of the m elements and 2 zero eigenvalues from the trivial (2.15). All other eigenvalues are negative $\leq -\pi/h^4$. Thus, the existence theorem ([5, p281] or [65, p96]) guarantees that a $m + 2$ dimensional centre manifold $\mathcal{M}$ exists for (2.1) with the trivial (2.15) and IBCs (2.7–2.8) or (2.7–2.8). The centre manifold is global in u but local in γ and α. In practice α is a measure of the nonlinearity in u.

We parametrise the $m + 2$ dimensional centre manifold $\mathcal{M}$ by the $m + 2$ parameters γ, α and a measure of u in each element. Here we use the grid values u_j as the measure of u in each element and denote $\boldsymbol{u}$ as the collection of all such grid values. Thus $\mathcal{M}$ is

$$u(x, t) = v(x; \boldsymbol{u}, \gamma, \alpha)\,. \tag{2.17}$$

The corresponding amplitude condition is

$$u_j = v(x_j; \boldsymbol{u}, \gamma, \alpha)\,. \tag{2.18}$$

The existence theorem [5] also asserts that on the centre manifold the para-

meters u_j evolve deterministically

$$\dot{u}_j = g_j(\boldsymbol{u}, \gamma, \alpha)\,, \tag{2.19}$$

where $\dot{u}_j$ denotes du_j/dt, and g_j is the restriction of the Kuramoto–Sivashinsky equation (2.1) with the trivial (2.15) and IBCs (2.4–2.5) or (2.7–2.8) to $\mathcal{M}$. It is the evolution (2.19) of the grid points that gives the holistic model.

In this application, the centre manifold is quite abstract to visualize. Since the subgrid field is of great physical interest, here we investigate the appearance of the subgrid field $v_j(x; \boldsymbol{u}, \gamma, \alpha)$ (denoted by the subscript j) on the centre manifold $\mathcal{M}$.

We view the centre manifold as the union of all states of the collection of subgrid fields $v_j(x; \boldsymbol{u}, \gamma, \alpha)$ over the physical domain. The centre manifold $\mathcal{M}$ is related to the subgrid field $v_j(x; \boldsymbol{u}, \gamma, \alpha)$ in the following way. Any field $v(x; \boldsymbol{u}, \gamma, \alpha)$ on $\mathcal{M}$ may be written as

$$v(x; \boldsymbol{u}, \gamma, \alpha) = \sum_j v_j(x; \boldsymbol{u}, \gamma, \alpha)\, \chi_j(x)\,, \tag{2.20}$$

where the characteristic function $\chi_j(x)$ is 1 if $x_{j-1/2} < x < x_{j+1/2}$ and 0 otherwise.

2.2.2 The holistic model is relevant to the PDE

The application of centre manifold theory establishes that in principle we may find a low dimensional model (2.19), or for example (2.2). However, we need to support the claim that our description of the interacting elements (2.17–2.19) models the Kuramoto–Sivashinsky system (2.1).

The relevance theorem of centre manifolds, [5, p282] or [65, p128], guarantees that all solutions of the Kuramoto–Sivashinsky system (2.1) with (2.15)

and the IBCs (2.4–2.5) or (2.7–2.8), which remain in the neighbourhood of the fixed points u is piecewise constant and $\gamma = \alpha = 0$ in $(u(x), \gamma, \alpha)$ space are exponentially quickly attracted to a solution of the m evolution equations (2.19) of the discretisation. For our application of centre manifold theory to the holistic model we require this neighbourhood to include $\gamma = 1$ and α of interest. We estimate the rate of attraction by the leading negative eigenvalue, here $\lambda_1 = -\pi^4/h^4$. The actual rate of attraction may be less than $-\pi^4/h^4$ since we must evaluate the holistic model (2.17–2.19) at $\gamma = 1$.

Centre manifold theory similarly guarantees that the stability near the fixed points is the same in both the model and the original dynamics. After exponentially quick transients have died out, the evolution of the discretisation (2.19) on the centre manifold, accurately models the complete system (2.1) and the local IBCs (2.4–2.5) or the non-local IBCs (2.7–2.8).

2.2.3 Approximate the shape of the centre manifold

Having established that we may find a low dimensional description (2.17–2.19) of the interacting elements that is relevant to the Kuramoto–Sivashinsky system (2.1), we need to construct the shape of the centre manifold and the corresponding evolution on the manifold.

The approximation theorem of Carr & Muncaster [5, p283] assures us that upon substituting the ansatz (2.17–2.19) into the complete system and solving to some order of error in α and γ, then $\mathcal{M}$ and the evolution thereon will be approximated to the same order.

With this application we need to evaluate the approximations at $\gamma = 1$, because it is only then that the artificial internal boundaries are removed.

Therefore, although the order of error provides assurance, the actual error due to the evaluation at $\gamma = 1$ is not estimated. However, the holistic method for discretising the Kuramoto–Sivashinsky equation is supported by three main results: firstly, the smooth homotopy to $\gamma = 0$; secondly the holistic models developed with the local IBCs (2.4–2.5) or the non-local IBCs (2.7–2.8) are consistent with the Kuramoto–Sivashinsky equation to some order, see §2.5; thirdly, we see in Chapters 3–4 that the holistic models are supported by their excellent performance at modelling both steady state solutions and time dependent phenomena of the Kuramoto–Sivashinsky system.

2.3 Computer algebra handles the details

We now detail the construction of the centre manifold model for the Kuramoto–Sivashinsky equation (2.1). For definiteness, here we consider domains periodic in space.

To construct the centre manifold, we solve for the field v_j in each element. Recall from §2.2.1 that a state of the centre manifold (2.17) is effectively the union over j of all subgrid fields $v_j(x; \boldsymbol{u}(t), \gamma, \alpha)$ from the m elements. For (2.1) with periodic boundary conditions, by symmetry the subgrid field is identical in each element, except for the appropriate shift in the grid index j . Therefore, we construct the subgrid field for the general jth element.

The algebraic details of the derivation of the centre manifold model (2.17–2.19) are handled by computer algebra. In an algorithm introduced in [52], the program iterates to drive to zero the residuals of the governing differential equation (2.1) and its boundary conditions, either the local IBCs (2.4–2.5), or the non-local IBCs (2.7–2.8).

Since the algebraic details are tedious, they are not given here for the Kuramoto–Sivashinsky equation. Instead, the equations presented in §2.3.1 that form the holistic models are solved by the computer algebra program listed in A.1.2 and the resulting holistic models with errors $\mathcal{O}(\gamma^3, \alpha^2)$, $\mathcal{O}(\gamma^4, \alpha^2)$ and $\mathcal{O}(\gamma^5, \alpha^2)$ are listed in §2.3.2.

2.3.1 Solve symbolic equations for the centre manifold

Recall from §2.2 that the centre manifold (2.17) is parametrised by the grid values $\boldsymbol{u}$ and that the evolution of the grid values is given by (2.19). Therefore, to construct the subgrid field for the jth element we solve

$$\frac{\partial v_j}{\partial t} = \sum_k \frac{\partial v_j}{\partial u_k} g_k = -4\frac{\partial^4 v_j}{\partial x^4} - \alpha\left(\frac{\partial^2 v_j}{\partial x^2} + v_j \frac{\partial v_j}{\partial x}\right), \tag{2.21}$$

together with either the local IBCs (2.4–2.5) or the non-local IBCs (2.7–2.8) and the amplitude equation (2.18), to some order in γ and α.

The equations solved to construct the field in each element involve the symbolic parameters α, γ and the grid values u_j's. We implement an iteration scheme. We seek $v_j = \widetilde{v}_j + v'_j$ and $g_j = \widetilde{g}_j + g'_j$, where $\widetilde{v}_j, \widetilde{g}_j$ denote the current approximation and v'_j, g'_j are the sought corrections. In each iteration we solve a problem of the form,

$$-4\frac{\partial^4 v'_j}{\partial x^4} = g'_j + \text{Residual}\,, \tag{2.22}$$

where

$$\text{Residual} = \sum_k \frac{\partial \widetilde{v}_j}{\partial u_k} g_k + 4\frac{\partial^4 \widetilde{v}_j}{\partial x^4} + \alpha\left(\frac{\partial^2 \widetilde{v}_j}{\partial x^2} + \widetilde{v}_j \frac{\partial \widetilde{v}_j}{\partial x}\right), \tag{2.23}$$

together with the appropriate form of the IBCs, for updates to the subgrid field and the evolution of the grid values. The residual in (2.23) is the residual of the Kuramoto–Sivashinsky system for the current approximation.

The iteration scheme is started with the linear solution in each element, namely $v_j(x, \boldsymbol{u}, \gamma, \alpha) = \text{const} = u_j$ and $g_j(\boldsymbol{u}, \gamma, \alpha) = 0$. The REDUCE program in Appendix A.1.2 iterates to drive the residuals of the Kuramoto–Sivashinsky equation (2.21) and the IBCs to zero, to some order in γ and α.

2.3.2 Various holistic models

The holistic model is given by the evolution on the centre manifold (2.19). Recall from §2.1 that $\gamma = 1$ is the case of interest because the local IBCs (2.4–2.5) or the non-local IBCs (2.7–2.8) evaluated at $\gamma = 1$ ensure sufficient continuity to recover the original problem.

Here the holistic models of the Kuramoto–Sivashinsky equation (2.1) are listed to various orders in γ and α, written in terms of the centered difference and mean operators, $\delta u_j = u_{j+1/2} - u_{j-1/2}$ and $\mu u_j = (u_{j+1/2} + u_{j-1/2})/2$, respectively. The models listed here are constructed using the REDUCE program in Appendix A.1.2 which implements the algorithm described in §2.3.1.

Only holistic models that are low order in the nonlinearity, that is errors $\mathcal{O}(\alpha^2)$, are presented in detail here. Also listed are traditional centered difference approximations to the Kuramoto–Sivashinsky equation, which have the same stencil width as the holistic models presented.

In order to represent the spatial fourth derivative in the Kuramoto–Sivashinsky equation, we need to determine the interactions between at least

next-nearest neighbouring elements. Thus, the first approximation we may consider involves up to quadratic terms in γ and results in a 5 point stencil approximation.

The $\mathcal{O}(\gamma^3, \alpha^2)$ holistic models are

$$\begin{aligned} \dot{u_j} &= -\frac{\gamma\alpha}{h^2}\delta^2 u_j - \frac{\gamma\alpha}{h}u_j\delta\mu u_j - \frac{4\gamma^2}{h^4}\delta^4 u_j + \frac{\gamma^2\alpha}{12h^2}\delta^4 u_j \\ &\quad + \frac{\gamma^2\alpha}{48h}\left(8u_j\delta^3\mu u_j + \delta^2 u_j\delta^3\mu u_j + \delta^4 u_j\delta\mu u_j\right) \\ &\quad + \mathcal{O}\left(\gamma^3, \alpha^2\right), \end{aligned} \tag{2.24}$$

for the local IBCs (2.4–2.5), and

$$\begin{aligned} \dot{u_j} &= -\frac{\gamma\alpha}{h^2}\delta^2 u_j - \frac{\gamma\alpha}{h}u_j\delta\mu u_j - \frac{4\gamma^2}{h^4}\delta^4 u_j + \frac{\gamma^2\alpha}{12h^2}\delta^4 u_j \\ &\quad + \frac{\gamma^2\alpha}{12h}\left(2u_j\delta^3\mu u_j + \delta^2 u_j\delta^3\mu u_j + \delta^4 u_j\delta\mu u_j\right) \\ &\quad + \mathcal{O}\left(\gamma^3, \alpha^2\right), \end{aligned} \tag{2.25}$$

for the non-local IBCs (2.7–2.8). These low order models form 5 point stencil approximations, since the evolution of u_j involves $u_j, u_{j\pm1}$ and $u_{j\pm2}$. The first line of both (2.24) and (2.25) when evaluated at $\gamma = 1$, gives a 2nd order centered difference approximation for the hyper-diffusion term ($4u_{xxxx}$), a 4th order centered difference approximation to the linear growth term (αu_{xx}) and a second order centered difference approximation to the nonlinear advection term ($\alpha u u_x$). The second line of both holistic models gives the first correction which models some subgrid scale structure of the interaction between the nonlinearity and the inter-element coupling.

The holistic model (2.24), formed with the local IBCs, contains the approximation

$$\alpha u u_x|_{x_j} \approx \alpha\left(9u_j\frac{u_{j+1} - u_{j-1}}{16h} + \frac{u_{j+1}^2 - u_{j-1}^2}{16h} - \frac{u_{j+2}u_{j+1} - u_{j-2}u_{j-1}}{48h}\right.$$

$$-\frac{u_{j+2}u_j - u_{j-2}u_j}{16h}\Bigg) \,, \tag{2.26}$$

for the nonlinear term when evaluated at $\gamma = 1$. Similarly, the holistic model (2.25) formed with the non-local IBCs contains the approximation

$$\alpha u u_x|_{x_j} \approx \alpha \left(u_j \frac{u_{j+1} - u_{j-1}}{4h} + \frac{u_{j+1}^2 - u_{j-1}^2}{4h} - \frac{u_{j+2}u_{j+1} - u_{j-2}u_{j-1}}{12h} \right) . \tag{2.27}$$

when evaluated at $\gamma = 1$.

The approximation (2.26) is a $9/8 : 1/4 : -1/8 : -1/4$ mix of the approximations (1.2), (1.3), (2.3) and

$$\alpha u u_x\big|_{x_j} \approx \alpha \frac{u_{j+2}u_j - u_{j-2}u_j}{4h} \,, \tag{2.28}$$

respectively. Similarly, (2.27) is a $1/2 : 1 : -1/2$ mix of the approximations (1.2), (1.3) and (2.3). These non-standard approximations (2.26–2.27) to the nonlinear term $\alpha u u_x$, arise due to the modelling of subgrid scale interactions between the Kuramoto–Sivashinsky equation and the inter-element coupling.

One of the aims here is to determine which IBCs provides the best model for the subgrid scale interactions of the Kuramoto–Sivashinsky equation.

The $\mathcal{O}\left(\gamma^4, \alpha^2\right)$ holistic models are

$$\begin{aligned}
\dot{u}_j \;=\; & -\frac{\gamma\alpha}{h^2}\delta^2 u_j - \frac{\gamma\alpha}{h} u_j \delta\mu u_j - \frac{4\gamma^2}{h^4}\delta^4 u_j + \frac{\gamma^2\alpha}{12h^2}\delta^4 u_j \\
& + \frac{2\gamma^3}{3h^4}\delta^6 u_j - \frac{\gamma^3\alpha}{90h^2}\delta^6 u_j \\
& + \frac{\gamma^2\alpha}{48h}\left(8u_j\delta^3\mu u_j + \delta^2 u_j \delta^3 \mu u_j + \delta^4 u_j \delta\mu u_j\right) \\
& - \frac{\gamma^3\alpha}{3840h}\Big(128\, u_j\delta^5\mu u_j + 102\, \delta^4 u_j \delta^3 \mu u_j + 80\, \delta^2 u_j \delta^3 \mu u_j \\
& \quad + 80\, \delta^4 u_j \delta\mu u_j + 70\, \delta^2 u_j \delta^5 \mu u_j + 36\, \delta^6 u_j \delta\mu u_j \\
& \quad + 17\, \delta^4 u_j \delta^5 \mu u_j + 17\, \delta^6 u_j \delta^3 \mu u_j\Big) + \mathcal{O}\left(\gamma^4, \alpha^2\right) \,,
\end{aligned} \tag{2.29}$$

for the local IBCs (2.4–2.5), and

$$\begin{aligned}\dot{u_j} &= -\frac{\gamma\alpha}{h^2}\delta^2 u_j - \frac{\gamma\alpha}{h}u_j\delta\mu u_j - \frac{4\gamma^2}{h^4}\delta^4 u_j + \frac{\gamma^2\alpha}{12h^2}\delta^4 u_j \\ &\quad + \frac{2\gamma^3}{3h^4}\delta^6 u_j - \frac{\gamma^3\alpha}{90h^2}\delta^6 u_j \\ &\quad + \frac{\gamma^2\alpha}{12h}\left(2u_j\delta^3\mu u_j + \delta^2 u_j\delta^3\mu u_j + \delta^4 u_j\delta\mu u_j\right) \\ &\quad - \frac{\gamma^3\alpha}{480h}\left(16\,u_j\delta^5\mu u_j + 30\,\delta^4 u_j\delta^3\mu u_j + 40\,\delta^2 u_j\delta^3\mu u_j\right. \\ &\qquad + 40\,\delta^4 u_j\delta\mu u_j + 28\,\delta^2 u_j\delta^5\mu u_j + 14\,\delta^6 u_j\delta\mu u_j \\ &\qquad \left. + 7\delta^4 u_j\delta^5\mu u_j + 7\delta^6 u_j\delta^3\mu u_j\right) + \mathcal{O}\left(\gamma^4, \alpha^2\right), \end{aligned} \tag{2.30}$$

for the non-local IBCs (2.7–2.8). These discretisations form 7 point stencil approximations, involving $u_j, u_{j\pm1}, u_{j\pm2}$ and $u_{j\pm3}$. The first two lines of (2.29) and (2.30) when evaluated at $\gamma = 1$, give a 4th order centered difference approximation to the hyper-diffusion term, a 6th order centered difference approximation to the linear growth term and a second order centered difference approximation to the nonlinear advection term. The third and remaining lines for both holistic models account for higher order subgrid scale dynamics of the nonlinearity and its inter-element coupling.

The $\mathcal{O}\left(\gamma^5, \alpha^2\right)$ holistic models are

$$\begin{aligned}\dot{u_j} &= -\frac{\gamma\alpha}{h^2}\delta^2 u_j - \frac{\gamma\alpha}{h}u_j\delta\mu u_j - \frac{4\gamma^2}{h^4}\delta^4 u_j + \frac{\gamma^2\alpha}{12h^2}\delta^4 u_j \\ &\quad + \frac{2\gamma^3}{3h^4}\delta^6 u_j - \frac{\gamma^3\alpha}{90h^2}\delta^6 u_j - \frac{7\gamma^4}{60h^4}\delta^8 u_j + \frac{\gamma^4\alpha}{560h^2}\delta^8 u_j \\ &\quad + \frac{\gamma^2\alpha}{48h}\left(8u_j\delta^3\mu u_j + \delta^2 u_j\delta^3\mu u_j + \delta^4 u_j\delta\mu u_j\right) \\ &\quad - \frac{\gamma^3\alpha}{3840h}\left(128\,u_j\delta^5\mu u_j + 102\,\delta^4 u_j\delta^3\mu u_j + 80\,\delta^2 u_j\delta^3\mu u_j\right. \\ &\qquad + 80\,\delta^4 u_j\delta\mu u_j + 70\,\delta^2 u_j\delta^5\mu u_j + 36\,\delta^6 u_j\delta\mu u_j \\ &\qquad \left. + 17\,\delta^4 u_j\delta^5\mu u_j + 17\,\delta^6 u_j\delta^3\mu u_j\right) \end{aligned}$$

$$
\begin{aligned}
&+\frac{\gamma^4\alpha}{967680h}\Big(6912\,u_j\delta^7\mu u_j+17640\,\delta^2u_j\delta^5\mu u_j+8982\,\delta^2u_j\delta^7\mu u_j\\
&\quad+25704\,\delta^4u_j\delta^3\mu u_j+28315\,\delta^4u_j\delta^5\mu u_j+5631\,\delta^4u_j\delta^7\mu u_j\\
&\quad+1008\,\delta^6u_j\delta\mu u_j+22065\,\delta^6u_j\delta^3\mu u_j+9658\,\delta^6u_j\delta^5\mu u_j\\
&\quad+902\,\delta^6u_j\delta^7\mu u_j+3132\,\delta^8u_j\delta\mu u_j+3827\,\delta^8u_j\delta^3\mu u_j\\
&\quad+902\,\delta^8u_j\delta^5\mu u_j\Big)+\mathcal{O}\left(\gamma^5,\alpha^2\right)\,. \qquad (2.31)
\end{aligned}
$$

for the local IBCs (2.4–2.5) and

$$
\begin{aligned}
\dot{u}_j \;=\;& -\frac{\gamma\alpha}{h^2}\delta^2u_j-\frac{\gamma\alpha}{h}u_j\delta\mu u_j-\frac{4\gamma^2}{h^4}\delta^4u_j+\frac{\gamma^2\alpha}{12h^2}\delta^4u_j\\
&+\frac{2\gamma^3}{3h^4}\delta^6u_j-\frac{\gamma^3\alpha}{90h^2}\delta^6u_j\\
&-\frac{7\gamma^4}{60h^4}\delta^8u_j+\frac{\gamma^4\alpha}{560h^2}\delta^8u_j\\
&+\frac{\gamma^2\alpha}{12h}\left(2u_j\delta^3\mu u_j+\delta^2u_j\delta^3\mu u_j+\delta^4u_j\delta\mu u_j\right)\\
&-\frac{\gamma^3\alpha}{480h}\Big(16\,u_j\delta^5\mu u_j+30\,\delta^4u_j\delta^3\mu u_j+40\,\delta^2u_j\delta^3\mu u_j\\
&\quad+40\,\delta^4u_j\delta\mu u_j+28\,\delta^2u_j\delta^5\mu u_j+14\,\delta^6u_j\delta\mu u_j\\
&\quad+7\delta^4u_j\delta^5\mu u_j+7\delta^6u_j\delta^3\mu u_j\Big)\\
&+\frac{\gamma^4\alpha}{60480h}\Big(432\,u_j\delta^7\mu u_j+3528\,\delta^2u_j\delta^5\mu u_j+1507\,\delta^2u_j\delta^7\mu u_j\\
&\quad+3780\,\delta^4u_j\delta^3\mu u_j+3951\,\delta^4u_j\delta^5\mu u_j+984\,\delta^4u_j\delta^7\mu u_j\\
&\quad+1764\,\delta^6u_j\delta\mu u_j+3419\,\delta^6u_j\delta^3\mu u_j+1414\,\delta^6u_j\delta^5\mu u_j\\
&\quad+164\,\delta^6u_j\delta^7\mu u_j+523\,\delta^8u_j\delta\mu u_j+656\,\delta^8u_j\delta^3\mu u_j\\
&\quad+164\,\delta^8u_j\delta^5\mu u_j\Big)+\mathcal{O}\left(\gamma^5,\alpha^2\right)\,, \qquad (2.32)
\end{aligned}
$$

for the non-local IBCs (2.7–2.8). These discretisations form 9 point stencil approximations, involving $u_j, u_{j\pm1}, u_{j\pm2}, u_{j\pm3}$ and $u_{j\pm4}$. The first two lines of (2.31) and (2.32) when evaluated at $\gamma = 1$ give a 6th order centered difference approximation for the hyperdiffusion term, an 8th order centered difference

approximation for the linear growth term and a 2nd order centered difference approximation for the nonlinear advection term. The third and remaining lines account for higher order subgrid scale interactions.

Note that holistic models retaining terms up to γ^p result in approximations that are of $(2p+1)$ stencil width. The order of α terms retained in the model does not affect the stencil width of the approximation.

Since the holistic approximations have a large number of terms, I do not suggest that the approximations should be coded manually for any particular application. The computer algebra program listed in Appendix A.1.2 is used in conjunction with the unix editor SED to automatically write the discretisation in a form that is implemented in MATLAB for numerical exploration.

Compare to conventional centered difference models. Here 5 point, 7 point and 9 point centered difference approximations are listed. A direct 5 point stencil centered difference approximation to the Kuramoto–Sivashinsky equation (2.1) is

$$\dot{u_j} = -\frac{\alpha}{h} u_j \delta\mu u_j - \frac{\alpha}{h^2}\delta^2 u_j - \frac{4}{h^4}\delta^4 u_j + \mathcal{O}\left(h^2\right) . \tag{2.33}$$

A 7 point stencil centered difference approximation to the Kuramoto–Sivashinsky equation is given by

$$\begin{aligned} \dot{u_j} = & -\frac{\alpha}{h}\left(u_j\delta\mu u_j - \frac{1}{6}\,u_j\delta^3\mu u_j\right) - \frac{\alpha}{h^2}\left(\delta^2 u_j - \frac{1}{12}\,\delta^4 u_j\right) \\ & - \frac{4}{h^4}\left(\delta^4 u_j - \frac{1}{6}\,\delta^6 u_j\right) + \mathcal{O}\left(h^4\right) , \end{aligned} \tag{2.34}$$

and a 9 point stencil centered difference approximation to the Kuramoto–Sivashinsky equation is

$$\dot{u_j} = -\frac{\alpha}{h}\left(u_j\delta\mu u_j - \frac{1}{6}\,u_j\delta^3\mu u_j + \frac{1}{30}\,u_j\delta^5\mu u_j\right)$$

$$- \frac{\alpha}{h^2}\left(\delta^2 u_j - \frac{1}{12}\,\delta^4 u_j + \frac{1}{90}\,\delta^6 u_j\right)$$
$$- \frac{4}{h^4}\left(\delta^4 u_j - \frac{1}{6}\,\delta^6 u_j + \frac{7}{240}\,\delta^6 u_j\right) + \mathcal{O}\left(h^6\right) . \qquad (2.35)$$

There is a different view of the errors for the holistic models (2.24–2.32) compared to the centered difference approximations (2.33–2.35). Centre manifold theory supports the holistic approximations for finite h, with errors to some order in the inter-element coupling parameter γ, and the nonlinearity α. In contrast, the centered difference approximations are justified by consistency in the limit $h \to 0$. However, the particular choices of the IBCs (2.4–2.5) or (2.7–2.8), presented in §2.1 ensure that the holistic approximations are also consistent with (2.1) in the limit $h \to 0$.

2.4 Illustration of subgrid field enhances our view

Is §2.2.1 we explored the link between the abstract centre manifold description of the holistic models and the physical subgrid field. Recall that the collection of subgrid fields (2.20) over the physical domain form a state on the centre manifold. Here we examine some plots of example subgrid fields for various holistic models constructed with the non-local IBCs (2.7–2.8). In particular, we examine subgrid fields of the holistic models of steady states of the Kuramoto–Sivashinsky equation (2.1) at $\alpha = 20$ and $\alpha = 50$. This is not intended to be an in depth numerical study of the performance of the holistic models (reserved for Chapters 3–4) of the Kuramoto–Sivashinsky equation but rather an illustration of the link between the abstract centre manifold description and the physical subgrid fields for the low order holistic models

(2.25,2.30,2.32).

Traditional centered difference approximations may be developed using a Lagrangian interpolant to construct the subgrid field. In contrast, the subgrid field of the holistic method is constructed by actual solutions of the governing dynamics as discussed in §2.3.1.

We consider a grid of 8 equi-spaced elements on the interval $[0, \pi]$. We restrict our attention to odd symmetric solutions that are 2π-periodic. This is chosen to compare with the numerical investigations of Jolly et al. [25] which we consider in much more detail in Chapters 3–4. The subgrid fields are plotted for some approximations to the steady states of the Kuramoto–Sivashinsky equation (2.1) with these periodic boundary conditions, computed using holistic models with the non-local IBCs at $\alpha = 20$ and $\alpha = 50$.

Figure 2.3 displays an accurate solution[1] (blue curve) of the Kuramoto–Sivashinsky equation to compare with the subgrid field (green curve) of the 5 point stencil $\mathcal{O}(\gamma^3, \alpha^2)$ holistic approximation (2.25) (green discs), and the Lagrangian interpolant (magenta curve) constructed through a 2nd order centered difference approximation (magenta discs), for a steady state at $\alpha = 20$. Observe the collection of subgrid fields forms the field u which is a state on the centre manifold. The subgrid field of the holistic model more accurately represents the steady state of the Kuramoto–Sivashinsky equation at $\alpha = 20$, on this coarse grid. The jump across the subgrid fields at element boundaries is greater for the 2nd order centered difference approximation.

Higher order holistic models improve the accuracy and continuity of the subgrid field. Figure 2.4 displays the subgrid fields of various holistic models

[1]The accurate solutions shown in this Chapter are computed using a 6th order centered difference approximation with 48 grid points on $[0, \pi]$.

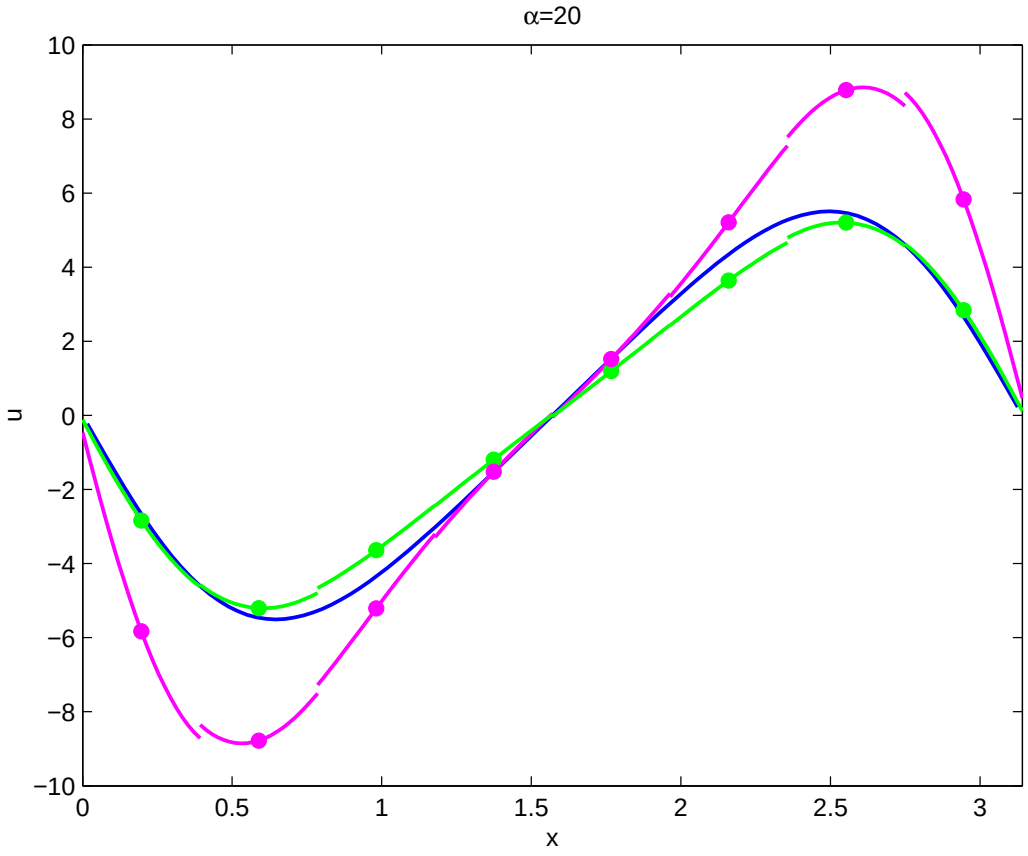

Figure 2.3: Subgrid field (green curve) of the holistic model (2.25) (green discs) and a Lagrangian interpolant (magenta curve) constructed through a 2nd order centered difference approximation (magenta discs) for a steady state of the Kuramoto–Sivashinsky equation at $\alpha = 20$, with 8 elements on $[0, \pi]$. An accurate solution is also plotted (blue curve).

for the same steady state of the Kuramoto–Sivashinsky equation depicted in Figure 2.3 for $\alpha = 20$. The $\mathcal{O}(\gamma^3, \alpha^2)$ holistic model (2.25) (green) is the least accurate and has the largest jump at the element boundaries. The $\mathcal{O}(\gamma^4, \alpha^2)$ (2.30) model (olive green) displays improvement over the holistic $\mathcal{O}(\gamma^3, \alpha^2)$ approximation. The $\mathcal{O}(\gamma^5, \alpha^2)$ (2.32) model (cyan) is the most accurate and has the smallest jump at the element boundaries.

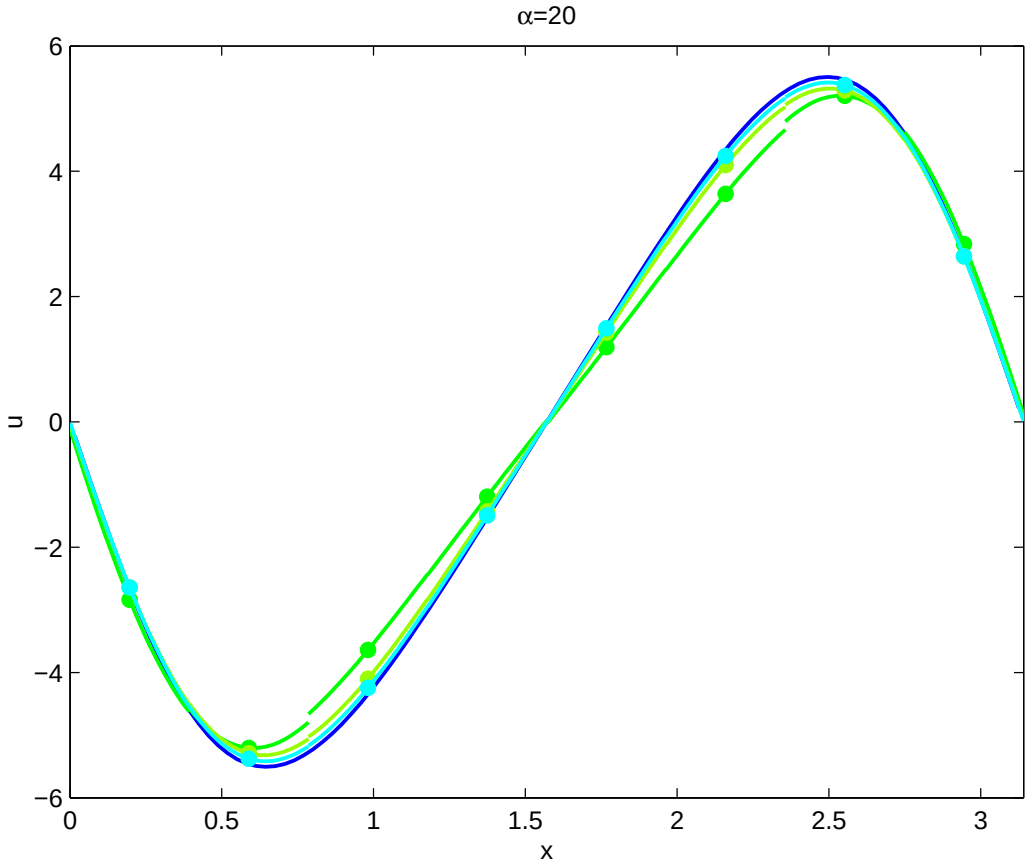

Figure 2.4: Subgrid fields of the holistic models with errors $\mathcal{O}(\gamma^3, \alpha^2)$ (2.25) (green), $\mathcal{O}(\gamma^4, \alpha^2)$ (2.30) (olive green) and $\mathcal{O}(\gamma^5, \alpha^2)$ (2.32) (cyan), for a steady state of the Kuramoto–Sivashinsky equation at $\alpha = 20$, with 8 elements on $[0, \pi]$. An accurate solution is also plotted (blue curve).

Figure 2.5 illustrates a steady state of the Kuramoto–Sivashinsky equation at $\alpha = 50$. For this value of the nonlinearity there is no steady state solution for centered difference approximations of either 2nd (2.33), 4th (2.34) or 6th order (2.35) on this coarse grid of 8 elements on $[0, \pi]$. However, the 5 point stencil holistic approximation with errors $\mathcal{O}(\gamma^3, \alpha^2)$ (2.25) (green) models this steady state of the Kuramoto–Sivashinsky equation even for such a large value of the nonlinearity on this coarse grid. This $\mathcal{O}(\gamma^3, \alpha^2)$ holistic model has large jumps across the subgrid field at the element boundaries, especially at $x = \pi/8$ and $x = 7\pi/8$. The $\mathcal{O}(\gamma^3, \alpha^2)$ subgrid field is not symmetric and is most inaccurate near the centre of the spatial domain considered here. The accurate field (blue curve), is symmetric. The 7 point stencil holistic approximation with errors $\mathcal{O}(\gamma^4, \alpha^2)$ (2.30) (olive green) shows improvement in accuracy and smaller jumps across the subgrid fields. This $\mathcal{O}(\gamma^4, \alpha^2)$ approximation is also not symmetric. The 9 point stencil holistic approximation with errors $\mathcal{O}(\gamma^5, \alpha^2)$ (2.32) (cyan) is the most accurate of the holistic models illustrated here. The subgrid field for the $\mathcal{O}(\gamma^5, \alpha^2)$ approximation is symmetric and the jumps across the subgrid fields are almost indiscernible.

These illustrations of the subgrid fields of steady states of the Kuramoto–Sivashinsky equation at $\alpha = 20$ and $\alpha = 50$ show the holistic models perform well at these values of the nonlinearity. More in-depth numerical investigations of the performance of the holistic models are explored in Chapter 3 for steady states and Chapter 4 for modelling time dependent solutions of the Kuramoto–Sivashinsky equation.

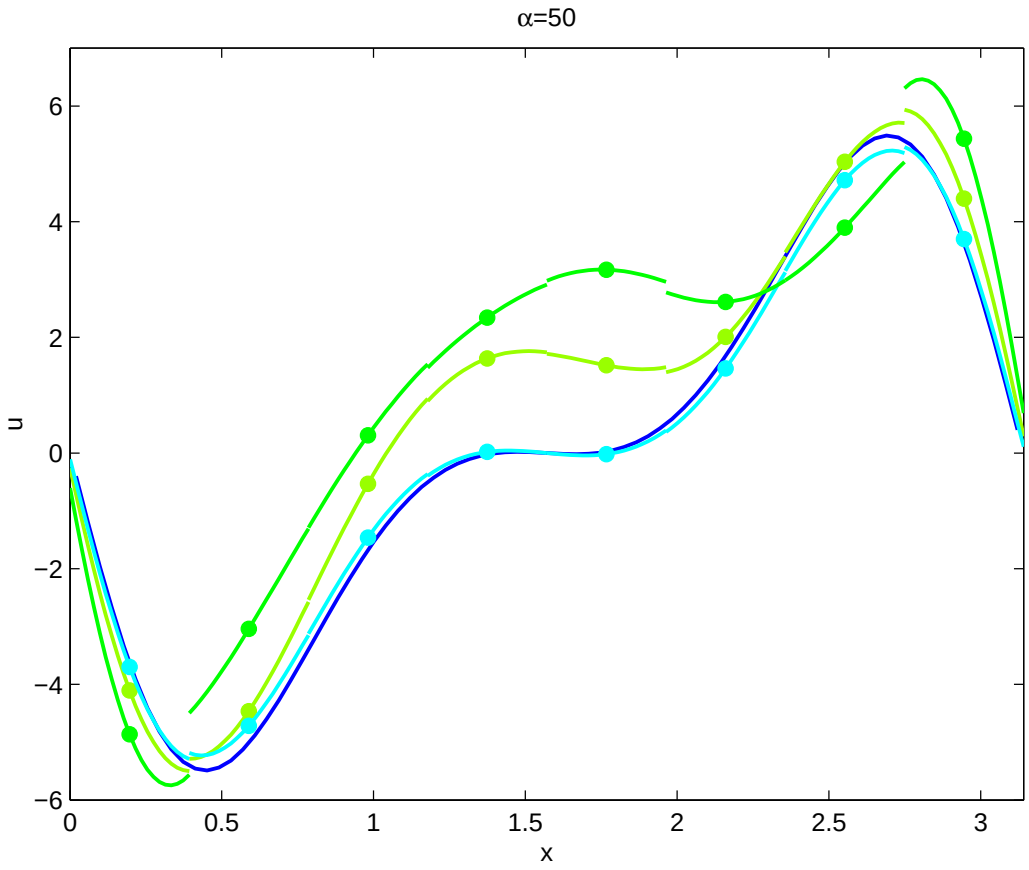

Figure 2.5: Subgrid fields of the holistic models with errors $\mathcal{O}(\gamma^3, \alpha^2)$ (2.25) (green), $\mathcal{O}(\gamma^4, \alpha^2)$ (2.30) (olive green) and $\mathcal{O}(\gamma^5, \alpha^2)$ (2.32) (cyan), for a steady state of the Kuramoto–Sivashinsky equation at $\alpha = 50$, with 8 elements on $[0, \pi]$. An accurate solution (blue curve) is also plotted.

2.5 Holistic models are consistent as $h \to 0$

Holistic models constructed by implementing the IBCs presented in §2.1 have a dual justification [46]. That is, they are supported by centre manifold asymptotics in α and γ, as well as justified by their consistency in grid size h.

Here we examine the equivalent PDEs for the holistic models (2.24–2.32) evaluated at $\gamma = 1$, and the centered difference approximations (2.33–2.35). The purpose of listing the equivalent PDEs for these approximations is to establish $\mathcal{O}\left(h^{2p-2}\right)$ consistency with the Kuramoto–Sivashinsky equation for holistic models retaining terms up to γ^p. High order consistency is not a primary goal of using this holistic approach, since we aim to develop and support models for finite element size h. However consistency is a well established feature of numerical models which we also maintain.

It has been proven in [46] that using IBCs of the form introduced in §2.1 and retaining terms up to γ^p in the holistic approximations results in approximations which are consistent with the linear terms of the Kuramoto–Sivashinsky equation (2.1) to $\mathcal{O}\left(h^{2p-2}\right)$ for $p \geq 2$. However, it appears that using IBCs (2.4–2.5) or (2.7–2.8) and retaining γ^p terms in the holistic discretisation ensures $\mathcal{O}\left(h^{2p-2}\right)$ consistency for the nonlinear terms as well. As yet no formal proof exists of this nonlinear consistency, but all holistic models of the Kuramoto–Sivashinsky equation, containing terms up to γ^7 and α^4 and constructed using IBCs (2.4–2.5) or (2.7–2.8), although not listed here, are nonlinearly consistent.

The equivalent PDEs for the various discretisations are found by expand-

ing the approximations in h about the point x_j. That is,

$$u_{j+1} = u_j + h\frac{\partial u_j}{\partial x} + \frac{h^2}{2}\frac{\partial^2 u_j}{\partial x^2} + \sum_{k=3}^{\infty} \frac{h^k}{k!}\frac{\partial^k u_j}{\partial x^k}\,, \tag{2.36}$$

and similarly for other $u_{j\pm m}$ to whatever order in h is required.

The equivalent PDEs for the 5 point stencil $\mathcal{O}(\gamma^3, \alpha^2)$ holistic models (2.24) and (2.25), which retain terms up to γ^2, are

$$\begin{aligned}\frac{\partial u}{\partial t} &= -\alpha\left(u\frac{\partial u}{\partial x} + \frac{\partial^2 u}{\partial x^2}\right) - 4\frac{\partial^4 u}{\partial x^4} - \frac{2h^2}{3}\frac{\partial^6 u}{\partial x^6} + \frac{h^4}{20}\frac{\partial^8 u}{\partial x^8} \\ &\quad + \alpha h^4\left(\frac{1}{12}\frac{\partial^3 u}{\partial x^3}\frac{\partial^2 u}{\partial x^2} + \frac{1}{12}\frac{\partial^4 u}{\partial x^4}\frac{\partial u}{\partial x} + \frac{1}{30}u\frac{\partial^5 u}{\partial x^5} + \frac{1}{20}\frac{\partial^6 u}{\partial x^6}\right) \\ &\quad + \mathcal{O}(h^6)\,,\end{aligned} \tag{2.37}$$

and

$$\begin{aligned}\frac{\partial u}{\partial t} &= -\alpha\left(u\frac{\partial u}{\partial x} + \frac{\partial^2 u}{\partial x^2}\right) - 4\frac{\partial^4 u}{\partial x^4} - \frac{2h^2}{3}\frac{\partial^6 u}{\partial x^6} + \frac{h^4}{20}\frac{\partial^8 u}{\partial x^8} \\ &\quad + \alpha h^4\left(\frac{1}{48}\frac{\partial^3 u}{\partial x^3}\frac{\partial^2 u}{\partial x^2} + \frac{1}{48}\frac{\partial^4 u}{\partial x^4}\frac{\partial u}{\partial x} + \frac{1}{30}u\frac{\partial^5 u}{\partial x^5} + \frac{1}{90}\frac{\partial^6 u}{\partial x^6}\right) \\ &\quad + \mathcal{O}(h^6)\,,\end{aligned} \tag{2.38}$$

respectively. The equivalent PDE for the 5 point centered difference approximation (2.33) is

$$\begin{aligned}\frac{\partial u}{\partial t} &= -\alpha\left(u\frac{\partial u}{\partial x} + \frac{\partial^2 u}{\partial x^2}\right) - 4\frac{\partial^2 u}{\partial x^2} \\ &\quad - h^2\left(\alpha\frac{1}{6}\frac{\partial^3 u}{\partial x^3}\frac{\partial u}{\partial x} + \alpha\frac{1}{12}\frac{\partial^4 u}{\partial x^4} + \frac{2}{3}\frac{\partial^6 u}{\partial x^6}\right) \\ &\quad + \mathcal{O}(h^4)\,.\end{aligned} \tag{2.39}$$

Observe that all three equivalent PDEs (2.37–2.39) are $\mathcal{O}(h^2)$ accurate. Note that the coefficients of the higher order terms are different in each of the these equivalent PDEs. The relative sizes of these higher order terms are not

discussed here, as our primary goal is to construct accurate approximations for finite h. This high order consistency is an added bonus.

The equivalent PDEs for the 7 point stencil $\mathcal{O}(\gamma^4, \alpha^2)$ holistic models (2.29) and (2.30), which retain terms up to γ^3, are

$$\begin{aligned}\frac{\partial u}{\partial t} &= -\alpha\left(u\frac{\partial u}{\partial x}+\frac{\partial^2 u}{\partial x^2}\right)-4\frac{\partial^4 u}{\partial x^4}-\frac{7h^4}{60}\frac{\partial^8 u}{\partial x^8}+\frac{13h^6}{756}\frac{\partial^{10} u}{\partial x^{10}}\\ &\quad -\alpha h^6\left(\frac{1}{16}\frac{\partial^4 u}{\partial x^4}\frac{\partial^3 u}{\partial x^3}+\frac{7}{120}\frac{\partial^5 u}{\partial x^5}\frac{\partial^2 u}{\partial x^2}+\frac{7}{240}\frac{\partial^6 u}{\partial x^6}\frac{\partial u}{\partial x}\right.\\ &\quad \left.+\frac{1}{140}u\frac{\partial^7 u}{\partial x^7}+\frac{1}{560}\frac{\partial^8 u}{\partial x^8}\right)\\ &\quad +\mathcal{O}(h^8)\,, \end{aligned} \tag{2.40}$$

and

$$\begin{aligned}\frac{\partial u}{\partial t} &= -\alpha\left(u\frac{\partial u}{\partial x}+\frac{\partial^2 u}{\partial x^2}\right)-4\frac{\partial^4 u}{\partial x^4}-\frac{7h^4}{60}\frac{\partial^8 u}{\partial x^8}+\frac{13h^6}{756}\frac{\partial^{10} u}{\partial x^{10}}\\ &\quad -\alpha h^6\left(\frac{17}{640}\frac{\partial^4 u}{\partial x^4}\frac{\partial^3 u}{\partial x^3}+\frac{7}{384}\frac{\partial^5 u}{\partial x^5}\frac{\partial^2 u}{\partial x^2}+\frac{3}{320}\frac{\partial^6 u}{\partial x^6}\frac{\partial u}{\partial x}\right.\\ &\quad \left.+\frac{1}{140}u\frac{\partial^7 u}{\partial x^7}+\frac{1}{560}\frac{\partial^8 u}{\partial x^8}\right)\\ &\quad +\mathcal{O}(h^8)\,. \end{aligned} \tag{2.41}$$

respectively. The equivalent PDE for the 7 point centered difference approximation (2.34) is

$$\begin{aligned}\frac{\partial u}{\partial t} &= -\alpha\left(u\frac{\partial u}{\partial x}+\frac{\partial^2 u}{\partial x^2}\right)-4\frac{\partial^2 u}{\partial x^2}\\ &\quad -h^4\left(\alpha\frac{1}{30}\frac{\partial^5 u}{\partial x^5}\frac{\partial u}{\partial x}+\alpha\frac{1}{90}\frac{\partial^6 u}{\partial x^6}+\frac{7}{60}\frac{\partial^8 u}{\partial x^8}\right)\\ &\quad +\mathcal{O}(h^6)\,. \end{aligned} \tag{2.42}$$

Observe that the three equivalent PDEs (2.40–2.42) are $\mathcal{O}(h^4)$ accurate.

The equivalent PDEs for the 9 point stencil $\mathcal{O}(\gamma^5, \alpha^2)$ holistic models (2.29) and (2.30), which retain terms up to γ^4, are

$$\begin{aligned}\frac{\partial u}{\partial t} &= -\alpha\left(u\frac{\partial u}{\partial x}+\frac{\partial^2 u}{\partial x^2}\right)-4\frac{\partial^4 u}{\partial x^4}-\frac{41h^6}{1890}\frac{\partial^{10}u}{\partial x^{10}}+\frac{13h^8}{2700}\frac{\partial^{12}u}{\partial x^{12}}\\ &\quad+\alpha h^8\left(\frac{341}{6720}\frac{\partial^5 u}{\partial x^5}\frac{\partial^4 u}{\partial x^4}+\frac{2537}{60480}\frac{\partial^6 u}{\partial x^6}\frac{\partial^3 u}{\partial x^3}+\frac{1507}{60480}\frac{\partial^7 u}{\partial x^7}\frac{\partial^2 u}{\partial x^2}\right.\\ &\quad\left.+\frac{523}{60480}\frac{\partial^8 u}{\partial x^8}\frac{\partial u}{\partial x}+\frac{1}{630}u\frac{\partial^9 u}{\partial x^9}+\frac{1}{3150}\frac{\partial^{10}u}{\partial x^{10}}\right)\\ &\quad+\mathcal{O}(h^{10})\,,\end{aligned}\tag{2.43}$$

and

$$\begin{aligned}\frac{\partial u}{\partial t} &= -\alpha\left(u\frac{\partial u}{\partial x}+\frac{\partial^2 u}{\partial x^2}\right)-4\frac{\partial^4 u}{\partial x^4}-\frac{41h^6}{1890}\frac{\partial^{10}u}{\partial x^{10}}+\frac{13h^8}{2700}\frac{\partial^{12}u}{\partial x^{12}}\\ &\quad+\alpha h^8\left(\frac{3433}{138240}\frac{\partial^5 u}{\partial x^5}\frac{\partial^4 u}{\partial x^4}+\frac{5927}{322560}\frac{\partial^6 u}{\partial x^6}\frac{\partial^3 u}{\partial x^3}+\frac{499}{53760}\frac{\partial^7 u}{\partial x^7}\frac{\partial^2 u}{\partial x^2}\right.\\ &\quad\left.+\frac{29}{8960}\frac{\partial^8 u}{\partial x^8}\frac{\partial u}{\partial x}+\frac{1}{630}u\frac{\partial^9 u}{\partial x^9}+\frac{1}{3150}\frac{\partial^{10}u}{\partial x^{10}}\right)\\ &\quad+\mathcal{O}(h^{10})\,.\end{aligned}\tag{2.44}$$

respectively. The equivalent PDE for the 9pt centered difference approximation (2.35) is

$$\begin{aligned}\frac{\partial u}{\partial t} &= -\alpha\left(u\frac{\partial u}{\partial x}+\frac{\partial^2 u}{\partial x^2}\right)-4\frac{\partial^2 u}{\partial x^2}\\ &\quad-h^6\left(\alpha\frac{1}{140}\frac{\partial^7 u}{\partial x^7}\frac{\partial u}{\partial x}+\alpha\frac{1}{560}\frac{\partial^8 u}{\partial x^8}+\frac{41}{1890}\frac{\partial^{10}u}{\partial x^{10}}\right)\\ &\quad+\mathcal{O}(h^8)\,.\end{aligned}\tag{2.45}$$

Observe that the three equivalent PDEs (2.43–2.45) are $\mathcal{O}(h^6)$ accurate.

This section confirms that the holistic models (2.24–2.32) constructed by retaining terms up to γ^p are consistent with the Kuramoto–Sivashinsky equation (2.1) to $\mathcal{O}(h^{2p-2})$. The proof of nonlinear consistency in general is left for further research.

2.6 Summary

Holistic discretisation [54] is straightforwardly extended to 4th order dissipative PDEs through the example of the Kuramoto–Sivashinsky equation [34]. We divide our domain into elements and introduce artificial internal boundary conditions (§2.1) which isolate the elements when $\gamma = 0$ and are relevant to the Kuramoto–Sivashinsky equation when $\gamma = 1$. Then centre manifold theory §2.2.1 supports a discrete model.

We have introduced two different possibilities for isolating the elements, namely the local IBCs (2.4–2.5) and the non-local IBCs (2.7–2.8). These IBCs are an extension to fourth order of the IBCs presented by Roberts [54, 46] for second order PDEs. The detailed numerical exploration of Chapter 3 shows the non-local IBCs are superior.

The holistic models listed in §2.3.2 have a dual justification (§2.5): they are supported by centre manifold theory for finite h; and they are consistent with the Kuramoto–Sivashinsky equation as the grid spacing $h \to 0$.

No formal error bounds exist at this time for the holistic method because the approximations are evaluated at $\gamma = 1$. However, a detailed numerical investigation of the holistic models of the steady states (Chapter 3) and time dependent (Chapter 4) solutions of the Kuramoto–Sivashinsky equation demonstrate that the holistic models evaluated at $\gamma = 1$ result in excellent performance on coarse grids.

The straightforward application of the holistic method to higher order systems such as the Kuramoto–Sivashinsky equation studied here, along with the excellent performance of the holistic models of Kuramoto–Sivashinsky equation demonstrated in Chapters 3–4, serves as further evidence that this

approach is a robust and useful method for discretising PDEs.

Chapter 3

Holistic models are accurate for steady states of the Kuramoto–Sivashinsky equation

Contents

The holistic method described in Chapter 2 provides a systematic approach to generate numerical approximations to the Kuramoto–Sivashinsky equation (2.1). These numerical approximations, such as those listed in §2.3.2 are of varying orders in the coupling parameter γ, which controls the order of inter-element interaction and the nonlinearity controlled by α. The approach is rigourously supported by centre manifold theory which guarantees the approximations are accurate and relevant for sufficiently small γ and α, as discussed in §2.2. However, the holistic models must be evaluated at $\gamma = 1$ to model the dynamics relevant to the Kuramoto–Sivashinsky equation, see §2.1. The remarkable performance of the holistic approximations on coarse grids, investigated here for the Kuramoto–Sivashinsky equation, supports the argument that the holistic approach is an accurate and useful method for discretising dissipative PDEs.

Here we investigate the accuracy of the holistic models by constructing and comparing bifurcation diagrams of the holistic approximations to conventional explicit centered difference approximations and to the bifurcation

diagrams presented by Jolly et al. [25] for various traditional Galerkin and nonlinear Galerkin approximations.

The Galerkin methods compared here are global approximations while the holistic approximations are local. Although both the holistic method and the nonlinear Galerkin methods make use of the inertial manifold of the Kuramoto–Sivashinsky equation, the analysis of the holistic method is based upon the dynamics of localised elements. The local nature makes the holistic technique a very robust method for modelling physical boundary conditions [53] and spatially varying PDEs.

We limit the investigation of this chapter to spatially periodic boundary solutions of period $L = 2\pi$. We also require odd symmetry such that $u(x,t)$ satisfies

$$u(x,t) = u(x+L,t) \quad \text{and} \quad u(x,t) = -u(L-x,t)\,. \tag{3.1}$$

We also restrict our investigation of the nonlinear parameter to $0 \leq \alpha \leq 70$. These restrictions are to compare our results to those of Jolly et al. [25] for approximate inertial manifold methods. For this range of α the trivial solution $u = 0$ undergoes pitchfork bifurcations at $\alpha = 4, 16, 36, 64$ leading to the unimodal, bimodal, trimodal and quadrimodal branches respectively (see bifurcation diagram Figure 3.1).

We compare steady state solutions of the holistic models of the Kuramoto–Sivashinsky equation to conventional centered differences by comparing bifurcation diagrams. The bifurcation diagrams are constructed by the method outlined in §3.1 using XPPAUT [12].

In §3.3 we see the $\mathcal{O}(\gamma^3, \alpha^2)$ holistic model is remarkably successful in reconstructing qualitatively the dynamics of the Kuramoto–Sivashinsky equa-

tion for, $0 \leq \alpha \leq 35$, with just 8 elements on the interval $[0, \pi]$. The higher order $\mathcal{O}(\gamma^5, \alpha^2)$ holistic model achieves impressive performance for $0 \leq \alpha \leq 70$ on the same coarse grid. In comparison explicit centered difference approximations only resolve the dynamics qualitatively for $0 \leq \alpha \leq 20$ for the 2nd order approximation and $0 \leq \alpha \leq 40$ for a 6th order approximation on this same coarse grid.

In §3.4.2, holistic models constructed using the nonlocal IBCs (2.7–2.8) and the local IBCs (2.4–2.5) are explored and we find that the holistic approximations constructed using the nonlocal IBCs are far superior.

In §3.5 we see the holistic models compare well to Galerkin approximations of Jolly et al. [25]. We examine the bifurcation diagrams for the Galerkin approximations and compare to the holistic models. In particular we find the $\mathcal{O}(\gamma^5, \alpha^2)$ holistic model with 8 elements on $[0, \pi]$ compares well to the 8 mode traditional Galerkin approximation.

To conclude we compare the performance of approximations of similar accuracy on different grid resolutions in §3.6. The holistic $\mathcal{O}(\gamma^5, \alpha^2)$ approximation on a grid of 8 elements has similar accuracy to a 2nd order centered difference approximation on a grid of 16 points. Consequently the holistic model allows a maximum time step of an order of magnitude longer than that of the explicit centered difference approximation of similar accuracy, while maintaining numerical stability. The accuracy of the holistic approximations to the Kuramoto–Sivashinsky equation on coarse grids and subsequent improved performance justifies further application of the holistic method and future investigation of the approach.

3.1 Bifurcation diagrams show steady states

We use bifurcation diagrams to indicate the accuracy of the holistic approximations to the Kuramoto–Sivashinsky equation (2.1) on coarse grids. The bifurcation diagrams usefully summarise in one diagram, qualitative and quantitative information for a large range of the nonlinear parameter α.

Here I describe the process for constructing bifurcation diagrams of various ODE models of the Kuramoto–Sivashinsky equation (2.1) listed in §2.3.2. I use the software package XPPAUT [12]. XPPAUT incorporates the continuation software AUTO [11], to calculate the bifurcation information. The information is then filtered through a function written in MATLAB to draw the bifurcation diagram.

The input to XPPAUT is a text `.ode` file describing the set of ODEs. For example, consider solving the Kuramoto–Sivashinsky equation (2.1) with a 2nd order centered difference approximation. Introducing m equispaced grid points $x_j = (j - 1/2)\pi/m$, over $[0, \pi]$ and representing the grid values by $u_j = u(x_j, t)$, the evolution of the jth grid value is approximated by (2.33), namely

$$\begin{aligned} \dot{u}_j &= -4\frac{u_{j+2} - 4u_{j+1} + 6u_j - 4u_{j-1} + u_{j-2}}{h^4} \\ &\quad - \alpha\left(\frac{u_{j+1} - 2u_j + u_{j-1}}{h^2} + u_j\frac{u_{j+1} - u_{j-1}}{2h}\right) . \end{aligned} \tag{3.2}$$

The following is the text file used by XPPAUT to generate the bifurcation information for this 2nd order centred difference approximation to the Kuramoto–Sivashinsky equation with 8 elements on the interval $[0, \pi]$. Note that the periodicity and the odd symmetry are built into the ODEs. That is, $u_0 = -u_1$, $u_{-1} = -u_2$, $u_9 = -u_8$ and $u_{10} = -u_7$.

```
u[1]'=h^(-4)*(-24*u[1]+16*u[2]-4*u[3]+16*(-1)*u[1]-4*(-1)*u[2])
+h^(-2)*a*(2*u[1]-u[2]-(-1)*u[1])
+h^(-1)*a*1/2*(u[1]*((-1)*u[1]-u[2]))
u[2]'=h^(-4)*(-24*u[2]+16*u[3]-4*u[4]+16*u[1]-4*(-1)*u[1])
+h^(-2)*a*(2*u[2]-u[3]-u[1])
+h^(-1)*a*1/2*(u[2]*(u[1]-u[3]))
u[3]'=h^(-4)*(-24*u[3]+16*u[4]-4*u[5]+16*u[2]-4*u[1])
+h^(-2)*a*(2*u[3]-u[4]-u[2])
+h^(-1)*a*1/2*(u[3]*(u[2]-u[4]))
u[4]'=h^(-4)*(-24*u[4]+16*u[5]-4*u[6]+16*u[3]-4*u[2])
+h^(-2)*a*(2*u[4]-u[5]-u[3])
+h^(-1)*a*1/2*(u[4]*(u[3]-u[5]))
u[5]'=h^(-4)*(-24*u[5]+16*u[6]-4*u[7]+16*u[4]-4*u[3])
+h^(-2)*a*(2*u[5]-u[6]-u[4])
+h^(-1)*a*1/2*(u[5]*(u[4]-u[6]))
u[6]'=h^(-4)*(-24*u[6]+16*u[7]-4*u[8]+16*u[5]-4*u[4])
+h^(-2)*a*(2*u[6]-u[7]-u[5])
+h^(-1)*a*1/2*(u[6]*(u[5]-u[7]))
u[7]'=h^(-4)*(-24*u[7]+16*u[8]-4*(-1)*u[8]+16*u[6]-4*u[5])
+h^(-2)*a*(2*u[7]-u[8]-u[6])
+h^(-1)*a*1/2*(u[7]*(u[6]-u[8]))
u[8]'=h^(-4)*(-24*u[8]+16*(-1)*u[8]-4*(-1)*u[7]+16*u[7]-4*u[6])
+h^(-2)*a*(2*u[8]-(-1)*u[8]-u[7])
+h^(-1)*a*1/2*(u[8]*(u[7]-(-1)*u[8]))
param a=0, h=0.3926990817
@total=10, dt=0.05, xhi=10
```

Because the holistic models contain a large number of terms the `.ode` files are generated automatically. The algorithm to construct the holistic models §2.3.1 coded in REDUCE handles the details of the computer algebra to generate the holistic models. Then a function written in MATLAB parses the output from REDUCE and generates the `.ode` file required by AUTO. This MATLAB function incorporates the odd symmetry into the `.ode` file.

3.2 Accurate steady state solutions

Here we introduce accurate solutions for the steady states of the Kuramoto–Sivashinsky equation (2.1) over the range $0 \leq \alpha \leq 70$ as summarised in the bifurcation diagram of Figure 3.1.

Accurate solutions are produced by a 6th order centered difference approximation (2.35) with 48 grid points on the spatial interval $[0, \pi]$. This approximation on the grid of 48 points, gives sufficient accuracy to capture the important dynamics of the Kuramoto–Sivashinsky for $0 \leq \alpha \leq 70$ and thus provides the reference to an accurate solution for the approximations on coarse grids.

3.2.1 Conventions for the bifurcation diagrams

For all the bifurcation diagrams in this dissertation a signed solution norm is plotted against the nonlinear parameter α. This is different to the convention adopted by Jolly et al. [25] but empowers us to investigate more detail by defining positive and negative branches. We view the positive and negative branches separately as stability may differ along these branches. For example, we see this to be evident in Figure 3.1 along the bimodal branches. The negative bimodal branch is stable for $16.140 < \alpha < 22.556$, whereas the positive bimodal branch is unstable for this range of α.

The open squares denote steady state bifurcations and the black squares denote Hopf bifurcations. This convention is maintained throughout this dissertation.

The solution norm is signed corresponding to the sign of the the first grid value, $u_1 = u(x_1)$. The blue curves are branches of stable fixed points and

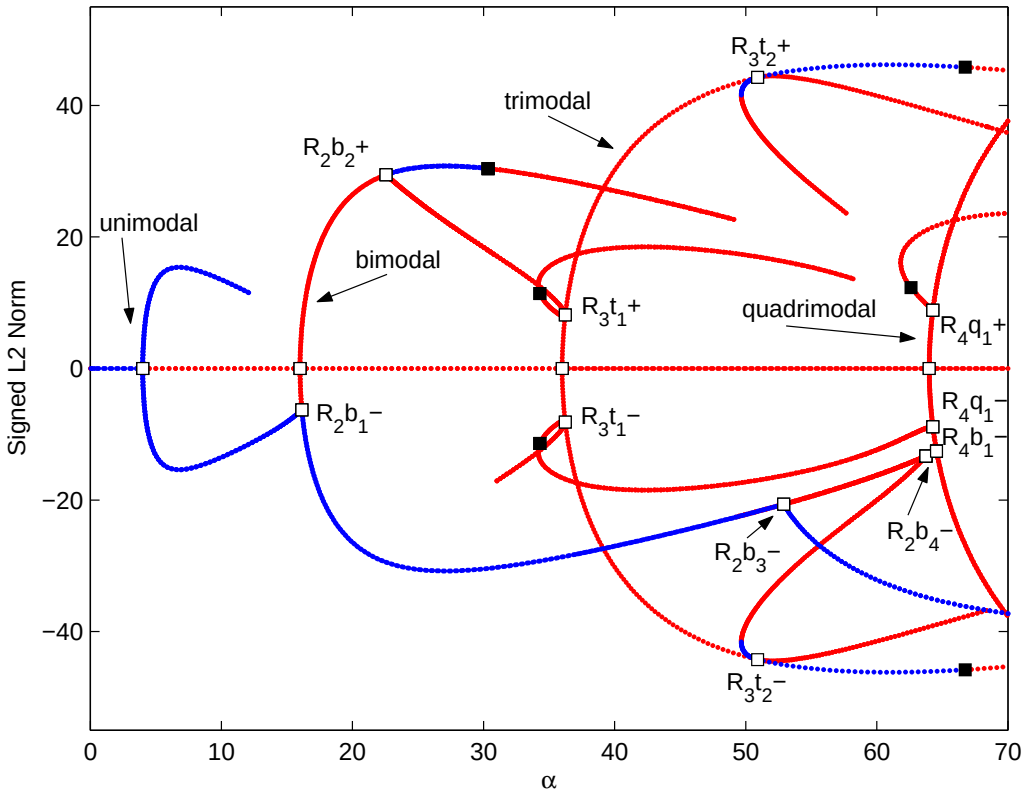

Figure 3.1: Accurate bifurcation diagram $0 \leq \alpha \leq 70$ for the Kuramoto–Sivashinsky equation, using a 6th order centered difference approximation with 48 points on the interval $[0, \pi]$. A signed L_2 norm is plotted against α.

the red curves are branches of unstable fixed points. This colour convention for stability of the steady states is adopted for all of the bifurcation diagrams.

The labelling scheme used in Figure 3.1 follows that of Jolly et al. [25] and Scovel [59] with the addition of a plus or minus sign depending upon the sign of u_1. For example, the secondary bifurcation on the negative bimodal branch is labelled R_2b_1- following the labelling scheme of Scovel with the addition of the $-$ sign because it occurs on the negative branch.

Figure 3.1 shows several apparent discontinuities. For example, the posi-

tive unimodal branch ends at approximately $\alpha = 12$. This apparent discontinuity arises due to the convention adopted here of taking the sign of u_1 to sign the norm. Figure 3.2 illustrates why this discontinuity occurs. Both the

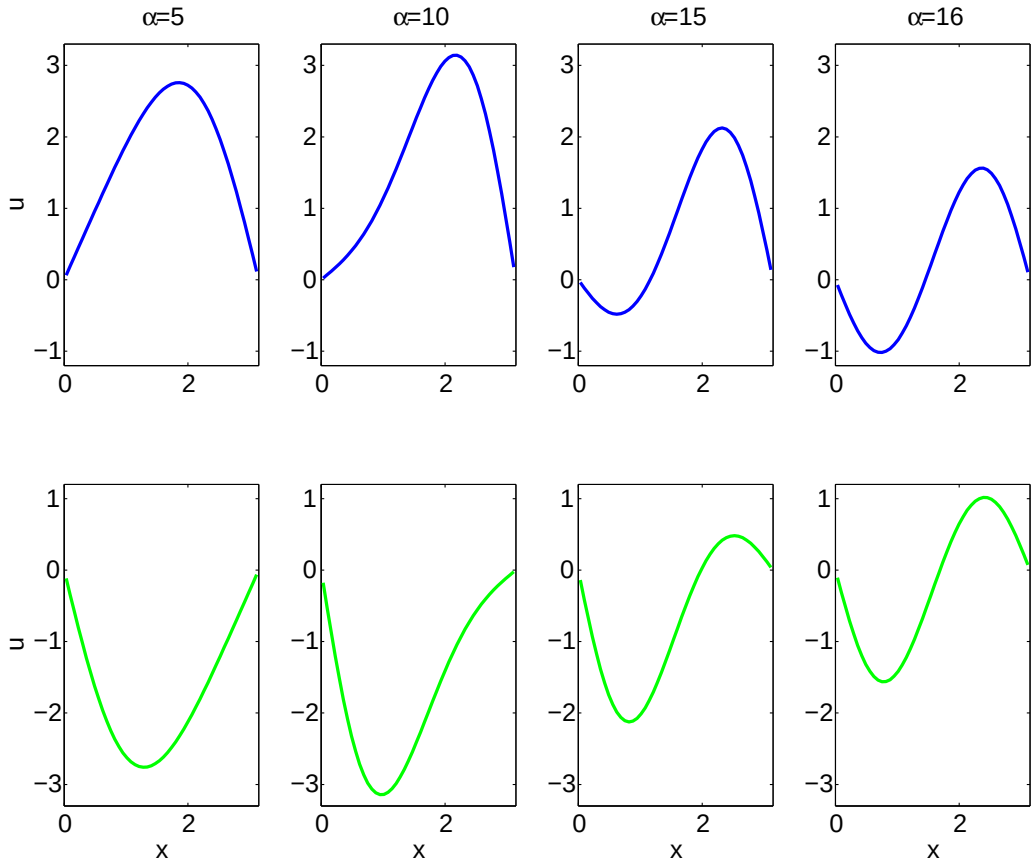

Figure 3.2: Steady state solutions along the unimodal branch. The blue curves are solutions along the positive branch and the green curves are solutions along the negative branch.

positive unimodal branch and the negative unimodal branch transform into the negative bimodal branch. It is straightforward to sign the branch near the trivial solution, but away from the trivial solution the distinction between positive and negative is not clear. Figure 3.3 is a plot of the leftmost grid

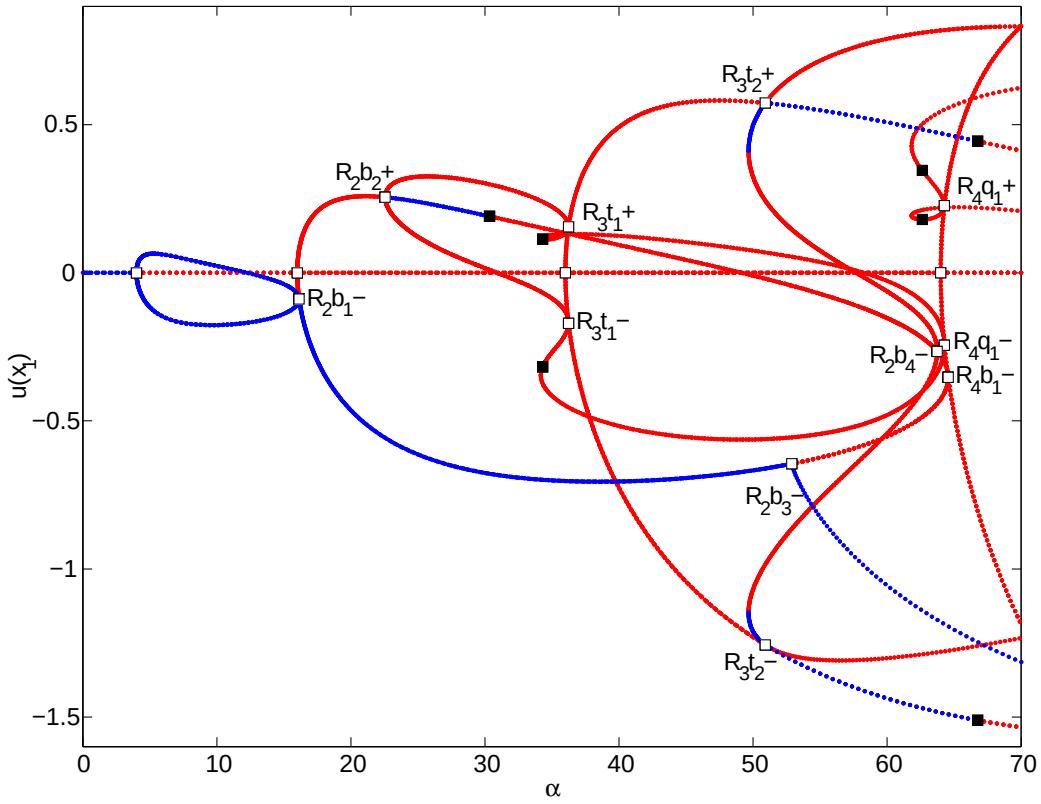

Figure 3.3: Accurate bifurcation diagram $0 \leq \alpha \leq 70$ for the Kuramoto–Sivashinskyequation, using a 6th order centered difference approximation with 48 points on the interval $[0, \pi]$. u_1 is plotted against α.

value u_1 against the nonlinear parameter α. This plot further illustrates why discontinuities occur in the bifurcation diagrams solely due to the convention adopted here for the signed norm.

3.2.2 Explore some steady state solutions

Here we examine some of the stable equilibria to familiarize ourselves with solutions of Kuramoto–Sivashinsky equation in the region of interest, $0 \leq \alpha \leq 70$. Figure 3.4 illustrates *stable* solutions of the Kuramoto–Sivashinsky equation at various values of α. These steady states have been computed from a 6th order centered difference approximation with 48 grid points on the interval $[0, \pi]$. Figures 3.4a,b,c are solutions on the negative unimodal branch at $\alpha = 1, 5, 10$ respectively. Figures 3.4d,e,f are solutions on the negative bimodal branch at $\alpha = 20, 30, 40$ respectively. The dark blue curves in Figures 3.4g,h,i are solutions on the negative bimodal branch and the light blue curves are solutions on the negative trimodal branch at $\alpha = 50, 55, 60$ respectively.

3.3 Holistic models are accurate on coarse grids

We begin investigating the performance of the holistic models by considering the $\mathcal{O}(\gamma^5, \alpha^2)$ holistic model (2.32) (9 point stencil, $\mathcal{O}(h^6)$ consistent), constructed with the non-local IBCs (2.7–2.8). We investigate its performance at reproducing the steady states of the Kuramoto–Sivashinsky system on coarse grids on the interval $[0, \pi]$.

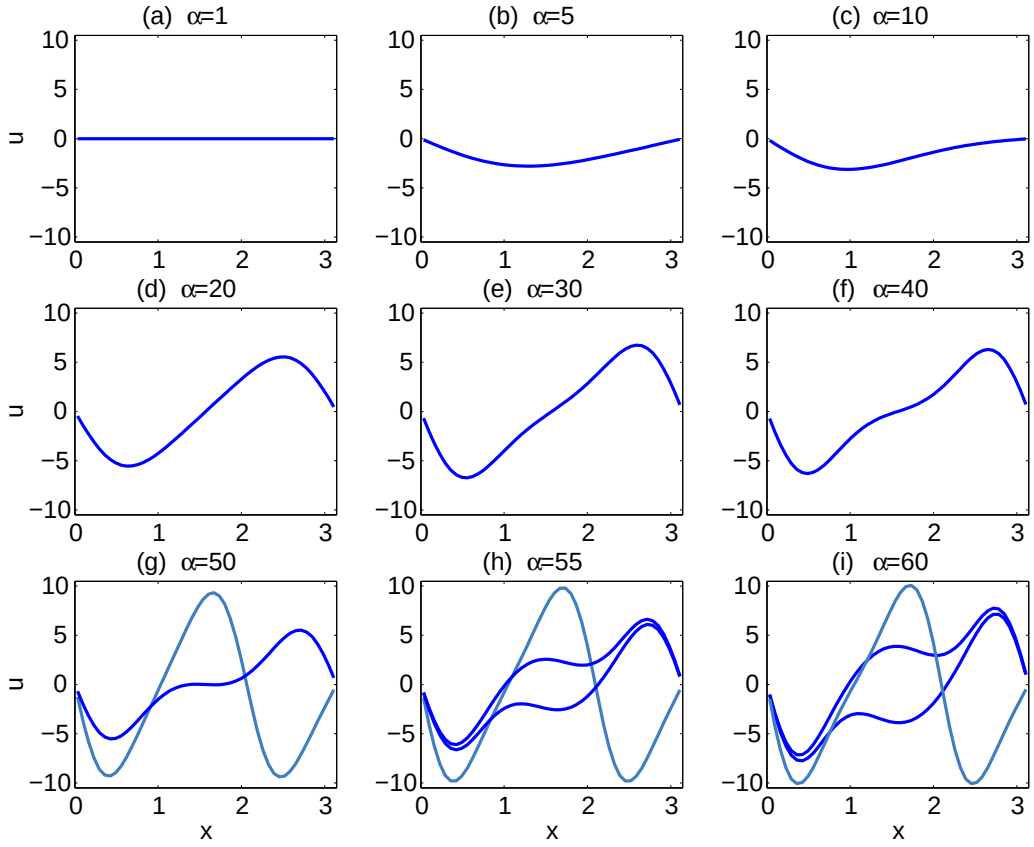

Figure 3.4: Some examples of the stable equilibria of the Kuramoto–Sivashinsky equation. Dark blue curves are solutions along the negative unimodal and bimodal branches. Light blue curves are stable solutions along the negative trimodal branch.

Figure 3.5 shows accurate solutions in blue of the Kuramoto–Sivashinsky equation (2.1) with odd symmetry. The holistic model with errors $\mathcal{O}(\gamma^5, \alpha^2)$ and non-local IBCs for 8 elements is shown in green and the 6th order centered difference approximation (2.35) with 8 grid points is shown in magenta. The 6th order centered difference approximation is compared to the $\mathcal{O}(\gamma^5, \alpha^2)$ holistic model here because it is of equal stencil width. Figure 3.5 g,h,i shows the holistic model with errors $\mathcal{O}(\gamma^5, \alpha^2)$ and non-local IBCs gives the stable bimodal and trimodal solutions at $\alpha = 50$ and $\alpha = 55$ and the stable bimodal solution at $\alpha = 60$. The 6th order centered difference approximation does not give any stable solutions for $\alpha = 50, 55$ or 60. To compare in more detail we now turn to the bifurcation diagrams for these approximations.

3.3.1 Bifurcation diagrams show success

Here we compare for $0 \leq \alpha \leq 70$, the bifurcation diagram of the $\mathcal{O}(\gamma^5, \alpha^2)$ holistic model (2.32) with non-local IBCs to the bifurcation diagram of the 6th order centered difference approximation (2.35), on coarse grids. To demonstrate the success of the holistic approach we firstly examine the bifurcation diagrams on a coarse grid of 8 elements and then on a coarse grid of 6 elements.

Figure 3.6 is a side by side comparison of the holistic model with non-local IBCs and errors $\mathcal{O}(\gamma^5, \alpha^2)$ with 8 elements on $[0, \pi]$ and the 6th order centered difference approximation with 8 grid points on $[0, \pi]$. These approximations are compared because they are both 9 point stencil approximations. The accurate bifurcation diagram is also plotted in grey but without any stability information. The signed L_2 norms for the bifurcation diagrams on the

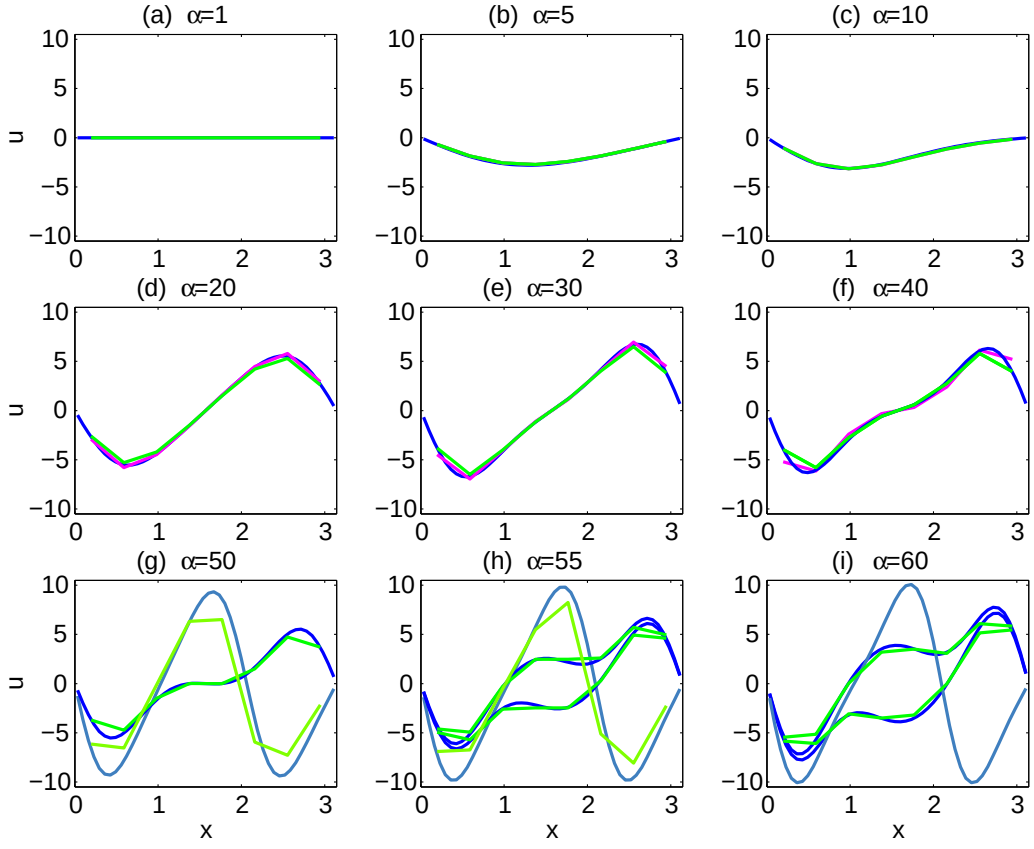

Figure 3.5: Some accurate solutions plotted with holistic and centered difference approximations on coarse grids. Blue curves are accurate solutions, green curves are the holistic approximation with non-local IBCs (2.7–2.8) with errors $\mathcal{O}\left(\gamma^5, \alpha^2\right)$ on 8 elements. Magenta curves are a 6th order centered difference approximation with 8 grid points.

coarse grid of 8 elements are adjusted by a factor of $\sqrt{6}$ to allow comparison to the accurate bifurcation diagram constructed with 48 grid points on $[0, \pi]$. Throughout this dissertation when comparing bifurcation diagrams of different grid resolutions, the signed L_2 norms are adjusted this way to provide a consistent reference.

Figure 3.6a shows the $\mathcal{O}(\gamma^5, \alpha^2)$ holistic model, gives good agreement with the accurate bifurcation diagram for $\alpha < 40$ and qualitatively reproduces most of the bifurcation picture for $40 < \alpha \leq 70$. The $\mathcal{O}(\gamma^5, \alpha^2)$ holistic model does not detect the bifurcation points $R_3 t_2 \pm$ on this coarse grid and the bifurcation points $R_3 t_1 \pm$ are incorrectly identified as fold points. However, the $\mathcal{O}(\gamma^5, \alpha^2)$ holistic model finds all of the other bifurcation points in this range of α. Figure 3.6b shows the 6th order centered difference approximation gives good agreement with the accurate bifurcation diagram for $\alpha < 20$ and qualitatively reproduces the bifurcation diagram for $20 < \alpha < 40$. The 6th order centered difference approximation performs poorly for $\alpha > 40$. The values of α at which the bifurcation points occur are listed in Table 3.1 and confirm the $\mathcal{O}(\gamma^5, \alpha^2)$ holistic model performs better than the 6th order centered difference approximation on this coarse grid of 8 elements.

Figure 3.7 is a side by side comparison of the same $\mathcal{O}(\gamma^5, \alpha^2)$ holistic model with non-local IBCs to the 6th order centered difference approximation, on an even coarser grid of just 6 elements. Again an accurate bifurcation diagram is plotted in grey. The superior performance of the holistic model is again evident. Figure 3.7a shows the holistic model with errors $\mathcal{O}(\gamma^5, \alpha^2)$ gives good agreement with the accurate bifurcation diagram for $\alpha < 20$ and qualitatively reproduces the bifurcation diagram for $20 < \alpha < 50$. Even on

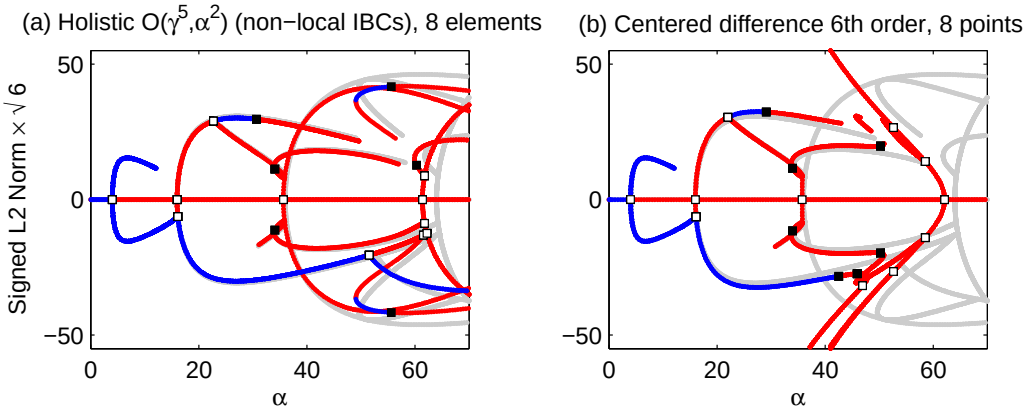

Figure 3.6: Bifurcation diagrams for coarse grid approximations with 8 elements on $[0, \pi]$ for (a) holistic model $\mathcal{O}(\gamma^5, \alpha^2)$ with non-local IBCs, (b) centered difference 6th order.

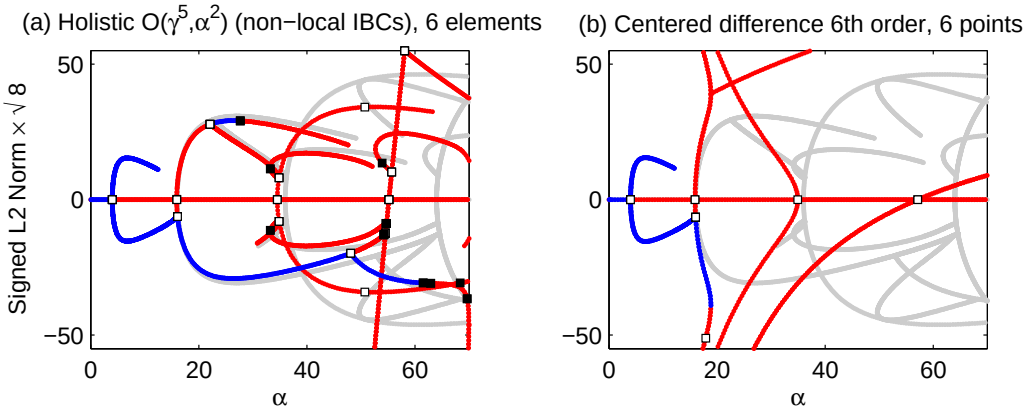

Figure 3.7: Bifurcation diagrams for coarse grid approximations with 6 elements on $[0, \pi]$ for (a) holistic model $\mathcal{O}(\gamma^5, \alpha^2)$ with non-local IBCs, (b) centered difference 6th order.

this very coarse grid the holistic model qualitatively reproduces the unstable trimodal steady state branch to at least $\alpha = 50$. Figure 3.7b shows the 6th order centered difference approximation gives good agreement with the accurate bifurcation diagram for $\alpha < 15$, but reproduces little of the bifurcation diagram for $\alpha > 15$.

We conjecture that the superior performance of the holistic approximation is due to the accurate subgrid scale modelling of the holistic method. These bifurcation diagrams, Figures 3.6 and 3.7 give excellent support to the holistic approach to generating approximations for the Kuramoto–Sivashinsky equation.

3.4 Non-local IBCs are superior

Having established above that the $\mathcal{O}(\gamma^5, \alpha^2)$ holistic model with non-local IBCs (2.7–2.8) performs well for modelling the steady states of the Kuramoto–Sivashinsky equation (2.1) on coarse grids, we now compare the performance of the holistic models constructed with the non-local IBCs to holistic models constructed with the local IBCs (2.4–2.5). In §3.4.1 we examine the superior performance of the holistic model with non-local IBCs for the lowest order holistic model, that is the $\mathcal{O}(\gamma^3, \alpha^2)$ approximation (2.32), by comparing bifurcation diagrams for $0 \leq \alpha \leq 70$.

We also investigate the effect of higher order holistic models on accuracy by comparing bifurcation diagrams of holistic models of higher orders, constructed with both IBCs. In particular, in §3.4.2 we examine bifurcation diagrams for holistic models with non-local IBCs and local IBCs with errors $\mathcal{O}(\gamma^p, \alpha^q)$, for $p = 3, 4, 5$ and $q = 2, 3, 4$. We find that retaining terms of

higher order in γ, corresponding to wider stencil approximations, gives much greater improvement in accuracy than retaining terms of higher order in the nonlinearity α.

3.4.1 Bifurcation diagrams of low order holistic models

We compare the performance of the holistic models constructed with the non-local IBCs (2.7–2.8) to those constructed with the local IBCs (2.4–2.5) by examining the bifurcation diagrams of low order approximations constructed by both IBCs on a grid of 8 elements on $[0, \pi]$.

Figure 3.8 is a side by side comparison of bifurcation diagrams for the $\mathcal{O}(\gamma^3, \alpha^2)$ holistic models (2.25) and (2.24) respectively. These holistic models with errors $\mathcal{O}(\gamma^3, \alpha^2)$ are 5 point stencil approximations and are the lowest order holistic models that capture the dynamics of the hyper-diffusion and the nonlinearity.

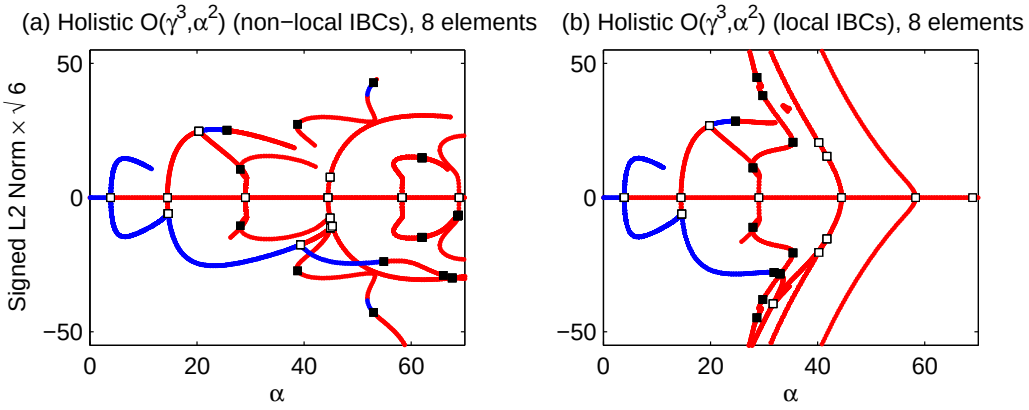

Figure 3.8: Bifurcation diagrams for $\mathcal{O}(\gamma^3, \alpha^2)$ holistic models, (a) holistic model with non-local IBCs and (b) holistic model with local IBCs.

Figure 3.8 shows the $\mathcal{O}(\gamma^3, \alpha^2)$ holistic model with non-local IBCs qualitatively reproduces more of the steady state dynamics of the Kuramoto–Sivashinsky system than the same order holistic model with local IBCs. Both models qualitatively reproduce the stable bimodal branch to at least $\alpha = 30$. However we observe the performance of the holistic model with the non-local IBCs is superior because it reproduces:

- the stable branch of solutions at $R_2 b_3-$;
- the unstable branch of solutions joining $R_3 t_1-$ to $R_4 q1-$.
- the correct behaviour for the unstable quadrimodal branch.

Both low order holistic models are not very accurate on this coarse grid for the range of α investigated here. The unimodal, bimodal, trimodal and quadrimodal branches occur at $\alpha = 3.9, 14.5, 29.0$ and 44.5 instead of $\alpha = 4, 16, 36$ and 64 respectively. However, the holistic approach provides a systematic method for deriving higher order approximations §2.3 and we now compare the performance of the holistic models with different IBCs at higher orders.

3.4.2 Higher order models confirm non-local IBCs better

Here we investigate the effect of higher order holistic models for both the non-local IBCs (2.7–2.8) and the local IBCs (2.4–2.5). We investigate all holistic models constructed with the non-local IBCs and the local IBCs, up to and including the $\mathcal{O}(\gamma^5, \alpha^4)$ holistic models.

Figure 3.9 shows the bifurcation diagrams for the holistic models constructed with non-local IBCs up to and including the $\mathcal{O}(\gamma^5, \alpha^4)$ holistic model.

Surveying across the columns of Figure 3.9 we see the bifurcation diagrams for holistic models of increasing order of γ, corresponding to approximations of increasing stencil width. For example, Figure 3.9a,b,c shows the bifurcation diagrams for the holistic models (2.25), (2.30) and (2.32) respectively. Surveying down the rows of Figure 3.9 we see the bifurcation diagrams for increasing orders of the nonlinearity α.

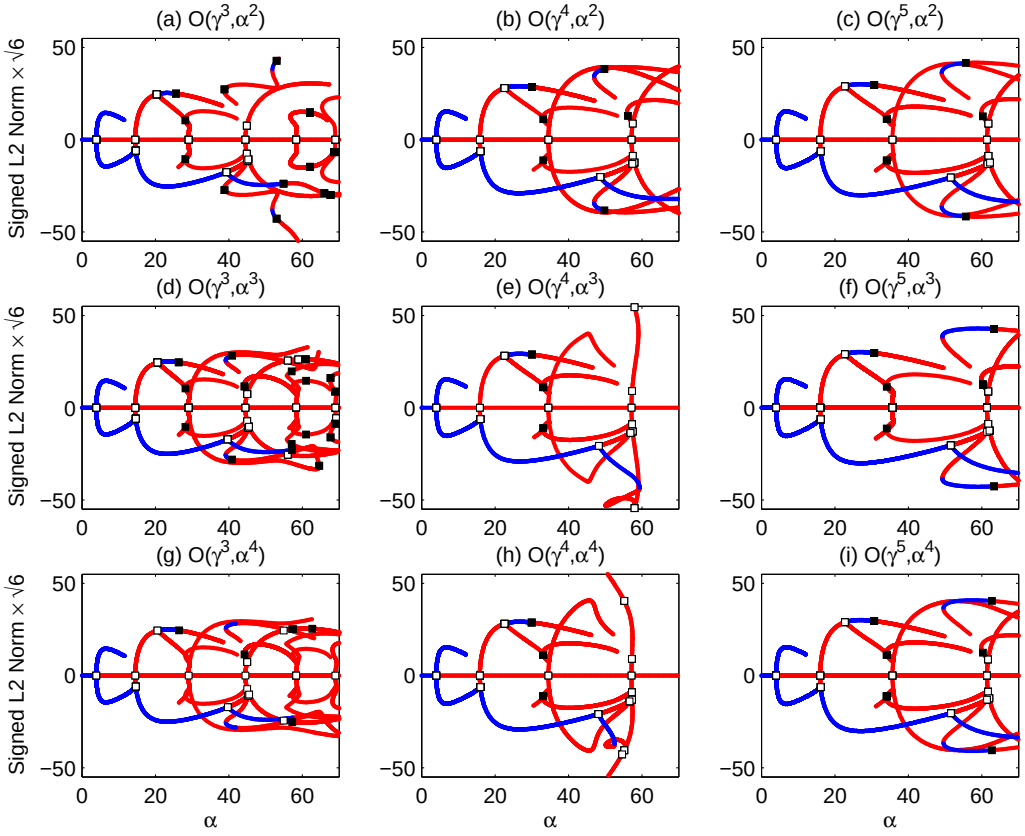

Figure 3.9: **Holistic models (non-local IBCs):** Bifurcation diagrams for the holistic models with non-local IBCs (2.7–2.8) and 8 elements on the interval $[0, \pi]$.

Figure 3.9 illustrates the improvement in accuracy of the higher order

holistic models with non-local IBCs. A first point to note is the dramatic improvement in accuracy gained by moving from left to right across figure 3.9, corresponding to approximations of higher orders in γ. A second point of interest is that less improvement is gained by moving from top to bottom of Figure 3.9, corresponding to approximations of higher order in α.

There are some peculiarities about this series of bifurcation pictures for holistic models of increasing order in α. For the 5 point stencil approximations displayed in the first column of Figures 3.9, higher orders in α appear to gain some improvement. In particular Figures 3.9d,g show the $\mathcal{O}(\gamma^3, \alpha^3)$ and $\mathcal{O}(\gamma^3, \alpha^4)$ holistic models reproduce the unstable trimodal branches that were missing from the $\mathcal{O}(\gamma^3, \alpha^2)$ bifurcation diagram shown in Figure 3.9a. However, for the 7 point stencil approximations displayed in the second column of Figure 3.9, holistic models of higher orders in α lose some features of the Kuramoto–Sivashinsky system. The correct behaviour of the unstable trimodal and quadrimodal branches is reproduced for the $\mathcal{O}(\gamma^4, \alpha^2)$ model shown in Figure 3.9b, but not reproduced for the higher order $\mathcal{O}(\gamma^4, \alpha^3)$ and $\mathcal{O}(\gamma^4, \alpha^4)$ models shown in Figures 3.9e,h respectively. For the 9 point stencil approximations, displayed in the third column of Figures 3.9, the $\mathcal{O}(\gamma^5, \alpha^2)$ holistic model shown in Figure 3.9c, reproduces the unstable trimodal branch whereas the higher order $\mathcal{O}(\gamma^5, \alpha^3)$ model shown in Figure 3.9f, does not reproduce the unstable trimodal branch. These peculiarities suggest that while we have observed excellent performance of the holistic models constructed with the non-local IBCs on coarse grids, it may be possible that modifications could be made to the non-local IBCs such that higher order approximations in the nonlinear parameter are improved. Such modifications are not considered

in the scope of this dissertation.

Despite the pecularities mentioned above Figure 3.9 does show that for the holistic models of low order in α, higher orders in γ result in great improvement in accuracy.

Figure 3.10 shows the bifurcation diagrams for the holistic models constructed with local IBCs up to and including the $\mathcal{O}(\gamma^5, \alpha^4)$ holistic model. The bifurcation diagrams for higher orders are displayed similarly to Figure 3.9 in that surveying across the the columns of Figure 3.10 we see the bifurcation diagrams for holistic models of increasing order of γ, whereas surveying down the rows of Figure 3.10 we see the bifurcation diagrams for increasing orders of α. Figure 3.10a,b,c shows the bifurcation diagrams for the holistic models (2.24), (2.29) and (2.31) respectively.

Figure 3.10 illustrates the effect on accuracy of the higher order holistic models with local IBCs. These holistic approximations constructed with the local IBCs do not display the same excellent performance as the approximations derived with the non-local IBCs. However, an important characteristic of both IBCs is that great improvement is gained by using approximations of higher orders in γ, corresponding to approximations with increasing stencil widths. Since the holistic models with local IBCs have not performed as well as the non-local IBCs models, we restrict our analysis to the non-local IBCs (2.7–2.8) for the remainder of this dissertation.

3.4.3 Holistic models outperform centered differences

In §3.3.1 we saw that the performance of the $\mathcal{O}(\gamma^5, \alpha^2)$ holistic model (2.32), constructed with non-local IBCs, was far superior to the explicit 6th or-

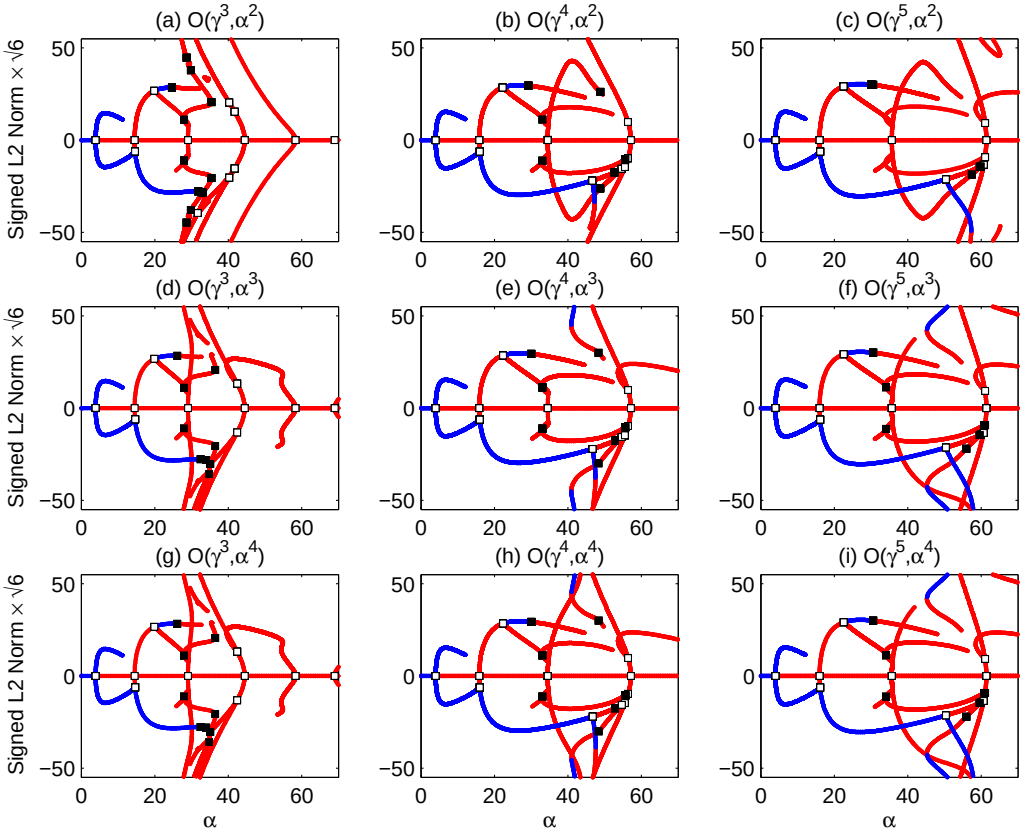

Figure 3.10: **Holistic models (local IBCs):** Bifurcation diagrams for the holistic models with local IBCs (2.4–2.5) and 8 elements on the interval $[0, \pi]$.

der centered difference approximation (2.35). To complete the comparison of holistic models to explicit centered difference schemes, we compare the $\mathcal{O}(\gamma^3, \alpha^2)$ (2.25) and $\mathcal{O}(\gamma^4, \alpha^2)$ (2.30) holistic models to the 2nd order (2.33) and 4th order (2.34) centered difference approximations respectively. Recall that the $\mathcal{O}(\gamma^3, \alpha^2)$ holistic model and the 2nd order centered difference approximation are both 5 point stencil approximations, and the $\mathcal{O}(\gamma^4, \alpha^2)$ holistic model and the 4th order centered difference approximation are both 7 point stencil approximations.

The first row of Figure 3.11 is a side by side comparison of the $\mathcal{O}(\gamma^3, \alpha^2)$ holistic model and the 2nd order centered difference approximation with 8 elements on $[0, \pi]$. The second row of Figure 3.11 is a side by side comparison of the $\mathcal{O}(\gamma^4, \alpha^2)$ holistic model and the 4th order centered difference approximation on the same grid. The accurate bifurcation diagram is plotted in grey without any stability information.

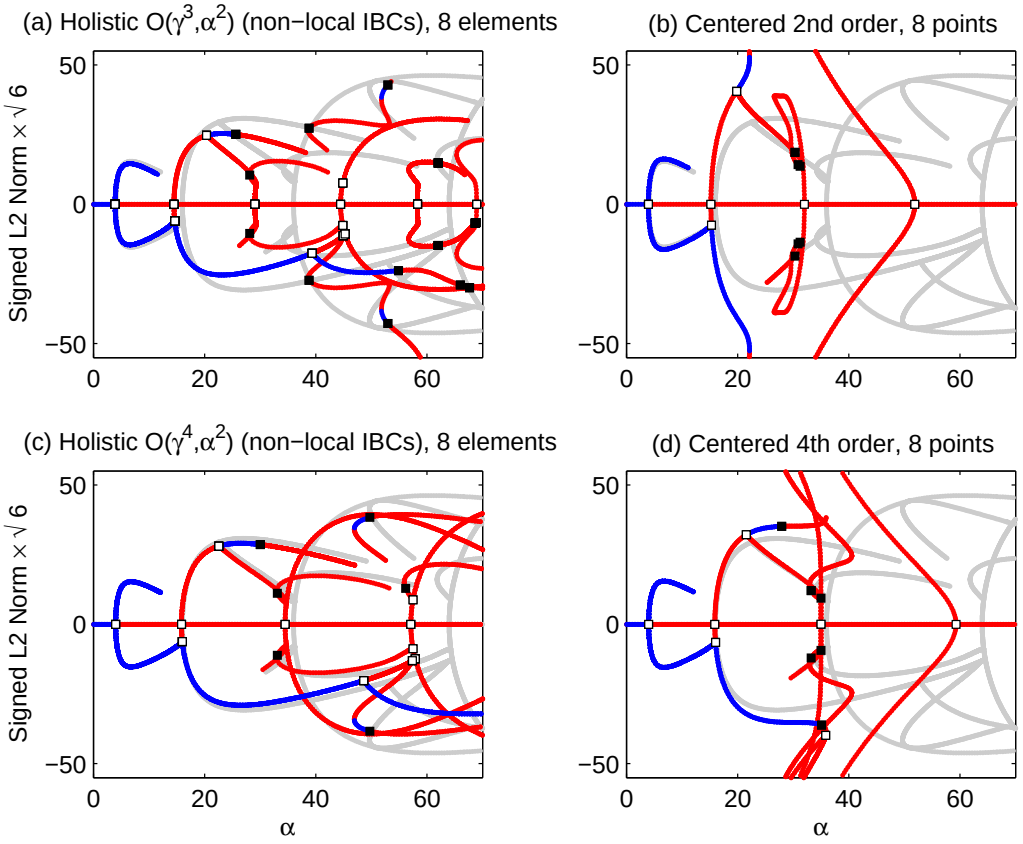

Figure 3.11: Bifurcation diagrams for (a) $\mathcal{O}(\gamma^3, \alpha^2)$ holistic model, (b) 2nd order centered difference, (c) $\mathcal{O}(\gamma^4, \alpha^2)$ holistic model and (d) 4th order centered difference all with 8 elements on the interval $[0, \pi]$

Although comparing Figures 3.11b,d shows some improvement is gained

by taking higher order centered difference approximations, this improvement is not as pronounced as for the holistic models on this coarse grid shown in Figures 3.11a,c. Both the 2nd order and 4th order centered difference approximations fail to reproduce the correct behaviour of the unstable trimodal and quadrimodal branches. In contrast, even the 5 point stencil $\mathcal{O}(\gamma^3, \alpha^2)$ holistic approximation qualitatively reproduces the trimodal and quadrimodal branches on the same coarse grid. The values at which the bifurcation points occur are listed in Table 3.1 and confirm that these holistic models outperform the centered difference approximations on this coarse grid of 8 elements on $[0, \pi]$.

3.4.4 Grid refinement improves accuracy

Further grid refinement results in improved accuracy for the holistic models. This is clear from examining the equivalent PDEs for the $\mathcal{O}(\gamma^3, \alpha^2)$, $\mathcal{O}(\gamma^4, \alpha^2)$ and $\mathcal{O}(\gamma^5, \alpha^2)$ holistic models. Since the equivalent PDE's for these holistic models (2.38), (2.41) and (2.44) are of $\mathcal{O}(h^2)$, $\mathcal{O}(h^4)$ and $\mathcal{O}(h^6)$ respectively, grid refinement is expected to result in improved accuracy.

Figure 3.12 shows the bifurcation diagrams of the holistic models up to and including the $\mathcal{O}(\gamma^4, \alpha^3)$ model on a finer grid of 12 elements on $[0, \pi]$. Comparing Figure 3.12 with Figure 3.9 confirms the improved accuracy for the holistic models on this refined grid. Table 3.1 also shows the bifurcation points are more accurately reproduced for the holistic models on this refined grid. Again more improvement in accuracy is gained by using higher order approximations in γ, or equivalently, using wider stencil approximations.

Figure 3.13 is a side by side comparison of the bifurcation diagrams of

Approximation	R_2b_1	R_2b_2	R_2b_3	R_2b_4	R_3t_1	R_3t_2	R_4b_1	R_4q_1
Accurate 48pts								
6th order	16.140	22.556	52.891	63.737	36.234	50.911	64.559	64.275
Holistic 8 elements								
$\mathcal{O}\left(\gamma^3,\alpha^2\right)$	14.644	20.361	39.339	44.959	29.284*	—	45.280	44.868
$\mathcal{O}\left(\gamma^3,\alpha^3\right)$	14.648	20.520	39.663	45.163	29.328*	—	45.470	44.956
$\mathcal{O}\left(\gamma^3,\alpha^4\right)$	14.648	20.533	39.722	45.207	29.334*	—	45.509	44.974
$\mathcal{O}\left(\gamma^4,\alpha^2\right)$	15.995	22.555	48.616	57.378	34.733*	—	57.888	57.494
$\mathcal{O}\left(\gamma^4,\alpha^3\right)$	15.995	22.564	48.248	56.842	34.732*	—	57.453	57.279
$\mathcal{O}\left(\gamma^4,\alpha^4\right)$	15.995	22.570	48.102	56.625	34.730*	—	57.303	57.214
$\mathcal{O}\left(\gamma^5,\alpha^2\right)$	16.128	22.717	51.541	61.544	35.894*	—	62.197	61.780
$\mathcal{O}\left(\gamma^5,\alpha^3\right)$	16.128	22.733	51.531	61.366	35.906*	—	62.037	61.703
$\mathcal{O}\left(\gamma^5,\alpha^4\right)$	16.128	22.734	51.599	61.378	35.907*	—	62.024	61.694
Centered 8 pts								
2nd order	15.296	19.812	—	—	—	—	—	—
4th order	16.022	21.548	—	—	35.936*	—	—	—
6th order	16.118	21.989	—	—	35.8205*	—	—	—
Holistic 12 elements								
$\mathcal{O}\left(\gamma^3,\alpha^2\right)$	15.446	21.669	45.962	53.935	32.858	45.982	54.491	54.174
$\mathcal{O}\left(\gamma^3,\alpha^3\right)$	15.447	21.691	46.051	54.001	32.866	46.332	54.551	54.204
$\mathcal{O}\left(\gamma^4,\alpha^2\right)$	16.110	22.624	51.934	62.099	35.901	50.915	62.829	62.515
$\mathcal{O}\left(\gamma^4,\alpha^3\right)$	16.110	22.624	51.936	62.097	35.901	50.936	62.828	62.515
Centered 12 pts								
2nd order	15.766	21.675	48.334	57.627	34.358	44.696	58.344	58.357
4th order	16.115	22.368	51.742	62.326	35.979	48.620	63.111	62.979

Table 3.1: α values at which bifurcation points occur for the various coarse grid approximations. * Denotes bifurcation point identified as fold point.

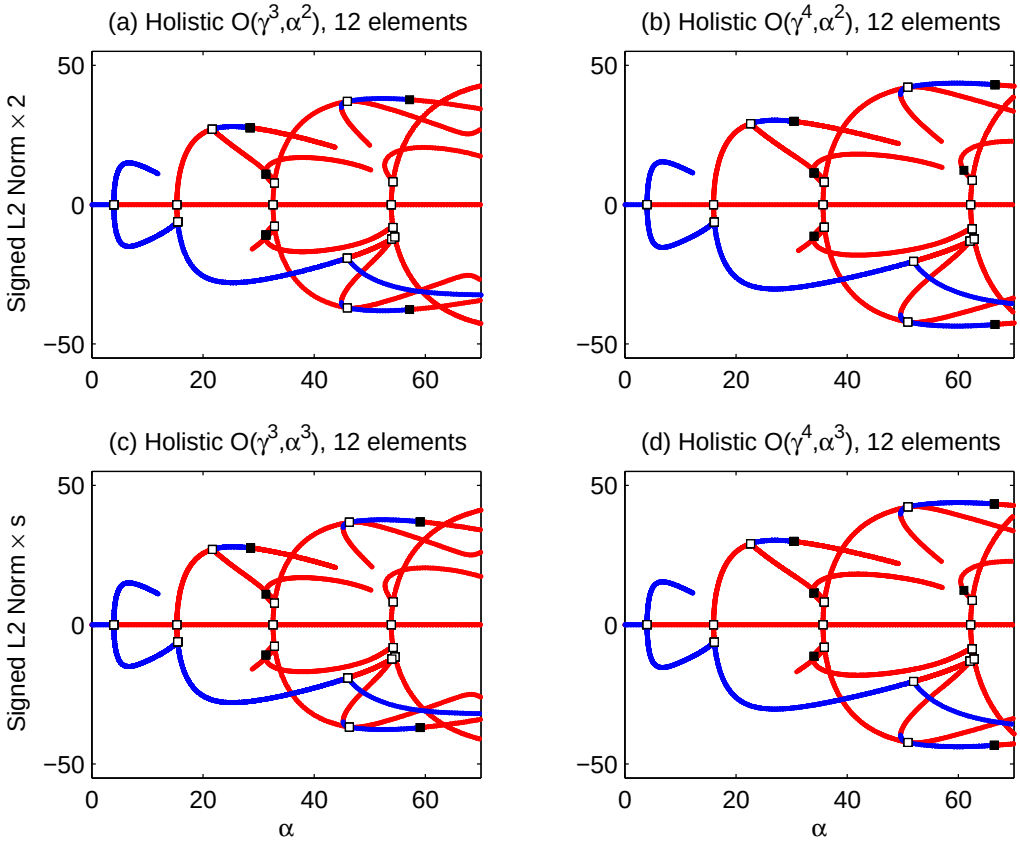

Figure 3.12: Bifurcation diagrams for the holistic models with the non-local IBCs with 12 elements on the interval $[0, \pi]$.

the $\mathcal{O}(\gamma^4, \alpha^2)$ holistic model and the 4th order centered difference approximation (2.34). The accurate bifurcation diagram is shown in grey. From Figure 3.13 we see the $\mathcal{O}(\gamma^4, \alpha^2)$ holistic model is more accurate for $0 \leq \alpha \leq 70$, but the improvement is not as pronounced as it is on the coarser grid of 8 elements. We suggest that this is because the major benefit to using the holistic models comes from application on coarser grids where greater benefit is derived from the subgrid scale modelling.

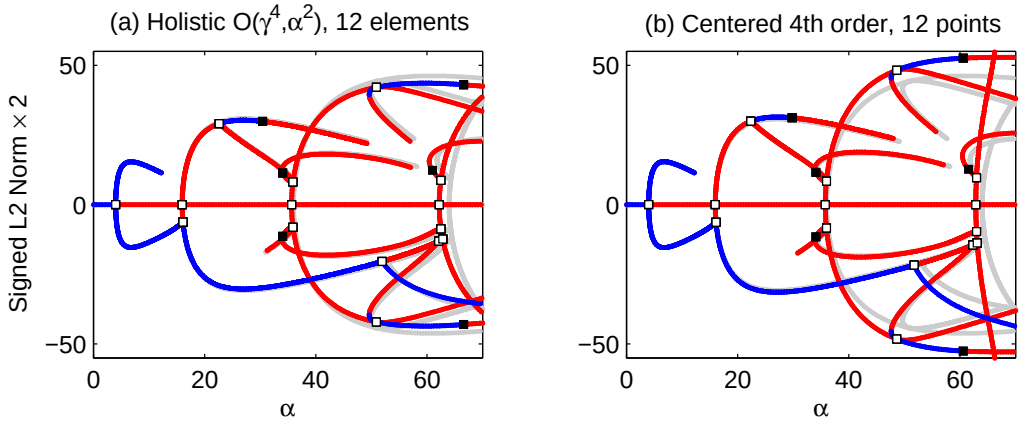

Figure 3.13: Bifurcation diagrams for (a) $\mathcal{O}(\gamma^4, \alpha^2)$ holistic model, (b) 4th order centered difference approximations with 12 elements on the interval $[0, \pi]$

3.5 Comparison to Galerkin approximations

Here we investigate the traditional Galerkin and non-linear Galerkin approximations detailed in [25] for the Kuramoto–Sivashinsky equation (2.1) with periodic and odd symmetry. We find that the holistic models compare well with the Galerkin methods. The $\mathcal{O}(\gamma^5, \alpha^2)$ holistic model on a coarse grid of 8 elements on $[0, \pi]$ is not as accurate as the 8 mode Galerkin approximations. However, as we saw in §3.3, the holistic models perform significantly better than explicit centered difference approximations.

While the Galerkin methods are of superior accuracy for solving the Kuramoto–Sivashinsky system (2.1) with periodic boundary conditions, because of their global nature they lack the flexibility of the mixed local-global nature of the holistic models discussed in §1. Although not explored here, this mixed local-global nature of the holistic models empowers its use with boundary

conditions other than periodic in space [53].

3.5.1 The Galerkin approximations

We seek solutions of the form

$$u(x,t) = \sum_{k=1}^{m} b_k(t)\sin(kx)\,. \tag{3.3}$$

The $m-$mode traditional Galerkin approximation [25] is

$$\frac{db_k}{dt} \approx \left(-4k^4 + \alpha k^2\right) b_k - \alpha\beta_k^m\,, \quad 1 \le k \le m\,, \tag{3.4}$$

where

$$\beta_k^m(b_1,\ldots,b_m) = \frac{1}{2}\sum_{j=1}^{m} j b_j \left[b_{k+j} + \mathrm{sign}(k-j)b_{|k-j|}\right]\,. \tag{3.5}$$

The $m-$mode first iterate nonlinear Galerkin approximation [25] is

$$\frac{db_k}{dt} \approx \left(-4k^4 + \alpha k^2\right) b_k - \alpha\beta_k^{2m}(b_1,\ldots,b_m,\phi_{m+1},\ldots,\phi_{2m})\,, \tag{3.6}$$

for $1 \le k \le m$, where

$$\phi_j = -\frac{\alpha}{4j^4}\beta_j^{2m}\left(b_1,\ldots,b_m,0,\ldots,0\right)\,, \tag{3.7}$$

for $m+1 \le j \le 2m$ and β_j^{2m} is given by (3.5).

3.5.2 Bifucation diagrams for the Galerkin approximations

We examine the bifurcation diagrams of the traditional Galerkin approximation (3.3–3.5) and the first iterate nonlinear Galerkin approximation (3.3,3.5–3.7) for $0 \le \alpha \le 70$ to compare with the bifurcation diagrams of the holistic models on coarse grids, presented in §3.3.

Figure 3.14 shows the Bifurcation diagrams for the 3 mode, 4 mode, 6 mode and 8 mode first iterate nonlinear Galerkin approximations on $[0, \pi]$. Note at least 4 modes are needed to qualitatively reproduce the behaviour of the stable bimodal branch.

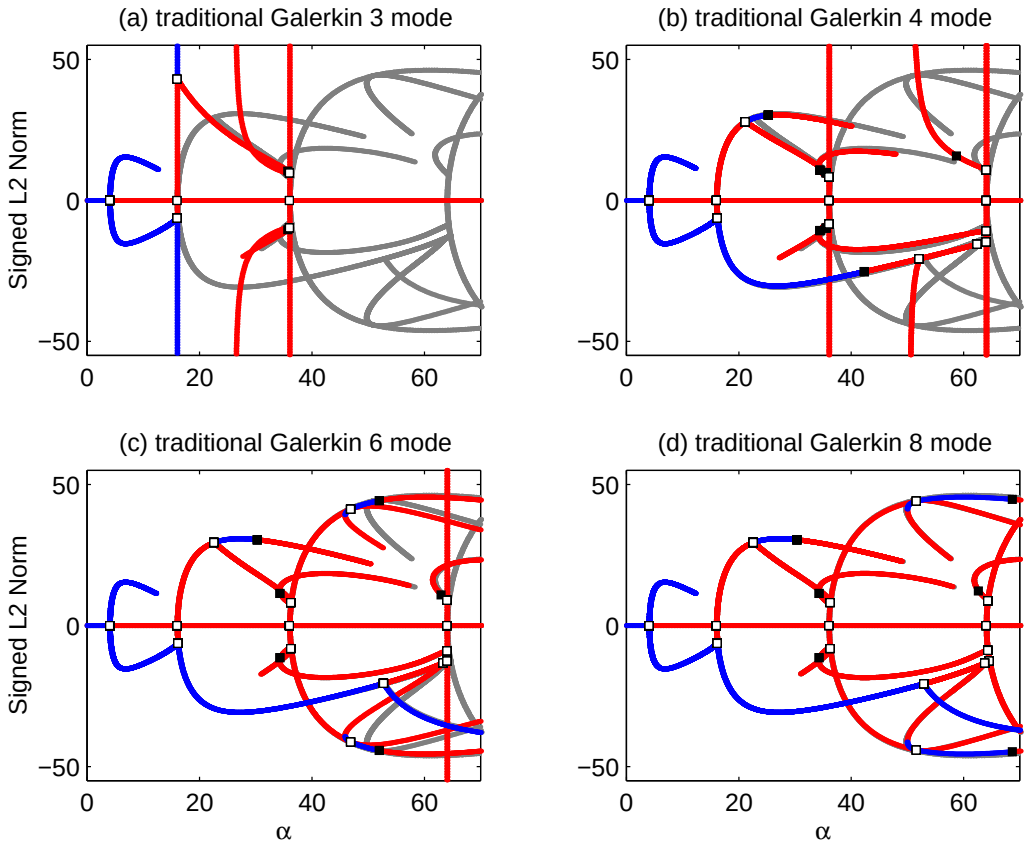

Figure 3.14: Bifurcation diagrams for (a) 3 mode, (b) 4 mode, (c) 6 mode and (d) 8 mode traditional Galerkin approximations on $[0, \pi]$.

Comparing the $\mathcal{O}(\gamma^5, \alpha^2)$ holistic model with 6 elements on $[0, \pi]$ from Figure 3.7a, to the 6 mode traditional Galerkin approximation we observe the $\mathcal{O}(\gamma^5, \alpha^2)$ holistic model qualitatively models most steady state dynamics that are reproduced by the 6 mode traditional Galerkin approximation.

Neither the $\mathcal{O}(\gamma^5, \alpha^2)$ holistic model nor the 6 mode traditional Galerkin approximation qualitatively reproduce the correct behaviour of the unstable quadrimodal branch. Similarly by comparing the $\mathcal{O}(\gamma^5, \alpha^2)$ holistic model with 8 elements on $[0, \pi]$ from Figure 3.6a, to the 8 mode traditional Galerkin approximation we observe the $\mathcal{O}(\gamma^5, \alpha^2)$ holistic model qualitatively models most steady state dynamics that are reproduced by the 8 mode traditional Galerkin approximation. However, the 8 mode traditional Galerkin approximation is more accurate in reproducing the steady state dynamics of the Kuramoto–Sivashinsky system for $0 \leq \alpha \leq 70$.

Figure 3.15 shows the Bifurcation diagrams for the 3 mode, 4 mode, 6 mode and 8 mode first iterate nonlinear Galerkin approximations on $[0, \pi]$. We see impressive accuracy for the low mode first iterate nonlinear Galerkin approximations. The 6 mode nonlinear Galkerin approximation reproduces all of the steady state dynamics for the range $0 \leq \alpha \leq 70$. There is no discernible difference between the bifurcation diagram of the 8 mode nonlinear Galerkin approximation and the accurate bifurcation diagram for this range of α.

Table 3.5.2 lists the values of α at which the bifurcation points occur for the coarse grid holistic models and the Galerkin approximations [25]. From this table we see the impressive accuracy of the holistic models with just 8 elements on $[0, \pi]$ compared to the Galerkin approximations.

Figure 3.16 is a side by side plot of the $\mathcal{O}(\gamma^5, \alpha^2)$ holistic model with 8 elements on $[0, \pi]$ and the 8 mode traditional Galerkin approximation. We see the $\mathcal{O}(\gamma^5, \alpha^2)$ holistic model compares well to the 8 mode traditional Galerkin approximation.

Approximation	R_2b_1	R_2b_2	R_2b_3	R_2b_4	R_3t_1	R_3t_2	R_4b_1	R_4q_1
Accurate 48pts								
6th order	16.140	22.556	52.891	63.737	36.234	50.911	64.559	64.275
Holistic 8 elements								
$\mathcal{O}\left(\gamma^3, \alpha^2\right)$	14.644	20.361	39.339	44.959	29.284*	—	45.280	44.868
$\mathcal{O}\left(\gamma^3, \alpha^3\right)$	14.648	20.520	39.663	45.163	29.328*	—	45.470	44.956
$\mathcal{O}\left(\gamma^3, \alpha^4\right)$	14.648	20.533	39.722	45.207	29.334*	—	45.509	44.974
$\mathcal{O}\left(\gamma^4, \alpha^2\right)$	15.995	22.555	48.616	57.378	34.733*	—	57.888	57.494
$\mathcal{O}\left(\gamma^4, \alpha^3\right)$	15.995	22.564	48.248	56.842	34.732*	—	57.453	57.279
$\mathcal{O}\left(\gamma^4, \alpha^4\right)$	15.995	22.570	48.102	56.625	34.730*	—	57.303	57.214
$\mathcal{O}\left(\gamma^5, \alpha^2\right)$	16.128	22.717	51.541	61.544	35.894*	—	62.197	61.780
$\mathcal{O}\left(\gamma^5, \alpha^3\right)$	16.128	22.733	51.531	61.366	35.906*	—	62.037	61.703
$\mathcal{O}\left(\gamma^5, \alpha^4\right)$	16.128	22.734	51.599	61.378	35.907*	—	62.024	61.694
Holistic 12 elements								
$\mathcal{O}\left(\gamma^3, \alpha^2\right)$	15.446	21.669	45.962	53.935	32.858	45.982	54.491	54.174
$\mathcal{O}\left(\gamma^3, \alpha^3\right)$	15.447	21.691	46.051	54.001	32.866	46.332	54.551	54.204
$\mathcal{O}\left(\gamma^4, \alpha^2\right)$	16.110	22.624	51.934	62.099	35.901	50.915	62.829	62.515
$\mathcal{O}\left(\gamma^4, \alpha^3\right)$	16.110	22.624	51.936	62.097	35.901	50.936	62.828	62.515
Galerkin [25]								
3-m Euler-Galerkin	16.103	20.590	246.14	—	36.206	—	—	—
3-m Pseudo-stdy II	16.130	21.928	102.90	—	36.206	—	—	—
3-m Pseudo-stdy	16.131	22.009	93.913	—	36.238	63.908	—	—
12-m traditional	16.140	22.556	52.891	63.737	36.234	50.911	64.559	64.275
6-m traditional	16.140	22.547	52.721	63.278	36.234	46.851	64.000	64.000
3-m traditional	16.140	16.000	16.0??	16.0??	36.000	36.0??	—	—

Table 3.2: α values at which bifurcation points occur for the various coarse grid holistic models and low mode Galerkin approximations

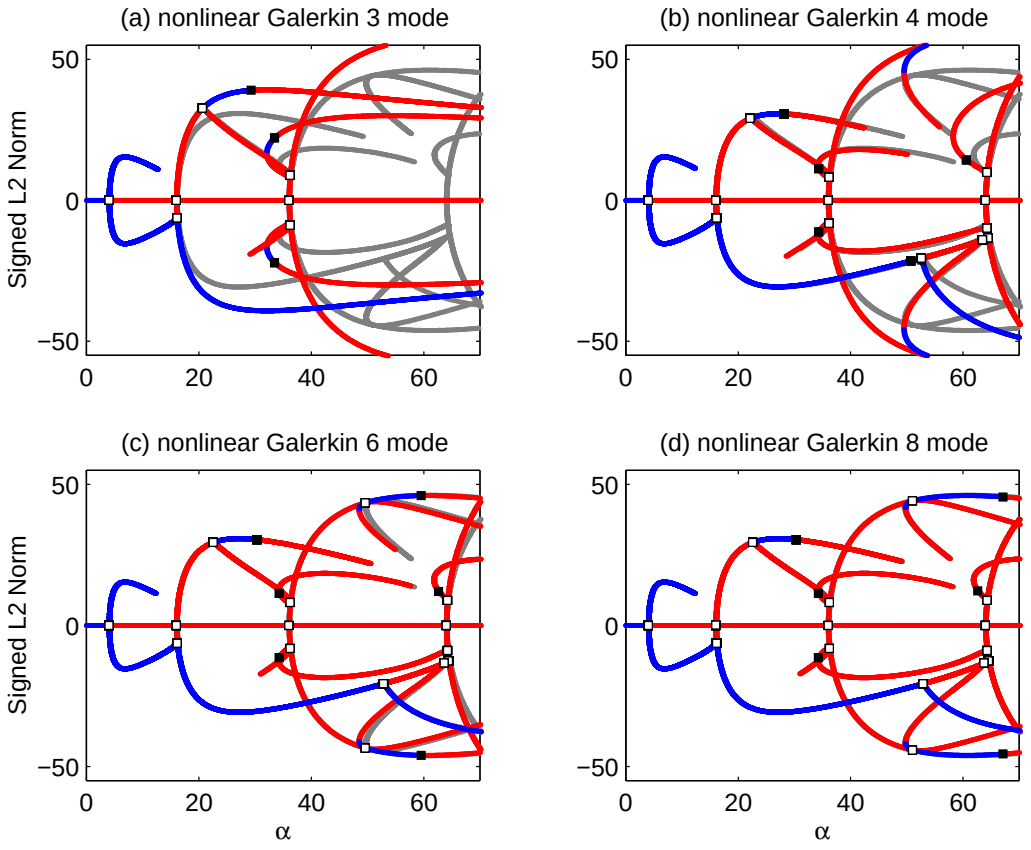

Figure 3.15: Bifurcation diagrams for (a) 3 mode, (b) 4 mode, (c) 6 mode and (d) 8 mode first iterate nonlinear Galerkin approximations on $[0, \pi]$.

3.6 Coarse grid allows larger time steps

A major benefit of accurate approximations on coarse grids is that larger time steps are possible while maintaining numerical stability. In §3.3 we saw the remarkable accuracy of the $\mathcal{O}(\gamma^5, \alpha^2)$ holistic model (2.32) on a coarse grid of 8 elements. This holistic model captures most of the steady state dynamics of the Kuramoto–Sivashinsky system (2.1) and (3.1).

Here we investigate the maximum stable time step for explicit time integration for various holistic models. Implicit schemes are not considered.

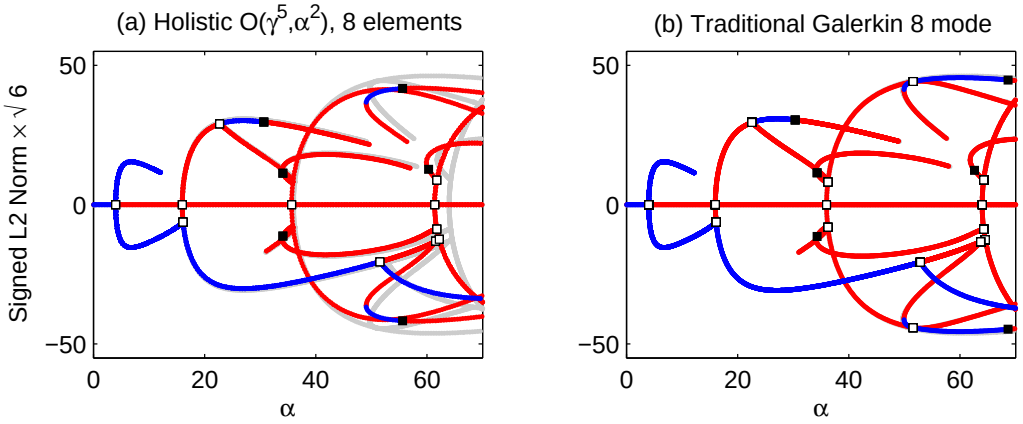

Figure 3.16: Bifurcation diagrams for (a) the $\mathcal{O}\left(\gamma^5, \alpha^2\right)$ holistic model with 8 elements on $[0, \pi]$, (b) the 8 mode traditional Galerkin approximation.

We also compare approximations of similar accuracy but different grid resolutions to demonstrate the superior performance of the holistic models. Figure 3.17 is a side by side comparison of the bifurcations diagrams of the $\mathcal{O}\left(\gamma^5, \alpha^2\right)$ holistic model with 8 elements on $[0, \pi]$ and the 2nd order centered difference approximation (2.33) with 16 grid points on $[0, \pi]$. The accurate bifurcation diagram is shown in grey. Figure 3.17 shows the $\mathcal{O}\left(\gamma^5, \alpha^2\right)$ holistic model on a coarse grid of 8 elements is of similar accuracy the 2nd order centered difference approximation on the more refined grid.

Numerical experiments were conducted using a 4th order Runge-Kutta scheme to estimate the maximum possible time step for different holistic models and centered difference approximations at various values of α. Table 3.3 lists the approximate maximum time steps that maintain numerical stability, along the negative unimodal branch at $\alpha = 10$, and the negative bimodal branch at $\alpha = 20$ and $\alpha = 30$.

For the $\mathcal{O}\left(\gamma^5, \alpha^2\right)$ holistic model with 8 elements on $[0, \pi]$, the maxi-

Approximation	$\alpha = 10$	$\alpha = 20$	$\alpha = 30$
Holistic 8 elements			
$\mathcal{O}(\gamma^3, \alpha^2)$	.0011	.0014	.0017
$\mathcal{O}(\gamma^3, \alpha^3)$	.0011	.0014	.0017
$\mathcal{O}(\gamma^3, \alpha^4)$	.0011	.0014	.0017
$\mathcal{O}(\gamma^4, \alpha^2)$	.0006	.0007	.0008
$\mathcal{O}(\gamma^4, \alpha^3)$	.0006	.0007	.0008
$\mathcal{O}(\gamma^4, \alpha^4)$	.0006	.0007	.0008
$\mathcal{O}(\gamma^5, \alpha^2)$	.0005	.0005	.0006
$\mathcal{O}(\gamma^5, \alpha^3)$	.0005	.0005	.0006
$\mathcal{O}(\gamma^5, \alpha^4)$	.0005	.0005	.0006
Centered 8 points			
2nd order	.0011	.0012	—
4th order	.0006	.0007	.0008
6th order	.0005	.0005	.0006
Centered 16 points			
2nd order	.00006	.00006	.00006

Table 3.3: Approximate maximum time steps for stability of 4th order Runge-Kutta scheme.

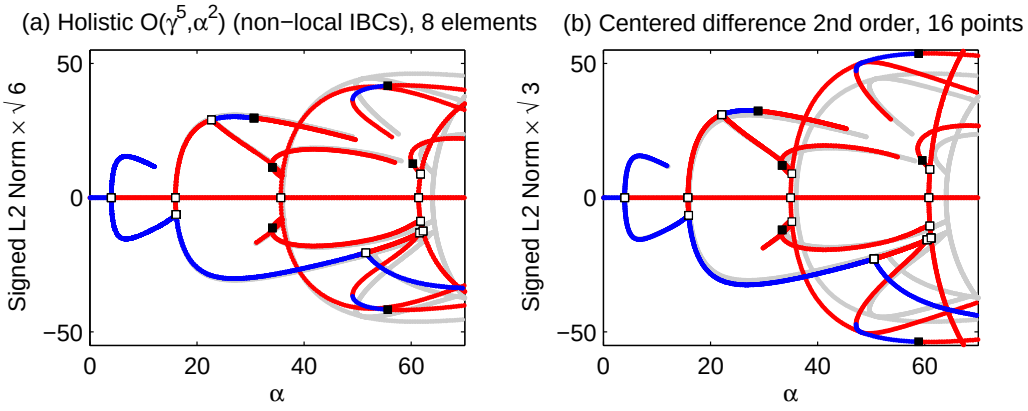

Figure 3.17: Bifurcation diagrams of (a) $\mathcal{O}(\gamma^5, \alpha^2)$ holistic model, with 8 elements on $[0, \pi]$, and (b) 2nd order centered difference approximation with 16 grid points on $[0, \pi]$. Accurate bifurcation diagram is shown in grey.

mum time step maintaining numerical stability is approximately 10 times larger than the corresponding time step for the 2nd order centered difference approximation with 16 grid points on $[0, \pi]$. The $\mathcal{O}(\gamma^5, \alpha^2)$ holistic model requires approximately 3 times the number of floating point operations at each time step compared to the 2nd order centered difference approximation. However, on a coarse grid of 16 points the 2nd order centered difference approximation must be applied at twice as many grid points. Therefore there is still an order of magnitude difference in computational time while maintaining similar accuracy for time integration of the $\mathcal{O}(\gamma^5, \alpha^2)$ holistic model with 8 elements on $[0, \pi]$ and the 2nd order centered difference approximation with 16 grid points on $[0, \pi]$.

An important observation from Table 3.3, is that the higher order terms in the nonlinearity α, generated by the holistic method do not reduce numerical stability. Wider stencil holistic approximations have reduced numerical

stability, but so do the wider stencil conventional centered difference approximations. This reduced stability is not as pronounced as the reduction in numerical stability imposed by grid refinement. Therefore, it is important to balance the accuracy gained by using higher order approximation in γ or wider stencil approximations, with the reduction in numerical stability.

3.7 Summary

Excellent performance of the holistic models for reproducing steady states of the Kuramoto–Sivashinsky system is observed on coarse macroscale grids. The holistic models constructed with non-local IBCs outperform those constructed with the local IBCs in §3.4 and are preferred throughout this dissertation.

The $\mathcal{O}(\gamma^3, \alpha^2)$ holistic model is remarkably successful in reconstructing qualitatively the dynamics of the Kuramoto–Sivashinsky equation for, $0 \leq \alpha \leq 35$, with just 8 elements on the interval $[0, \pi]$. The higher order $\mathcal{O}(\gamma^5, \alpha^2)$ holistic model achieves impressive performance for $0 \leq \alpha \leq 70$ on the same grid of 8 elements. In comparison, explicit centered difference approximations of equal stencil width only resolve the dynamics qualitatively for $0 \leq \alpha \leq 20$ for the 2nd order approximation and $0 \leq \alpha \leq 40$ for a 6th order approximation.

The bifurcation diagrams of §3.4 show that more accuracy is gained by taking higher order holistic models in γ, the inter-element coupling parameter than by taking higher order models in the nonlinearity α.

The performance of the holistic models on coarse grids was compared to the approximate inertial manifold methods of [25] in §3.5. The $\mathcal{O}\left(\gamma^5, \alpha^2\right)$

holistic models perform well in comparison to these Galerkin approximations on a coarse grid of just 8 elements on $[0, \pi]$.

In §3.6 we saw the $\mathcal{O}(\gamma^5, \alpha^2)$ holistic model with 8 elements on $[0, \pi]$ has similar accuracy to a second order centered difference approximation with a grid of 16 points. This increased accuracy on a coarse grid allows larger time steps of approximately an order of magnitude greater for explicit time integration schemes.

The accuracy of the holistic approximations to the Kuramoto–Sivashinsky equation on coarse macroscale grids and subsequent improved performance justifies further application of the holistic method and future investigation of the approach.

Chapter 4

Holistic models are accurate for time dependent phenomena of Kuramoto–Sivashinsky system

Contents

The Kuramoto–Sivashinsky equation (2.1) has rich dynamics. Many studies have shown that it exhibits complex time dependent behaviour [30, 25, 29, 59, 8, 23, 9, 2]. Having established the excellent performance of the holistic models for reproducing the steady states of the Kuramoto–Sivashinsky system in Chapter 3, we now investigate the holistic models performance at reproducing time dependent phenomena. The Kuramoto–Sivashinsky equation provides us with a test system that exhibits complex time dependent behaviour such as limit cycles, period doubling and spatio-temporal chaos. Thus it is a suitable system to investigate the performance of the holistic models for a wide range of time dependent phenomena on relatively coarse macroscale grids.

Here we investigate the performance of the low order holistic models for modelling time dependent phenomena of the Kuramoto–Sivashinsky equation (2.1). We restrict attention to 2π-periodic solutions,

$$u(x,t) = u(x+2\pi,t)\,. \tag{4.1}$$

We consider two forms of Kuramoto–Sivashinsky system in this Chapter. We investigate time dependent phenomena of the Kuramoto–Sivashinsky equation (2.1) with odd symmetry (3.1) as investigated in Chapter 3. We also consider travelling wave solutions by removing odd symmetry and investigate (2.1) with spatially periodic boundary conditions (4.1).

The Kuramoto–Sivashinsky system (2.1) with odd symmetry exhibits time dependent phenomena for the range $0 \leq \alpha \leq 70$ [25, 29, 59]. Figure 3.1 reveals Hopf bifurcations in the bifurcation diagram. The Hopf bifurcation

that occurs at $\alpha = 30.345$ gives rise to stable periodic solutions that undergo a period doubling bifurcation at $\alpha = 32.969$ leading a period doubling cascade to chaos.

We compare the eigenvalues near steady states of the $\mathcal{O}(\gamma^3, \alpha^2)$ (2.25), $\mathcal{O}(\gamma^4, \alpha^2)$ (2.30) and $\mathcal{O}(\gamma^5, \alpha^2)$ (2.32) holistic models to explicit centered difference approximations of equal stencil width in §4.1. The holistic models are more accurate on coarse grids of 8 elements on $[0, \pi]$. We introduce a generalised bifurcation diagram that displays the eigenvalues of the Kuramoto–Sivashinsky system colour coded across the bifurcation diagram. We see that the $\mathcal{O}(\gamma^5, \alpha^2)$ holistic model reproduces much of the eigenvalue information for $0 \leq \alpha \leq 70$ on a macroscale grid of 8 elements. In §4.2 we explore the bifurcation diagrams near the first Hopf bifurcation. We investigate the extended Hopf bifurcation to capture the stable limit cycles and period doubling sequence. Holistic models are more accurate than explicit centered difference approximations of equal stencil width.

Removing the odd symmetry requirement of the Kuramoto–Sivashinsky system, the stable steady state solutions become stable travelling wave or periodic solutions. Higher values of α lead to more complex behaviour and spatio-temporal chaos. Higher α is equivalent to increasing the spatial length in the form of the Kuramoto–Sivashinsky system investigated by Holmes et al. [23] and Dankowicz et al. [9] with fixed α.

In §4.3 we investigate the second form of the Kuramoto–Sivashinsky system. We compare holistic models to explicit centered difference approximations on coarse grids for $\alpha = 5$ and 10. We compare subgrid fields at specific time slices to the accurate solution. The holistic models are superior

to the centered difference approximations of equal stencil width and more accurately model the amplitude and the wave speed of the travelling wave solution.

We consider higher values of α, namely 20, 50 and 200 and compare the $\mathcal{O}(\gamma^5, \alpha^2)$ holistic model to 6th order and 2nd order centered difference approximations by examining space time plots and time averaged power spectrums. We find in §4.3.2 that the $\mathcal{O}(\gamma^5, \alpha^2)$ holistic model achieves similar accuracy to the 6th order centered difference approximation with approximately $\frac{3}{4}$ of the number of elements. For example, the $\mathcal{O}(\gamma^5, \alpha^2)$ holistic model with 8 macroscale elements achieves similar accuracy to the 6th order centered difference approximation with 12 grid points. We refer to this as the $\mathcal{O}(\gamma^5, \alpha^2)$ holistic model achieving similar accuracy to the 6th order centered difference approximately with $\frac{3}{4}$ of the grid resolution. The $\mathcal{O}(\gamma^5, \alpha^2)$ holistic approximation also has similar accuracy to the 2nd order centered difference approximation with approximately $\frac{1}{3}$ of the grid resolution. Such accuracy on coarser grids allows larger step sizes for explicit time integration schemes.

4.1 Dynamics near the steady states are reproduced

We begin investigating the performance of holistic models for reproducing time dependent phenomena the Kuramoto–Sivashinsky system, namely (2.1) with odd symmetry, by examining eigenvalues near the steady states. More accurate modelling of the eigenvalues near the steady states indicates more

accurate modelling of the dynamics of the Kuramoto–Sivashinsky system.

Firstly we investigate the four dominant eigenvalues along the negative bimodal branch (defined in §3.1) for the holistic models on coarse grids. In §4.1.1 we see that the low order holistic models outperform explicit centered difference approximations of equal stencil widths on a grid of 8 elements on $[0, \pi]$. In a similar manner to Chapter 3 the reference for the accurate solution is found using a 6th order centered difference approximation with 48 grid points on $[0, \pi]$.

Secondly in §4.1.2 we examine a generalised bifurcation diagram that depicts the 8 dominant eigenvalues by colour. We use this bifurcation diagram to compare the $\mathcal{O}(\gamma^5, \alpha^2)$ holistic model (2.32) on a grid of 8 elements on $[0, \pi]$ to the corresponding diagram displaying eigenvalue information for the accurate Kuramoto–Sivashinsky system. We investigate the eigenvalues near the steady states over the same range as the bifurcation diagrams in §3.2, namely $0 \leq \alpha \leq 70$. We find that the $\mathcal{O}(\gamma^5, \alpha^2)$ holistic model on a coarse grid of 8 elements on $[0, \pi]$ accurately reproduces the eigenvalues of the Kuramoto–Sivashinsky system across most of the bifurcation diagram for this range of α.

4.1.1 Compare eigenvalues along the bimodal branch

To investigate dynamical information near the stable bimodal branch we examine the real part of the four dominant eigenvalues for low order holistic models and compare to explicit centered difference approximations on a coarse grid of 8 elements on $[0, \pi]$. Figure 4.1 shows the four largest eigenvalues for the $\mathcal{O}(\gamma^3, \alpha^2)$ (2.25), $\mathcal{O}(\gamma^4, \alpha^2)$ (2.30) and $\mathcal{O}(\gamma^5, \alpha^2)$ (2.32) holistic

models in green and the accurate solution in blue. Recall the $\mathcal{O}(\gamma^3, \alpha^2)$, $\mathcal{O}(\gamma^4, \alpha^2)$ and $\mathcal{O}(\gamma^5, \alpha^2)$ holistic models have 5 point, 7 point and 9 point stencils, respectively. Figure 4.1a, shows that even the lowest order $\mathcal{O}(\gamma^3, \alpha^2)$ holistic model qualitatively reproduces the behaviour of the stable bimodal branch for at least $\alpha < 40$. Figure 4.1c, shows the four dominant eigenvalues for the $\mathcal{O}(\gamma^5, \alpha^2)$ holistic model closely matches the accurate solution for $0 \leq \alpha \leq 60$.

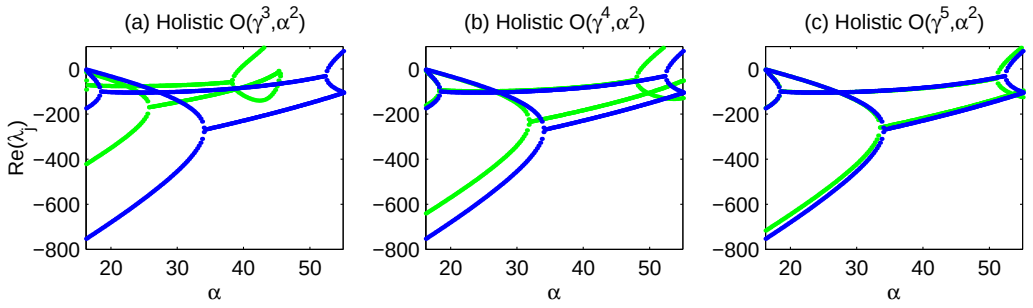

Figure 4.1: The four dominant eigenvalues along the stable bimodal branch for the (a) $\mathcal{O}(\gamma^3, \alpha^2)$, (b) $\mathcal{O}(\gamma^4, \alpha^2)$, (c) $\mathcal{O}(\gamma^5, \alpha^2)$ holistic models shown in green for 8 elements on $[0, \pi]$. The accurate eigenvalues are shown in blue.

Similarly, Figure 4.2 shows the four dominant eigenvalues for the 2nd order (2.33), 4th order (2.34) and 6th order (2.35) explicit centered difference approximations in magenta on the same coarse grid and the accurate solution in blue. Recall that the 2nd order, 4th order and 6th order approximations have 5 point, 7 point and 9 point stencils, respectively. Consequently the centered difference approximations shown here are of equal stencil width to the holistic models in Figure 4.1. Figure 4.2a, shows that the 2nd order centered difference approximation only qualitatively reproduces the dynamics near the stable bimodal branch for $\alpha < 20$. Even the 6th order centered

difference approximation, Figure 4.2c, is inferior to the $\mathcal{O}(\gamma^4, \alpha^2)$ holistic model for $\alpha > 30$. This is despite the 6th order centered difference model having a wider stencil of 9 points compared to the 7 point stencil of the $\mathcal{O}(\gamma^4, \alpha^2)$ holistic model. The 6th order centered difference approximation also loses stability along this branch at $\alpha = 42.5$, compared to $\alpha = 51.5$ for the $\mathcal{O}(\gamma^5, \alpha^2)$ holistic model and the accurate $\alpha = 52.9$ for the Kuramoto–Sivashinsky system.

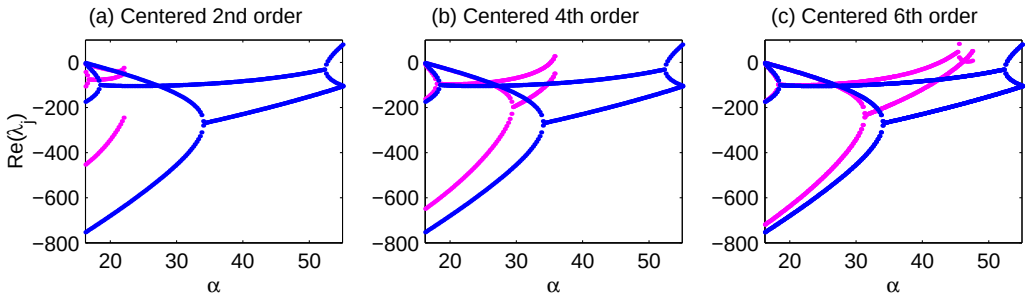

Figure 4.2: The four dominant eigenvalues along the stable bimodal branch for the (a) 2nd order, (b) 4th order, (c) 6th order centered difference approximations shown in magenta for 8 grid points on $[0, \pi]$. The accurate eigenvalues are shown in blue.

Figure 4.1 and Figure 4.2 show that the low order holistic models are superior to the centered difference approximations of equal stencil widths for reproducing the dynamics near the stable bimodal branch on this coarse grid of 8 elements on $[0, \pi]$.

4.1.2 Compare eigenvalues across the bifurcation diagram

The investigation of the eigenvalues of the stable bimodal branch §4.1.1 suggests that a more detailed comparison of the eigenvalues of the holistic models on coarse grids to the accurate Kuramoto–Sivashinsky system (2.1) is warranted. Here we explore a generalised view of the bifurcation diagrams that depicts the real part of the 8 dominant eigenvalues by colour. For this example we compare the eigenvalues of the $\mathcal{O}(\gamma^5, \alpha^2)$ (2.32) holistic model on the coarse grid of 8 elements on $[0, \pi]$ to the accurate Kuramoto–Sivashinsky system for $0 \leq \alpha \leq 70$.

Figure 4.3 is a bifurcation diagram of the $\mathcal{O}(\gamma^5, \alpha^2)$ holistic model displaying the 8 dominant eigenvalues by colour. The magnitude of the real part of the eigenvalues is colour coded according to the colour bar shown on the right of the bifurcation diagram. As in the bifurcation diagrams shown in Chapter 3, the open squares denote bifurcation points and the black squares denote Hopf bifurcations.

Figure 4.4 is a bifurcation diagram of the accurate Kuramoto–Sivashinsky system displaying the 8 dominant eigenvalues by colour. Again the eigenvalues are colour coded according to the same colour bar reproduced again to the right of the bifurcation diagram.

Figure 4.3 and Figure 4.4 are nearly identical which shows that in addition to reproducing the stability of the accurate Kuramoto–Sivashinsky system for $0 \leq \alpha \leq 70$, as discussed in §3.3, the $\mathcal{O}(\gamma^5, \alpha^2)$ holistic model reproduces well the eigenvalues for most of this range of α. Accurate modelling of the eigenvalues indicates accurate modelling of the dynamics of the Kuramoto–

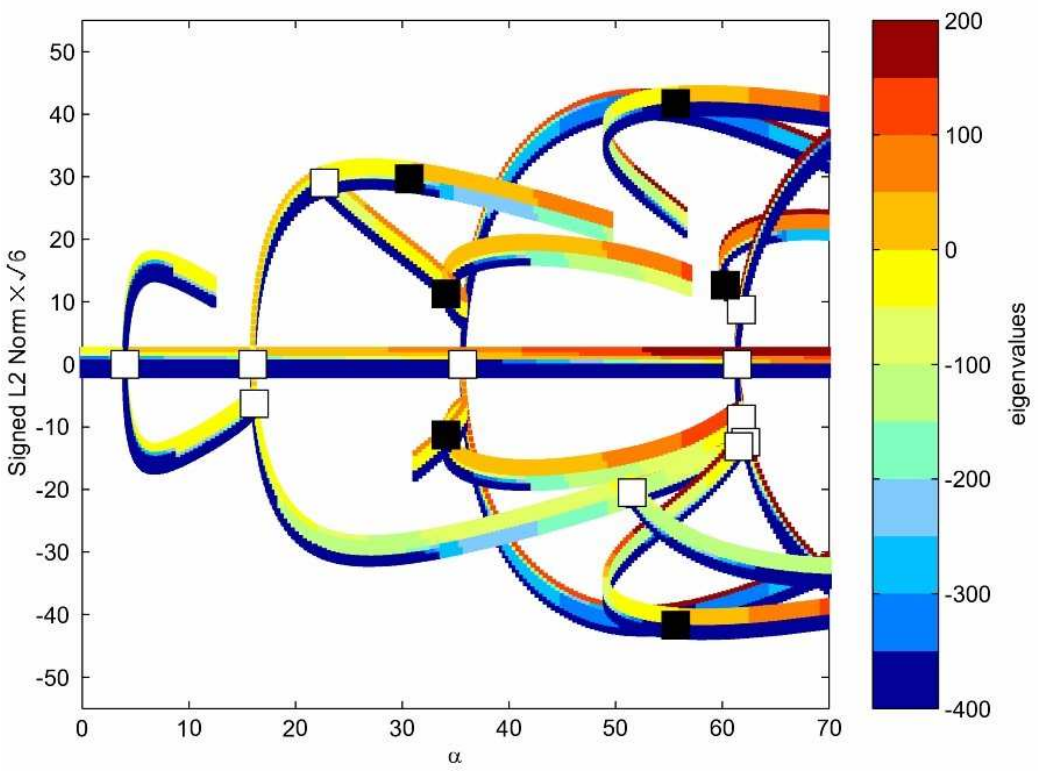

Figure 4.3: Bifurcation diagram of the $\mathcal{O}(\gamma^5, \alpha^2)$ holistic model with 8 elements on $[0, \pi]$, depicting the 8 dominant eigenvalues colour coded according to the colour bar shown.

Sivashinsky system.

4.2 Extend the Hopf bifurcations

Hopf bifurcations give rise to periodic solutions or limit cycles. Investigating the performance of the holistic models for modelling the Hopf bifurcations gives further evidence that the holistic models are a useful description of the dynamics of the Kuramoto–Sivashinsky system (2.1).

Here we compare the bifurcation diagrams obtained by extending the first

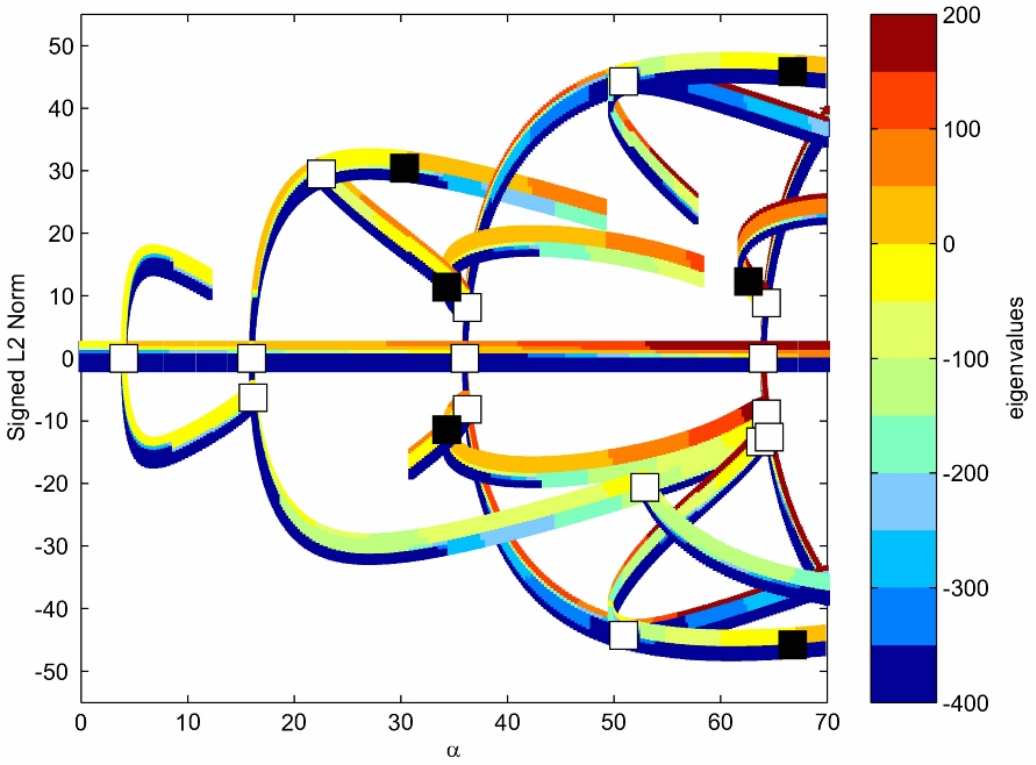

Figure 4.4: Bifurcation diagram of the accurate Kuramoto–Sivashinsky system, depicting the 8 dominant eigenvalues colour coded according to the colour bar shown.

Hopf bifurcation on the positive bimodal branch and the period doubling sequence that results. In particular we examine the bifurcation diagram near the first Hopf bifurcation at $\alpha = 30.345$. We compare the bifurcation diagrams of low order holistic models to explicit centered difference models on a coarse grid of 8 elements on $[0, \pi]$ and to the accurate bifurcation diagram of the Kuramoto–Sivashinsky system. We find that the holistic models outperform the centered difference approximations of equal stencil width for modelling these time dependent phenomena.

In §4.2.2 we investigate the sequence of values at which the period dou-

bling continues from the first Hopf bifurcation and compare these values for the $\mathcal{O}(\gamma^5, \alpha^2)$ (2.32) holistic model to the 6th order centered difference approximation (2.35) and the accurate period doubling sequence. By comparing this sequence of values at which the period doubling occurs we see the $\mathcal{O}(\gamma^5, \alpha^2)$ holistic model outperforms the 6th order centered difference approximation.

4.2.1 Investigate the first Hopf bifurcation

We investigate the holistic models near the first Hopf bifurcation on a coarse macroscale grid of 8 elements on $[0, \pi]$. The first Hopf bifurcation which occurs on the positive bimodal branch is labeled HB_1, see Figure 4.5 for example. The stable limit cycles that continue from this bifurcation point undertake a period doubling sequence commencing at a point labeled PD in Figure 4.5. The pair of unstable limit cycles born at PD give rise to the period doubling sequence of asymmetric limit cycles leading to chaotic solutions.

Figure 4.5 shows the bifurcation diagrams of the low order holistic models and the accurate bifurcation diagram near this first Hopf bifurcation. The stable limit cycles are displayed in light blue and the unstable limit cycles are displayed in orange. The period doubling point PD is denoted by a yellow square.

The accurate bifurcation diagram shown in Figure 4.5d is produced using a 6th order centered difference approximation with 24 grid points on $[0, \pi]$. The accurate solution is produced with only 24 grid points here because of the computational time required using XPPAUT to generate the bifurcation

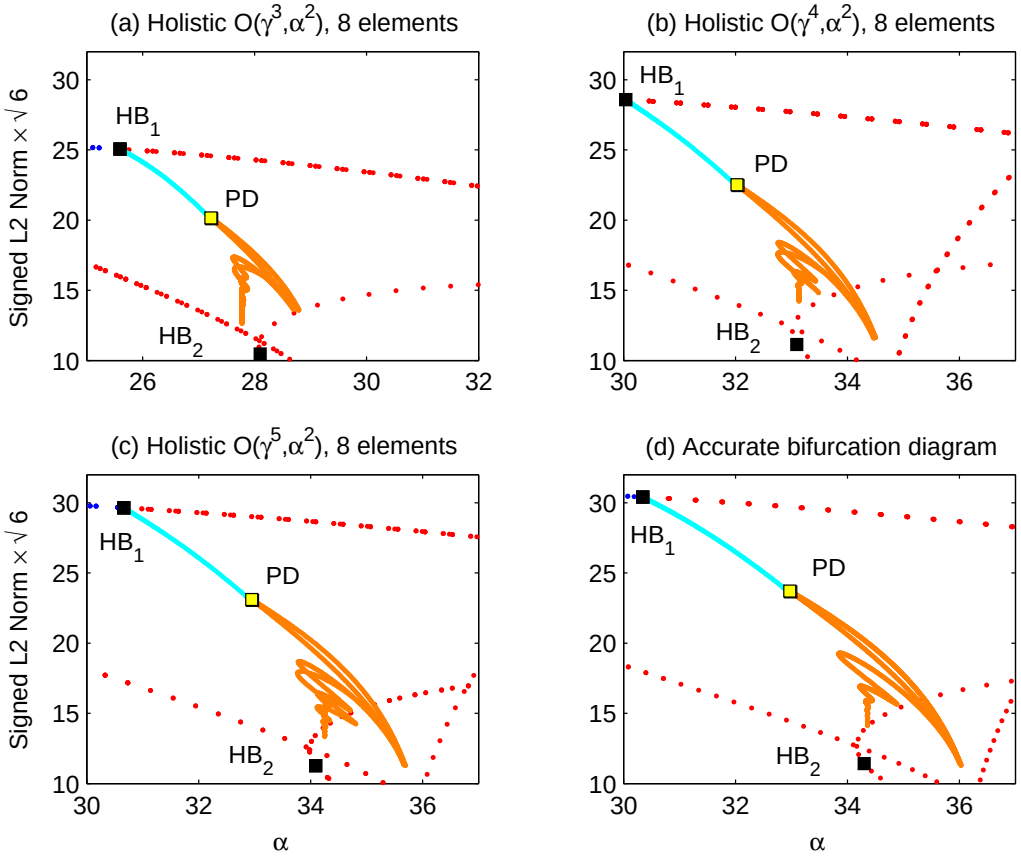

Figure 4.5: Bifurcation diagrams for the (a) $\mathcal{O}(\gamma^3, \alpha^2)$, (b) $\mathcal{O}(\gamma^4, \alpha^2)$, (c) $\mathcal{O}(\gamma^5, \alpha^2)$ holistic models near the first Hopf bifurcation with 8 elements on $[0, \pi]$ and (d) an accurate bifurcation diagram. Stable limit cycles are shown in light blue and unstable limit cycles are shown in orange.

diagram of the periodic solutions for higher resolutions. However, a comparison of the accurate bifurcation diagram shown here and the bifurcation diagram for the same range of α produced by Jolly et al. [25] using the 8 mode traditional Galerkin approximation, shows that the 6th order centered difference approximation with 24 grid points on $[0, \pi]$ is sufficiently good as a reference accurate solution near the first Hopf bifurcation.

Figure 4.5a shows that even the lowest order $\mathcal{O}(\gamma^3, \alpha^2)$ (2.25) holistic model reproduces the the first Hopf bifurcation and finds the period doubling point on this coarse grid of 8 elements. In comparison, the 2nd order centered difference approximation which is of equal stencil width, does not reproduce the first Hopf bifurcation at all, see Figure 3.11b. Note that Figure 4.5a displays the bifurcation diagram for $25 \leq \alpha \leq 32$ compared to $30 \leq \alpha \leq 37$ for the other diagrams. This is done so the bifurcation windows displayed are of the same size. However, since the first Hopf bifurcation for the $\mathcal{O}(\gamma^3, \alpha^2)$ holistic model occurs at $\alpha = 25.595$ the bifurcation diagram is shifted to contain the important dynamics.

Figure 4.5b,c show that higher order holistic models more accurately model the first Hopf bifurcation and the resulting stable and unstable limit cycles. The accuracy of the $\mathcal{O}(\gamma^5, \alpha^2)$ (2.32) holistic model for reproducing these periodic solutions of the Kuramoto–Sivashinsky system is remarkable on this coarse grid.

Figure 4.6 shows the corresponding bifurcation diagrams for the 4th order and 6th order centered difference approximations with 8 grid points on $[0, \pi]$. Comparing Figure 4.6 and Figure 4.5 we see that the 6th order centered difference approximation, which has a nine point stencil, does not perform as

well as the $\mathcal{O}(\gamma^4, \alpha^2)$ (2.30) holistic model which has a seven point stencil.

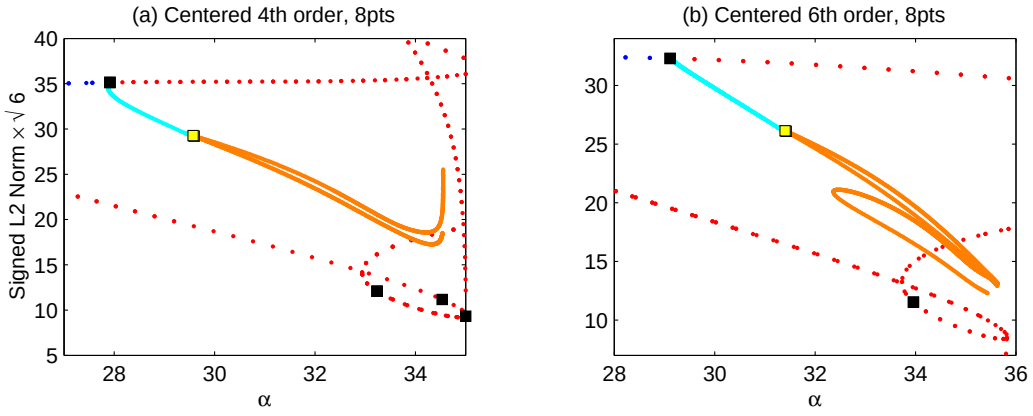

Figure 4.6: Bifurcation diagrams near the first Hopf bifurcation for (a) 4th order, (b) 6th order centered difference approximations with 8 grid points on $[0, \pi]$. Stable limit cycles are shown in light blue and unstable limit cycles are shown in orange.

Table 4.2.1 lists the parameter values α for the Hopf bifurcations, HB_1 and the initial period doubling point PD. The table shows that both the $\mathcal{O}(\gamma^4, \alpha^2)$ and $\mathcal{O}(\gamma^5, \alpha^2)$ holistic models are more accurate than the 4th order and 6th order centered difference approximations for reproducing the first Hopf bifurcation and the resulting period doubling point.

4.2.2 Period doubling is more accurately modelled

Here we examine the values at which the period doubling subsequent to the first Hopf bifurcation occurs for the $\mathcal{O}(\gamma^5, \alpha^2)$ (2.25) holistic model and the 6th order centered difference approximation on a coarse grid of 8 elements on $[0, \pi]$ and compare both to the values at which the period doubling sequence PD, of the accurate Kuramoto–Sivashinsky system (2.1) occurs. We find

Approximation	HB_1	PD
Holistic 8 elements		
$\mathcal{O}(\gamma^3, \alpha^2)$	25.595	27.220
$\mathcal{O}(\gamma^4, \alpha^2)$	30.038	32.028
$\mathcal{O}(\gamma^5, \alpha^2)$	30.660	32.947
Centered 8 points		
2nd order	—	—
4th order	27.914	29.572
6th order	29.113	31.403
Accurate	30.345	32.969

Table 4.1: α values for the first Hopf bifurcation point HB_1 and resulting period doubling point PD.

the $\mathcal{O}(\gamma^5, \alpha^2)$ holistic model more accurately models the period doubling sequence.

Figure 4.7 shows the period doubling sequence starting at PD for the accurate Kuramoto–Sivashinsky system: it plots the $\sin(2x)$ component against the $\sin(x)$ component. We see the period doubling sequence occuring at $\alpha = 32.96$, 32.985, 32.990 and 32.997. Figure 4.8 shows the period doubling sequence starting at PD for the $\mathcal{O}(\gamma^5, \alpha^2)$ holistic model on a coarse grid of 8 elements at $\alpha = 32.94$, 32.958, 32.963 and 32.970. Figure 4.9 shows the same sequence for the 6th order centered difference approximation on the same grid at $\alpha = 31.40$, 31.418, 31.423 and 31.431. Comparing the values of the nonlinearity α at which these three period doubling sequences occur shows the $\mathcal{O}(\gamma^5, \alpha^2)$ holistic model accurately reproduces this period

doubling sequence on this coarse grid.

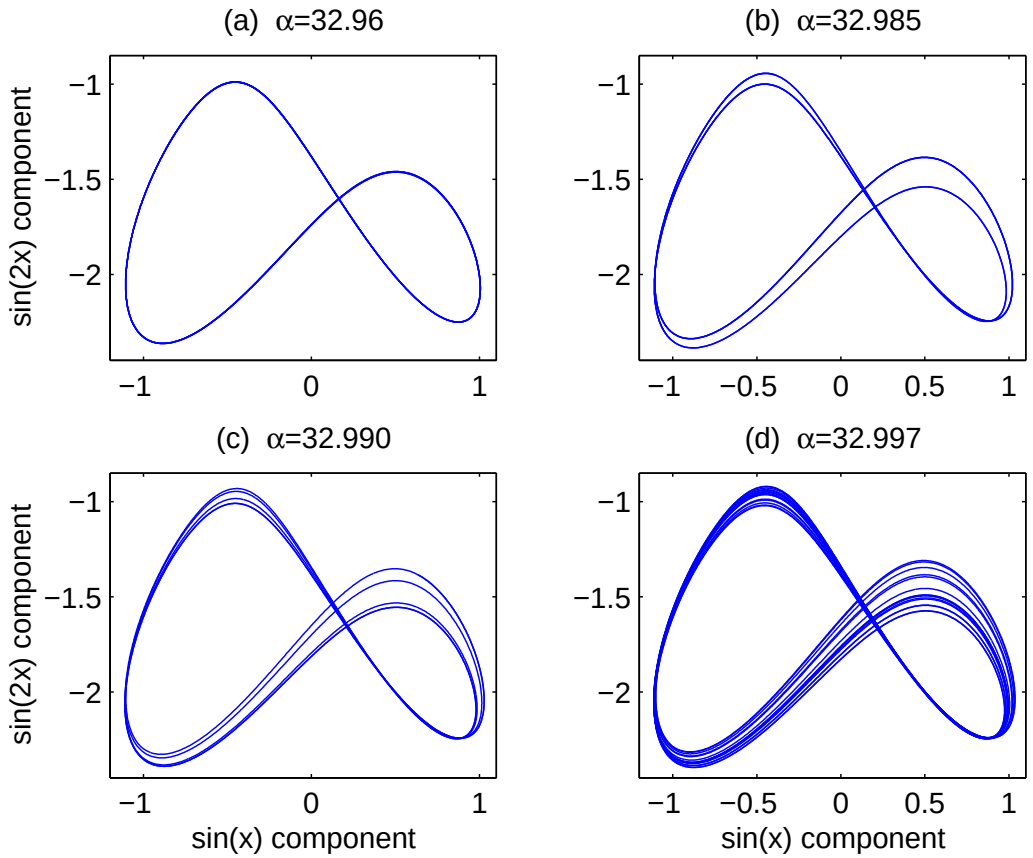

Figure 4.7: The period doubling sequence starting at PD for the accurate Kuramoto–Sivashinsky system. The $\sin(2x)$ component is plotted against the $\sin(x)$ component for (a) $\alpha = 32.96$, (b) $\alpha = 32.985$, (c) $\alpha = 32.990$ and (d) $\alpha = 32.997$.

4.3 Investigate travelling wave solutions

We consider the performance of the low order holistic models on coarse grids for the Kuramoto–Sivashinsky system (2.1) without odd symmetry. By re-

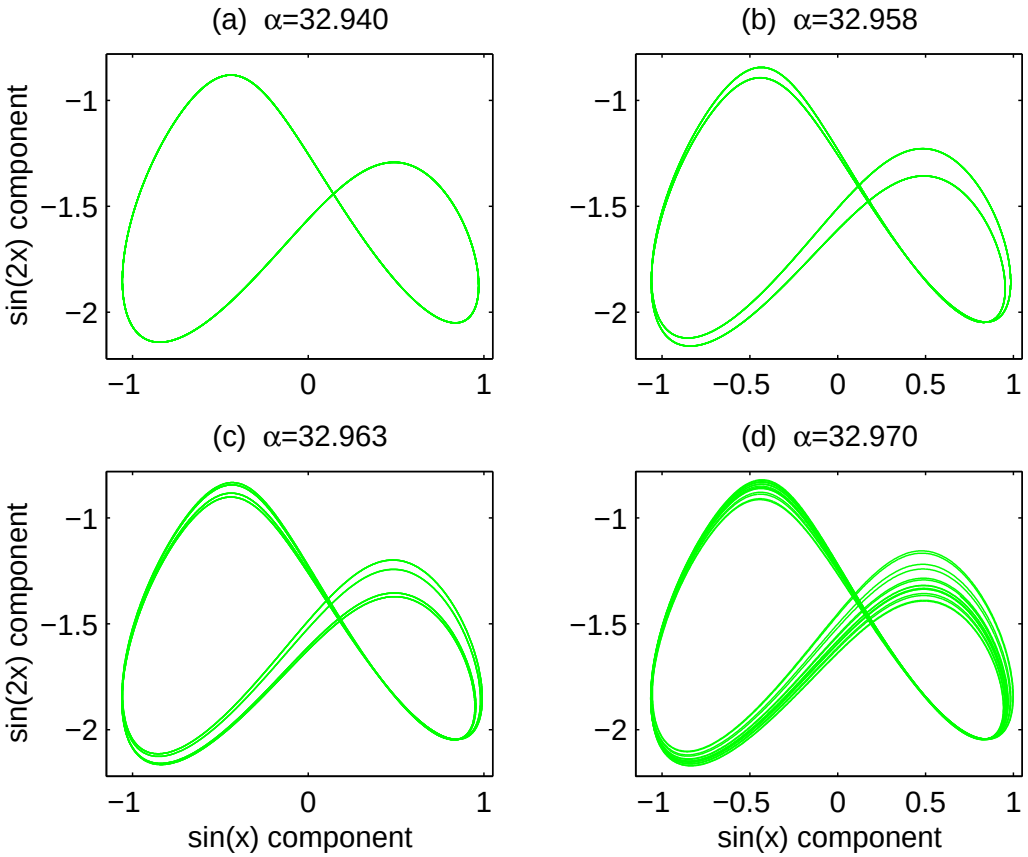

Figure 4.8: The period doubling sequence starting at PD for the $\mathcal{O}(\gamma^5, \alpha^2)$ holistic model with 8 elements on $[0, \pi]$. The $\sin(2x)$ component is plotted against the $\sin(x)$ component for (a) $\alpha = 32.94$, (b) $\alpha = 32.958$, (c) $\alpha = 32.963$ and (d) $\alpha = 32.970$.

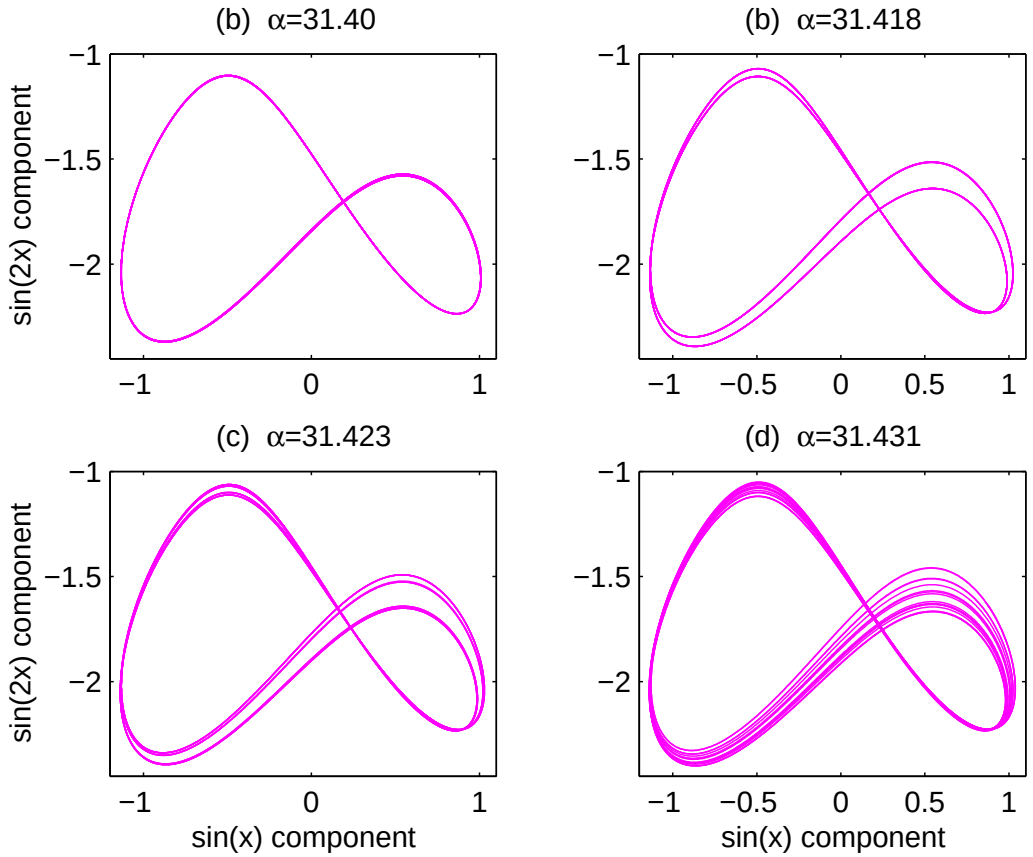

Figure 4.9: The period doubling sequence starting at PD for 6th order centered difference approximation with 8 grid points on $[0, \pi]$. The $\sin(2x)$ component is plotted against the $\sin(x)$ component for (a) $\alpha = 31.40$, (b) $\alpha = 31.418$, (c) $\alpha = 31.423$ and (d) $\alpha = 31.431$.

moving the odd symmetry requirement, the steady state solutions seen in Chapter 3 are translationally invariant leading to travelling wave solutions. For this system we consider the coarse macroscale grids on the spatial interval $[0, 2\pi]$. Consequently, investigating this form of the Kuramoto–Sivashinsky system allows us to compare the holistic models on coarse grids for time dependent travelling wave solutions at low α. Also, in this form we can investigate the holistic models performance for modelling the spatio-temporal chaos that occurs at higher values of α.

Firstly, we examine solutions of the Kuramoto–Sivashinsky system for low values of α. In particular we investigate holistic models with 8 elements on $[0, 2\pi]$ for $\alpha = 5$ and $\alpha = 10$ and compare to the accurate solution and explicit centered difference approximations at several time slices. We use the half-wave initial condition of $u(x, 0) = \sin(x/2)$ for the numerical simulations reported here. We find the holistic models to be superior to the centered difference approximations of equal stencil widths.

Secondly, we consider higher values of α and the $\mathcal{O}(\gamma^5, \alpha^2)$ (2.25) holistic model on relatively coarse grids. As α increases the Kuramoto–Sivashinsky system exhibits more complex behaviour and holistic models need more elements to reproduce properties of the system. We compare holistic models to accurate solutions and explicit centered difference approximations on coarse grids by comparing space-time plots and time averaged power spectra. Holmes et al. [23] and Dankowicz et al. [9] used this representation to investigate numerical models of the complex behaviour of the Kuramoto–Sivashinsky system. We investigate $\alpha = 20, 50$ and 200. We find the $\mathcal{O}(\gamma^5, \alpha^2)$ holistic model to have similar accuracy to the 6th order centered

difference approximations on a grid with approximately 3/4 the resolution. We also find that the the $\mathcal{O}(\gamma^5, \alpha^2)$ holistic model achieves similar accuracy to the 2nd order centered difference approximations on a grid of approximately 1/3 the resolution.

4.3.1 Good performance for holistic models at low α

We consider the performance of the holistic models of the 2π-peridodic solution of the Kuramoto–Sivashinsky system (2.1) for $\alpha = 5$ and $\alpha = 10$, on coarse grids of 8 elements on $[0, 2\pi]$. Figure 4.10 shows the lowest order $\mathcal{O}(\gamma^3, \alpha^2)$ (2.25) holistic model for $\alpha = 5$ in green, the accurate solution in blue and the explicit 2nd order centered difference approximation (2.33) with 8 points on $[0, 2\pi]$, in magenta. The solutions are shown at times $t = 0, 0.2, 0.4, 0.6, 0.8, 1$. We see that the $\mathcal{O}(\gamma^3, \alpha^2)$ holistic model is superior to the 2nd order centered difference approximation. In particular, the amplitude of the travelling wave solution and the wave speed are more accurately reproduced by the $\mathcal{O}(\gamma^3, \alpha^2)$ holistic model for $\alpha = 5$.

Similarly, Figure 4.11 shows the same time slices for $\alpha = 10$. The $\mathcal{O}(\gamma^3, \alpha^2)$ (2.25) holistic model is shown in green; the $\mathcal{O}(\gamma^4, \alpha^2)$ (2.30) model is shown in light green; and the $\mathcal{O}(\gamma^5, \alpha^2)$ (2.32) holistic model in light blue with 8 elements on $[0, 2\pi]$. For $\alpha = 10$ the 2nd order (2.33) and 4th order (2.34) centered difference approximations do not reproduce the accurate dynamics on this coarse grid. However, the 6th order centered difference approximation (2.35) does reproduce the travelling wave solution and is shown in red. The $\mathcal{O}(\gamma^3, \alpha^2)$ holistic model (green) is the least accurate but it does reproduce a stable periodic solution with only a 5 point stencil

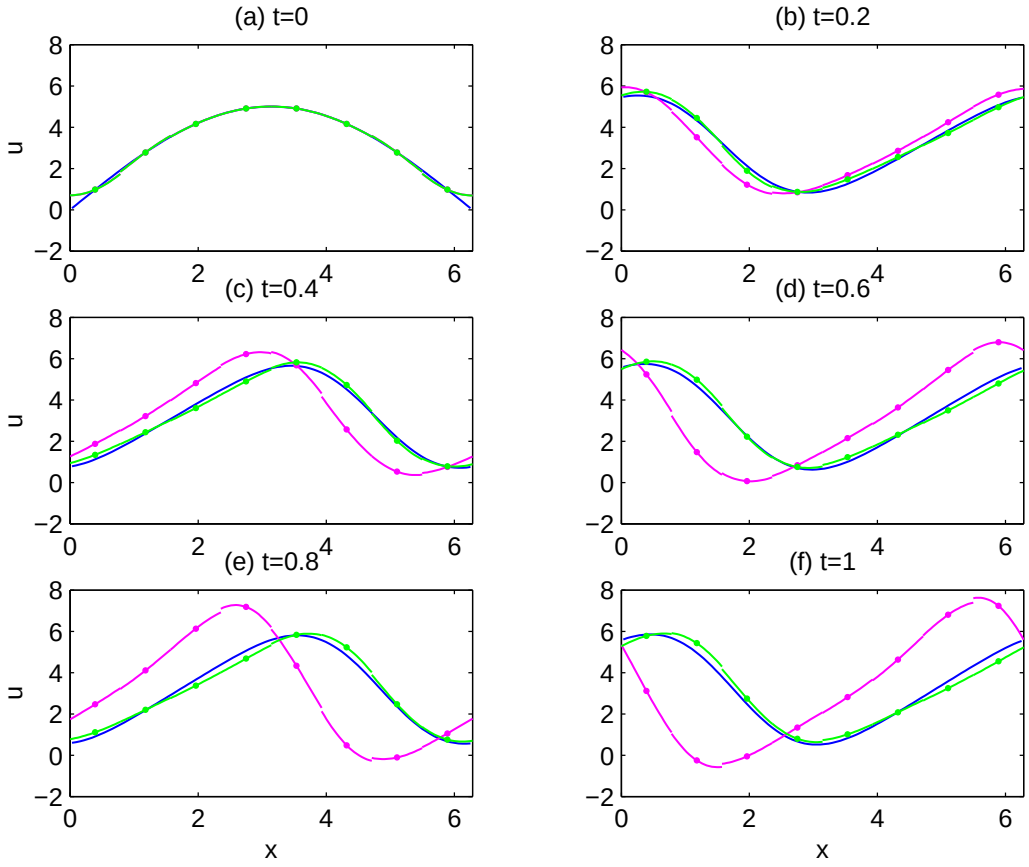

Figure 4.10: Periodic solutions for $\alpha = \mathbf{5}$ at $t = 0, 0.2, 0.4, 0.6, 0.8, 1$ for the $\mathcal{O}(\gamma^3, \alpha^2)$ holistic model shown in green and the 2nd order centered difference approximation in magenta with 8 elements on $[0, 2\pi]$. The accurate solution is shown in blue.

approximation. The $\mathcal{O}(\gamma^4, \alpha^2)$ holistic model (light green) more accurately models the amplitude of the solution compared to the 6th order centered difference approximation despite having a smaller stencil width. The $\mathcal{O}(\gamma^5, \alpha^2)$ holistic model is the most accurate for reproducing both the amplitude and the wave speed of the stable periodic solution for $\alpha = 10$ on this grid of 8 elements.

4.3.2 Good performance for more complex behaviour

In §4.3.1 we investigated the performance of the holistic models on coarse grids by examining specific time slices. For low values of α for which the Kuramoto–Sivashinsky system (2.1) exhibits simple travelling wave solutions this simple approach is suitable. For higher values of α the Kuramoto–Sivashinsky system exhibits more complex behaviour, including spatio-temporal chaos. Since the dynamics are chaotic, a detailed "pointwise" comparison is not appropriate. Consequently, we look at the broad qualitative nature of the evolution and compare time averaged power spectra as used by Holmes et al. [23] and Dankowicz et al. [9].

We investigate the performance of the holistic models for the higher values of $\alpha = 20$, 50 and 200. The focus here is to show the good performance of the holistic models on coarse grids, continues for the Kuramoto–Sivashinsky equation for ranges of α that contain more complex dynamics. Again, we use the half-wave initial condition of $u(x, 0) = \sin(x/2)$ for the numerical simulations and the repeatability of the results is not explored here. We focus on investigating the improved performance of the $\mathcal{O}(\gamma^5, \alpha^2)$ holistic model compared to the 6th order centered difference approximation which

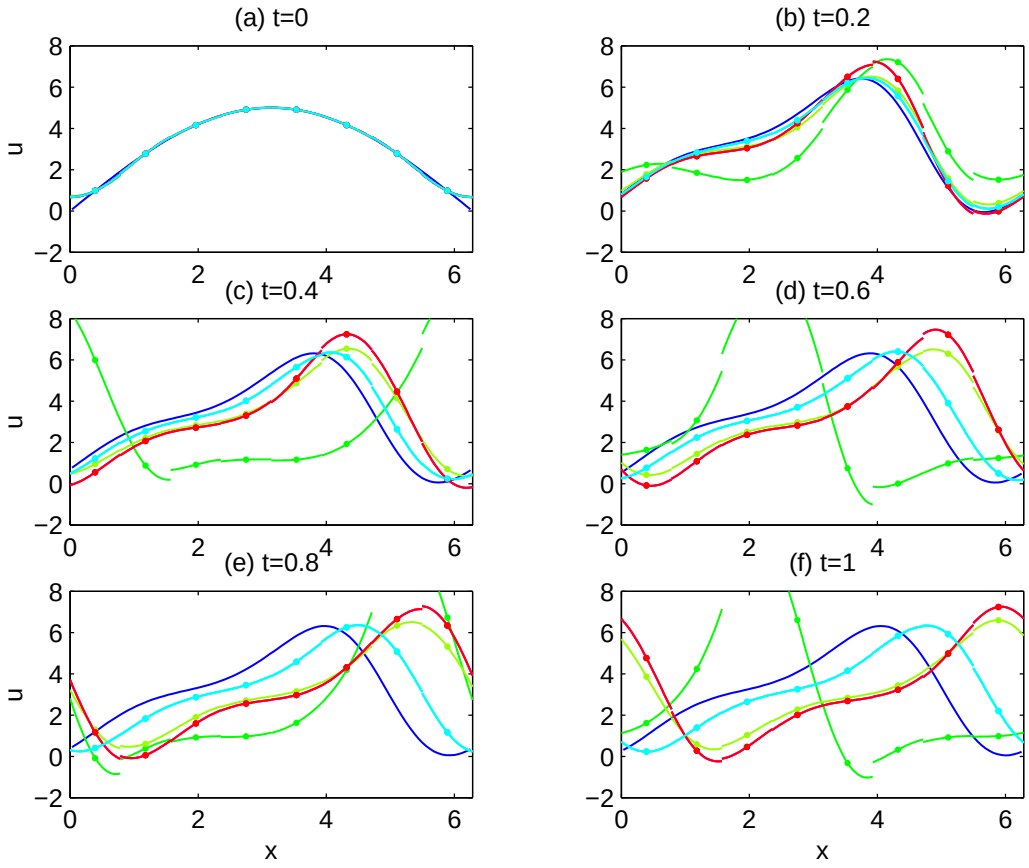

Figure 4.11: Periodic solutions for $\alpha = \mathbf{10}$ at $t = 0, 0.2, 0.4, 0.6, 0.8, 1$ for the $\mathcal{O}(\gamma^3, \alpha^2)$, $\mathcal{O}(\gamma^4, \alpha^2)$ and $\mathcal{O}(\gamma^5, \alpha^2)$ holistic models shown in green, light green and light blue respectively and the 6th order centered difference approximation shown in red with 8 elements on $[0, 2\pi]$. The accurate solution is shown in blue.

is of equal stencil width. The superior performance of the holistic models compared to equal stencil width explicit centered difference approximations that we see here follows for the other holistic models but is not reported here.

We also compare the $\mathcal{O}(\gamma^5, \alpha^2)$ holistic model on coarse grids to the 2nd order centered difference approximations of similar accuracy. We find the $\mathcal{O}(\gamma^5, \alpha^2)$ holistic model has comparable accuracy to 2nd order centered difference approximations with grids of approximately 1/3 the resolution.

Figure 4.12 shows space time plots for the $\mathcal{O}(\gamma^5, \alpha^2)$ holistic model with 12 elements on $[0, 2\pi]$, a 6th order centered difference approximation with 12 grid points on $[0, 2\pi]$, and the accurate solution[1]. We see the $\mathcal{O}(\gamma^5, \alpha^2)$ holistic model reproduces much of the complex structure of the accurate solution for $\alpha = 20$ with just 12 elements. Figure 4.12b, shows that the 6th order centered difference approximation incorrectly finds a periodic solution after approximately $t = 0.2$.

Since the Kuramoto–Sivashinsky system exhibits more complex time dependent behaviour than simple travelling wave solutions for $\alpha = 20$, we compare time averaged power spectra. The time averaged power spectra is denoted here as $S(k)$ for wavenumber k. Figure 4.13a shows a log-log plot of the time average power spectrums of the $\mathcal{O}(\gamma^5, \alpha^2)$ holistic model in light blue and the 6th order centered difference approximation on a coarse grid of 12 elements on $[0, 2\pi]$ in red. The accurate spectrum is shown in blue. For a coarse grid of only 12 elements only 5 wavenumbers are displayed as

[1]The accurate solutions plotted here are computed using a 6th order centered difference approximation and 256 grid points on the interval $[0, 2\pi]$. This is sufficient grid resolution to capture the important dynamics of the Kuramoto–Sivashinsky system for the values of α investigated here

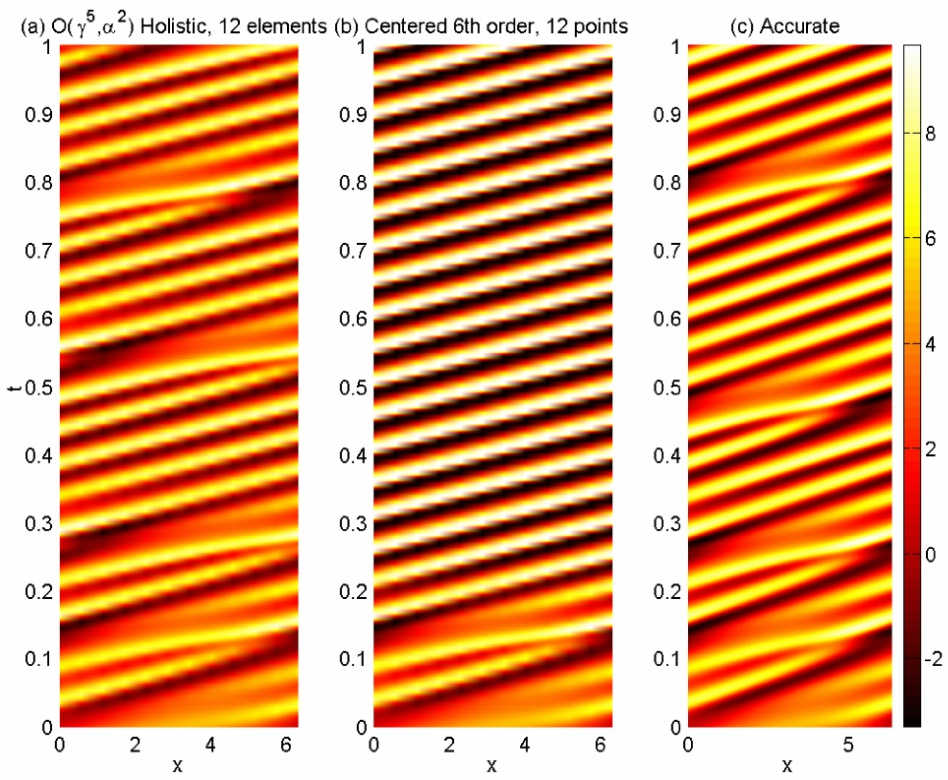

Figure 4.12: Space time plots for $\alpha = 20$ for (a) the $\mathcal{O}(\gamma^5, \alpha^2)$ holistic model with 12 elements on $[0, 2\pi]$, (b) 6th order centered difference approximation with 12 grid points on $[0, 2\pi]$ and (c) the accurate solution

the $k = 0$ constant component is not displayed in the graph. We see that the $\mathcal{O}(\gamma^5, \alpha^2)$ holistic model is superior to the 6th order centered difference approximation with just 12 elements. These time averaged power spectra reinforce the differences seen in Figure 4.12 but are more discernible.

Figure 4.13b compares the time average power spectrum of the $\mathcal{O}(\gamma^5, \alpha^2)$ holistic model in light blue with 12 elements and the 6th order centered difference approximation with 16 grid points. The $\mathcal{O}(\gamma^5, \alpha^2)$ holistic model achieves similar accuracy on a coarser grid.

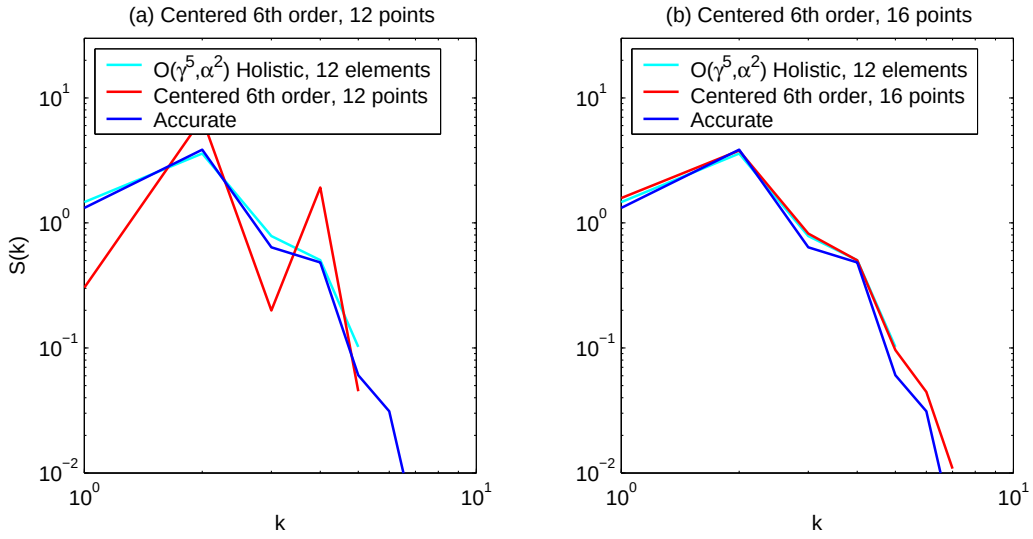

Figure 4.13: Time averaged power spectrums for $\alpha = 20$ for the $\mathcal{O}(\gamma^5, \alpha^2)$ holistic model with 12 elements on $[0, 2\pi]$ shown in light blue, and the 6th order centered difference approximation in red for (a) 12 grid points on $[0, 2\pi]$ and (b) 16 grid points on $[0, 2\pi]$. The accurate spectrum is shown in blue.

The power spectra of the $\mathcal{O}(\gamma^5, \alpha^2)$ holistic model on a coarse grid of 12 elements and the 2nd order centered difference approximation on the more refined grids of 24 and 36 points are shown in Figures 4.13a,b respectively. We see that a refined grid of 36 points is needed achieve similar accuracy to the $\mathcal{O}(\gamma^5, \alpha^2)$ holistic model on a coarse grid of 12 elements on $[0, 2\pi]$.

For $\alpha = 50$ the Kuramoto–Sivashinsky system exhibits even more complex behaviour. Figure 4.15 shows space time plots for $\alpha = 50$. The $\mathcal{O}(\gamma^5, \alpha^2)$ holistic model using 24 elements on $[0, 2\pi]$ is shown in Figure 4.15a. From this figure we see that the $\mathcal{O}(\gamma^5, \alpha^2)$ holistic model more accurately reproduces the Kuramoto–Sivashinsky system than the 6th order centered difference approximation. The 6th centered difference approximation, shown

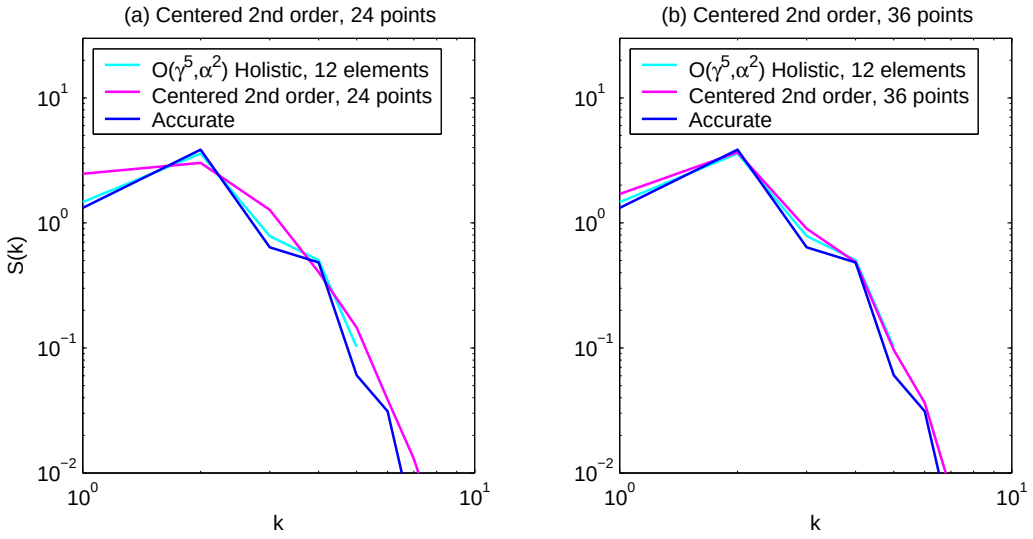

Figure 4.14: Time averaged power spectrums for $\alpha = 20$ for the $\mathcal{O}(\gamma^5, \alpha^2)$ holistic model with 12 elements on $[0, 2\pi]$ shown in light blue, and the 2nd order centered difference approximation in magenta for (a) 24 grid points on $[0, 2\pi]$ and (b) 36 grid points on $[0, 2\pi]$. The accurate solution is shown in blue.

in Figure 4.15b, exhibits a periodic solution for α greater than approximately 0.1 which does not reproduce the more irregular behaviour seen in the accurate solution and the $\mathcal{O}(\gamma^5, \alpha^2)$ holistic model on this coarse grid.

Again we examine time averaged power spectra to investigate the performance of the $\mathcal{O}(\gamma^5, \alpha^2)$ holistic model in a more discernible way. Figure 4.16 compares the time averaged power spectrum of the $\mathcal{O}(\gamma^5, \alpha^2)$ holistic model in light blue using 24 elements on $[0, 2\pi]$ to the 6th order centered difference approximation in red, for (a) 24 grid points and (b) 32 grid points on $[0, 2\pi]$, for $\alpha = 50$. The accurate solution is shown in blue. The improved performance of the $\mathcal{O}(\gamma^5, \alpha^2)$ holistic model is readily seen from the more accurate

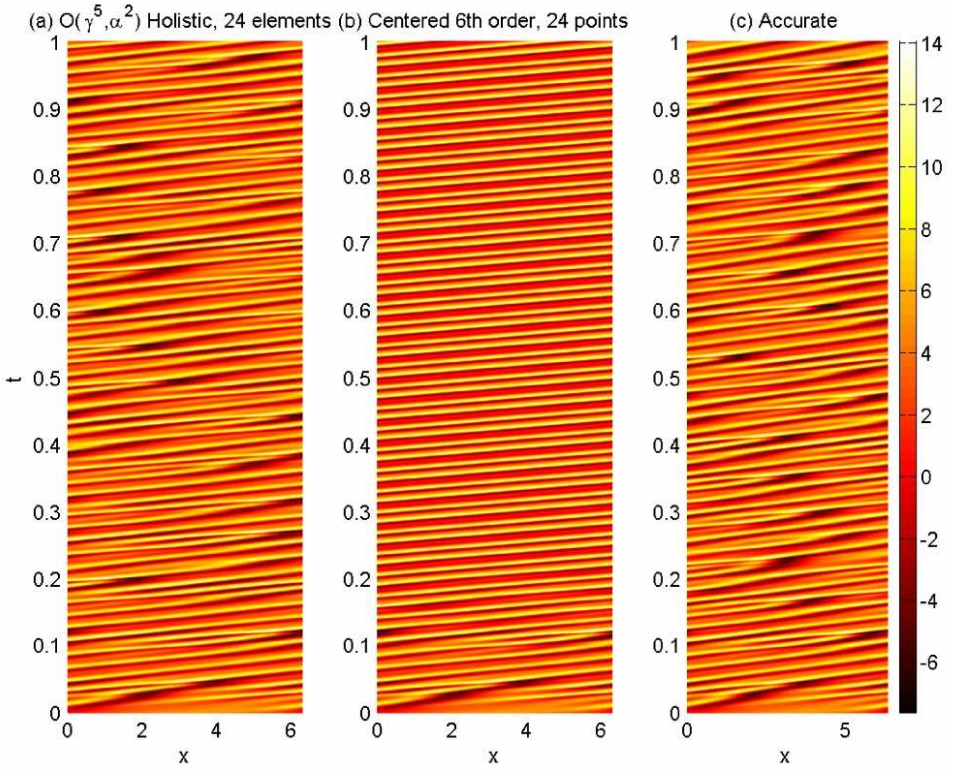

Figure 4.15: Space time plots for $\alpha = 50$ for (a) the $\mathcal{O}(\gamma^5, \alpha^2)$ holistic model with 24 elements on $[0, 2\pi]$, (b) 6th order centered difference approximation with 24 grid points on $[0, 2\pi]$ and (c) the accurate solution

power spectrum in Figure 4.16a using 24 elements. Figure 4.16b shows the 6th order centered difference approximation with 32 grid points has similar accuracy to the $\mathcal{O}(\gamma^5, \alpha^2)$ holistic model using just 24 elements for $\alpha = 50$.

Figure 4.17 compares time averaged power spectrums of the $\mathcal{O}(\gamma^5, \alpha^2)$ holistic model with 24 elements on $[0, 2\pi]$ to the 2nd order centered difference approximation with (a) 48 grid points and (b) 60 grid points on $[0, 2\pi]$ for $\alpha = 50$. Here we see a more refined grid of approximately 60 grid points is needed to reproduce the accuracy of the $\mathcal{O}(\gamma^5, \alpha^2)$ holistic model on the

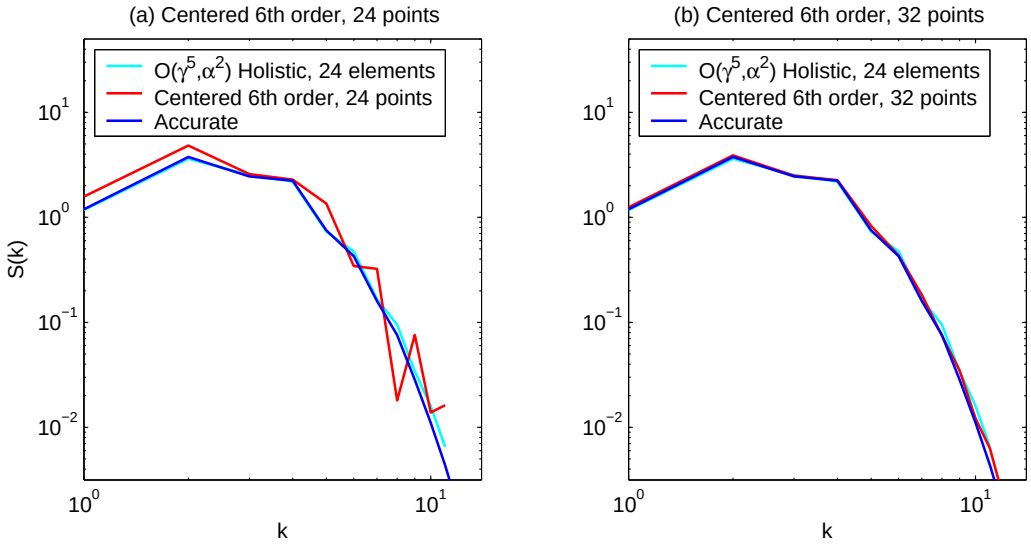

Figure 4.16: Time averaged power spectra for $\alpha = 50$ for the $\mathcal{O}(\gamma^5, \alpha^2)$ holistic model with 24 elements on $[0, 2\pi]$ shown in light blue, and the 6th order centered difference approximation in red for (a) 24 grid points on $[0, 2\pi]$ and (b) 32 grid points on $[0, 2\pi]$. The accurate spectrum is shown in blue.

coarser grid of 24 elements.

Finally, we investigate the performance of the $\mathcal{O}(\gamma^5, \alpha^2)$ holistic model on a coarse grid for $\alpha = 200$. For this large value of α the Kuramoto–Sivashinsky system exhibits characteristics of spatio-temporal chaos. Figure 4.18 shows space time plots for the $\mathcal{O}(\gamma^5, \alpha^2)$ holistic model with 36 elements on $[0, 2\pi]$, the 6th order centered difference approximation with 38 grid points on $[0, 2\pi]$ and the accurate solution. The 6th order centered difference approximation is displayed with 38 grid points because the 36 point scheme is not stable for $\alpha = 200$. The increased complexity of the Kuramoto–Sivashinsky dynamics for $\alpha = 200$ is evident from this plot. It is also difficult to discern the accuracy of either approximation by examining these space time plots.

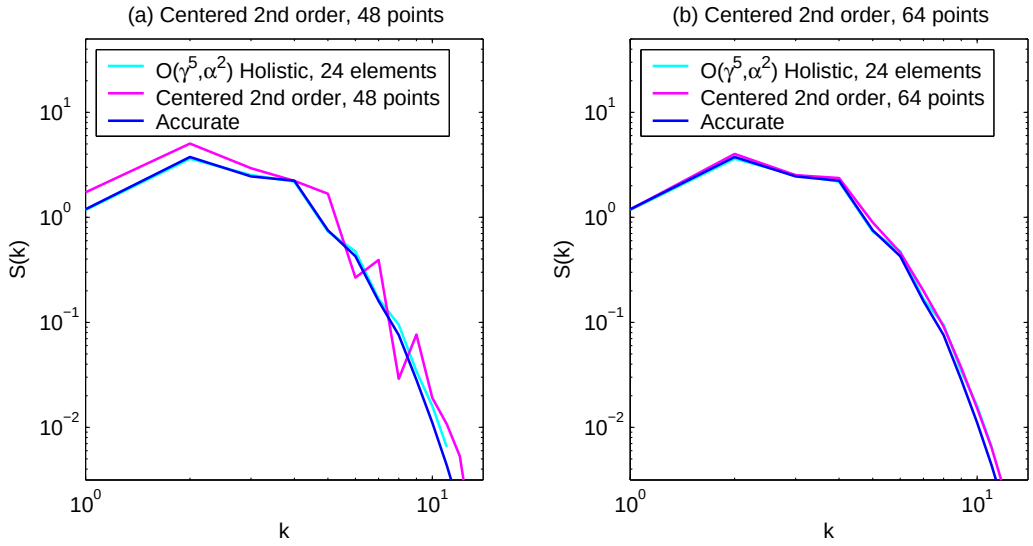

Figure 4.17: Time averaged power spectras for $\alpha = 50$ for the $\mathcal{O}(\gamma^5, \alpha^2)$ holistic model with 24 elements on $[0, 2\pi]$ shown in light blue, and the 2nd order centered difference approximation in magenta for (a) 48 grid points on $[0, 2\pi]$ and (b) 60 grid points on $[0, 2\pi]$. The accurate spectrum is shown in blue.

Again we compare time average power spectra to compare the performance of the coarse grid approximations. Figure 4.19 compares the power spectra of the $\mathcal{O}(\gamma^5, \alpha^2)$ holistic model with 36 elements on $[0, 2\pi]$ to the 6th order centered difference approximation with (a) 38 grid points and (b) 48 grid points on $[0, 2\pi]$ for $\alpha = 200$. Here we see that approximately 48 grid points are needed for the 6th order centered difference approximation to achieve the accuracy of the $\mathcal{O}(\gamma^5, \alpha^2)$ holistic model using just 36 elements for $\alpha = 200$.

Comparing the $\mathcal{O}(\gamma^5, \alpha^2)$ holistic model with 36 elements $[0, 2\pi]$ to the 2nd order centered difference approximation on a more refined grid we again

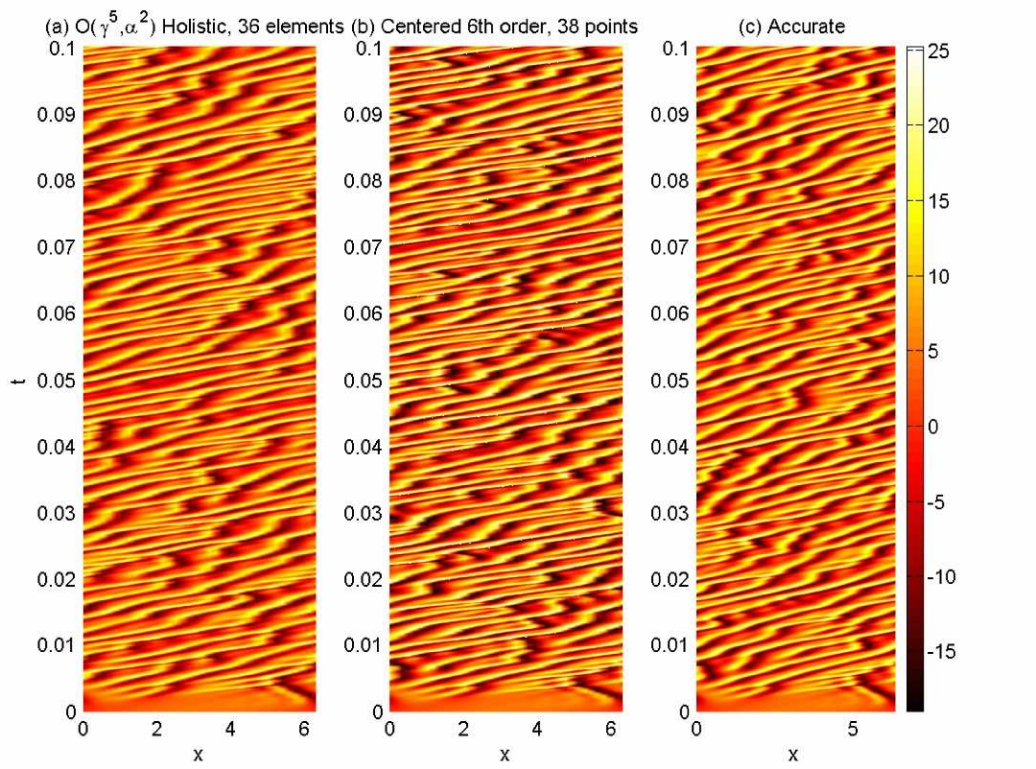

Figure 4.18: Space time plots for $\alpha = 200$ for (a) the $\mathcal{O}(\gamma^5, \alpha^2)$ holistic model with 36 elements on $[0, 2\pi]$, (b) 6th order centered difference approximation with 38 grid points on $[0, 2\pi]$ and (c) the accurate solution

see the improved accuracy on this coarse grid for the $\mathcal{O}(\gamma^5, \alpha^2)$ holistic model. Figure 4.20 compares the $\mathcal{O}(\gamma^5, \alpha^2)$ holistic model with 36 elements on $[0, 2\pi]$ to the 2nd order centered difference approximation with 80 grid points and 108 grid points on $[0, 2\pi]$ for $\alpha = 200$. From Figure 4.20b we see that similar accuracy is achieved for the 2nd order centered difference approximation with 108 grid points and the $\mathcal{O}(\gamma^5, \alpha^2)$ holistic model on a grid of 36 elements.

The investigation of the $\mathcal{O}(\gamma^5, \alpha^2)$ holistic model on coarse grids for $\alpha = 20,\ 50$ and 200 has shown it reproduces similar accuracy to the 2nd order

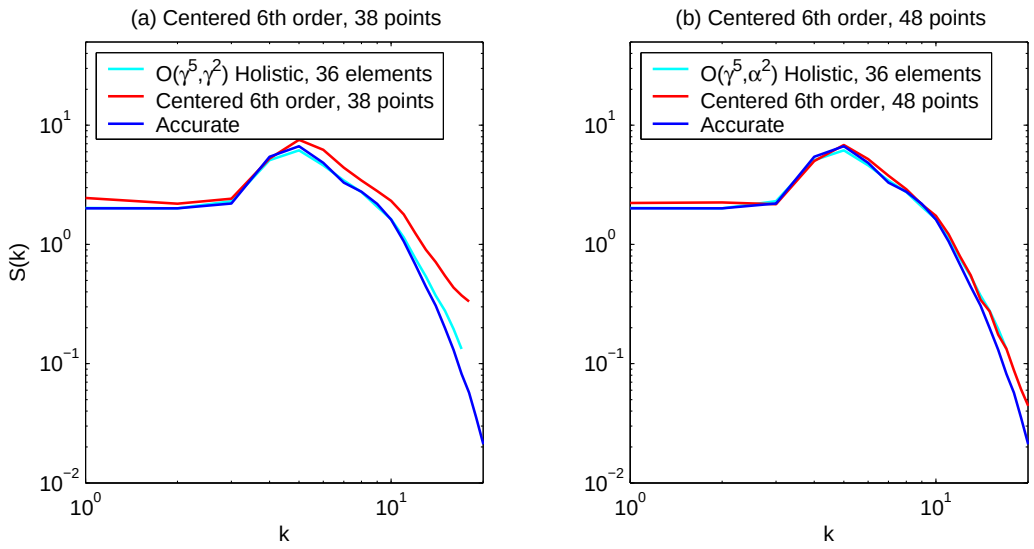

Figure 4.19: Time averaged power spectra for $\alpha = 200$ for the $\mathcal{O}(\gamma^5, \alpha^2)$ holistic model with 36 elements on $[0, 2\pi]$ shown in light blue, and the 6th order centered difference approximation in red for (a) 38 grid points on $[0, 2\pi]$ and (b) 48 grid points on $[0, 2\pi]$. The accurate spectrum is shown in blue.

centered difference approximation on a coarser grid with approximately $\frac{1}{3}$ the resolution. We have also seen that the $\mathcal{O}(\gamma^5, \alpha^2)$ holistic model achieves similar accuracy to the 6th order centered difference approximation with a grids of approximately $\frac{3}{4}$ the resolution. This increased accuracy on coarser grids allows larger time steps for explicit time integration schemes, as discussed in §3.6 but not investigated here.

4.4 Summary

The good performance for the holistic models on coarse grids continues for time dependent phenomena of the Kuramoto–Sivashinsky system. In par-

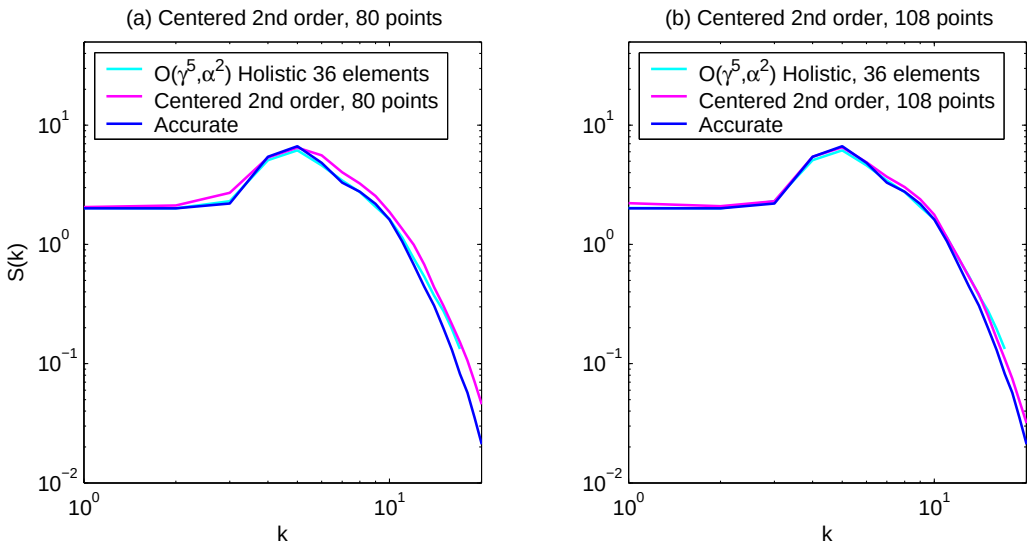

Figure 4.20: Time averaged power spectra for $\alpha = 200$ for the $\mathcal{O}(\gamma^5, \alpha^2)$ holistic model with 36 elements on $[0, 2\pi]$ shown in light blue, and the 2nd order centered difference approximation in magenta for (a) 80 grid points on $[0, 2\pi]$ and (b) 108 grid points on $[0, 2\pi]$. The accurate spectrum is shown in blue.

ticular in §4.1 we saw that the holistic models more accurately model the eigenvalues near the steady states of the Kuramoto–Sivashinsky system with odd symmetry compared to explicit centered difference approximations of equal stencil widths. We also explored in §4.2 how the coarse grid holistic models more accurately model the first Hopf bifurcation and the resulting period doubling sequence.

In §4.3 we saw the improved performance of the holistic models on coarse grids in comparison with explicit centered difference models for the 2π-periodic Kuramoto–Sivashinsky system. We saw good performance for the $\mathcal{O}(\gamma^5, \alpha^2)$ holistic model at higher values of α corresponding to more complex

time dependent behaviour. We saw by comparing time averaged power spectra that the $\mathcal{O}(\gamma^5, \alpha^2)$ holistic model achieves similar accuracy to the 2nd order and 6th order centered difference approximations on grid resolutions of approximately $\frac{1}{3}$ and $\frac{3}{4}$ respectively.

This good performance of the holistic models for accurately reproducing the time dependent phenomena of the Kuramoto–Sivashinsky system, together with the good performance for modelling the steady states seen in Chapter 3 is evidence that the holistic approach is a useful method for approximating dissipative PDEs on coarse grids.

Having established good results for the application of holistic approach to modelling the dynamics of the Kuramoto–Sivashinsky system, the remainder of this dissertation will be concerned with proof of concept type arguments for extending the application of the holistic approach.

Chapter 5

Shear dispersion in a $2D$ channel is modelled by holistic discretisation

Contents

Consider the dispersion of a pollutant or other tracer along a river, channel or pipe. Because of the long narrow geometry we are primarily interested in the evolution along the river, channel or pipe. Thus instead of solving a three-dimensional advection-diffusion equation we typically seek a one-dimensional model describing the longitudinal dynamics. Then numerical solutions are used for predictions.

For definiteness we consider here the advection-diffusion of a contaminant of concentration $c(x, y, t)$ in a two-dimensional channel of width $2b$ as shown in Figure 5.1. The governing advection-diffusion equation is

$$\frac{\partial c}{\partial t} + u\frac{\partial c}{\partial x} = \boldsymbol{\nabla} \cdot (\kappa \boldsymbol{\nabla} c) \quad \text{in} \quad -b < y < b \tag{5.1}$$

where x measures distance along the channel, $u(y)$ is the laterally varying, longitudinal advection velocity, and κ is the coefficient of diffusion.

Originally Taylor [62] derived the corresponding one-dimensional model

$$\frac{\partial C}{\partial t} = -U\frac{\partial C}{\partial x} + D\frac{\partial^2 C}{\partial x^2} \tag{5.2}$$

for the cross-channel averaged concentration $C(x, t)$, where U is the cross-channel mean advection velocity and $D \propto U^2 b^2/\kappa$ is an effective dispersion coefficient along the channel. Observe that the dispersion coefficient D is large when the molecular diffusivity κ is small. The Taylor model (5.2) is then be discretised on some numerical grid, to say

$$\frac{\partial C_j}{\partial t} \approx -\frac{U}{2h}\left(C_{j+1} - C_{j-1}\right) + \frac{D}{h^2}\left(C_{j+1} - 2C_j + C_{j-1}\right), \tag{5.3}$$

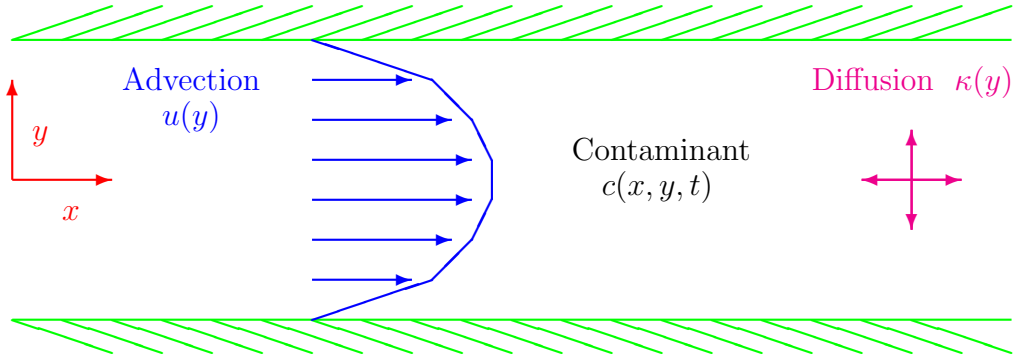

Figure 5.1: The physical processes of advection and diffusion spread a contaminant along a channel.

in order to make predictions in any given situation. However, there are difficulties in deducing the correct boundary conditions to use at the upstream inlet and the downstream outlet as discussed by Smith [61]. Roberts [48] developed arguments for deriving the appropriate boundary conditions for the Taylor model, but the required techniques are difficult even for this simple problem.

As an alternative approach we explore a holistic derivation which bypasses the one-dimensional Taylor model (5.2) by instead deriving a numerical model, such as (5.3) or more accurately (5.15), *directly* from the physical dynamics expressed in the two-dimensional advection-diffusion problem (5.1). The analysis is a variant of holistic discretisation introduced in [54] and described in detail in Chapter 2 for the Kuramoto–Sivashinsky equation (2.1). All of the results of this chapter are published in [36].

Here we explore the benefits of this single step approach of deriving an

$\mathcal{O}(\gamma^3, \mathcal{P}^3)$ holistic model (5.15) directly from (5.1). In §5.2 we see how to extend the holistic technique to this shear dispersion problem by dividing the domain into $2D$ elements that span the entire width of the channel and applying non-local artificial internal boundary conditions IBCs (5.7–5.8) adapted from §2.1.2. The application of centre manifold theory in §5.3 provides a direct connection between the one-dimensional numerical model obtained in §5.4 and the original two-dimensional advection-diffusion equation.

We show in §5.5 that deriving numerical discretisations at and near the inlet and outlet is straightforward, as introduced for Burgers' equation in [53]. We only consider physical inlet and outlet conditions for which analytic solutions to the subgrid field exists for the $\mathcal{O}(\gamma^3, \mathcal{P}^3)$ holistic model near the boundaries.

Based upon centre manifold theory, for example [4, 5], as argued in §5.2–5.3 we are reasonably assured of fidelity between the numerical model and the original equations. Indeed it is this assurance of fidelity that ensures we derive the appropriate shear dispersion coefficient $D \propto U^2b^2/\kappa$ in the numerical model (5.3), *without ever assuming large x scales*, an assumption formerly absolutely crucial in deriving Taylor's model (5.2).

We do not explore the numerical simulation of the holistic models of the shear dispersion in a $2D$ channel in this dissertation. We expect the major benefit of the holistic methodology for application to the shear dispersion problem to be highlighted with simulations involving non constant inlet and outlet conditions where treatment near the boundaries for the $1D$ Taylor model is not obvious. The numerical construction of the subgrid field is required for more general inlet and outlet boundary conditions. This is the

subject of Chapter 8 and has not yet been applied to this shear dispersion problem. Therefore, detailed numerical simulations of the holistic models are left for further research.

5.1 The cross-channel advection velocity and diffusion profile

To make the problem even more definite we follow Watt and Roberts [66] by deciding that the cross-channel profile of the advection velocity and the coefficient of diffusion are both parabolic:

$$u = U\frac{3}{2}(1 - y^2/b^2)\,, \quad \text{and} \quad \kappa = \mathcal{K}\,(1 - y^2/b^2)\,. \tag{5.4}$$

The advantage of these particular choices is that the subgrid scale field is conveniently found analytically—other choices require numerical solutions in deriving the numerical model, as detailed in §8.5.1 for the $2D$ real-valued Ginzburg–Landau equation (7.1). These choices are physically relevant to dispersion in a river, estuary or channel where turbulent mixing varies across the channel due to, for example, cross-channel variations in depth. Partnering this choice for the (turbulent) diffusivity $\kappa(y)$ are boundary conditions of zero flux of contaminant c across the sides of the channel: because $\kappa \to 0$ as $y \to \pm b$ a sufficient condition is

$$\frac{\partial c}{\partial y} \text{ is bounded on } y = \pm b\,. \tag{5.5}$$

We non-dimensionalise with respect to the channel half-width, b, and a cross channel diffusion time, $b^2/\mathcal{K}$: in effect $b = \mathcal{K} = 1$ and U is replaced by the Peclet number $\mathcal{P} = Ub/\mathcal{K}$. See that $\mathcal{P}b$ is the downstream advection

distance in a cross channel diffusion time. In application the Peclet number is typically large.

These specific choices form a problem which was studied by Watt and Roberts [66]. They derived the one-dimensional Taylor model using the assumption that longitudinal variations are slowly varying. The model generalised to higher order is

$$\begin{aligned}\frac{\partial C}{\partial t} &= -\mathcal{P}\frac{\partial C}{\partial x} + \left(\frac{2}{3} + \frac{\mathcal{P}^2}{30}\right)\frac{\partial^2 C}{\partial x^2} + \left(-\frac{2\mathcal{P}}{45} + \frac{\mathcal{P}^3}{630}\right)\frac{\partial^3 C}{\partial x^3} \\ &\quad + \left(\frac{2}{135} - \frac{\mathcal{P}^2}{315} - \frac{13\mathcal{P}^4}{189000}\right)\frac{\partial^4 C}{\partial x^4} + \cdots, \end{aligned} \tag{5.6}$$

where $C(x,t)$ represents any reasonable measure of the contaminant at station x such as the mid-channel value which we use herein. The generalised Taylor model reappears in the equivalent PDE (5.18) of the holistic model (5.15) derived in §5.4.

5.2 The domain is divided into elements

We divide the physical domain into m elements. Artificial boundaries are applied between elements to isolate each from its neighbours and centre manifold theory is applied as discussed in §5.3. Rosencrans [56] analogously divided a periodically varying channel into elements in order to use multiple scales to derive a Taylor model for the large scale dispersion. Here, the isolating internal boundaries are later removed in the analysis to form the relevant discretisation.

Here we divide the domain into rectangular elements of longitudinal size h and extending across the whole channel, $-1 < y < 1$ as illustrated in Figure 5.2.

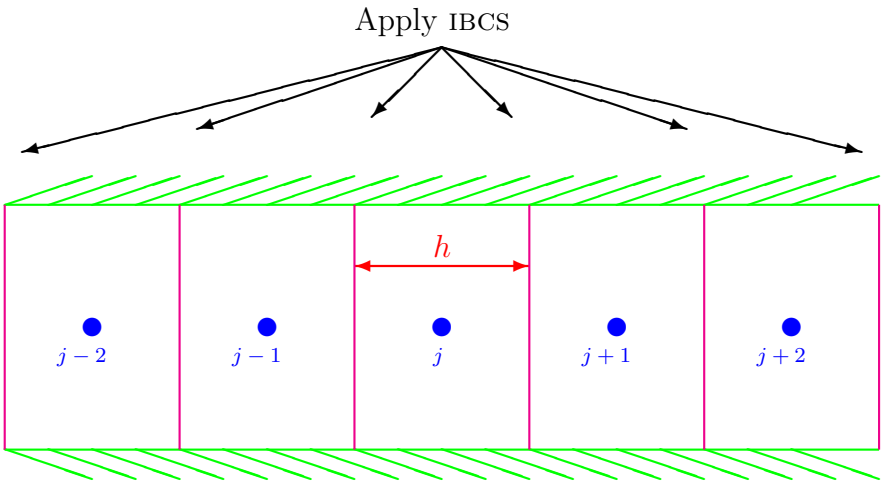

Figure 5.2: The discretisation of the $2D$ channel into rectangular elements. The jth element is centred upon the grid point x_j.

5.2.1 Use a $2D$ version of the non-local IBCs

We place grid points, $x_j = jh$ and $y_j = 0$, at the centre of these elements. Other shaped elements are also possible, but we only consider rectangular elements herein. We then apply the following internal boundary conditions (IBCS) to each of the elements

$$c_j(x_{j+1}, y, t) - c_j(x_j, y, t) = \gamma \left[c_{j+1}(x_{j+1}, y, t) - c_j(x_{j+1}, y, t) \right] , \quad (5.7)$$

$$c_j(x_j, y, t) - c_j(x_{j-1}, y, t) = \gamma \left[c_j(x_{j-1}, y, t) - c_{j-1}(x_{j-1}, y, t) \right] , \quad (5.8)$$

except for the elements immediately adjacent to the physical extreme upstream and downstream boundaries at the inlet and the outlet as discussed in §5.4. In $1D$ these non-local IBCs ensure consistency [46] and here are straightforwardly extended to $2D$ by requiring the $1D$ IBCs at each position y across the channel. In Chapters 3 and 4 we saw superior performance of

the non-local IBCs (2.7–2.8) over the local IBCs (2.4–2.5) for the $1D$ Kuramoto–Sivashinsky equation (2.1). As a result, here we only consider non-local IBCs (5.7–5.8).

Important features of the internal boundary conditions are that when evaluated at $\gamma = 0$ the elements are effectively isolated from each other and thus providing the basis for the application of centre manifold theory whereas, when evaluated at $\gamma = 1$ the continuity in the concentration field between elements is effectively restored and the resulting discretisation models the original advection-diffusion dynamics throughout the channel. This is similar the $1D$ application of the non-local IBCs discussed in 2.1.2.

The parameter γ is an inter-element coupling parameter. It controls the flow of information between adjacent elements: if only γ terms are retained in the asymptotic expansions then each element is coupled with the adjacent element on the left and right; if γ^2 terms are retained then each element is coupled with the nearest two elements on the left and right; and so on.

5.3 Centre manifold theory provides the justification

Centre manifold theory provides sound theoretical support for the discretisation. We develop the application of the theory from that introduced in [54] for the one dimensional Burgers' equation and extended to two dimensions in [36].

The approach is based upon a linear picture of the dynamics. We begin by the mathematical trick of formally adjoining the dynamically trivial

equations

$$\frac{\partial \gamma}{\partial t} = \frac{\partial \mathcal{P}}{\partial t} = 0 \tag{5.9}$$

to the advection-diffusion equation (5.1), side boundary condition (5.5) and the internal boundary condition (5.7–5.8). The introduction of (5.9) allows us to treat all terms multiplied by γ or $\mathcal{P}$ as "nonlinear" perturbations. With the isolating boundaries, (5.7–5.8) with $\gamma = 0$, around each element the "linear" dynamics, namely the diffusion equation

$$\frac{\partial c}{\partial t} = \boldsymbol{\nabla} \cdot \Big((1 - y^2) \boldsymbol{\nabla} c \Big) \quad \text{such that} \quad c(x_{j\pm1}, y, t) = c(x_j, y, t), \tag{5.10}$$

as $\mathcal{P} = 0$, result in the concentration of contaminant in each element evolving exponentially quickly to a constant value in each element. This is a set of fixed points in the extended state space $(c(x, y), \gamma, \mathcal{P})$. We then use series expansions in the nonlinear parameters γ and $\mathcal{P}$ to perturb this fixed point to account for coupling between the elements (non-zero γ) and downstream advection (non-zero $\mathcal{P}$). By theory [5, p281], since (5.10) has m zero eigenvalues and (5.9) has two, there exists an $m + 2$ dimensional centre manifold.

The centre manifold is parametrized by $\gamma, \mathcal{P}$ and a measure of c in each element—we choose the grid value

$$c_j = c(x_j, 0, t)\,. \tag{5.11}$$

This centre manifold $\mathcal{M}$ and the evolution thereon is

$$c(x, y, t) = v(x, y; \mathbf{c}, \gamma, \mathcal{P}) \quad \text{such that} \quad \dot{c_j} = g_j(\mathbf{c}, \gamma, \mathcal{P})\,, \tag{5.12}$$

where $\mathbf{c}$ denotes the vector of m grid values c_j. The evolution equation (5.12), evaluated at $\gamma = 1$, gives a discrete model for the advection-diffusion in the channel.

Using dynamical systems theory to develop such finite difference approximations provides sound theoretical support for the method. As well as existence, centre manifold theory assures:

- the relevance of the $m+2$ dimensional dynamics, through exponentially quick decay to $\mathcal{M}$ [5], as an accurate and stable model of the original advection-diffusion dynamics at finite grid size h;
- and that we may approximate the shape of the centre manifold and the evolution thereon by approximately solving the associated PDE (5.13) obtained by substituting (5.12) into (5.1), [5].

While centre manifold theory guarantees useful properties in the neighbourhood of the fixed points in $(c(x,y),\gamma,\mathcal{P})$ space, we must evaluate the model (5.12) at $\gamma = 1$. However, the good properties that have been observed in applications of this technique [46, 54, 53, 34, 36] such as consistency, increased accuracy and stability for certain regions of the nonlinear parameters, together with the extensive numerical experiments of Chapters 3 and 4 for the Kuramoto–Sivashinsky (2.1), is evidence that $\gamma = 1$ is within the useful neighbourhood of the origin. Further, in this application the Taylor model (5.2) for the shear dispersion appears in our numerical model.

5.4 Shear dispersion appears with a low order approximation

To develop the centre manifold model for the contaminant dispersion in a channel we substitute (5.12) into the advection-diffusion equation (5.1) and

solve the following resultant PDE

$$\frac{\partial c}{\partial t} = \sum_j \frac{\partial v}{\partial c_j} g_j = \boldsymbol{\nabla} \cdot \Big((1-y^2) \boldsymbol{\nabla} v \Big) - \mathcal{P} \frac{3}{2} (1-y^2) \frac{\partial v}{\partial x} \,, \tag{5.13}$$

together with IBCs (5.7–5.8), the side channel condition (5.5) and the amplitude equation (5.11). We use computer algebra to handle the algebraic details of constructing the manifold and evolution on the manifold. The basic algorithm introduced by Roberts in [52, 54] iterates to drive the residuals of the governing equation (5.1), the side channel condition (5.5) and the boundary conditions (5.7–5.8) to zero. In each iteration, we solve a problem of the form

$$\boldsymbol{\nabla} \cdot \Big((1-y^2) \boldsymbol{\nabla} v' \Big) = g' + \text{residual} \tag{5.14}$$

for updates g' and v' to the subgrid scale structure of the concentration. Generally these subgrid problems have to be solved numerically, but for this particular choice $\kappa(y)$ and $u(y)$ these are all done algebraically.

The REDUCE program for the construction of the holistic model is listed in §A.2.2. The method of undetermined coefficients is used to solve for the subgrid field and its evolution. The program iterates until the residuals constructed in lines 76–81 are zero to the desired order of accuracy. The nested loop of lines 92–123 construct the subgrid field and its evolution for the inlet and outlet boundary conditions detailed in §5.5.

5.4.1 The $\mathcal{O}\left(\gamma^3, \mathcal{P}^3\right)$ holistic model

Executing the computer algebra to construct a discretisation and retaining up to quadratic terms in the coupling γ and the Peclet number $\mathcal{P}$, the holistic

model for the shear dispersion in a channel is

$$\begin{aligned}\frac{\partial c_j}{\partial t} &= \frac{2}{3}h^{-2}\left(\gamma\delta^2-\frac{\gamma^2}{12}\delta^4\right)c_j+(\gamma-\gamma^2)\frac{\mathcal{P}^2}{8}\delta^2c_j+\gamma^2\frac{\mathcal{P}^2}{30}h^{-2}\delta^2c_j\\ &\quad-\mathcal{P}h^{-1}\left(\gamma\mu\delta-\frac{\gamma^2}{6}\mu\delta^3\right)c_j-\gamma^2\frac{2\mathcal{P}}{45}h^{-3}\mu\delta^3c_j\\ &\quad+\gamma^2\left(\frac{2}{135}+\frac{\mathcal{P}^2h^2}{72}-\frac{\mathcal{P}^2h^4}{20}\right)h^{-4}\delta^4c_j+\mathcal{O}\left(\mathcal{P}^3,\gamma^3\right)\,. \qquad (5.15)\end{aligned}$$

This model is written in terms of centred difference and mean operators, $\delta c_j = c_{j+1/2}-c_{j-1/2}$ and $\mu c_j = \left(c_{j+1/2}+c_{j-1/2}\right)/2$ respectively.

To discuss the discretisation relevant to the original PDE we evaluate the numerical model at $\gamma = 1$. Observe in (5.15) that

- the first term on the right-hand side is an $\mathcal{O}\left(h^4\right)$ estimate of the mean longitudinal molecular diffusion

$$\bar{\kappa}\frac{\partial^2 c}{\partial x^2}\,; \qquad (5.16)$$

- the second term, if truncated to errors $\mathcal{O}\left(\gamma^2\right)$, would stabilise the discretisation for large advection velocities $\mathcal{P}^2$, but here disappears when truncated to errors $\mathcal{O}\left(\gamma^3\right)$;

- *the third term gives the shear dispersion term*

$$D\frac{\partial^2 c}{\partial x^2} \quad \text{for} \quad D=\frac{\mathcal{P}^2}{30}\,, \qquad (5.17)$$

  as appears in the generalised Taylor model (5.6);

- whereas the fourth term (the first on the second line above) is an $\mathcal{O}\left(h^4\right)$ estimate of the longitudinal advection at the mean velocity $\mathcal{P}$;

- the fifth term is the first contribution to the skewness of solutions as seen in the corresponding term in (5.6);

- and lastly the sixth term contributes to the kurtosis.

The equivalent PDE for the $\mathcal{O}(\gamma^3, \mathcal{P}^3)$ holistic model (5.15) with $\gamma = 1$ is

$$\frac{\partial c}{\partial t} = -\mathcal{P}\frac{\partial c}{\partial x} + \left(\frac{2}{3} + \frac{\mathcal{P}^2}{30}\right)\frac{\partial^2 c}{\partial x^2} - \frac{2\mathcal{P}}{45}\frac{\partial^3 c}{\partial x^3} + \frac{2}{135}\frac{\partial^4 c}{\partial x^4} + \mathcal{O}(h^2). \tag{5.18}$$

The first two terms from this equivalent PDE are precisely the first two terms in the generalised Taylor model (5.6). The higher order terms are also components of the higher order generalised Taylor model; presumably higher order terms in the inter-element coupling parameter γ will complete the higher order terms. But see that the vitally important shear dispersion term appears as a $\gamma^2\mathcal{P}^2$ term.

In the interesting regime of large Peclet number,

$$\frac{\partial c_j}{\partial t} \approx \cdots + \left(\frac{\mathcal{P}^2 h^2}{72} - \frac{\mathcal{P}^2 h^4}{20}\right) h^{-4}\delta^4 c_j\,, \tag{5.19}$$

this last term is stabilising only when the grid spacing h is not too small: $h^2 \geq 5/18$. As is usual in coarse descriptions of shear dispersion [66, 40, e.g.] we cannot model structures which are too small in the longitudinal direction. Even though the equivalent PDE (5.18) is not stable for any h, interestingly the holistic model is stable for finite h.

5.4.2 View the subgrid field

We visualize the subgrid field for specific values of c_j. This does not represent an actual solution for the $2D$ channel rather an example of the advection diffusion dynamics and the element interaction. Figure 5.3 shows an example of the field c in the channel with $c_0 = 1$, $c_{j\pm1} = 0.5$ and all other grid values set to 0 and $\mathcal{P} = 2$ and $h = 1$. The subgrid field models the downstream

advection into neighbouring elements and cross-stream diffusion. The non-constant subgrid fields in each element reinforces the concept that the subgrid field is comprised of actual solutions of the governing advection-diffusion dynamics and the element interaction through the IBCs (5.7–5.8).

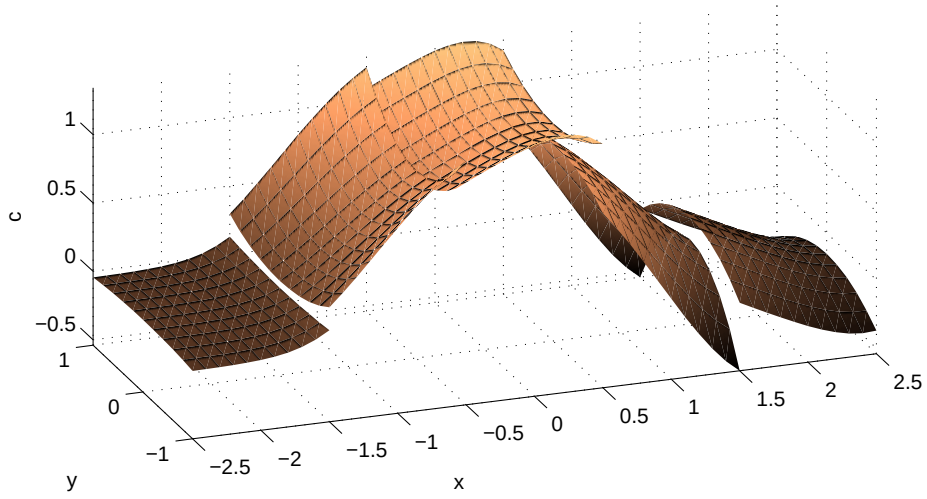

Figure 5.3: Plot of the two-dimensional subgrid field $c(x, y)$ for the $\mathcal{O}(\gamma^3, \mathcal{P}^3)$ holistic model, in the jth element when $c_{j\pm1} = 0.5, c_j = 1$ and all other grid values set to 0 and $\mathcal{P} = 2$ and $h = 1$.

5.5 Inlet and Outlet boundary conditions are easily incorporated

A great advantage of using this holistic technique to discretisation is that inlet and outlet boundary conditions are appropriately and easily incorporated into the analysis. We introduce a Dirichlet inlet boundary condition of

prescribed concentration and the Neumann zero diffusive flux outlet boundary condition as shown in Figure 5.4. Here we construct discretisations to be used for the elements near the inlet and outlet.

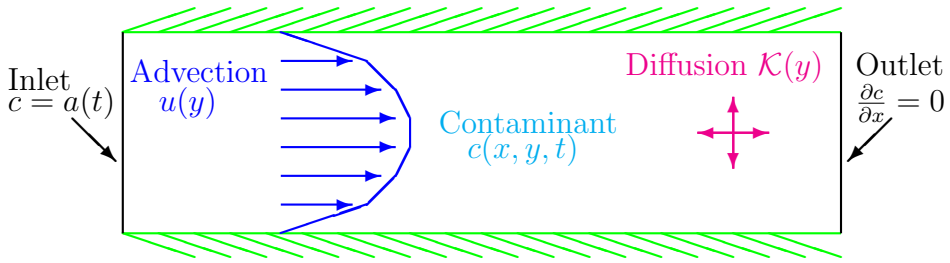

Figure 5.4: The fixed upstream boundary condition and the zero diffusive flux downstream boundary condition

We follow a similar treatment of the physical boundaries as introduced in [53]. We apply the Dirichlet inlet boundary condition at a grid point, say

$$c(x_0, y, t) = a(t)\,. \tag{5.20}$$

This may be viewed as making the first element a little longer as seen in Figure 5.5. We apply the Neumann outlet boundary condition at the right hand edge of the right most element, say

$$\frac{\partial c}{\partial x} = 0 \quad \text{at} \quad x = x_m + h/2\,, \tag{5.21}$$

as shown in Figure 5.5. Here we restrict attention to inlet and outlet conditions which are constant across the channel as the analysis can be done algebraically; more general inlet conditions will need numerical solutions for the subgrid problem.

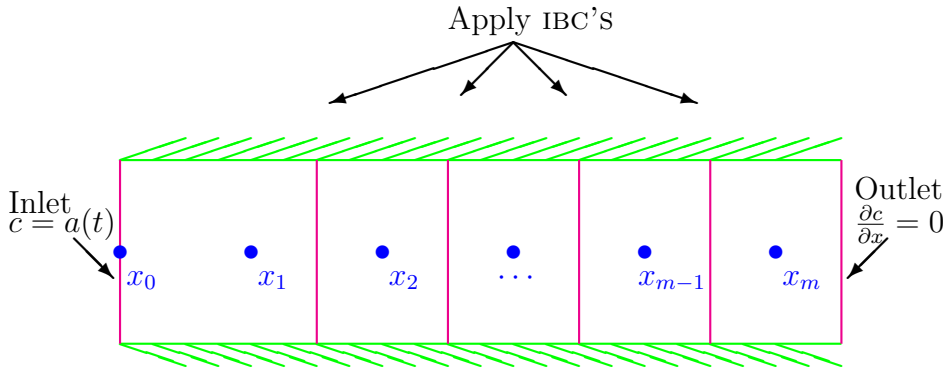

Figure 5.5: The physical boundary conditions are applied to the left hand side of the first element and the right hand side of the last element

To apply centre manifold theory, rewrite (5.20) in the form analogous to the IBC (5.7)

$$c_1(x_0, y, t) - c_1(x_1, y, t) = \gamma(c_1(x_0, y, t) - a(t)) \quad \text{at} \quad x = x_0\,. \tag{5.22}$$

The outlet boundary condition (5.21) is used as is. The arguments of §3 still apply to ensure theoretical support for the numerical model. The construction of the discretisation then proceeds as before but with special treatment of elements near the inlet or outlet.

5.5.1 The holistic models near the boundaries

After constructing the holistic model with $\mathcal{O}(\gamma^3, \mathcal{P}^3)$ errors and setting the coupling parameter $\gamma = 1$, we find the discretisations to be used near the inlet are

$$\begin{aligned}\frac{\partial c_1}{\partial t} &= \frac{1}{18h^2}(-c_3 + 16c_2 - 29c_1 + 14a) + \frac{\mathcal{P}}{12h}(c_3 - 8c_2 + 7a) \\ &\quad + \frac{1}{135h^4}(2c_3 - 8c_2 + 10c_1 - 4a) + \frac{\mathcal{P}}{45h^3}(-c_3 + 2c_2 - a)\end{aligned}$$

$$
\begin{aligned}
&+ \frac{\mathcal{P}^2}{80}\left(-4c_3 + 16c_2 - 25c_1 + 13a\right) \\
&+ \frac{\mathcal{P}^2}{360h^2}\left(5c_3 - 8c_2 + 7c_1 - 4a\right) + \mathcal{O}(\mathcal{P}^3, \dot{a})\,, \qquad (5.23)
\end{aligned}
$$

$$
\begin{aligned}
\frac{\partial c_2}{\partial t} &= \frac{1}{18h^2}\left(-c_4 + 16c_3 - 30c_2 + 16c_1 - a\right) + \frac{\mathcal{P}}{12h}\left(c_4 - 8c_3 + 8c_1 - a\right) \\
&+ \frac{1}{135h^4}\left(2c_4 - 8c_3 + 12c_2 - 8c_1 + 2a\right) \\
&+ \frac{\mathcal{P}}{45h^3}\left(-c_4 + 2c_3 - 2c_1 + a\right) \\
&+ \frac{\mathcal{P}^2}{20}\left(-c_4 + 4c_3 - 6c_2 + 4c_1 - a\right) \\
&+ \frac{\mathcal{P}^2}{360h^2}\left(5c_4 - 8c_3 + 6c_2 - 8c_1 + 5a\right) + \mathcal{O}(\mathcal{P}^3, \dot{a})\,. \qquad (5.24)
\end{aligned}
$$

Note that the time derivative of Dirichlet boundary condition $\dot{a}$ appears in these evolution equations. However, for the $\mathcal{O}\left(\mathcal{P}^3, \dot{a}\right)$ holistic model the $\dot{a}$ terms are neglected.

After constructing the holistic model with $\mathcal{O}(\gamma^3, \mathcal{P}^3)$ errors and setting the coupling parameter $\gamma = 1$, we find the discretisations to be used near the outlet are

$$
\begin{aligned}
\frac{\partial c_{m-1}}{\partial t} &= \frac{1}{18h^2}\left(15c_m - 30c_{m-1} + 16c_{m-2} - c_{m-3}\right) \\
&+ \frac{\mathcal{P}}{288h}\left(-167c_m - c_{m-1} + 192c_{m-2} - 24c_{m-3}\right) \\
&+ \frac{1}{135h^4}\left(-6c_m + 12c_{m-1} - 8c_{m-2} + 2c_{m-3}\right) \\
&+ \frac{\mathcal{P}}{1080h^3}\left(23c_m + c_{m-1} - 48c_{m-2} + 24c_{m-3}\right) \\
&+ \frac{\mathcal{P}^2}{23040}\left(3401c_m - 6857c_{m-1} + 4608c_{m-2} - 1152c_{m-3}\right) \\
&+ \frac{\mathcal{P}^2}{17280h^2}\left(-133c_m + 277c_{m-1} - 384c_{m-2} + 240c_{m-3}\right) \\
&+ \mathcal{O}(\mathcal{P}^3)\,, \qquad (5.25)
\end{aligned}
$$

$$
\frac{\partial c_m}{\partial t} = \frac{1}{18h^2}\left(-14c_m + 15c_{m-1} - c_{m-2}\right)
$$

$$
\begin{aligned}
&+\frac{\mathcal{P}}{1440h}\left(-937c_m+1073c_{m-1}-136c_{m-2}\right)\\
&+\frac{1}{135h^4}\left(4c_m-6c_{m-1}+2c_{m-2}\right)\\
&+\frac{\mathcal{P}}{1080h^3}\left(27c_m-52c_{m-1}+25c_{m-2}\right)\\
&+\frac{\mathcal{P}^2}{2560}\left(-431c_m+580c_{m-1}-149c_{m-2}\right)\\
&+\frac{\mathcal{P}^2}{17280h^2}\left(208c_m-461c_{m-1}+253c_{m-2}\right)+\mathcal{O}(\mathcal{P}^3)\,. \quad (5.26)
\end{aligned}
$$

5.6 Summary

Holistic discretisation provides a direct link between the two-dimensional advection-diffusion dynamics (5.1) and the one-dimensional numerical holistic model (5.15). In this application the $1D$ numerical model (5.15) was derived from the original $2D$ equations without first deriving a $1D$ continuum model such as the Taylor model. In §5.4 we found the shear dispersion term appeared in the $\mathcal{O}\left(\gamma^3,\mathcal{P}^3\right)$ holistic model (5.15).

The holistic technique naturally incorporates physical inlet and outlet boundary conditions. In §5.5 we saw how constant Dirichlet (5.20) and Neumann (5.21) boundary conditions across the channel at the inlet and outlet are incorporated in the holistic model and listed the $\mathcal{O}\left(\gamma^3,\mathcal{P}^3\right)$ holistic model for the evolution of grid values near the physical inlet (5.23–5.24) and outlet (5.25–5.26).

For more general inlet and outlet boundary conditions the subgrid field cannot be constructed analytically using the method of undetermined coefficients. The subgrid field and its evolution are found by numerical solution of (5.13) and either the IBCs (5.7–5.8) or the appropriate physical boundary conditions. Numerical construction of the subgrid field is detailed for

two-dimensional reaction-diffusion equations in §8.5.1 and has not yet been applied for $2D$ shear dispersion in a channel. This is left for further research.

Chapter 6

The Ginzburg–Landau equation is an example of a reaction-diffusion model

Contents

The original application by Roberts [54] of the holistic approach to discretising Burgers' equation was not specific to the nonlinear term uu_x. It applies readily to any second order diffusive PDE. We now consider a further application of the holistic approach to discretising another well known second order PDE, namely the real-valued Ginzburg–Landau equation with real coefficients

$$\frac{\partial u}{\partial t} = \frac{\partial^2 u}{\partial x^2} + \alpha \left(u - u^3 \right) . \tag{6.1}$$

This form is also referred to as the Allan–Cahn equation [18].

This equation models coarsening phenomena of the dynamics of interfaces [42, 18, 10]. It also is a representative of the class of reaction-diffusion equations. Here we also limit our investigation to real valued solutions of (6.1) and refer to this as the RGL equation. In this form the dynamics of the RGL are not as rich as for the Kuramoto–Sivashinsky equation (2.1).

My original intention of this chapter was to start by investigating the RGL equation as a preliminary study before exploring the complex Ginzburg–Landau equation (CGL), which exhibits more complex behaviour [8, 43, 31, 21]. The CGL is an amplitude equation and is a more widely applicable model equation for pattern formation. However, I have not yet extended the holistic approach to discretising the CGL so it does not form part of the scope of this dissertation. It is still valuable to examine the application of the holistic approach to discretising the RGL as a further second order example distinct from Burgers' equation. The RGL also has a bifurcation diagram which provides a useful reference for Chapter 8 for the numerical construction of a subgrid field and its evolution. The RGL is also explored in

Chapter 7 as an example of holistic discretisation in two spatial dimensions. For holistic discretisation in two or more spatial dimensions, the numerical construction of the subgrid field is required, as described in §8.5 for the $2D$ RGL.

Here we begin in §6.1.1 by discussing how the application of the holistic approach to discretising the RGL follows the application of Roberts [54] to Burgers' equation. In §6.2 we step through the iteration scheme to construct the simple example of the $\mathcal{O}(\gamma^2, \alpha^2)$ holistic model of the RGL. This serves as a reference for the numerical construction of the subgrid field detailed in §8.1.1.

We investigate the performance of the holistic models of the RGL on coarse grids and compare to the accurate solution and explicit centered difference approximations. We compare bifurcation diagrams for the RGL system (6.1) for $0 \leq \alpha \leq 20$ on a coarse grid of 8 elements on $[0, \pi]$. We restrict exploration to solutions that are both 2π periodic and odd: thus

$$u(x,t) = u(x+2\pi,t) \quad \text{and} \quad u(x,t) = -u(2\pi - x, t)\,. \tag{6.2}$$

In this way the comparison is similar to that done for the Kuramoto–Sivashinsky equation (2.1) in Chapter 3. The investigation here is briefer since the RGL is not as rich in its dynamics as the Kuramoto–Sivashinsky equation. We do not find the same excellent performance of the holistic models as was found for the Kuramoto–Sivashinsky equation. In fact, the $\mathcal{O}(\gamma^2, \alpha^2)$ holistic model does not perform as well as a second order explicit centered difference approximation. However, we do find improved performance of the holistic models as higher order models in γ are compared.

6.1 The Ginzburg–Landau equation with real coefficients

We begin by investigating the application of the holistic approach to discretising the one dimensional real-valued Ginzburg–Landau equation with real coefficients (RGL) (6.1). We discuss how the application of Roberts [54] for constructing holistic models of Burgers' equation (1.1) provides the theoretical support, based on centre manifold theory [4, 5] for this application to the RGL.

6.1.1 The application is similar to Burgers' equation

The linear dynamics of (6.1) are identical to the linear dynamics of Burgers' equation (1.1), namely the diffusion equation

$$\frac{\partial u}{\partial t} = \frac{\partial^2 u}{\partial x^2}\,. \tag{6.3}$$

The holistic approach is based upon the linear dynamics of the PDE and since the linear problem is the same for both Burgers' equation and the RGL, the arguments of Roberts [54] for Burgers' equation apply to deriving holistic models of the 1D RGL.

We divide the domain $[0,\pi]$ into m elements and use artificial internal boundary conditions (IBCs) which allow the application of centre manifold theory. Here we choose regular elements of width h. We place grid points $x_j = jh$, at the midpoint of each element as shown in Figure 6.1.

Following the analysis of Roberts [46], we express the field for the jth element by $u = v_j(x,t)$ and use the non-local IBCs

$$v_j(x_{j+1},t) - v_j(x_j,t) \;=\; \gamma\left(v_{j+1}(x_{j+1},t) - v_j(x_j,t)\right)\,, \tag{6.4}$$

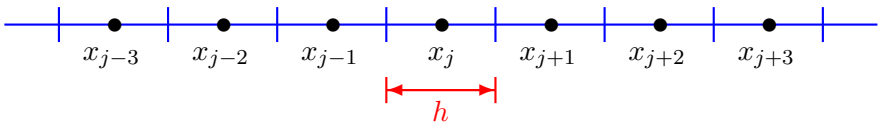

Figure 6.1: An example of the $1D$ grid with regular elements of width h. The jth element is centred about the grid point x_j.

$$v_j(x_j,t) - v_j(x_{j-1},t) \quad = \quad \gamma\left(v_j(x_j,t) - v_{j-1}(x_{j-1},t)\right) . \tag{6.5}$$

Note that field $v_j(x,t)$ must extend past the element boundaries to at least $x_{j\pm1}$ as shown in Figure 6.2, to allow the application of these IBCs. Again the parameter γ is the coupling parameter, controlling the flow between elements of information on the subgrid scale field and dynamics.

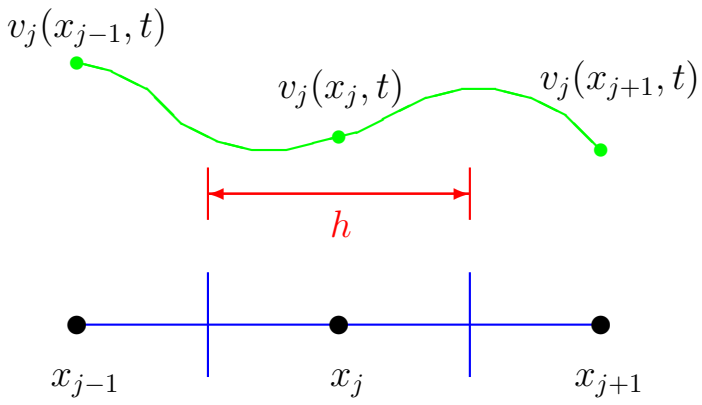

Figure 6.2: Example of the field $v_j(x,t)$ shown in green for the application of the holistic approach to 2nd order PDEs.

As Roberts details in [54, 46, 53] these IBCs facilitate construction of a centre manifold $\mathcal{M}$ based about the fixed point $u = \text{const}$, $\gamma = 0, \alpha = 0$. We parametrise the centre manifold by a measure of the field u in each element.

Here

$$u_j = v(x_j, t)\,, \tag{6.6}$$

parametrises the centre manifold. The centre manifold is given by

$$u(x,t) = v(x; \boldsymbol{u}, \gamma, \alpha)\,, \tag{6.7}$$

and the evolution on the centre manifold which forms the holistic model is

$$\dot{u}_j = g_j(\boldsymbol{u}, \gamma, \alpha)\,, \tag{6.8}$$

where $\boldsymbol{u}$ is the collection of u_js. As discussed in §2.2.1 we view the abstract centre manifold as the union of all states of the collection of subgrid fields $v_j(x, \boldsymbol{u}, \gamma, \alpha)$ over the physical domain.

Centre manifold theory guarantees

- the existence of an $m+2$ dimensional manifold
- the relevance of the $m+2$ dimensional dynamics, through exponentially quick decay to $\mathcal{M}$ [5], as an accurate and stable model of the original reaction–diffusion dynamics at finite grid size h;
- and that we may approximate the shape of the centre manifold and the evolution thereon by approximately solving the associated PDE (6.9) obtained by substituting (6.4–6.8) into (6.1), [5].

To construct the subgrid field and its evolution we solve the following symbolic equations:

$$\frac{\partial v_j(x,t)}{\partial t} = \sum_j \frac{\partial v_j(x,t)}{\partial u_j} g_j \quad = \quad \frac{\partial^2 v_j(x,t)}{\partial x^2} + \alpha\left(v_j(x,t) - v_j(x,t)^3\right)\,,$$

$$\begin{aligned} v_j(x_{j+1},t) - v_j(x_j,t) &= \gamma\left(v_{j+1}(x_{j+1},t) - v_j(x_j,t)\right) , \\ v_j(x_j,t) - v_j(x_{j-1},t) &= \gamma\left(v_j(x_j,t) - v_{j-1}(x_{j-1},t)\right) , \\ v_j(x_j,t) &= u_j . \end{aligned} \tag{6.9}$$

We expand the field $v_j(x;\boldsymbol{u},\gamma,\alpha)$ in power series in the inter-element coupling γ and nonlinearity α and truncate to some desired order of accuracy. These equations are solved via an iteration scheme discussed in detail in §6.2.

To make the model relevant to the PDE, it is evaluated at $\gamma = 1$ as discussed in [54] for Burgers' equation and in §2.2.2 for the Kuramoto–Sivashinsky equation.

6.2 The iteration scheme

Here we step through the iteration scheme for the simple example of the $\mathcal{O}(\gamma^2,\alpha^2)$ holistic model of the RGL (6.1). We examine the details here to appreciate the complexity of the symbolic system of equations needed to be solved to construct the holistic models. Presenting the details here for this analytical construction of a low order model also serves as a reference for the numerical construction of the subgrid field for the holistic model of the RGL examined in §8.1.1.

Within each element we solve (6.9). To simplify the algebra we introduce the scaled variable $\xi = (x - x_j)/h$: ξ ranges over $-1/2 < \xi < 1/2$ in the jth element; $\xi = 0$ is the midpoint; and $\xi = \pm 1$ are the neighbouring grid points. Then solve

$$\sum_j \frac{\partial v_j(\xi,t)}{\partial u_j} g_j = h^2 \frac{\partial^2 v_j(\xi,t)}{\partial \xi^2} + \alpha\left(v_j(\xi,t) - v_j(\xi,t)^3\right) , \tag{6.10}$$

$$v_j(1,t) - v_j(0,t) = \gamma\left(v_{j+1}(1,t) - v_j(0,t)\right) , \tag{6.11}$$

$$v_j(0,t) - v_j(-1,t) = \gamma\left(v_j(0,t) - v_{j-1}(-1,t)\right), \tag{6.12}$$

$$v_j(0,t) = u_j. \tag{6.13}$$

We employ an iteration scheme, developed by Roberts [52] to find $v_j = \widetilde{v}_j + v'_j$ and $g_j = \widetilde{g}_j + g'_j$, where $\widetilde{v}_j$, $\widetilde{g}_j$ denote the current approximation and v'_j, g'_j are desired corrections to the description of the centre manifold model.

We solve the following linear equations at each step of the iteration for the updates to the subgrid field and its corresponding evolution.

$$\begin{aligned} h^2\frac{\partial^2 v'_j}{\partial \xi^2} - g' &= \mathrm{Res}_{6.10}, \\ v_j(1,t) - v_j(0,t) &= \mathrm{Res}_{6.11}, \\ v_j(0,t) - v_j(-1,t) &= \mathrm{Res}_{6.12}, \\ v'_j(0,t) &= 0, \end{aligned} \tag{6.14}$$

where the residuals of the governing equations

$$\begin{aligned} \mathrm{Res}_{6.10} &= \sum_j \frac{\partial \widetilde{v}_j(\xi,t)}{\partial u_j}\widetilde{g}_j - h^2\frac{\partial^2 \widetilde{v}_j(\xi,t)}{\partial \xi^2} - \alpha\left(\widetilde{v}_j(\xi,t) - \widetilde{v}_j(\xi,t)^3\right), \\ \mathrm{Res}_{6.11} &= \widetilde{v}_j(1,t) - \widetilde{v}_j(0,t) - \gamma\left(\widetilde{v}_{j+1}(1,t) - \widetilde{v}_j(0,t)\right), \\ \mathrm{Res}_{6.12} &= \widetilde{v}_j(0,t) - \widetilde{v}_j(-1,t) - \gamma\left(\widetilde{v}_j(0,t) - \widetilde{v}_{j-1}(-1,t)\right). \end{aligned} \tag{6.15}$$

Iteration 1

We begin with the constant approximation within each subgrid field of

$$\widetilde{v}(\xi,t) = u_j \quad \text{and} \quad \widetilde{g}_j = 0. \tag{6.16}$$

Computing the residuals (6.15) for the initial values (6.16) gives

$$\begin{aligned} \mathrm{Res}_{6.10} &= \alpha(u_j - u_j^3), \\ \mathrm{Res}_{6.11} &= \gamma(-u_{j+1} + u_j), \\ \mathrm{Res}_{6.12} &= \gamma(-u_j + u_{j-1}). \end{aligned} \tag{6.17}$$

Solving the linear equations (6.14) with the residuals (6.17) gives

$$\begin{aligned} v'_j &= \gamma\left(\mu\delta u_j\xi + \frac{1}{2}\delta^2 u_j\xi^2\right), \\ g'_j &= \frac{\gamma}{h^2}\delta^2 u_j + \alpha\left(u_j - u_j^3\right). \end{aligned} \tag{6.18}$$

in terms of centered difference and mean operators, $\delta u_j = u_{j+1/2} - u_{j-1/2}$ and $\mu u_j = (u_{j+1/2} + u_{j-1/2})/2$, respectively. Updating the subgrid field and its evolution gives the new approximations

$$\widetilde{v}_j = u_j + \gamma\left(\mu\delta u_j\xi + \frac{1}{2}\delta^2 u_j\xi^2\right), \tag{6.19}$$

$$\widetilde{g}_j = \frac{\gamma}{h^2}\delta^2 u_j + \alpha\left(u_j - u_j^3\right). \tag{6.20}$$

With $\gamma = 1$, (6.19) is a classic quadratic interpolation and consequently (6.20) is the classic finite difference approximation.

Iteration 2

This iteration will find out about the dynamical interaction of the classic subgrid fields of (6.19). To begin the second iteration we use $\widetilde{v}_j$ from (6.19) and $\widetilde{g}_j$ from (6.20). We compute the residuals, remembering γ^2 and α^2 terms are neglected in this $\mathcal{O}(\gamma^2, \alpha^2)$ holistic model. We obtain

$$\begin{aligned} \text{Res}_{6.10} &= \alpha\gamma\left(\mu\delta u_j^3\xi + \frac{1}{2}\delta^2 u_j^3\xi^2 - 3u_j^2\mu\delta u_j\xi - \frac{3}{2}u_j^2\delta^2 u_j\xi^2\right), \\ \text{Res}_{6.11} &= 0, \\ \text{Res}_{6.12} &= 0. \end{aligned} \tag{6.21}$$

$\text{Res}_{6.10}$ provides information about subgrid scale interaction between the reaction and diffusion processes.

Solving (6.14) with the residuals (6.21) and discarding γ^2 and α^2 terms gives

$$\begin{aligned} v'_j &= \alpha\gamma h^2 \left(\frac{1}{6}\mu\delta u_j^3\xi - \frac{1}{6}\mu\delta u_j^3\xi^3 + \frac{1}{24}\delta^2 u_j^3\xi^2 - \frac{1}{24}\delta^2 u_j^3\xi^4 \right. \\ &\quad -\frac{1}{2}u_j^2\mu\delta u_j\xi + \frac{1}{2}u_j^2\mu\delta u_j\xi^3 - \frac{1}{8}u_j^2\delta^2 u_j\xi^2 \\ &\quad \left. +\frac{1}{8}u_j^2\delta^2 u_j\xi^4 \right) , \\ g'_j &= \alpha\gamma \left(\frac{1}{12}\delta^2 u_j^3 - \frac{1}{4}u_j^2\delta^2 u_j \right) . \end{aligned} \tag{6.22}$$

Updating the subgrid field and its evolution gives the new approximation

$$\begin{aligned} \widetilde{v}_j &= u_j + \gamma \left(\mu\delta u_j\xi + \frac{1}{2}\delta^2 u_j\xi^2 \right) \\ &\quad +\alpha\gamma h^2 \left(\frac{1}{6}\mu\delta u_j^3\xi - \frac{1}{6}\mu\delta u_j^3\xi^3 + \frac{1}{24}\delta^2 u_j^3\xi^2 - \frac{1}{24}\delta^2 u_j^3\xi^4 \right. \\ &\quad -\frac{1}{2}u_j^2\mu\delta u_j\xi + \frac{1}{2}u_j^2\mu\delta u_j\xi^3 - \frac{1}{8}u_j^2\delta^2 u_j\xi^2 \\ &\quad \left. +\frac{1}{8}u_j^2\delta^2 u_j\xi^4 \right) , \end{aligned} \tag{6.23}$$

$$\widetilde{g}_j = \frac{\gamma}{h^2}\delta^2 u_j + \alpha \left(u_j - u_j^3 \right) + \alpha\gamma \left(\frac{1}{12}\delta^2 u_j^3 - \frac{1}{4}u_j^2\delta^2 u_j \right) . \tag{6.24}$$

Iteration 3

To begin the third iteration we use $\widetilde{v}_j$ from (6.23) and $\widetilde{g}_j$ from (6.24). We compute the residual equations obtaining

$$\mathrm{Res}_{6.10} = \mathrm{Res}_{6.11} = \mathrm{Res}_{6.12} = 0 . \tag{6.25}$$

Since the residuals are all zero, there are no further updates to the subgrid field and its evolution for this holistic model with errors $\mathcal{O}(\gamma^2, \alpha^2)$. The subgrid field and its evolution is (6.23) and (6.24) respectively for the $\mathcal{O}(\gamma^2, \alpha^2)$ holistic model.

6.3 Computer algebra handles the details

The algebraic details of the iteration scheme become tedious for higher order models. Computer algebra [52] is used to generate the holistic models to varying orders of errors in γ and α, as outlined in [54, 46]. The same computer algebra program that constructs the holistic models for Burgers' equation is used to construct the holistic models of the RGL equation (6.1), with the small adjustment of changing the nonlinear term to $\alpha\,(u - u^3)$.

The REDUCE computer algebra program to generate holistic models of the RGL is listed in A.1.1. Note from the REDUCE code that the equations that form the subgrid field and its evolution are solved on lines 46-58 by iteration until the residuals are zero to the desired order of accuracy in parameters γ and α.

Here we list the $\mathcal{O}(\gamma^3, \alpha^2)$ and $\mathcal{O}(\gamma^3, \alpha^2)$ holistic models of the RGL which are generated by the REDUCE program A.1.1.

The $\mathcal{O}(\gamma^2, \alpha^2)$ holistic model is

$$\begin{aligned} \dot{u_j} &= \frac{\gamma}{h^2}\delta^2 u_j + \alpha\left(u_j - u_j^3\right) + \alpha\gamma\left(\frac{1}{12}\delta^2 u_j^3 - \frac{1}{4}u_j^2\delta^2 u_j\right) \\ &\quad + \mathcal{O}\left(\gamma^2, \alpha^2\right). \end{aligned} \tag{6.26}$$

The $\mathcal{O}(\gamma^3, \alpha^2)$ holistic model is

$$\begin{aligned} \dot{u_j} &= \frac{\gamma}{h^2}\delta^2 u_j + \alpha\left(u_j - u_j^3\right) + \alpha\gamma\left(\frac{1}{12}\delta^2 u_j^3 - \frac{1}{4}u_j^2\delta^2 u_j\right) \\ &\quad - \frac{1}{12}\delta^4 u_j + \alpha\gamma^2\left[-\frac{1}{60}\delta^2 u_j^3 - \frac{1}{90}\delta^4 u_j^3 - \frac{2}{15}\delta^2 u_j^2 u_j - \frac{1}{5}u_j(\mu\delta u_j)^2\right. \\ &\quad + \frac{1}{30}\mu\delta u_j \mu\delta u_j^2 + \frac{1}{60}\mu\delta^3 u_j \mu\delta u_j^2 + \frac{19}{60}u_j^2\delta u_j + \frac{1}{60}\delta^2 u_j \delta^2 u_j^2 \\ &\quad \left. + \frac{1}{20}u_j(\delta^2 u_j)^2 + \frac{1}{30}u_j^2\delta^4 u_j + \frac{1}{240}\delta^4 u_j \delta^2 u_j^2\right] \end{aligned}$$

$$+\mathcal{O}\left(\gamma^3, \alpha^2\right) . \tag{6.27}$$

The holistic models (6.26) and (6.27) are evaluated at $\gamma = 1$ before being used for the numerical experiments of the following sections.

6.4 Higher orders in coupling improve accuracy

The computer algebra mentioned above constructs higher order holistic models and here we investigate the performance of the higher order holistic models of the RGL (6.1) on coarse grids. We take a similar approach to the investigation of Chapter 3 and compare bifurcation diagrams of the holistic models to explicit centered difference approximations and to accurate solutions.

We consider periodic spatial boundary conditions across the entire physical domain. This is done to make the analysis for each element identical. Other boundary conditions are easily treated as introduced in [53] but are not considered in this dissertation. We also restrict exploration to odd solutions (6.2). This system (6.1) with (6.2) has a known bifurcation diagram.

We investigate the accuracy of the holistic models (6.26–6.27) and higher order holistic models by examining their bifurcation diagrams over the range $0 \leq \alpha \leq 20$. The bifurcation diagrams are constructed by the method described in §3.2 and again we use the bifurcation software XPPAUT [12].

6.4.1 The accurate bifurcation diagram

The accurate bifurcation diagram shown in Figure 6.3 acts as a reference to assess errors of the coarse grid approximations of the RGL (6.1). This bifurca-

tion diagram is constructed with a 6th order centred difference approximation with 48 grid points on $[0, \pi]$. This bifurcation diagram is accurate for the RGL over this range of α.

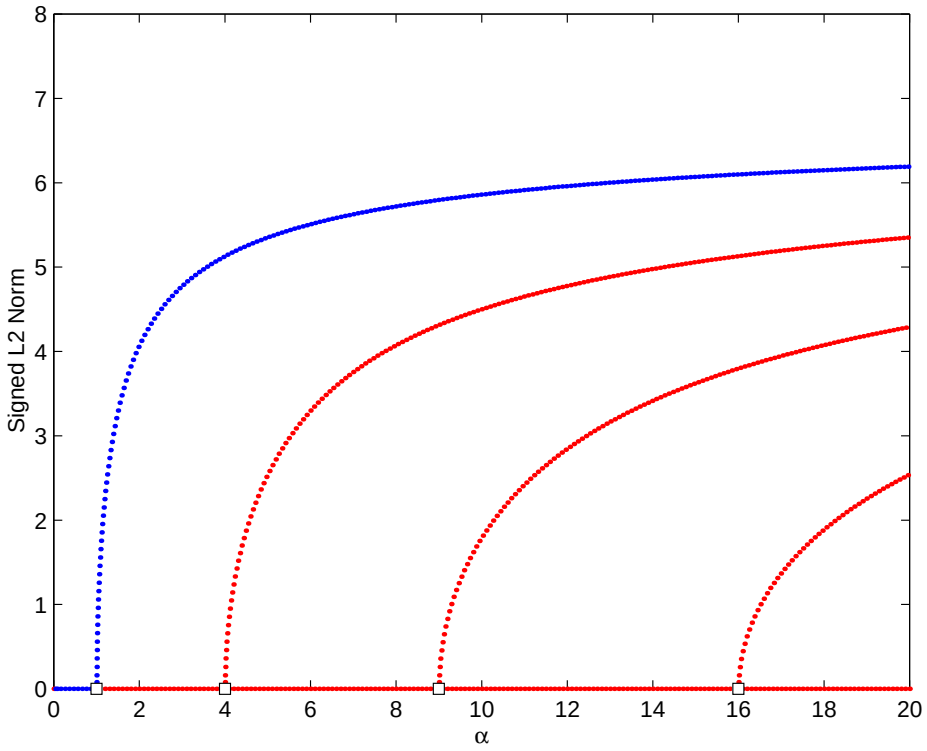

Figure 6.3: Accurate bifurcation diagram of the RGL system for $0 \leq \alpha \leq 20$. It is constructed with a 6th order centered difference approximation with 48 points on $[0, \pi]$. Blue curves indicate stable steady state solutions and red curves indicate unstable steady state solutions. The open squares indicate steady state bifurcations.

The bifurcation information is calculated using the continuation software AUTO [11] and XPPAUT [12] as outlined in §3.1 for the Kuramoto–Sivashinsky equation. Similarly to the bifurcation diagrams of Chapter 3 and 4 the blue curves indicate stable steady state solutions and red curves indicate unstable

steady state solutions. The open squares indicate steady state bifurcations.

The trivial solution undergoes steady state bifurcations at $\alpha = 1, 4, 9, 16$, leading to the unimodal, bimodal, trimodal and quadrimodal branches respectively. For $1 < \alpha < 20$, only the unimodal branch is stable and all other branches are unstable. The bifurcation diagram is much simpler than that for the Kuramoto–Sivashinsky equation.

For this form of the RGL system considered here, namely (6.1) and (6.2), the bifurcation diagram does not show dynamics as complex as for the Kuramoto–Sivashinsky equation. However, there are stable and unstable steady states and this provides a reference to compare the performance of the holistic models on coarse grids.

6.4.2 The $\mathcal{O}(\gamma^2, \alpha^2)$ holistic model underperforms

Figure 6.4 is a side by side comparison of the $\mathcal{O}(\gamma^2, \alpha^2)$ holistic model (6.26) and a 2nd order explicit centered difference approximation with 8 elements on $[0, \pi]$. The accurate bifurcation diagram is shown in grey. The $\mathcal{O}(\gamma^2, \alpha^2)$ holistic model does not perform as well as the 2nd order centered difference approximation on this coarse grid of 8 elements. Both of the approximations in Figure 6.4 are 3 point stencil approximations. The improved performance of the lowest order holistic model over the centered difference approximation of equal stencil width, observed for the Kuramoto–Sivashinsky equation in §3.3.1 is not repeated here for the RGL.

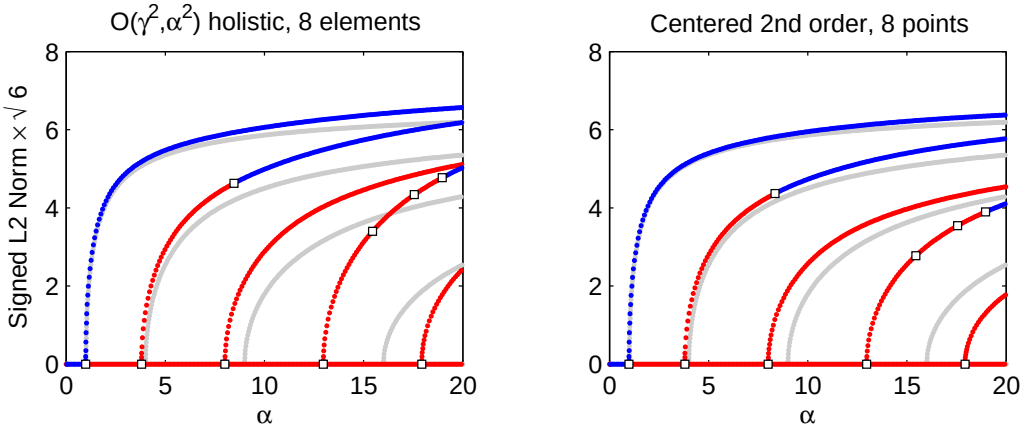

Figure 6.4: Bifurcation diagrams for the RGL with 8 elements on $[0, \pi]$ for (a) $\mathcal{O}(\gamma^2, \alpha^2)$ holistic model (b) 2nd order centered difference. Accurate bifurcation diagram is shown in grey.

6.4.3 Higher order models improve performance

Figure 6.5 is a side by side comparison of the $\mathcal{O}(\gamma^3, \alpha^2)$ holistic model (6.27) and a 4th order explicit centered difference approximation with 8 elements on $[0, \pi]$. Again the accurate bifurcation diagram is shown in grey. Both of these approximations are 5 point stencil approximations. See the improved performance for the $\mathcal{O}(\gamma^3, \alpha^2)$ holistic model (6.26) over the 4th order centered difference approximation: however, the improvement in performance is marginal. The 4th order centered difference approximation incorrectly produces a bifurcation point on the quadrimodal branch. Also, the incorrectly reproduced stable steady states on the bimodal branch occur earlier for the 4th order centered difference approximation.

Figure 6.6 is a side by side comparison of the $\mathcal{O}(\gamma^4, \alpha^2)$ holistic model and a 6th order explicit centered difference approximation with 8 elements

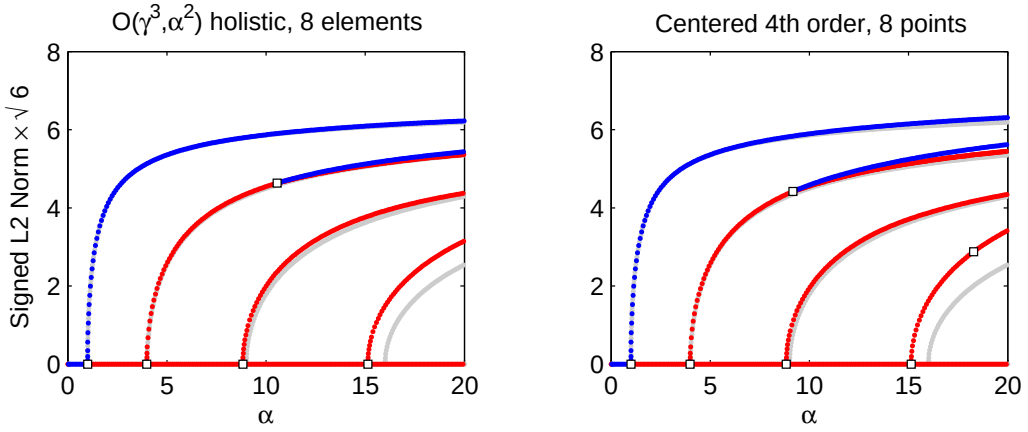

Figure 6.5: Bifurcation diagrams for the RGL with 8 elements on $[0, \pi]$ for (a) $\mathcal{O}(\gamma^3, \alpha^2)$ holistic model (b) 4th order centered difference. Accurate bifurcation diagram is shown in grey.

on $[0, \pi]$. Both of these approximations are 7 point stencil approximations. Here the $\mathcal{O}(\gamma^4, \alpha^2)$ holistic model performs better than the 6th order centered difference approximation but again the improvement is marginal. The improvement is most notable for the quadrimodal branch.

Figure 6.7 shows the holistic models of the RGL up to and including the $\mathcal{O}(\gamma^4, \alpha^3)$ model. Surveying across the columns of Figure 6.7 corresponds to increasing orders of γ or wider stencil approximations; whereas surveying down the rows corresponds to increasing order of the nonlinearity α. As observed in §3.4.2 for the Kuramoto–Sivashinsky equation, higher order holistic models in γ are more accurate but higher order models in α are not necessarily more accurate. A quick glance at Figure 6.7e,f appears to show the $\mathcal{O}(\gamma^3, \alpha^3)$ and $\mathcal{O}(\gamma^4, \alpha^3)$ holistic models more closely replicate the accurate bifurcation diagram. But close inspection reveals that they are less accurate than the $\mathcal{O}(\gamma^3, \alpha^2)$ and $\mathcal{O}(\gamma^4, \alpha^2)$ models respectively as the nonlinearity

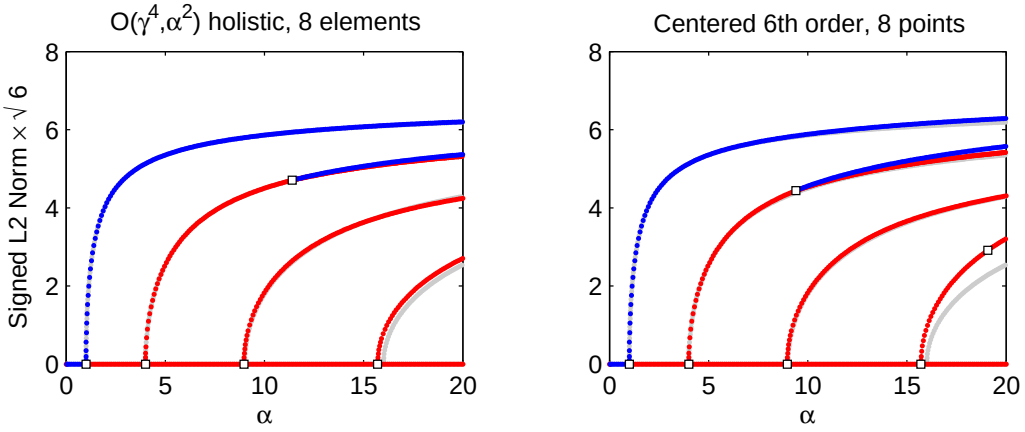

Figure 6.6: Bifurcation diagrams for the RGL with 8 elements on $[0, \pi]$ for (a) $\mathcal{O}(\gamma^4, \alpha^2)$ holistic model (b) 6th order centered difference. Accurate bifurcation diagram is shown in grey.

increases. However, the $\mathcal{O}(\gamma^3, \alpha^3)$ and $\mathcal{O}(\gamma^4, \alpha^3)$ models correctly identify the stability of the unstable bimodal branch that is incorrectly detected in the $\mathcal{O}(\gamma^3, \alpha^2)$ and $\mathcal{O}(\gamma^4, \alpha^2)$ models.

This investigation of bifurcation diagrams has shown the holistic approach to discretising the RGL system has not been as successful as for the Kuramoto–Sivashinsky equation. The reason for this is unclear. It is possible a different formulation of the IBCs could lead to better performance. Roberts and Kevrekidis [55] suggest using IBCs formulated in terms of the flux of the field u to link the microscopic subgrid scale dynamics to the macroscopic evolution of the discretised PDE. Their formulation of the IBCs and others are not investigated in this dissertation but may improve performance for discretising the RGL. However, the holistic approach has been applied to this second order PDE with the support of dynamical systems theory and the improved accuracy of the higher order holistic models in γ has again been

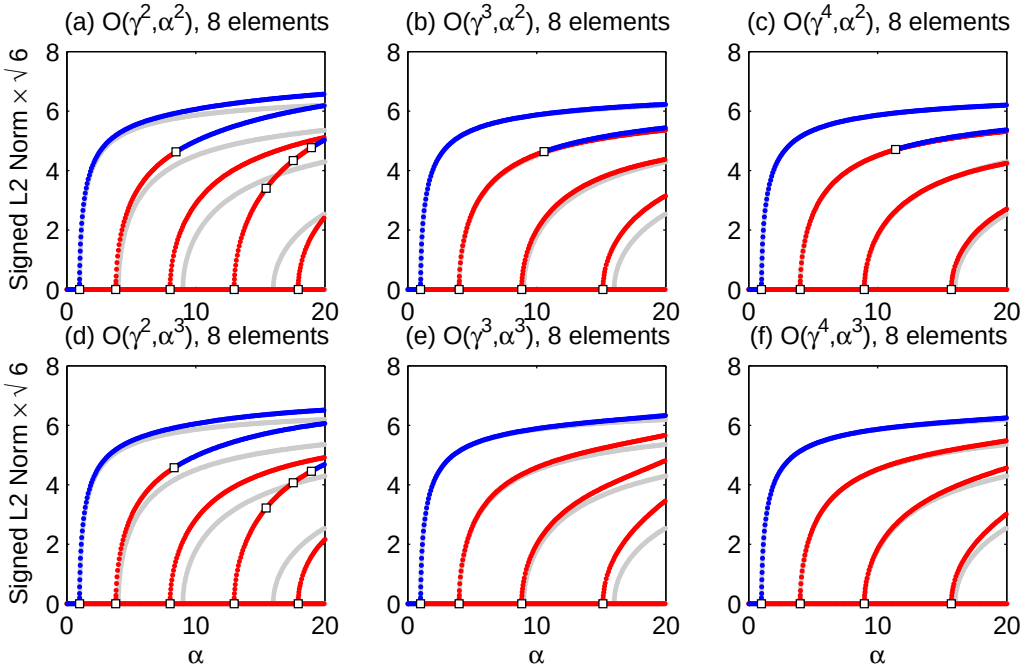

Figure 6.7: Bifurcation diagrams of increasing orders of holistic models of the RGL with 8 elements on the interval $[0, \pi]$. Accurate bifurcation diagram is shown in grey.

observed.

6.5 Summary

We explored the holistic approach to discretising the RGL (6.1) following the application of Roberts [54] for discretising Burgers' equation. The iteration scheme for the the $\mathcal{O}(\gamma^2, \alpha^2)$ holistic model was explored in detail in §6.2.

We investigated the performance of the holistic models on coarse grids and in §6.4 we did not find the same excellent performance that was found for the holistic models of the Kuramoto–Sivashinsky equation in Chapter 3.

However, we did observe improvement in performance for holistic models of higher orders in the coupling parameter γ.

The iteration scheme of §6.2 serves as a reference for the introduction of the concept of the numerical construction of the subgrid field which is the subject of Chapter 8 and the bifurcation diagrams of §6.4 will provide a reference for the performance of the numerically constructed holistic models in Chapter 8.

Chapter 7

Extension to two spatial dimensions provides challenges

Contents

Here we extend the holistic approach to a two dimensional nonlinear reaction-diffusion equation. This approach models accurately the subgrid scale processes and so we anticipate we will be able to use effectively a relatively coarse numerical grid with consequent improvements in speed and stability.

We consider in detail the real-valued two dimensional Ginzburg–Landau equation with real coefficients ($2D$ RGL), namely

$$u_t = \nabla^2 u + \alpha(u - u^3)\,. \tag{7.1}$$

This is the extension to two spatial dimensions of the $1D$ RGL (6.1) explored in Chapter 6.

We give a natural extension of the non-local IBCs (6.4–6.5) to two spatial dimensions in §7.1 and we examine how centre manifold theory is used to give theoretical support to the holistic models of PDEs of two spatial dimensions in §7.2. Earlier versions of §7.1–7.2 which detail the application of centre manifold theory to deriving the holistic models of second order PDEs but using local IBCs are published in [35].

The holistic approach to discretising PDEs has been extended to second order PDEs of two spatial dimensions in [36] for the parabolic parabolic Liouville equation [33]. In [36] a natural extension to $2D$ of the local IBCs (2.7) is used to construct holistic models of the $2D$ Liouville equation. However, in light of the superior performance of the non-local IBCs (2.7–2.8) of the holistic models of the Kuramoto–Sivashinsky equation seen in Chapters 3 and 4, the performance of the holistic models constructed with the local IBCs is not considered in this dissertation. Here we focus on the $2D$ extension

of the non-local IBCs (6.4–6.5). We also do not consider the Liouville equation here because its dynamics are relatively simple with spatially periodic boundary conditions. Instead, we explore the $2D$ RGL (7.1) which exhibits both non-trivial stable and unstable steady states, as seen in §6.4 for the $1D$ RGL.

The $\mathcal{O}(\gamma^2, \alpha^2)$ holistic model of the $2D$ RGL is listed in §7.3. We find it to be consistent with (7.1) to $\mathcal{O}(h^2)$. We find that higher order holistic models cannot be found by analytically constructing the subgrid field and its evolution. However, in Chapter 8, by numerically constructing the subgrid field and its evolution, we construct the $\mathcal{O}(\gamma^3, \alpha^2)$ holistic model.

In §7.5 we investigate the performance of the $\mathcal{O}(\gamma^2, \alpha^2)$ holistic model of the $2D$ RGL on a coarse grid by comparing bifurcation diagrams to an accurate solution. We find the $\mathcal{O}(\gamma^2, \alpha^2)$ holistic model is less accurate than an explicit 2nd order centered difference approximation on a coarse grid of 8×8 elements on $[0, \pi] \times [0, \pi]$. This result is similar to that observed for the performance of the $\mathcal{O}(\gamma^2, \alpha^2)$ holistic model of the $1D$ RGL in §6.4. Although higher order models cannot be found by constructing the subgrid field and its evolution analytically, the numerically constructed $\mathcal{O}(\gamma^3, \alpha^2)$ holistic model discussed in Chapter 8, is shown in §8.5.3 for 8×8 elements on $[0, \pi] \times [0, \pi]$ to give similar improvement to that observed in §6.4 for $\mathcal{O}(\gamma^3, \alpha^2)$ holistic model of the $1D$ RGL.

Although we do not present an exhaustive numerical study into the performance of the $2D$ holistic models we do show the holistic approach using non-local IBCs is extended to $2D$. Through the algorithm presented in Chapter 8 we show that holistic discretisation is used to construct higher order

holistic models for second order PDEs in $2D$.

7.1 Divide the domain into square elements

We place the discretisation of a two dimensional reaction-diffusion equation within the purview of centre manifold theory by dividing the domain into elements and introducing artificial isolating boundaries which are later removed. The discretisation is similar to §5.2 for shear dispersion in $2D$ channel. However, here the discretisation of elements is in both spatial dimensions, not just across the channel as for the shear dispersion application. For example, here we divide the domain into square elements as shown in Figure 7.1.

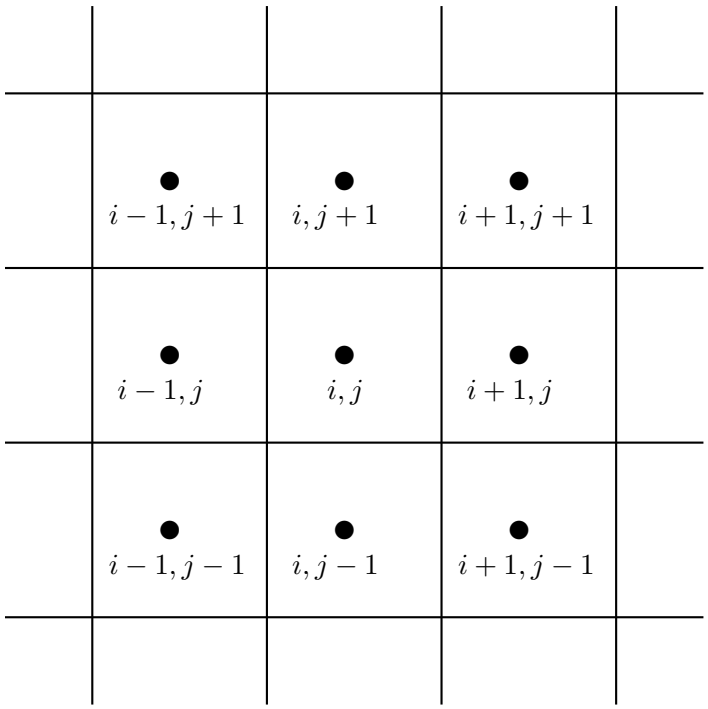

Figure 7.1: The discretisation of a $2D$ domain into square elements. The i, jth element is centred upon the grid point (x_i, y_j).

7.1.1 Extend the non-local IBCs to 2D

For the two dimensional reaction diffusion equation we use boundary conditions around each element of

$$v_{i,j}(x_{i\pm1},y,t)-v_{i,j}(x_j,y,t) = \gamma\left[v_{i\pm1,j}(x_{i\pm1},y,t)-v_{i,j}(x_i,y,t)\right], \quad (7.2)$$

$$v_{i,j}(x,y_{j\pm1},t)-v_{i,j}(x,y_{j\pm1},t) = \gamma\left[v_{i,j\pm1}(x,y_{j\pm1},t)-v_{i,j}(x,y_j,t)\right]. \quad (7.3)$$

These IBCs are a natural extension to $2D$ of IBCs (6.4–6.5) and divide the domain into a set of square elements, the i,jth element centred upon (x_i,y_j) and of width $\Delta x=\Delta y=h$. The crucial feature is: with $\gamma=0$ these elements are effectively isolated from each other, dividing the domain into independent elements; whereas with $\gamma=1$ they ensure sufficient continuity between elements to recover the physical problem as described in §6.1.1 for the $1D$ RGL (6.1) and detailed in §2.1.2 for the Kuramoto–Sivashinsky equation (2.1).

7.2 Centre manifold theory is applied

In this section we describe in detail how the IBC's (7.2–7.3) lead to the application of centre manifold theory deriving a finite difference numerical model for (7.1).

When $\gamma=0$ the right hand side of (7.2–7.3) disappears. The elements are effectively isolated from each other and so the solution is particularly simple. Exponentially quickly in time, u becomes independently constant within each element. We use this simple family of solutions as a basis for analysing the $\gamma\neq0$ case when the elements are coupled together. We are particularly interested in the approximation at $\gamma=1$ when the PDE is effectively restored

over the whole domain because (7.2–7.3) then ensure sufficient continuity between adjacent elements as described in §2.1.2 for the Kuramoto–Sivashinsky equation (2.1).

The following application of centre manifold theory is based upon a linear picture of the dynamics. Adjoin the dynamically trivial equations

$$\frac{\partial\alpha}{\partial t} = \frac{\partial\gamma}{\partial t} = 0\,, \tag{7.4}$$

and consider the dynamics in the extended state space $(u(x,y),\gamma,\epsilon)$. Within each element $\alpha=\gamma=0$, $u=$ constant forms a subspace E of fixed points. Linearized about each fixed point, that is to an error $\mathcal{O}(\alpha^2+\gamma^2)$, the PDE within each element is

$$\frac{\partial u}{\partial t} = \nabla^2 u\,,$$

together with

$$u_{i,j}(x_{i\pm1},y,t) - u_{i,j}(x_j,y,t) = 0, \tag{7.5}$$

$$u_{i,j}(x,y_{j\pm1},t) - u_{i,j}(x,y_{j\pm1},t) = 0\,, \tag{7.6}$$

namely the diffusion equation with the IBCs. There are thus the following linear eigenmodes associated with each element:

$$\alpha=\gamma=0\,,$$

$$u \propto e^{\lambda_{k,l}t}\{\cos[k\pi(x-x_{i-1/2})/h]\times\cos[l\pi(y-y_{j-1/2}/h]\}\,, \tag{7.7}$$

inside the element and zero outside the element for $k,l=0,1,\ldots$, where the decay rate of each mode is

$$\lambda_{k,l} = -\frac{(k^2+l^2)\pi^2}{h^2}\,; \tag{7.8}$$

together with the trivial modes γ = constant and $\alpha = u = 0$, and α = constant and $\gamma = u = 0$. In a domain with m elements, evidentally all eigenvalues are negative, $-\pi^2/h^2$ or less, except for $m+2$ zero eigenvalues: 1 associated with each of the m elements and 2 from the trivial (7.4). Thus, provided the nonlinear terms in (7.1) are sufficiently well behaved, the existence theorem ([5, p281] or [65, p96]) guarantees that a $m+2$ dimensional centre manifold $\mathcal{M}$ exists for (7.1–7.4). The centre manifold $\mathcal{M}$ is parametrized by γ, α and a measure of u in each element, say $u_{i,j}$: using $\boldsymbol{u}$ to denote the collection of such parameters, $\mathcal{M}$ is written as

$$u(x, y, t) = v(x, y; \boldsymbol{u}, \gamma, \alpha)\,. \tag{7.9}$$

Theory also asserts that on the centre manifold the parameters $u_{i,j}$ evolve deterministically

$$\dot{u}_{i,j} = g_{i,j}(\boldsymbol{u}, \gamma, \alpha)\,, \tag{7.10}$$

where $\dot{u}_{i,j}$ denotes $du_{i,j}/dt$, and $g_{i,j}$ is the restriction of (7.1–7.4) to $\mathcal{M}$. In this approach the parameters of the description of the centre manifold may be anything that sensibly measures the size of u in each element—we simply choose the value of u at the grid points, $u_{i,j}(t) = u(x_i, y_j, t)$. This provides the necessary amplitude conditions, namely that $u_{i,j} = v(x_i, y_j; \boldsymbol{u}, \gamma, \alpha)$. The above application of the theorem establishes that in principle we may find the dynamics (7.10) of the interaction between the elements of the discretisation.

Centre manifold theory then assures

- the existence of an $m+2$ dimensional centre manifold parametrized by the values $u_{i,j}$;

- the relevance of the $m+2$ dimensional dynamics as an accurate and stable model of the original dynamics (7.1);
- and that we may approximate the shape of the centre manifold and the evolution thereon by approximately solving the associated PDE (7.11).

7.3 The dynamics on the manifold form the discretisation

We now examine the centre manifold model for the $2D$ RGL equation (7.1). Substituting (7.9) and (7.10), the PDE we then solve to form the model is

$$u_t = \sum_{i,j} \frac{\partial v}{\partial u_{i,j}} g_{i,j} = \nabla^2 v + \alpha \left(v - v^3 \right) . \tag{7.11}$$

The algebraic details of the derivation of the centre manifold model (7.9–7.10) from (7.11) are handled by computer algebra as discussed §6.3 for the $1D$ RGL. In an algorithm introduced in [52], the program iterates to drive to zero the residuals of the governing differential equation (7.11) and its boundary conditions (7.2–7.3). Hence by the Approximation theorem we construct appropriate approximations to the centre manifold model.

The computer algebra program implemented in REDUCE to generate the holistic models is given in §A.2.1. Note from the REDUCE code that the residual of the RGL is formed on line 48 and the residuals of the IBCs on lines 50–57. The method of undetermined coefficients is then implemented through lines 59–73 to solve for updates to the subgrid field and its evolution to the desired order of accuracy in parameters γ and α.

7.3.1 The $\mathcal{O}\left(\gamma^2, \alpha^2\right)$ holistic model

The $\mathcal{O}\left(\gamma^2, \alpha^2\right)$ holistic model is given by

$$\begin{aligned} \dot{u_j} &= \frac{\gamma}{h^2}\delta^2 u_j + \alpha\left(u_j - u_j^3\right) + \alpha\gamma\left(\frac{1}{12}\delta^2 u_j^3 - \frac{1}{4}u_j^2\delta^2 u_j\right) \\ &\quad + \mathcal{O}\left(\gamma^2, \alpha^2\right), \end{aligned} \tag{7.12}$$

where in this chapter

$$\delta^2 u_{i,j} = u_{i+1,j} + u_{i-1,j} + u_{i,j+1} + u_{i,j-1} - 4u_{i,j}\,.$$

Note that this model is simply the extension of the $1D$ $\mathcal{O}\left(\gamma^2, \alpha^2\right)$ holistic model (6.26) of the RGL to two spatial dimensions.

7.3.2 The holistic model has dual justification

Here we set $\gamma = 1$ so the holistic model is relevant to (7.1). The equivalent PDE for the $\mathcal{O}\left(\gamma^2, \alpha^2\right)$ holistic model (7.12) is

$$\begin{aligned} u_t &= \nabla^2 u + \alpha(u - u^3) \\ &\quad + \left[\frac{\alpha}{2}u||\nabla u||^2 + \frac{1}{12}\nabla^4 u\right] + \mathcal{O}\left(h^4\right). \end{aligned} \tag{7.13}$$

The $\mathcal{O}\left(\gamma^2, \alpha^2\right)$ holistic model is $\mathcal{O}\left(h^2\right)$ consistent, maintaining the dual justification discussed in §2.5 in $2D$. That is, the holistic model is supported by centre manifold asymptotics in α and γ, as well as justified by its consistency in grid size h.

7.4 Illustration of the subgrid field in 2D

Here we view a plot of the subgrid fields for a coarse grid solution of the $\mathcal{O}\left(\gamma^2, \alpha^2\right)$ holistic model (7.12) of the $2D$ RGL (7.1). We restrict our attention

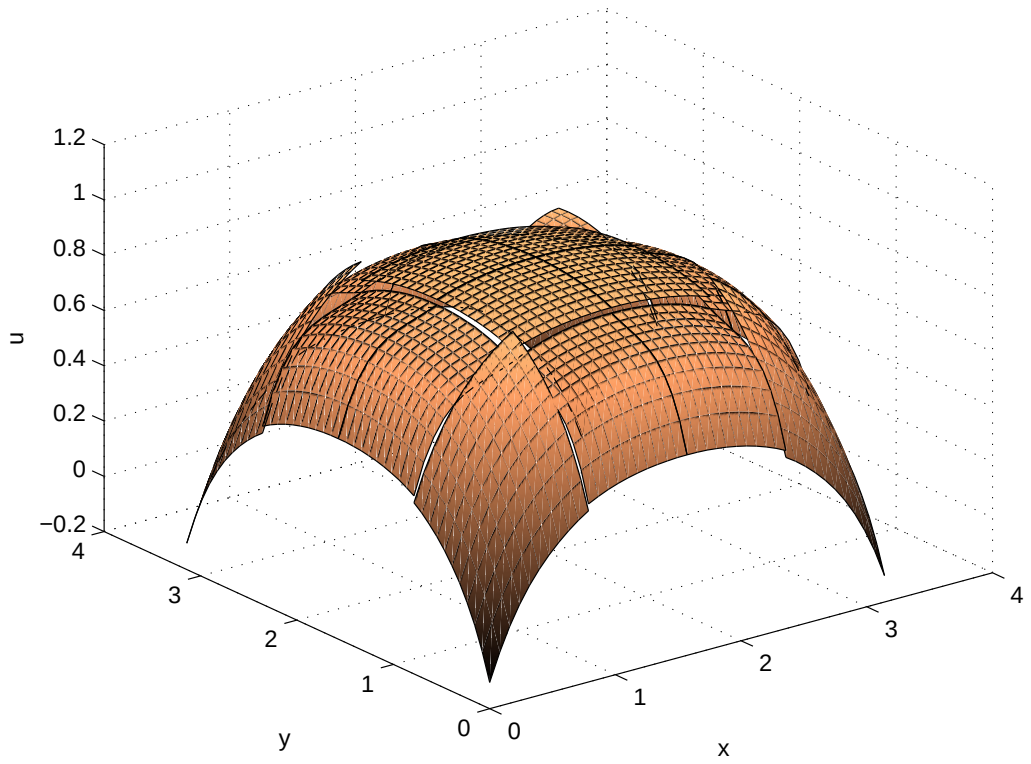

Figure 7.2: Subgrid fields for the $\mathcal{O}(\gamma^2, \alpha^2)$ holistic model with 4×4 elements on $[0, \pi] \times [0, \pi]$ at $\alpha = 6$

to a doubly odd symmetric solution that is 2π–doubly periodic. That is,

$$u(x, y, t) = u(x + 2\pi, y, t), \quad u(x, y, t) = -u(2\pi - x, y, t)$$
$$u(x, y, t) = u(x, y + 2\pi, t), \quad u(x, y, t) = -u(x, 2\pi - y, t)\,. \tag{7.14}$$

Figure 7.2 shows the subgrid fields for the $\mathcal{O}(\gamma^2, \alpha^2)$ holistic model with 4×4 elements on $[0, \pi] \times [0, \pi]$ at $\alpha = 6$. The subgrid fields exhibit the nonlinear structure of the $2D$ RGL and its interaction through the IBCs. The subgrid fields are comprised of actual solutions of the $2D$ RGL.

Note the subgrid fields have distinct jumps across the boundaries of the elements. Higher order holistic models should reduce these jumps across

the boundaries as seen for the holistic models of the Kuramoto–Sivashinsky equation (2.1) in §2.4.

7.5 The $\mathcal{O}(\gamma^2, \alpha^2)$ holistic model is poor

We investigate the performance of the $\mathcal{O}(\gamma^2, \alpha^2)$ holistic model on coarse grids by comparing its bifurcation diagram to an accurate solution. Again we restrict our attention to doubly odd symmetric solutions that are 2π–doubly periodic (7.14).

The bifurcation information is calculated using the continuation software AUTO [11] and XPPAUT [12] as outlined in §3.1 for the Kuramoto–Sivashinsky equation. Similarly to the bifurcation diagrams of earlier chapters, the blue curves indicate stable steady state solutions and red curves indicate unstable steady state solutions. The open squares indicate steady state bifurcations.

Figure 7.3 shows the accurate solution of the $2D$ RGL. It is constructed with a 4th order centered difference approximation with 24×24 points on $[0, \pi] \times [0, \pi]$. The trivial solution undergoes steady state bifurcations at $\alpha = 2, 8, 18$ leading to the unimodal, bimodal and trimodal branches respectively. For $1 < \alpha < 30$, only the unimodal branch is stable and all other branches are unstable.

Figure 7.4 shows a comparison of the $\mathcal{O}(\gamma^2, \alpha^2)$ holistic model (6.26) and a 2nd order explicit centered difference approximation with 8×8 elements on $[0, \pi] \times [0, \pi]$. The accurate bifurcation diagram is shown in grey. The $\mathcal{O}(\gamma^2, \alpha^2)$ holistic model does not perform as well as the 2nd order centered difference approximation, similarly to the performance observed in §6.4.2 for the $1D$ RGL.

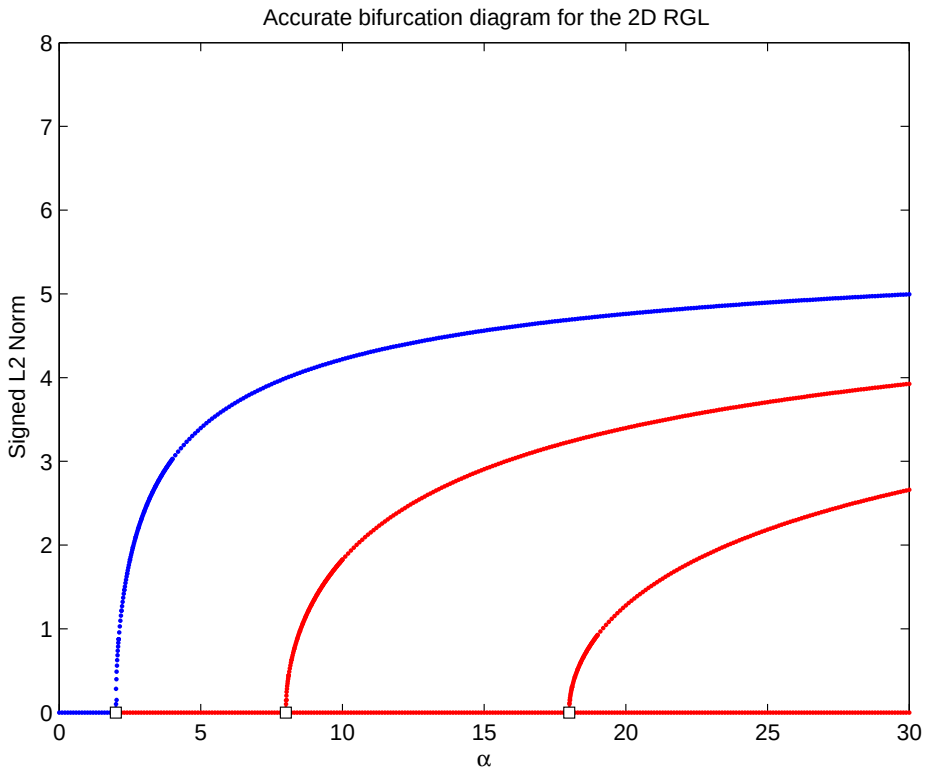

Figure 7.3: Accurate bifurcation diagram of the $2D$ RGL system for $0 \leq \alpha \leq 30$. It is constructed with a 4th order centered difference approximation with 24×24 points on $[0, \pi] \times [0, \pi]$. Blue curves indicate stable steady state solutions and red curves indicate unstable steady state solutions. The open squares indicate steady state bifurcations.

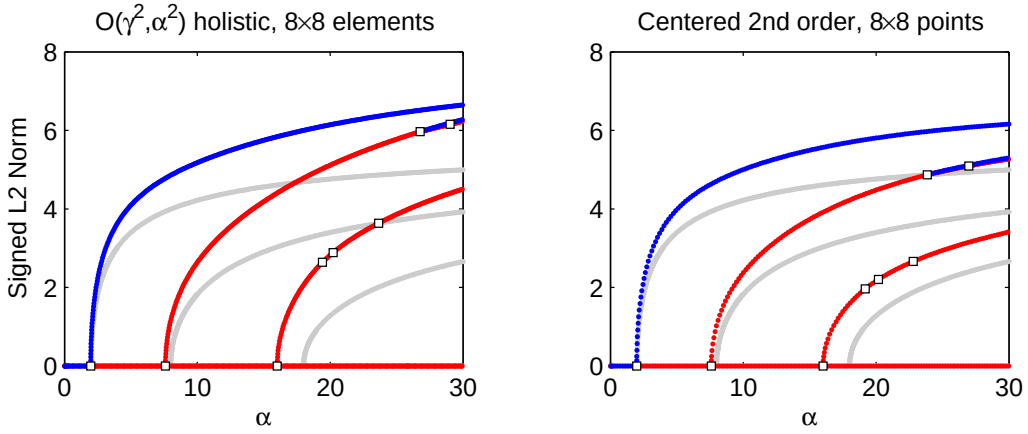

Figure 7.4: Bifurcation diagrams for the $2D$ RGL with 8×8 elements on $[0, \pi] \times [0, \pi]$ for (a) $\mathcal{O}(\gamma^2, \alpha^2)$ holistic model (b) 2nd order centered difference. Accurate bifurcation diagram is shown in grey.

7.6 Higher order models need numerical construction

In §6.4.3 we observed improved performance for the $\mathcal{O}(\gamma^3, \alpha^2)$ holistic model of the $1D$ RGL over the $\mathcal{O}(\gamma^3, \alpha^2)$ model. It is reasonable to expect similar improvement for the $\mathcal{O}(\gamma^3, \alpha^2)$ holistic model of the $2D$ RGL. However, it is not possible to analytically construct the $\mathcal{O}(\gamma^3, \alpha^2)$ holistic model in $2D$. Numerical methods must be used to solve the subgrid problem. In Chapter 8 we see how this is achieved and find that the numerically constructed $\mathcal{O}(\gamma^3, \alpha^2)$ holistic model does indeed give similar improvement in $2D$ over the $\mathcal{O}(\gamma^2, \alpha^2)$ model to that observed in §6.4.3 for the $1D$ RGL.

7.7 Summary

We have extended the application of the holistic method to discretising PDEs of second order in two spatial dimension. In particular we have used a natural extension of the non-local IBCs, namely (7.2–7.3). The $\mathcal{O}(\gamma^3, \alpha^2)$ holistic model was listed in §7.6 and found to be an extension of the $1D$ $\mathcal{O}(\gamma^2, \alpha^2)$ holistic model of the $1D$ RGL. The $\mathcal{O}(\gamma^2, \alpha^2)$ holistic model in $2D$ is also $\mathcal{O}(h^2)$ consistent showing that the dual justification property of the holistic method extends to $2D$ PDEs for this low order holistic model. No proof exists of this property for higher order holistic models and is left for further research.

The $\mathcal{O}(\gamma^2, \alpha^2)$ holistic model was found to perform poorly compared to an explicit 2nd order centered difference approximation on a coarse grid of 8×8 elements on $[0, \pi] \times [0, \pi]$. This was also observed for the $\mathcal{O}(\gamma^2, \alpha^2)$ holistic model of the $1D$ RGL in §6.4.3. Higher order holistic models can not be found analytically but the numerical methods presented in Chapter 8 show the numerically constructed $\mathcal{O}(\gamma^3, \alpha^2)$ holistic model gives similar improvement over the $\mathcal{O}(\gamma^2, \alpha^2)$ model as observed in §6.4.3 for the $1D$ RGL. Exhaustive numerical investigations of the holistic models of second order reaction-diffusion equations has been left for further research. While excellent performance of the holistic models has not been observed for the RGL in either $1D$ or $2D$ it serves as a proof of principle for applying the holistic method to PDEs of two spatial dimensions.

Chapter 8

Generally compute 2D subgrid fields numerically

Contents

The holistic discretisation of PDEs is based upon centre manifold theory [4, 5, 51, 54]. As discussed in previous chapters, to apply the holistic technique to generating discretisations of dissipative PDE's, we divide the physical domain into finite elements by introducing artificial isolating internal boundary conditions. We then construct a subgrid field in each element, parametrised by the surrounding grid values, based upon centre manifold theory and governed by the dynamics of the PDE and by coupling adjacent element, as described in §2.2, §5.2, §6.1 and §7.2. Finally, we remove the artificial internal boundary conditions to obtain a discretisation relevant to the original PDE.

This subgrid field cannot always be constructed analytically as commented in §5.6 and §7.6. The subgrid field may be constructed analytically for Burgers' equation (1.1) [54] and the Kuramoto–Sivashinsky equation (2.1) [34] in one spatial dimension. In Chapter 5 it was discussed that for non-parabolic choices of cross-channel advection velocity, the coefficient of diffusion or for non-constant boundary conditions the subgrid field must be found numerically. The shear dispersion example of Chapter 5 provides a link between the two dimensional advection-diffusion dynamics and the one dimensional holistic model. The subgrid field for PDE's of two spatial

dimensions cannot, in general, be found analytically. In Chapter 7, by requiring an analytic solution to the subgrid scale field, we are able to find only low order holistic approximations to the $2D$ real–valued Ginzburg–Landau equation (RGL) (7.1).

Here the subgrid field is constructed numerically. This introduces new complexities to constructing the holistic models. Although the spatial structure is obtained numerically, the centre manifold is also parametrised by the grid values, the coupling parameter and the nonlinear parameter. Therefore, even though the subgrid field is discretised in space, the construction of the centre manifold model involves symbolic parameters. The algorithm required to develop the holistic model must efficiently solve the corresponding mixed discrete and symbolic problem.

In this chapter we investigate numerical construction of the subgrid fields for developing holistic models of the RGL in $1D$ (6.1) and $2D$ (7.1) and the Kuramoto–Sivashinsky equation (2.1) in $1D$. *The primary focus of this chapter is on the numerical construction of the subgrid fields and not the performance of the holistic models.* Numerical construction of the subgrid field introduces errors which are separate from the orders of errors of the holistic model. It is these errors from the numerical construction of the holistic models that are of major concern in this chapter.

The numerical construction of the subgrid field and its evolution has challenging details: How should the subgrid problem be solved? What subgrid resolutions will accurately reproduce the analytical holistic models? What is an efficient implementation?

In this chapter we begin to answer these important questions. We argue

that the numerical methodology implemented to solve the subgrid problem is not an important issue. Consequently, for simplicity we use second order explicit centred difference approximations for all spatial derivatives in the subgrid problem.

We begin in §8.1 by exploring how the subgrid field is discretised in $1D$ for the numerical construction of $1D$ holistic models of the RGL (6.1). We then consider a low resolution two point subgrid resolution example of the numerical construction of the $\mathcal{O}\left(\gamma^2, \alpha^2\right)$ holistic model of the RGL to outline the method. We see that the coefficients for the numerically constructed holistic models converge to the analytical models for $O(\gamma^2, \alpha^2)$ holistic model (6.26) of the RGL (6.1) and the $O(\gamma^3, \alpha^2)$ holistic model (2.25) of the Kuramoto–Sivashinsky equation (2.1).

In §8.2 we use Richardson extrapolation [58] to estimate the coefficients of the holistic models to higher order accuracy, for the numerically constructed subgrid fields. This extrapolation procedure usefully improves the second order convergence of the numerical construction of the holistic models. This is especially useful when increased resolution of the numerically constructed subgrid is not practical to implement due to computational limitations encountered with higher spatial dimensions.

In §8.4 I present the algorithm for constructing the subgrid field, based on the iterative algorithm of Roberts [52], but adapted to numerically solve for the spatial structure of the subgrid field. The algorithm is implemented using the computer algebra system REDUCE [22]. It is also implemented using MATHEMATICA [67] but the performance of the REDUCE version is vastly superior. The algorithm implements the iteration scheme with an entirely

discrete linear operator and solves for the subgrid field and its evolution using LU factorisation [45]. The linear operator for the iteration scheme is discrete and It is decomposed only once, during the first iteration. However, the subgrid field is parametrised by neighbouring grid values, the coupling parameter and the nonlinearity and these algebraic dependencies are maintained throughout.

We investigated the performance of the holistic models of the $1D$ Kuramoto–Sivashinsky equation (2.1) and the $1D$ RGL (6.1) for modelling steady states in Chapters 3 and 6 respectively. Here we use the bifurcation diagrams of the holistic models constructed analytically to compare these constructed here numerically. This provides a comparison of the errors introduced by the discretisation of the subgrid field structure. We demonstrate in §8.3 that the numerically constructed $\mathcal{O}(\gamma^5, \alpha^2)$ holistic model generated with just a 6 interval subgrid achieves the improved performance of the powerful analytic $\mathcal{O}(\gamma^5, \alpha^2)$ holistic model (2.32) of the Kuramoto–Sivashinsky equation for $0 \leq \alpha \leq 70$ detailed in Chapters 3 and 4. We also find that the numerically constructed $\mathcal{O}(\gamma^2, \alpha^2)$ holistic model of the $1D$ RGL (6.1) reproduces the analytical holistic model (6.26), detailed in Chapter 6, with just a 4 interval subgrid for $0 \leq \alpha \leq 30$.

In §8.5.1 the algorithm extends to second order PDEs *in two spatial dimensions*. We compare the numerically constructed $\mathcal{O}(\gamma^2, \alpha^2)$ holistic model of the $2D$ RGL (7.1) to the analytical model (7.12) in §8.5.2. We find that a low resolution 4×4 interval subgrid reproduces the analytical holistic model for $0 \leq \alpha \leq 30$.

Finally in §8.5.3 we compare the bifurcation diagrams of the $\mathcal{O}(\gamma^2, \alpha^2)$

holistic model and the numerically constructed $\mathcal{O}\left(\gamma^3, \alpha^2\right)$ holistic model of the $2D$ RGL. We find similar improvement in $2D$ to that found in §6.4 for the RGL in $1D$.

The numerical construction of the subgrid field enables the construction of higher order holistic models in $2D$. The good performance of the low resolution subgrid numerical holistic models shown in §8.3 and §8.5.2 provides good support for using the numerical construction of the subgrid field to extend the application of the holistic approach to PDEs in higher spatial dimensions. However, only PDEs in one and two spatial dimensions are considered in this dissertation; three dimensional problems are left for later study.

8.1 Discretise the subgrid field structure

We begin our investigation into the numerical construction of the subgrid field structure by considering the $1D$ RGL (6.1). Because the RGL is second order it provides a simple example to explore.

Recall from Chapter 6 that to construct holistic models of the RGL we solve

$$\begin{aligned}
\frac{\partial v_j(x,t)}{\partial t} = \sum_j \frac{\partial v_j(x,t)}{\partial u_j} g_j &= \frac{\partial^2 v_j(x,t)}{\partial x^2} + \alpha\left(v_j(x,t) - v_j(x,t)^3\right) , \\
v_j(x_{j+1},t) - v_j(x_j,t) &= \gamma\left(v_{j+1}(x_{j+1},t) - v_j(x_j,t)\right) , \\
v_j(x_j,t) - v_j(x_{j-1},t) &= \gamma\left(v_j(x_j,t) - v_{j-1}(x_{j-1},t)\right) , \\
v_j(x_j,t) &= u_j , \qquad (8.1)
\end{aligned}$$

to find the subgrid field structure v_j and the evolution of the grid points $\dot{u}_j = g_j$, which forms the holistic discretisation. To solve this problem nu-

merically we first discretise the subgrid field as illustrated in Figure 8.1. The

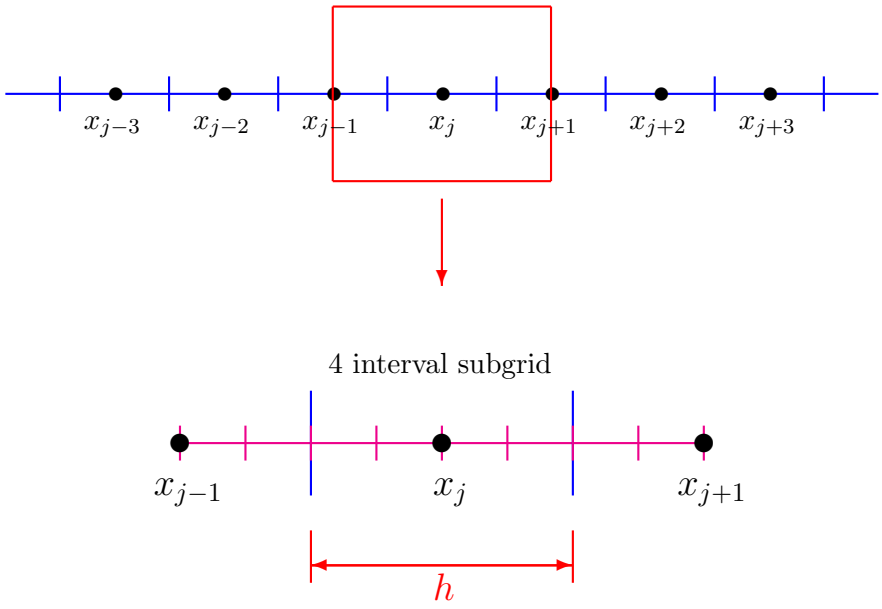

Figure 8.1: An example of a 4 interval subgrid (microscale) shown in magenta. The macroscale grid element boundaries are shown in blue. Note that for the nonlocal IBCs the jth subgrid extends past the boundaries of the jth element to at least $x_{j\pm1}$.

particular discretisation shown here is for a 4 interval subgrid resolution. After discretising the subgrid field, numerical approximations are derived for the spatial derivatives of the subgrid field. Then the discretised equations are solved at each of the subgrid points. The difficulty that arises is that although we discretise the spatial derivatives, the resulting system of equations is still described algebraically in γ, α, h and the grid values u_j. Therefore, to construct a holistic model that is general for these variables we solve a mixed

discrete and symbolic system of equations.

8.1.1 A low resolution subgrid illustrates the iteration scheme

To demonstrate this mixed discrete and symbolic problem we consider the 2 interval subgrid shown in Figure 8.2 to construct the $\mathcal{O}(\gamma^2, \alpha^2)$ holistic model of the RGL (6.1).

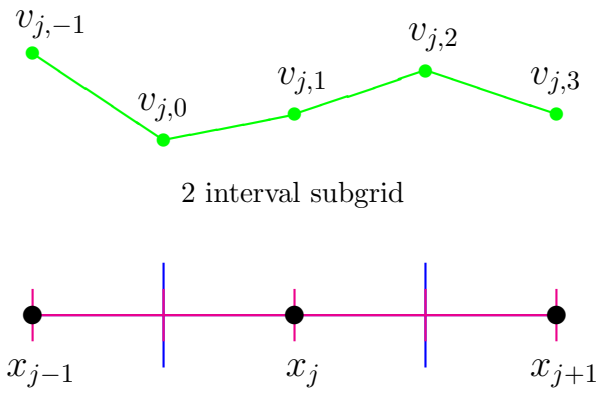

Figure 8.2: The subgrid field (green) for a 2 interval subgrid (magenta). The macroscale grid element boundaries are shown in blue.

We argue that the order of the numerical methodology used to solve the subgrid problem is not an important issue because at the subgrid scale higher order numerical methods make only a relatively small contribution to the macroscale dynamics which are of primary interest. Therefore, we use a simple second order centered difference approximation to discretise the spatial derivatives. For this 2 interval subgrid we use, for example

$$\frac{\partial^2 v'_{j,i}}{\partial x^2} \approx \frac{v'_{j,i-1} - 2v'_{j,i} + v'_{j,i+1}}{(h/2)^2}\,, \tag{8.2}$$

where $v_{j,i}$ is the ith subgrid point of the subgrid field v in the jth element. Here the subgrid interval size is $h/2$.

We employ an iteration scheme to find $v_j = \widetilde{v}_j + v'_j$ and $g_j = \widetilde{g}_j + g'_j$, where $\widetilde{v}_j$, $\widetilde{g}_j$ denote the current approximation and v'_j, g'_j are corrections to be sought in each iteration. The iteration scheme follows that shown in §6.2 for the analytical construction of the subgrid field. The difference here is that we discretise the subgrid field in space and therefore need to solve for the subgrid field v_j at each of the subgrid points in our discretisation, namely $v_{j,-1}$,$v_{j,0}$,$v_{j,1}$,$v_{j,2}$ and $v_{j,3}$ for this 2 interval subgrid.

The discretised RGL and IBCs (8.1) at the current approximation are

$$\sum_j \frac{\partial \widetilde{v}_{j,0}}{\partial u_j}\widetilde{g}_j = (4\widetilde{v}_{j,-1} - 8\widetilde{v}_{j,0} + 4\widetilde{v}_{j,1})/h^2 + \alpha\left(\widetilde{v}_{j,0} - \widetilde{v}^3_{j,0}\right), \tag{8.3}$$

$$\sum_j \frac{\partial \widetilde{v}_{j,1}}{\partial u_j}\widetilde{g}_j = (4\widetilde{v}_{j,0} - 8\widetilde{v}_{j,1} + 4\widetilde{v}_{j,2})/h^2 - \alpha\left(\widetilde{v}_{j,1} - \widetilde{v}^3_{j,1}\right), \tag{8.4}$$

$$\sum_j \frac{\partial \widetilde{v}_{j,2}}{\partial u_j}\widetilde{g}_j = (4\widetilde{v}_{j,1} - 8\widetilde{v}_{j,2} + 4\widetilde{v}_{j,3})/h^2 - \alpha\left(\widetilde{v}_{j,2} - \widetilde{v}^3_{j,2}\right), \tag{8.5}$$

$$\widetilde{v}_{j,3} - \widetilde{v}_{j,1} = \gamma\left(\widetilde{v}_{j+1,1} - \widetilde{v}_{j,1}\right), \tag{8.6}$$

$$\widetilde{v}_{j,1} - \widetilde{v}_{j,-1} = \gamma\left(\widetilde{v}_{j,1} - \widetilde{v}_{j-1,1}\right). \tag{8.7}$$

At each iteration the following equations are solved for the updates $\boldsymbol{v'_j}$ and g'

$$\begin{aligned}
(v'_{j,-1} - 2v'_{j,0} + v'_{j,1})4/h^2 - g'_j &= \mathrm{Res}_{8.3}\,,\\
(v'_{j,0} - 2v'_{j,1} + v'_{j,2})4/h^2 - g'_j &= \mathrm{Res}_{8.4}\,,\\
(v'_{j,1} - 2v'_{j,2} + v'_{j,3})4/h^2 - g'_j &= \mathrm{Res}_{8.5}\,,\\
v'_{j,3} - v'_{j,1} &= \mathrm{Res}_{8.6}\,,\\
v'_{j,1} - v'_{j,-1} &= \mathrm{Res}_{8.7}\,,\\
v'_{j,1} &= 0\,.
\end{aligned} \tag{8.8}$$

This iteration scheme will construct the subgrid field in the jth element and the evolution of the jth grid point, $\dot{u}_j = g_j$. Since we only consider periodic solutions across the physical domain, the analysis is identical in each element such that v_j is the same as v_k with mapping $j \mapsto k$.

Iteration 1

To start the iteration scheme we use the linear solution in each element of

$$\widetilde{\boldsymbol{v}}_j = \begin{bmatrix} \widetilde{v}_{j,-1} \\ \widetilde{v}_{j,0} \\ \widetilde{v}_{j,1} \\ \widetilde{v}_{j,2} \\ \widetilde{v}_{j,3} \end{bmatrix} = \begin{bmatrix} u_j \\ u_j \\ u_j \\ u_j \\ u_j \end{bmatrix} \quad \text{and} \quad g_j = 0\,. \tag{8.9}$$

Evaluating the residual equations (8.7), we obtain

$$\begin{aligned} \text{Res}_{8.3} &= -\alpha\left(u_j - u_j^3\right)\,, \\ \text{Res}_{8.4} &= -\alpha\left(u_j - u_j^3\right)\,, \\ \text{Res}_{8.5} &= -\alpha\left(u_j - u_j^3\right)\,, \\ \text{Res}_{8.6} &= \gamma\left(u_{j+1} - u_j\right)\,, \\ \text{Res}_{8.7} &= \gamma\left(u_j - u_{j-1}\right)\,. \end{aligned} \tag{8.10}$$

Note that the system (8.8) with right-hand sides (8.10) is a mixed discrete and symbolic system because it is described in terms of γ, α, h and the u_j's.

Solving this linear system gives

$$\boldsymbol{v}'_j = \begin{bmatrix} \gamma(-u_j + u_{j-1}) \\ \gamma(-0.25\,u_j - 0.125\,u_{j+1} + 0.375\,u_{j-1}) \\ 0 \\ \gamma(-0.25\,u_j + 0.375\,u_{j+1} - 0.125\,u_{j-1}) \\ \gamma(-u_j + u_{j+1}) \end{bmatrix}, \tag{8.11}$$

and

$$g'_j = \frac{\gamma}{h^2}\,(u_{j+1} - 2u_j + u_{j-1}) + \alpha(u_j - u_j^3)\,. \tag{8.12}$$

Updating $\boldsymbol{v}_j$ and g_j gives the $\widetilde{\boldsymbol{v}}_j$ and $\widetilde{g}_j$ for the second iteration:

$$\widetilde{\boldsymbol{v}}_j = \begin{bmatrix} u_j + \gamma(-u_j + u_{j-1}) \\ u_j + \gamma(-0.25\,u_j - 0.125\,u_{j+1} + 0.375\,u_{j-1}) \\ u_j \\ u_j + \gamma(-0.25\,u_j + 0.375\,u_{j+1} - 0.125\,u_{j-1}) \\ u_j + \gamma(-u_j + u_{j+1}) \end{bmatrix}, \tag{8.13}$$

and

$$\widetilde{g}_j = \frac{\gamma}{h^2}\,(u_{j+1} - 2u_j + u_{j-1}) + \alpha(u_j - u_j^3)\,. \tag{8.14}$$

We see that even though the subgrid field is known only roughly, the discretisation for the macroscale field is precisely a classic $\mathcal{O}\,(h^2)$ finite difference.

Iteration 2

We compute the residual equations for the second iteration, remembering that γ^2 terms and α^2 terms are neglected in this $\mathcal{O}\,(\gamma^2, \alpha^2)$ approximation. We obtain

$$\mathrm{Res}_{8.3} \;=\; \alpha\gamma\left(-0.5\,u_j^3 + 1.125\,u_{j+1}u_j^2 - 0.375\,u_{j+1}^3\right.$$

$$
\begin{aligned}
& -0.375\,u_{j-1}u_j^2 + 0.125\,u_{j-1}^3\Big)\,, \\
\mathrm{Res}_{8.4} &= 0\,, \\
\mathrm{Res}_{8.5} &= \alpha\gamma\Big(-0.5\,u_j^3 - 0.375\,u_{j+1}u_j^2 + 0.125\,u_{j+1}^3 \\
& \quad +1.125\,u_{j-1}u_j^2 - 0.375\,u_{j-1}^3\Big)\,, \\
\mathrm{Res}_{8.6} &= 0\,, \\
\mathrm{Res}_{8.7} &= 0\,. \qquad (8.15)
\end{aligned}
$$

Solving the discrete and symbolic system of equations (8.8) with the right-hand sides (8.15) gives

$$
\boldsymbol{v}'_j = \begin{bmatrix}
0 \\
\alpha\gamma h^2\Big(0.03125\,u_j^3 + 0.0703125\,u_{j+1}u_j^2 - 0.0234375\,u_{j+1}^3 \\
\quad -0.1171875\,u_{j-1}u_j^2 + 0.0390625\,u_{j-1}^3\Big) \\
0 \\
\alpha\gamma h^2\Big(0.03125\,u_j^3 - 0.1171875\,u_{j+1}u_j^2 + 0.0390625\,u_{j+1}^3 \\
\quad +0.0703125\,u_{j-1}u_j^2 - 0.0234375\,u_{j-1}^3\Big) \\
0
\end{bmatrix}, \qquad (8.16)
$$

and

$$
\begin{aligned}
g'_j &= \alpha\gamma\Big(0.25\,u_j^3 - 0.1875\,u_{j+1}u_j^2 + 0.0625\,u_{j+1}^3 - 0.1875\,u_{j-1}u_j^2 \\
& \quad +0.0625\,u_{j-1}^3\Big)\,. \qquad (8.17)
\end{aligned}
$$

Updating $\boldsymbol{v_j}$ and g_j gives

$$\widetilde{\boldsymbol{v}}_j = \begin{bmatrix} u_j + \gamma(-u_j + u_{j-1}) \\ u_j + \gamma(-0.25\,u_j - 0.125\,u_{j+1} + 0.375\,u_{j-1}) + \alpha\gamma h^2 \left(0.03125\,u_j^3 \right. \\ \quad + 0.0703125\,u_{j+1}u_j^2 - 0.0234375\,u_{j+1}^3 - 0.1171875\,u_{j-1}u_j^2 \\ \quad \left. + 0.0390625\,u_{j-1}^3\right) \\ u_j \\ u_j + \gamma(-0.25\,u_j + 0.375\,u_{j+1} - 0.125\,u_{j-1}) + \alpha\gamma h^2 \left(0.03125\,u_j^3 \right. \\ \quad - 0.1171875\,u_{j+1}u_j^2 + 0.0390625\,u_{j+1}^3 + 0.0703125\,u_{j-1}u_j^2 \\ \quad \left. - 0.0234375\,u_{j-1}^3\right) \\ u_j + \gamma(-u_j + u_{j+1}) \end{bmatrix}, \tag{8.18}$$

and

$$\begin{aligned} \widetilde{g}_j &= \frac{\gamma}{h^2}\,(u_{j+1} - 2u_j + u_{j-1}) + \alpha(u_j - u_j^3) \\ &\quad + \alpha\gamma \left(0.25\,u_j^3 - 0.1875\,u_{j+1}u_j^2 + 0.0625\,u_{j+1}^3 - 0.1875\,u_{j-1}u_j^2 \right. \\ &\quad \left. + 0.0625\,u_{j-1}^3\right)\,. \end{aligned} \tag{8.19}$$

Iteration 3

Computing the residual equations (8.3–8.7) for the third iteration gives,

$$\begin{aligned} \mathrm{Res}_{8.3} &= 0\,, \\ \mathrm{Res}_{8.4} &= 0\,, \\ \mathrm{Res}_{8.5} &= 0\,, \\ \mathrm{Res}_{8.6} &= 0\,, \\ \mathrm{Res}_{8.7} &= 0\,. \end{aligned} \tag{8.20}$$

Since the residuals (8.20) at the third iteration are all zero, $\boldsymbol{v}'_j$ and g'_j are zero for all further iterations for this $\mathcal{O}(\gamma^2, \alpha^2)$ holistic model. Therefore, there is no further update to the subgrid field nor the the evolution of the grid values to errors $\mathcal{O}(\gamma^2, \alpha^2)$.

The iteration scheme successfully constructs the subgrid field and the evolution of the grid values which forms the holistic model. The $\mathcal{O}(\gamma^2, \alpha^2)$ holistic model is

$$\boldsymbol{v}_j = \begin{bmatrix} u_j + \gamma(-u_j + u_{j-1}) + \mathcal{O}(\gamma^2, \alpha^2) \\ u_j + \gamma(-0.25\,u_j - 0.125\,u_{j+1} + 0.375\,u_{j-1}) + \alpha\gamma h^2 \big(0.03125\,u_j^3 \\ \quad + 0.0703125\,u_{j+1}u_j^2 - 0.0234375\,u_{j+1}^3 - 0.1171875\,u_{j-1}u_j^2 \\ \quad + 0.0390625\,u_{j-1}^3\big) + \mathcal{O}(\gamma^2, \alpha^2) \\ u_j + \mathcal{O}(\gamma^2, \alpha^2) \\ u_j + \gamma(-0.25\,u_j + 0.375\,u_{j+1} - 0.125\,u_{j-1}) + \alpha\gamma h^2 \big(0.03125\,u_j^3 \\ \quad - 0.1171875\,u_{j+1}u_j^2 + 0.0390625\,u_{j+1}^3 + 0.0703125\,u_{j-1}u_j^2 \\ \quad - 0.0234375\,u_{j-1}^3\big) + \mathcal{O}(\gamma^2, \alpha^2) \\ u_j + \gamma(-u_j + u_{j+1}) + \mathcal{O}(\gamma^2, \alpha^2) \end{bmatrix}, \tag{8.21}$$

and

$$\begin{aligned} g_j \;=\; & \frac{\gamma}{h^2}(u_{j+1} - 2u_j + u_{j-1}) + \alpha(u_j - u_j^3) \\ & + \alpha\gamma\left(0.25\,u_j^3 - 0.1875\,u_{j+1}u_j^2 + 0.0625\,u_{j+1}^3 - 0.1875\,u_{j-1}u_j^2\right. \\ & \left. +0.0625\,u_{j-1}^3\right) + \mathcal{O}\left(\gamma^2, \alpha^2\right), \end{aligned} \tag{8.22}$$

for the 2 interval subgrid. Compare (8.22) to the analytically constructed $O(\gamma^2, \alpha^2)$ holistic model (6.26) to see that by numerically constructing the subgrid field we find all of the terms from (6.26) but with numerical errors in the coefficients. For example, the coefficient of the $\alpha\gamma u_j^3$ term in the 2

interval subgrid model (8.22) of g_j is 0.25 compared to 1/3 in the analytically constructed holistic model.

8.1.2 Coefficients converge to analytic holistic model

Here we list the coefficients of the $O(\gamma^2, \alpha^2)$ holistic model (6.24) of the RGL (6.1) and the $O(\gamma^3, \alpha^2)$ holistic model (2.25) of the Kuramoto–Sivashinsky equation (2.1) for subgrid resolutions of 2, 4, 6 and 8 intervals. We see that the coefficients have second order convergence to the coefficients of the analytically constructed holistic models. This is expected since the subgrid problem is solved here with explicit second order centered differences.

The $O(\gamma^2, \alpha^2)$ holistic model of the RGL

We write the $\mathcal{O}(\gamma^2, \alpha^2)$ holistic model of the RGL in the form

$$\begin{aligned} \dot{u_j} &= \frac{\gamma}{h^2}\delta^2 u_j + \alpha\left(u_j - u_j^3\right) \\ &\quad + \gamma\alpha\left(c_1\delta^2 u_j^3 + c_2 u_j^2\delta^2 u_j\right) + \mathcal{O}\left(\gamma^2, \alpha^2\right), \end{aligned} \tag{8.23}$$

where the $c_1 = 0.08333333$, $c_2 = -0.25$ to 8 decimal places for the analytically constructed subgrid field listed in §6.2. The linear terms of the numerically constructed holistic models are exact for all subgrid resolutions for the $O(\gamma^2, \alpha^2)$ holistic model of the $1D$ RGL. However, the coefficients of the nonlinear terms are approximations, but approximations that improve with subgrid resolution. Table 8.1 lists the values for these coefficients for the numerically constructed subgrid fields with subgrid resolutions of 2,4,6, and 8 intervals. Observe the expected second order convergence of the coefficients.

Subgrid resolution	c_1	c_2
2 intervals	0.0625	-0.1875
4 intervals	0.078125	-0.234375
6 intervals	0.08101852	-0.24305556
8 intervals	0.08203124	-0.24609375
Exact	0.08333333	-0.25

Table 8.1: Coefficients for the $\mathcal{O}(\gamma^2, \alpha^2)$ holistic model (8.23) of the RGL for subgrid resolutions of 2,4,6 and 8 intervals respectively. The last line gives the exact coefficients from §6.2.

The $O(\gamma^3, \alpha^2)$ holistic model of the Kuramoto–Sivashinsky equation

Turning from the RGL to the Kuramoto–Sivashinsky equation (2.1) we write the $\mathcal{O}(\gamma^3, \alpha^2)$ holistic model of the Kuramoto–Sivashinsky equation in the form

$$\begin{aligned} \dot{u_j} &= -\frac{\gamma\alpha}{h^2}\delta^2 u_j - \frac{\gamma\alpha}{h}u_j\delta\mu u_j - \frac{4\gamma^2}{h^4}\delta^4 u_j + \frac{\gamma^2\alpha}{h^2}c_1\delta^4 u_j \\ &\quad + \frac{\gamma^2\alpha}{h}\left(c_2 u_j\delta^3\mu u_j + c_3\delta^2 u_j\delta^3\mu u_j + c_4\delta^4 u_j\delta\mu u_j\right) \\ &\quad + \mathcal{O}\left(\gamma^3, \alpha^2\right), \end{aligned} \tag{8.24}$$

where the $c_1 = c_3 = c_4 = 0.08333333$ and $c_2 = 0.16666667$ to 8 decimal places for the analytically constructed subgrid field listed in §2.3.2. Table 8.2 lists the values for these coefficient for the numerically constructed subgrid fields with subgrid resolutions of 2,4,6, and 8 intervals. Again, as expected, the convergence of the coefficients is second order.

Subgrid resolution	c_1, c_3, c_4	c_2
2 intervals	0.0625	0.125
4 intervals	0.078125	0.15625
6 intervals	0.08101852	0.16203704
8 intervals	0.08203125	0.1640625
Exact	0.083333333	0.16666667

Table 8.2: Coefficients for the $\mathcal{O}(\gamma^3, \alpha^2)$ holistic model (8.24) of the Kuramoto–Sivashinsky equation for subgrid resolutions of 2,4,6 and 8 intervals respectively. The last line gives the exact coefficients from §2.3.2.

8.2 Extrapolation improves accuracy

Richardson extrapolation [58, e.g] improves the order of accuracy of the coefficients in our numerically constructed holistic model. Denote the coefficients of the holistic models as $c_n(\Delta x)$, for the subgrid size Δx. Then the extrapolated coefficient [58] is

$$\bar{c}_n = c_n(\Delta x_2) + \frac{c_n(\Delta x_1) - c_n(\Delta x_2)}{1 - (\Delta x_1/\Delta x_2)^2}\,. \tag{8.25}$$

Extrapolating from two $\mathcal{O}(\Delta x^2)$ accurate coefficients $c_n(\Delta x_1)$ and $c_n(\Delta x_2)$ such as those listed in Tables 8.1 and 8.2 we expect to achieve $\mathcal{O}(\Delta x^4)$ accuracy for $\bar{c}_n$ [58].

For example, consider the coefficients of the $O(\gamma^3, \alpha^2)$ holistic model for the Kuramoto–Sivashinsky equation (2.32) constructed numerically with subgrid resolutions of 6 and 8 intervals. Table 8.2 gives the coefficients $c_1 = 0.08101852$ and $c_2 = 0.16203704$ for a subgrid resolution of 6 intervals and $c_1 = 0.08203125$ and $c_2 = 0.1640625$ with 8 intervals. Extrapolating

with (8.25) gives $\bar{c}_1 = 0.08333333$ and $\bar{c}_2 = 0.16666667$. The exact coefficients are found due to the polynomial structure of the subgrid field. In general this is not the case but this extrapolation procedure does improve the order of accuracy of the coefficients.

In §8.4 I describe the computational difficulties associated with the numerical construction of the subrid field and its evolution. Richardson extrapolation is useful for obtaining improved accuracy for our numerically constructed holistic model without having to resort to the complications of a higher order accuracy subgrid discretisation nor the immense computational time of using a more refined subgrid resolution.

8.3 Low resolution subgrids are accurate

Errors are introduced into the coefficients of the holistic models by the numerical construction. Thus we now investigate what effect these errors have on the performance of the holistic models. We compare the bifurcation diagrams for analytically constructed holistic models seen in

- §6.4.2 for the $\mathcal{O}(\gamma^2, \alpha^2)$ holistic model (6.26) of the RGL (6.1);
- §3.3.1 for the $\mathcal{O}(\gamma^3, \alpha^2)$ holistic model (2.25) of the Kuramoto–Sivashinsky equation (2.1);
- §3.4.1 for the $\mathcal{O}(\gamma^5, \alpha^2)$ holistic model (2.32) of the Kuramoto–Sivashinsky equation;

to the bifurcation diagrams for numerically constructed holistic models with subgrid resolutions of 2,4,6 and 8 intervals. Recall that these bifurcation

diagrams were constructed with spatially periodic and odd boundary conditions (3.1). We find the bifurcation diagrams with subgrid resolutions of just 4 and 6 intervals for holistic models of the RGL and the Kuramoto–Sivashinsky equation respectively are almost indiscernible from the bifurcation diagrams of Chapters 3 and 6 for the analytically constructed subgrid fields.

The $\mathcal{O}(\gamma^2, \alpha^2)$ holistic model of the RGL

Figure 8.3 compares the bifurcation diagrams for the $\mathcal{O}(\gamma^2, \alpha^2)$ holistic model of the RGL system with 8 macroscale elements on $[0, \pi]$ for subgrid resolutions of (a) 2, (b) 4, (c) 6 and (d) 8 intervals. The analytically constructed holistic model shown in green is not the accurate solution of the RGL system but rather represents the analytically constructed $\mathcal{O}(\gamma^2, \alpha^2)$ holistic model.

Observe that the $\mathcal{O}(\gamma^2, \alpha^2)$ holistic model of the RGL system on this coarse macroscale grid constructed with a subgrid resolution of just 4 intervals is almost indiscernible from the bifurcation diagram of the analytically constructed holistic model.

The $\mathcal{O}(\gamma^3, \alpha^2)$ holistic model of the Kuramoto–Sivashinsky equation

Figure 8.4 compares the bifurcation diagrams for the $\mathcal{O}(\gamma^3, \alpha^2)$ holistic model of the Kuramoto–Sivashinsky system with 8 macroscale elements on $[0, \pi]$ for subgrid resolutions of (a) 2, (b) 4, (c) 6 and (d) 8 intervals. Observe that the $\mathcal{O}(\gamma^3, \alpha^2)$ holistic model of the Kuramoto–Sivashinsky system on this coarse grid constructed with a subgrid resolution of 6 intervals is almost indiscernible from the bifurcation diagram of the analytically constructed

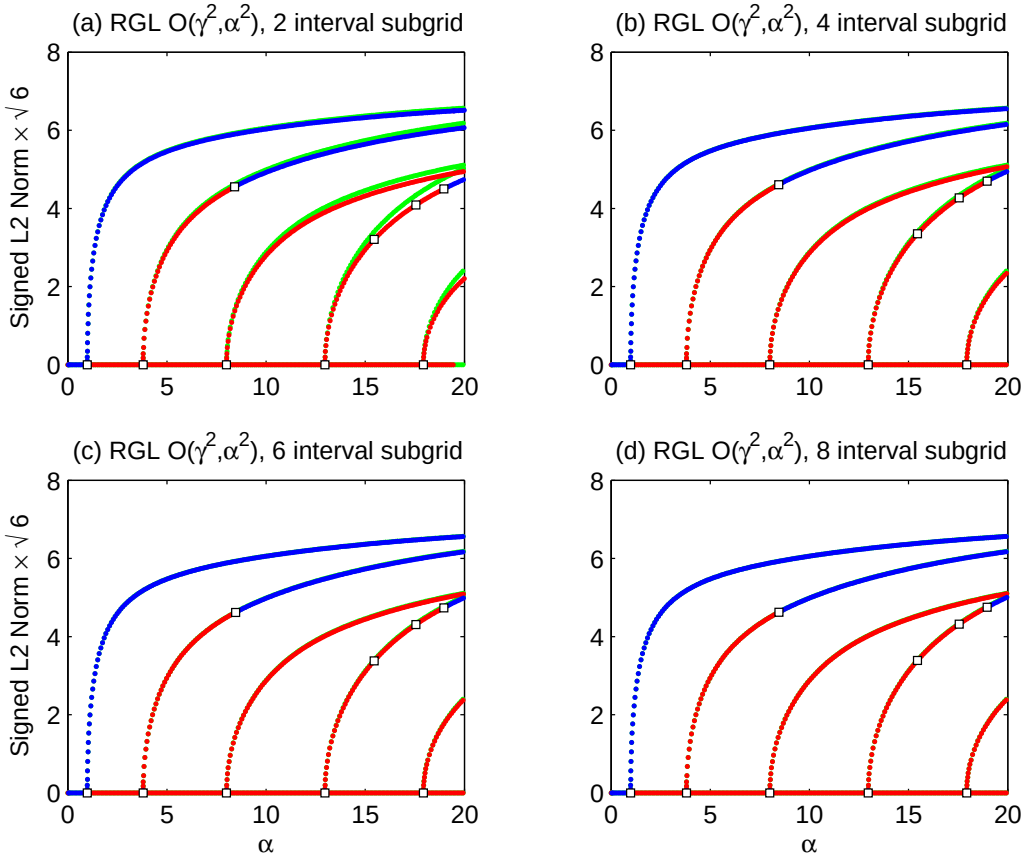

Figure 8.3: Bifurcation diagrams of the $O(\gamma^2, \alpha^2)$ holistic models of the RGL system with 8 macroscale elements on $[0, \pi]$ for subgrid resolutions of (a) 2, (b) 4, (c) 6 and (d) 8 intervals. The bifurcation diagram for the analytically constructed model is shown in green.

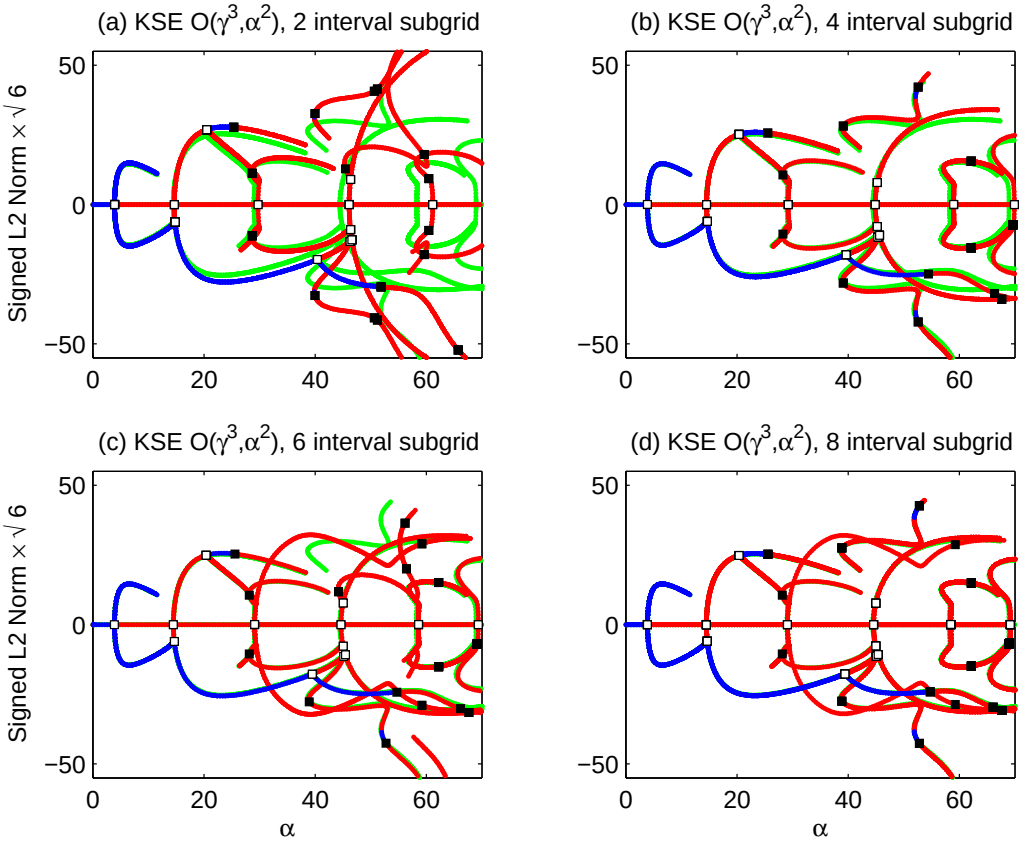

Figure 8.4: Bifurcation diagrams of the $O(\gamma^3, \alpha^2)$ holistic models of the Kuramoto–Sivashinsky system with 8 macroscale elements on $[0, \pi]$ for subgrid resolutions of (a) 2, (b) 4, (c) 6 and (d) 8 intervals. The bifurcation diagram for the analytically constructed model is shown in green.

holistic model. The 2 interval and 4 interval subgrid bifurcation diagrams show that the inaccuracies increase as the nonlinear parameter α increases.

Recall from Chapter 2, that the $\mathcal{O}(\gamma^3, \alpha^2)$ holistic model of the Kuramoto–Sivashinsky equation has a 5 point macroscale stencil and is $\mathcal{O}(h^2)$ consistent. The equivalent PDE for the numerically constructed $\mathcal{O}(\gamma^3, \alpha^2)$ holistic model with a 2 interval subgrid is

$$\begin{aligned} \frac{\partial u}{\partial t} &= -\alpha\left(u\frac{\partial u}{\partial x} + \frac{\partial^2 u}{\partial x^2}\right) - 4\frac{\partial^4 u}{\partial x^4} \\ &\quad -h^2\left(\frac{2}{3}\frac{\partial^6 u}{\partial x^6} + \alpha\frac{1}{24}\frac{\partial^3 u}{\partial x^3}u + \alpha\frac{1}{48}\frac{\partial^4 u}{\partial x^4}\right) + \mathcal{O}(h^4)\,. \end{aligned} \tag{8.26}$$

We see that this 2 interval subgrid holistic model is also $\mathcal{O}(h^2)$ consistent. Note that the coefficients of the linear terms in the equivalent PDE are the same as in (2.38) but the coefficients of the αh^2 terms are not the same as for the analytical model. However, the accuracy of the coefficients of the equivalent PDE converge to the analytical coefficients as the subgrid resolution increases.

The $\mathcal{O}(\gamma^5, \alpha^2)$ holistic model of the Kuramoto–Sivashinsky equation

Figure 8.5 compares the bifurcation diagrams for the $\mathcal{O}(\gamma^5, \alpha^2)$ holistic model of the Kuramoto–Sivashinsky system with 8 macroscale elements on $[0, \pi]$ for subgrid resolutions of (a) 2, (b) 4, (c) 6 and (d) 8 intervals. Again, observe that the $\mathcal{O}(\gamma^5, \alpha^2)$ holistic model of the Kuramoto–Sivashinsky system on this coarse grid of 8 macroscale elements constructed with a subgrid resolution of 6 intervals is almost indiscernible from the bifurcation diagram of the analytically constructed holistic model.

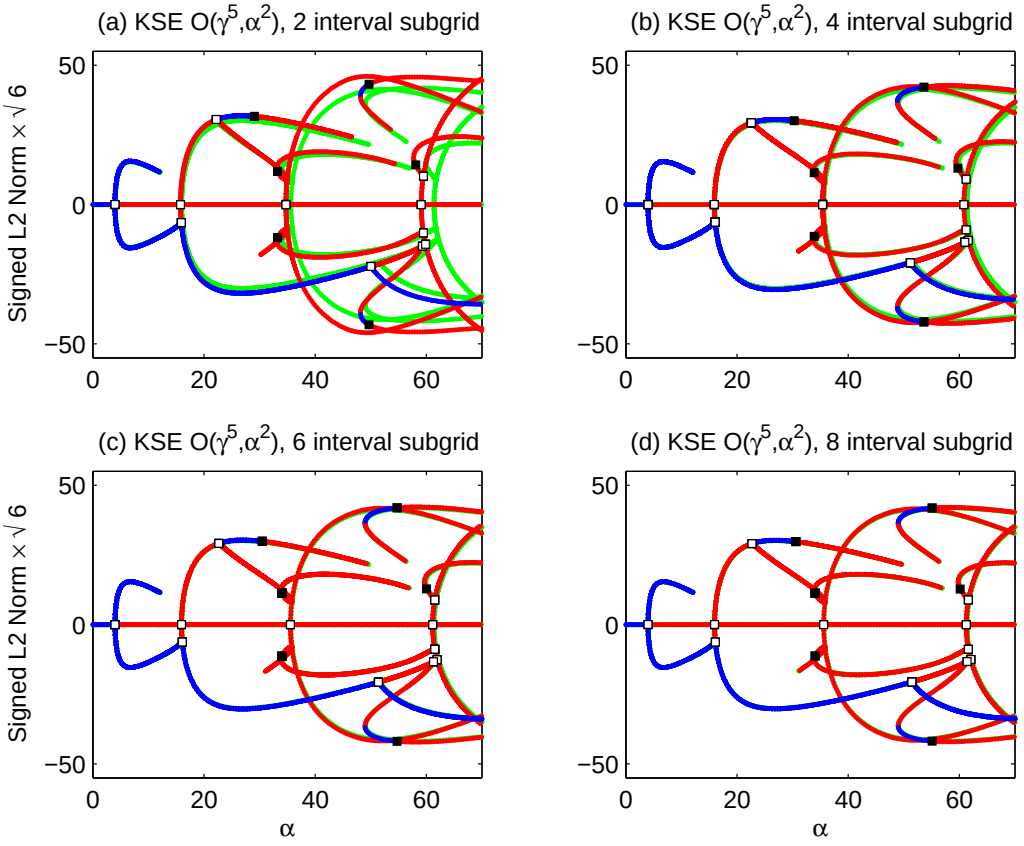

Figure 8.5: Bifurcation diagrams of the $O(\gamma^5, \alpha^2)$ holistic models of the Kuramoto–Sivashinsky system with 8 macroscale elements on $[0, \pi]$ for subgrid resolutions of (a) 2, (b) 4, (c) 6 and (d) 8 intervals. The bifurcation diagram for the analytically constructed model is shown in green.

Recall from Chapter 2, that the $\mathcal{O}(\gamma^5, \alpha^2)$ holistic model of the Kuramoto–Sivashinsky equation has a 9 point macroscale stencil and is $\mathcal{O}(h^6)$ consistent. The equivalent PDE for the numerically constructed $\mathcal{O}(\gamma^5, \alpha^2)$ holistic model with a 2 interval subgrid is

$$\begin{aligned}\frac{\partial u}{\partial t} &= -\alpha\left(u\frac{\partial u}{\partial x}+\frac{\partial^2 u}{\partial x^2}\right)-4\frac{\partial^4 u}{\partial x^4}\\ &\quad -h^2\left(\frac{\alpha}{24}\frac{\partial^3 u}{\partial x^3}+\frac{\alpha}{48}\frac{\partial^4 u}{\partial x^4}+\frac{1}{6}\frac{\partial^6 u}{\partial x^6}\right)\\ &\quad -h^4\left(\frac{\alpha}{1920}u\frac{\partial^5 u}{\partial x^5}+\frac{\alpha}{5760}\frac{\partial^6 u}{\partial x^6}+\frac{1}{320}\frac{\partial^8 u}{\partial x^8}\right)+\mathcal{O}(h^6)\,. \quad (8.27)\end{aligned}$$

The equivalent PDE is only $\mathcal{O}(h^2)$ consistent. Note that even the linear terms are only $\mathcal{O}(h^2)$ consistent. However as the subgrid resolution increases the equivalent PDE approaches $\mathcal{O}(h^6)$ consistency.

The good performance of the holistic models seen here for subgrid resolutions of just 6 subgrid intervals is good evidence to support that the numerically constructed holistic models are useful approximations even if a low resolution subgrid is used. This is important because for higher dimensional problems limitations of insufficient computer memory and enormous computational time make more refined subgrid problems difficult to construct.

8.4 An efficient computer algebra algorithm is the key

The difficulty associated with the numerical construction the subgrid field is the mixed discrete and symbolic nature of the equations involved in the iteration scheme. In §8.1.1 we saw an example of the iteration scheme to construct the $\mathcal{O}(\gamma^2, \alpha^2)$ holistic model (6.26) of the RGL (6.1) for a 2 interval

subgrid. Solving the mixed discrete and symbolic equations (8.8) is not difficult for this simple example. However, the size of the system of equations increases as the subgrid resolution increases and the complexity of the symbolic nonlinear residuals increases quickly as higher order holistic models are constructed. Therefore we need to employ an algorithm which is sensitive to the mixed discrete and symbolic nature of the procedure but is efficient enough to allow construction of holistic models on useful subgrid resolutions.

Computer algebra packages such as REDUCE [22] or MATHEMATICA [67] have routines that solve symbolic systems of equations such as (8.8). However, these solve routines are inefficient for higher resolutions and higher order holistic models. Even a low resolution 2 interval subgrid takes many minutes in both REDUCE and MATHEMATICA using the built in `solve` routines. They are slowed dramatic when the number of the higher order nonlinear terms increases. We develop an algorithm that is practical for implementation with a large number of high order symbolic terms.

Here I present an algorithm which formulates the iteration scheme described in §8.1.1 with an entirely discrete linear operator which is an approximation to the differential operator. In §8.4.1 we see how the linear part of the iteration scheme is constructed. We explore this by considering the 2 interval subgrid example of §8.1.1 for the RGL in detail. In §8.4.2 we discuss how the LU factorisation of the discrete linear operator is implemented and the REDUCE implementation of the algorithm for the $1D$ PDEs of second and fourth order is outlined in §8.4.3.

8.4.1 Formulate iteration scheme with discrete linear operator

At each step of the iteration scheme we solve a problem for updates to the subgrid field $\boldsymbol{v}'_j$ and its evolution g'_j of the form

$$\mathcal{L}\begin{bmatrix} \boldsymbol{v}'_j \\ g'_j \end{bmatrix} = \boldsymbol{Res}(\tilde{\boldsymbol{v}}_j)\,, \tag{8.28}$$

where $\mathcal{L}$ is a linear operator and $\mathrm{Res}_(\tilde{v}_j)$ is the vector of residuals of the equations. We form $\mathcal{L}$ as a discrete operator with no symbolic terms and this is the key to the algorithm presented here. We make use of the static structure of $\mathcal{L}$ and employ an LU factorisation algorithm to solve for updates at each iteration.

Examine the left hand side (the linear part) of equations (8.8), for the 2 interval subgrid field example and see a h^{-2} factor for each of the subgrid values $\boldsymbol{v}'_j$. Remove this dependence by multiplying (8.8) through by h^2. Also introduce a new variable $\mathcal{G}' = h^2 g'$ and then (8.8) becomes

$$\begin{aligned}
(4v'_{j,-1} - 8v'_{j,0} + 4v'_{j,1}) - \mathcal{G}' &= h^2\mathrm{Res}_{8.3}\,,\\
(4v'_{j,0} - 8v'_{j,1} + 4v'_{j,2}) - \mathcal{G}' &= h^2\mathrm{Res}_{8.4}\,,\\
(4v'_{j,1} - 8v'_{j,2} + 4v'_{j,3}) - \mathcal{G}' &= h^2\mathrm{Res}_{8.5}\,,\\
v'_{j,3} - v'_{j,1} &= \mathrm{Res}_{8.6}\,,\\
v'_{j,1} - v'_{j,-1} &= \mathrm{Res}_{8.7}\,,\\
v'_{j,1} = 0\,,&
\end{aligned} \tag{8.29}$$

which is in the form of (8.28) with

$$\mathcal{L} = \begin{bmatrix} 4 & -8 & 4 & 0 & 0 & -1 \\ 0 & 4 & -8 & 4 & 0 & -1 \\ 0 & 0 & 4 & -8 & 4 & -1 \\ 0 & 0 & -1 & 0 & 1 & 0 \\ -1 & 0 & 1 & 0 & 0 & 0 \\ 0 & 0 & 1 & 0 & 0 & 0 \end{bmatrix}. \tag{8.30}$$

This linear operator $\mathcal{L}$ does not change throughout the iteration scheme and therefore we construct and factor it once, at the beginning of the iteration scheme. When $\mathcal{G}'$ has been constructed to the desired order in γ and α, the evolution of the grid points is found by dividing by h^2 for this example.

Similarly, when constructing holistic models for the fourth order Kuramoto–Sivashinsky equation, the equations of (8.28) corresponding to the discretised PDE are multiplied by h^4 because of the fourth order spatial derivative.

8.4.2 Solve with LU factorisation

We perform an LU decomposition [45] of the linear operator $\mathcal{L} = LU$ into the product of a lower triangular matrix L and an upper triangular matrix U. The LU decomposition is performed once and requires approximately $\frac{1}{3}N^3$ executions of a loop which performs one add and one multiply for a system of N equations.

At each step of the iteration scheme the LU factorisation algorithm operates on the symbolic residual vector. Perhaps $2D$ & $3D$ problems can be solved efficiently through iterative multigrid [38, 3] or incomplete LU factorisation and Krylov subspace methods [28, 64]. However, this is not considered

in the scope of this dissertation.

8.4.3 The REDUCE implementation in $1D$

Here we examine in more detail the REDUCE implementation of the algorithm described in §8.4.1 for numerically constructing the subgrid field in $1D$. REDUCE is preferred to other computer algebra systems because of its ability to perform pattern matching "on the fly". That is, higher order terms to be neglected are removed from the internal representation of an expression during the algebraic manipulation of the expression rather than after the entire expression is evaluated [22]. For example, if a rule such as `let x^4=>0` is defined than all powers of x greater than or equal to 4 are set to zero. They are set to zero before evaluation of the entire expression. This "on the fly" pattern matching feature dramatically reduces the amount of storage and time needed to evaluate expressions and is particularly useful for nonlinear problems where a partial asymptotic expansion may generate a huge amount of unwanted high order terms.

Examples of the REDUCE implementation of the numerical construction of the subgrid fields is listed in §A.3.1 for second order PDEs such as RGL (6.1) and in §A.3.2 for fourth order PDEs such as Kuramoto–Sivashinsky equation (2.1). The listing of the REDUCE code serves as a reference for implementing the algorithm described in this dissertation.

Note the following important features of the REDUCE implementation of the algorithm in the code of §A.3.1. Both the discrete linear operator and the symbolic residual vector of (8.28) are stored in the matrix `eqns` on the first iteration. Note that the amplitude equation is built on line 43, the IBCs

on lines 46–49 and the interior discretisation of the PDE on lines 52–57. The discrete linear operator is stored in matrix `lu` and is setup by introducing `ud` and the variable `gd`. These variables `ud` and `gd` represent the updates to the subgrid field and its evolution. The coefficients of `gd` and `ud` form `lu`. This is done on lines 61–68 by setting all of the other terms in `eqns` to zero. On further iterations `gd` and `ud` are set to zero because the static linear structure has been built and only the symbolic RHS part of (8.29) is computed and stored in `eqns`. The iteration based on [52] continues until the residuals at all subgrid points are zero for the desired order of the holistic model.

The LU back substitution algorithm [45] overwrites the symbolic RHS vector with each solution component as it is computed. This reduces the amount of storage needed. Since the symbolic RHS vector can include a large number of higher order terms for each of a large number of subgrid points, it is important to reduce memory use through sharing storage of the large symbolic RHS and the large symbolic solution vector. Note that matrices are global in scope in REDUCE and therefore the names of the matrices in the procedures `lu_decomp` and `lu_backsub`, listed in §A.5, must be the same as in the main program code.

Section A.3.2 lists the REDUCE code for the numerical construction of the subgrid field for the holistic models of the 1D Kuramoto–Sivashinsky equation (2.1). This serves as a reference for applying the algorithm to fourth order PDEs in 1D. The code is very similar to the second order example in §A.3.1. Note the following important differences. The subgrid field must be extended to at least $x_{j\pm2}$ to apply the non-local IBCs (2.7–2.8) as discussed

in §2.1.2. Therefore, twice the number of subgrid points are needed for the same subgrid resolution of the second order problems. The extra IBCs (2.8) required for the holistic models of fourth order equations are constructed in lines 52–59.

I also implemented this algorithm in MATHEMATICA with some help from the MATHEMATICA users newsgroup and an example program is listed in §A.3.3. For this implementation of the algorithm the linear problem is solved through the inverse of $\mathcal{L}$ instead of using LU decomposition. This is done here because the built-in LU back substitution routine of MATHEMATICA does not work for symbolic solution vectors. My aim was to compare the performance of MATHEMATICA to REDUCE with regards to the increase in computational time with the increase in the number of symbolic terms at each of the subgrid points. The accuracy of the linear solve part of the iteration scheme was not of concern for this comparison nor was the speed of the solve step in each iteration. Note that both the REDUCE and MATHEMATICA implementations use an entirely discrete linear operator in the iteration scheme.

I found the REDUCE implementation of the algorithm to be more pratical to implement with regard to the number of symbolic terms in the holistic model than the MATHEMATICA version. Table 8.3 lists the computational time for the REDUCE implementation for constructing the $\mathcal{O}(\gamma^2, \alpha^2)$, $\mathcal{O}(\gamma^3, \alpha^2)$, $\mathcal{O}(\gamma^4, \alpha^2)$ holistic models of the $1D$ RGL with subgrid resolutions of 2, 4, 8 and 16 intervals. The $\mathcal{O}(\gamma^3, \alpha^2)$ holistic model has approximately 3 times the number of symbolic terms of the $\mathcal{O}(\gamma^2, \alpha^2)$ holistic model and the computational times increase by approximately a factor of 3. The $\mathcal{O}(\gamma^4, \alpha^2)$

holistic model has approximately 2.5 times the number of symbolic terms of the $\mathcal{O}(\gamma^3, \alpha^2)$ holistic model and the computational times increase by approximately a factor of 4. However, the computational time for the $\mathcal{O}(\gamma^4, \alpha^2)$ holistic models have a greater percentage of garbage collection time. These times were observed on a Pentium III 750MHz processor with 256Mb of RAM running REDUCE 3.7 under Windows XP.

REDUCE computational time

Subgrid resolution	$\mathcal{O}(\gamma^2, \alpha^2)$	$\mathcal{O}(\gamma^3, \alpha^2)$	$\mathcal{O}(\gamma^4, \alpha^2)$
2 intervals	0.1 s	0.2 s	1.1 s
4 intervals	0.2 s	0.8 s	3.1 s
8 intervals	0.6 s	2.0 s	8.3 s
16 intervals	2.0 s	6.2 s	23.7 s

MATHEMATICA computational time

Subgrid resolution	$\mathcal{O}(\gamma^2, \alpha^2)$	$\mathcal{O}(\gamma^3, \alpha^2)$	$\mathcal{O}(\gamma^4, \alpha^2)$
2 intervals	0.4 s	5.6 s	70.2 s
4 intervals	1.1 s	16.3 s	215.4 s
8 intervals	2.7 s	28.5 s	367.6 s
16 intervals	6.8 s	98.3 s	517.7 s

Table 8.3: REDUCE and MATHEMATICA computational times for numerical construction of the $\mathcal{O}(\gamma^2, \alpha^2)$, $\mathcal{O}(\gamma^3, \alpha^2)$ and $\mathcal{O}(\gamma^4, \alpha^2)$ holistic models of the $1D$ RGL

Table 8.3 also lists the computational time for the MATHEMATICA implementation for constructing the $\mathcal{O}(\gamma^2, \alpha^2)$, $\mathcal{O}(\gamma^3, \alpha^2)$, $\mathcal{O}(\gamma^4, \alpha^2)$ holistic models of the $1D$ RGL with subgrid resolutions of 2, 4, 8 and 16 intervals. The computational times of the $\mathcal{O}(\gamma^3, \alpha^2)$ holistic model are approximately

15 times the $\mathcal{O}(\gamma^2, \alpha^2)$ model despite only containing approximately 3 times the number of symbolic terms. The computational times of the $\mathcal{O}(\gamma^4, \alpha^2)$ holistic model are approximately 15 times the $\mathcal{O}(\gamma^3, \alpha^2)$ model despite only containing approximately 2.5 times the number of symbolic terms. Note that these times have been observed on a Pentium III 750MHz processor with 256Mb of RAM running MATHEMATICA 3.0 under Windows XP.

The REDUCE implementation is vastly superior to the MATHEMATICA implementation as the number of higher order terms increase. It is likely the "on the fly" pattern matching feature of REDUCE mentioned above is the reason it is superior.

REDUCE is an interpreted language and as such it must interpret each command and allocate memory as each command is executed at runtime. This slows down the execution of the algorithm but is a limitation of most computer algebra systems. It could be possible to build a compiled type of computer algebra system with only the features needed to specifically handle these iteration schemes, but extensive development time would be needed and the REDUCE implementation of this algorithm is adequate. The algorithm also lends itself to parallel computation which would be a more worthwhile avenue to explore than building specific implementations of this algorithm in a compiled language. Neither of these options have been considered in the scope of this dissertation.

8.5 Discretise the subgrid field structure in two spatial dimensions

We have seen in §8.3 that the numerically constructed holistic models accurately produce the analytic holistic models in $1D$, especially with Richardson extrapolation. For the $1D$ problems we have explored, namely the RGL equation (6.1) and the Kuramoto–Sivashinsky equation (2.1), we already know that the subgrid fields can be found analytically, as shown in Chapter 2. However, in extending the holistic approach to $2D$ the subgrid field and its evolution cannot usually be constructed analytically, as discussed in §7.6. Only the $\mathcal{O}(\gamma^2, \alpha^2)$ holistic model of the RGL is found analytically in $2D$. Therefore, the numerical construction of the subgrid field and its evolution is required to develop higher order holistic models for PDEs of two or more spatial dimensions.

Here we explore the numerical construction of the subgrid field and its evolution for holistic models of the second order RGL in $2D$ (7.1). We begin in §8.5.1 by considering the changes to the $1D$ algorithm presented in §8.4 that are required for its application to second order PDEs of two spatial dimensions. We then show in §8.5.2 that a subgrid resolution of just 4×4 elements is sufficient to accurately reproduce the bifurcation diagram for $\mathcal{O}(\gamma^2, \alpha^2)$ holistic model of the RGL in $2D$ on a macroscale grid of 8×8 elements on $[0, \pi] \times [0, \pi]$, for $0 \leq \alpha \leq 30$. Finally, in §8.5.3 we examine the performance of the $\mathcal{O}(\gamma^3, \alpha^2)$ holistic model of the RGL in $2D$ by comparing bifurcation diagrams on macroscale grids of 8×8 elements on $[0, \pi] \times [0, \pi]$ to the accurate bifurcation diagram for $0 \leq \alpha \leq 30$. We find the $\mathcal{O}(\gamma^3, \alpha^2)$

holistic model gives improved performance over the $\mathcal{O}(\gamma^2, \alpha^2)$ holistic model of the RGL in $2D$.

8.5.1 The algorithm is extended to $2D$

We discretise the subgrid as shown in Figure 8.6. The subgrid is shown in magenta for this particular example of a 4×4 interval subgrid. Note that the subgrid field extends to just before $x_{i\pm1,j\pm1}$ to allow the application of the $2D$ non-local IBCs (7.2–7.3). The subgrid field is not extended to actually include $x_{i\pm1,j\pm1}$ because the Laplacian applied to the interior points does not involve the subgrid field at the corners. $x_{i\pm1,j\pm1}$ are therefore ignored and set to zero in the iteration scheme. Note that a 4×4 subgrid actually involves solving for the field on almost all of a 9×9 interval subgrid scale grid.

In a similar manner to the numerical construction of the holistic models in $1D$, we follow the iteration scheme (8.28), to solve for updates to the subgrid field and its evolution at each of the discretised subgrid field points. §A.4.1 lists the REDUCE implementation of the algorithm. The code is very similar to the $1D$ implementation with the following notable points. The matrices `uu` and `ud`, storing the subgrid field and its updates are now two dimensional. The $2D$ RGL is applied at all interior points in lines 77–86 and the IBCs are applied across the top, bottom, left and right boundaries in lines 61–74. The extreme corner points of the subgrid field are not needed and are set to zero in lines 48–52.

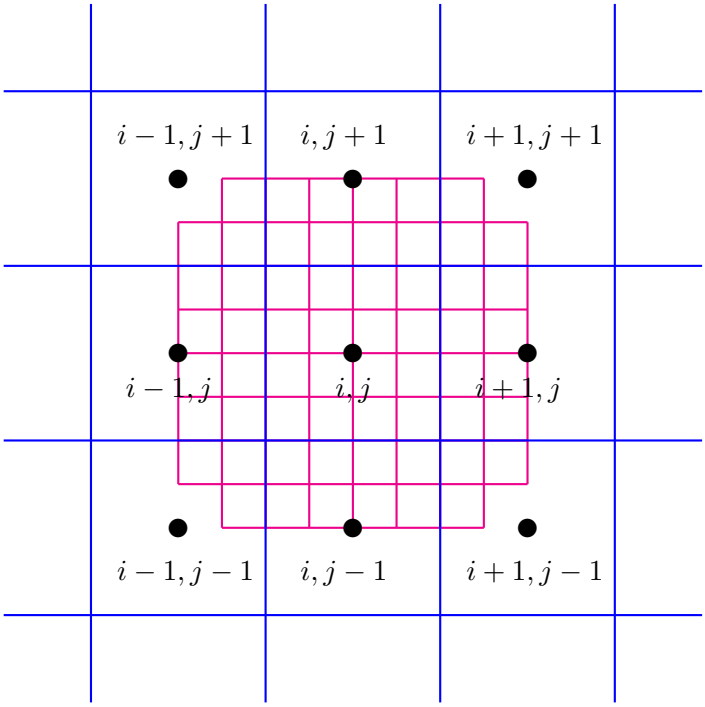

Figure 8.6: Example of the 4×4 interval subgrid in $2D$.

8.5.2 Low resolution subgrids are accurate in $2D$

For two spatial dimensions we cannot construct higher order holistic models analytically to provide a reference to measure the accuracy of the numerically constructed models. However, the $\mathcal{O}(\gamma^2, \alpha^2)$ holistic model of the RGL (7.1) in $2D$ is constructed analytically in §7.6. It provides a single reference case to compare the numerically constructed holistic models to an analytical model. Here we investigate the performance of the numerically constructed holistic models with subgrid resolutions of up to 8×8 subgrid intervals (285 subgrid values) by comparing bifurcation diagrams for $0 \leq \alpha \leq 30$.

Figure 8.3 shows the bifurcation diagrams for the $\mathcal{O}(\gamma^2, \alpha^2)$ holistic model of the RGL system with 8×8 macroscale elements on $[0, \pi] \times [0, \pi]$ for subgrid

resolutions of (a) 2×2, (b) 4×4, (c) 6×6 and (d) 8×8 intervals. In a similar manner to the investigation of §8.3 in $1D$, here the analytically constructed holistic model shown in green is not the accurate solution of the RGL system, but rather the analytically constructed $\mathcal{O}(\gamma^2, \alpha^2)$ holistic model in $2D$. Observe that with a subgrid resolution of just 4×4 intervals the bifurcation diagram for the numerically constructed $\mathcal{O}(\gamma^2, \alpha^2)$ holistic model is almost indiscernible from the analytic model.

Recall from §8.3 that for the numerically constructed $\mathcal{O}(\gamma^2, \alpha^2)$ holistic model in $1D$, a subgrid resolution of just 4 intervals was needed to accurately model the analytical holistic model for $0 \leq \alpha \leq 20$. Here a similar resolution of 4×4 intervals is needed in $2D$.

8.5.3 Higher order holistic models in $2D$

Here we consider the $\mathcal{O}(\gamma^3, \alpha^2)$ holistic model of the $2D$ RGL (7.1). This holistic model cannot be generated analytically. Thus we construct an approximation using a 6×6 and an 8×8 interval subgrid and apply the Richardson extrapolation procedure discussed in §8.2 to obtain the model to be explored. We examine the performance of this $\mathcal{O}(\gamma^3, \alpha^2)$ holistic model on a macroscale grid of 8×8 elements on $[0, \pi] \times [0, \pi]$ by comparing its bifurcation diagram to an accurate bifurcation diagram. We find improvement over the $\mathcal{O}(\gamma^2, \alpha^2)$ holistic model. The performance of the holistic models for the RGL system is not the emphasis of this section. Instead, it is presented here as a proof of concept that the holistic approach may be extended to PDEs of two spatial dimensions.

In deriving the $\mathcal{O}(\gamma^3, \alpha^2)$ model with an 8×8 interval subgrid there are

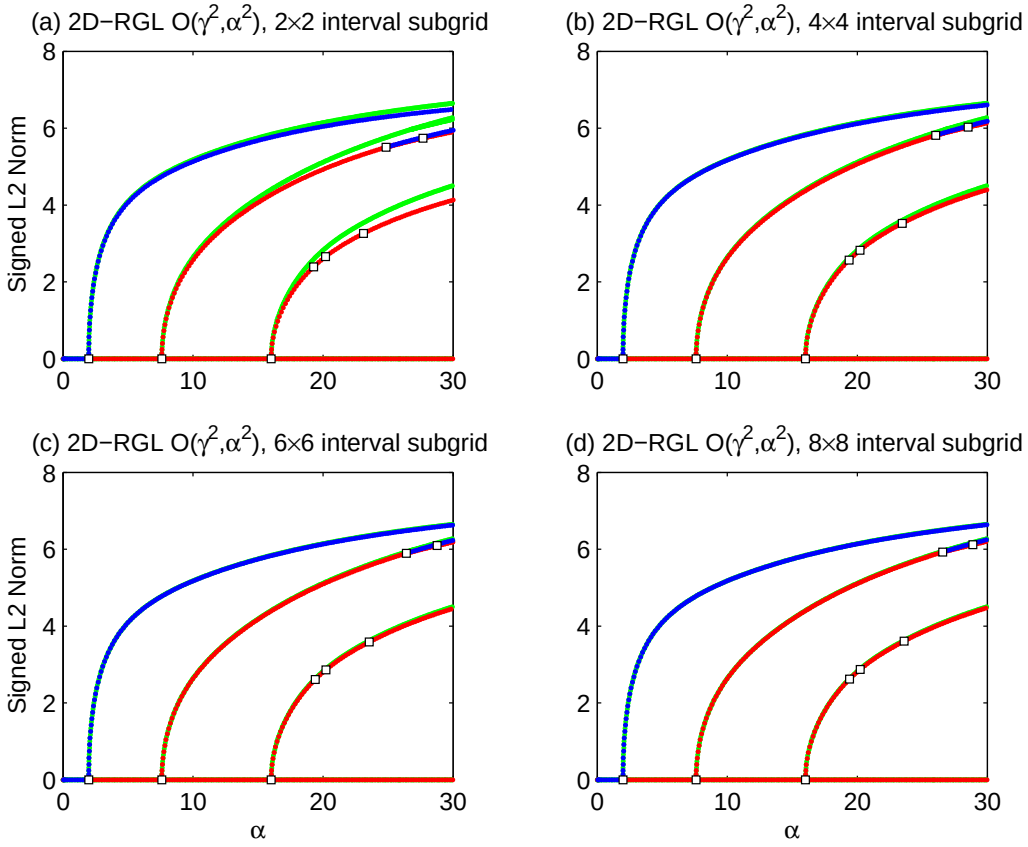

Figure 8.7: Bifurcation diagrams of the $O(\gamma^2, \alpha^2)$ holistic models of the $2D$ RGL system with 8×8 macroscale elements on $[0, \pi] \times [0, \pi]$ for subgrid resolutions of (a) 2×2, (b) 4×4, (c) 6×6 and (d) 8×8 intervals. The bifurcation diagram for the analytically constructed model is shown in green.

$(2 \times 8 + 1)^2 + 1 = 290$ equations with 290 unknowns to be solved for this second order system. The $\mathcal{O}(\gamma^3, \alpha^2)$ holistic model on the coarse grid is a 13 point stencil approximation; it involves the grid points $u_{i,j}$, $u_{i\pm1,j}$, $u_{i,j\pm1}$, $u_{i\pm2,j}$, $u_{i,j\pm2}$, and $u_{i\pm1,j\pm1}$.

Figure 8.8 shows a side by side comparison of the (a) $\mathcal{O}(\gamma^2, \alpha^2)$ holistic model constructed analytically and (b) $\mathcal{O}(\gamma^3, \alpha^2)$ holistic models constructed numerically with 8×8 macroscale elements on $[0, \pi] \times [0, \pi]$ for the $2D$ RGL. The accurate bifurcation diagram without stability information is shown in grey. Observe the improvement for the numerically constructed higher order $\mathcal{O}(\gamma^3, \alpha^2)$ holistic model over this range of α.

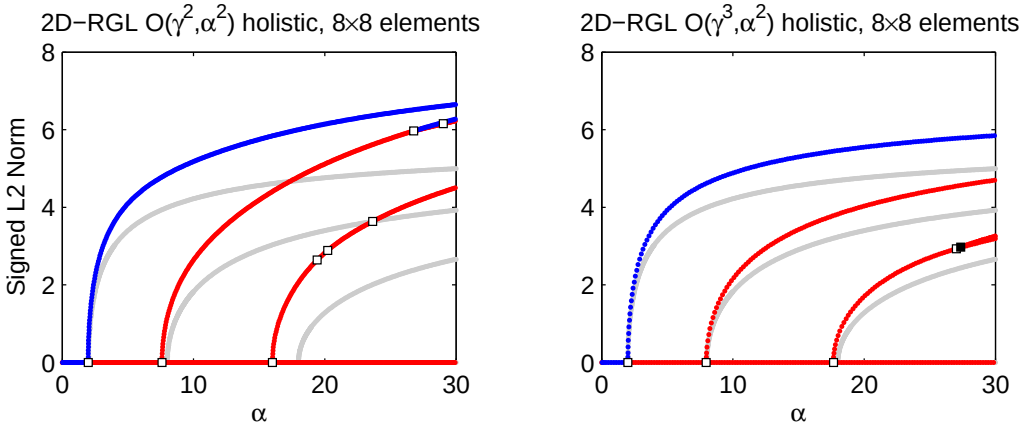

Figure 8.8: Bifurcation diagrams of the (a) $\mathcal{O}(\gamma^2, \alpha^2)$ and (b) $\mathcal{O}(\gamma^3, \alpha^2)$ holistic models of the $2D$ RGL system with 8×8 elements on $[0, \pi] \times [0, \pi]$. The accurate bifurcation diagram without stability information is shown in grey.

The improvement observed for the numerically constructed $\mathcal{O}(\gamma^3, \alpha^2)$ holistic model over the analytical $\mathcal{O}(\gamma^2, \alpha^2)$ holistic model in $2D$, shown in Figure 8.8 is similar to that seen for the corresponding holistic models of

the $1D$ RGL, investigated in §6.4.

8.6 Summary

We have explored an algorithm for the numerical construction of the subgrid field and the consequent macroscale model. This algorithm iterates with an entirely discrete linear operator to solve for updates to the subgrid field and the macroscale model using LU factorisation with a symbolic RHS. This is significant for developing holistic models in two or more spatial dimensions, since in general they cannot be constructed analytically, as discussed in §7.6. As a result of this work higher order holistic models in $2D$ may now be constructed as in the RGL example of §8.5.1.

Good results in 1D for the RGL (6.1) and Kuramoto–Sivashinsky (2.1) equation provide evidence that the numerically constructed holistic models are useful even when constructed on subgrids of fairly low resolution. By considering a macroscale grid of 8 elements on $[0, \pi]$ and comparing bifurcation diagrams in §8.3 we saw the $\mathcal{O}(\gamma^2, \alpha^2)$ holistic model of the RGL was accurately reproduced with just a 4 interval subgrid for $0 \leq \alpha \leq 20$. The $\mathcal{O}(\gamma^3, \alpha^2)$ holistic model of the Kuramoto–Sivashinsky equation was accurately reproduced for just 6 subgrid intervals on the same macroscale grid of 8 elements for $0 \leq \alpha \leq 70$. Similarly by comparing bifurcation diagrams for a macroscale grid of 8×8 elements on $[0, \pi] \times [0, \pi]$ for the $2D$ RGL (7.1), we observed the $\mathcal{O}(\gamma^2, \alpha^2)$ holistic model is accurately reproduced with just 4×4 subgrid intervals for $0 \leq \alpha \leq 30$. Evidently the numerical construction of the holistic models, even for low subgrid resolutions, can accurately reproduce the analytical holistic models.

Richardson extrapolation improves the order of accuracy of the numerical construction of the subgrid problem. Using Richardson extrapolation, a $\mathcal{O}(\gamma^3, \alpha^2)$ holistic model of the $2D$ RGL was constructed. In §8.5.3 we saw similar improvement for the $\mathcal{O}(\gamma^3, \alpha^2)$ holistic model over the $\mathcal{O}(\gamma^2, \alpha^2)$ model in $2D$ as was observed in $1D$ for the RGL §6.4 on coarse grids.

Extending the subgrid problem to $2D$ increases the computational difficulty for numerically constructing the subgrid field and the macroscale model. An 8×8 interval subgrid requires the solution of a mixed discrete and symbolic system of equation with 290 equations for second order systems.

We have not explored deeply the performance of holistic models $2D$ PDEs here. The good numerical results of Chapters 3 and 4 for the $1D$ Kuramoto–Sivashinsky equation suggest that holistic models of a $2D$ form of the Kuramoto–Sivashinsky equation could provide good support for the holistic approach to modelling complex time dependent behaviour in two spatial dimensions but is not considered in this dissertation. Primarily this chapter presents a proof of principle of the numerical construction of subgrid fields in holistic models.

Chapter 9

Conclusions

The holistic discretisation technique is a useful and accurate method for creating numerical discretisations of dynamical systems. In particular, I have extended the holistic technique to higher order systems such as the Kuramoto–Sivashinsky equation (2.1) (Chapter 2) and higher spatial dimensions (Chapters 5 and 7). The excellent performance of the holistic models on coarse grids for the Kuramoto–Sivashinsky equations (Chapters 3 and 4) provides evidence that the holistic technique is a useful method for creating numerical discretisations. I constructed a one-dimensional numerical model directly from the two-dimensional advection-diffusion model for shear dispersion in a channel (Chapters 5) that contains the shear dispersion term. I developed an algorithm for numerical construction of the subgrid field and its evolution (Chapter 8) which extends the application to discretising more general problems in higher spatial dimensions. The algorithm for numerical construction of the subgrid field makes the holistic models in three spatial dimensions possible. This is a vital step for the future application of the holistic technique generally for discretising the Navier–Stokes equations.

9.1 Summary of results

Holistic discretisation is extended to the fourth order Kuramoto–Sivashinsky equation (2.1) in §2.1–2.3. The holistic models are constructed with local (2.4–2.5) and non-local (2.4–2.5) forms of the IBCs. The holistic models listed in §2.3.2 are consistent with the Kuramoto–Sivashinsky equation shown in §2.5, confirming the dual justification property [46].

Excellent performance of the holistic models for reproducing steady states of the Kuramoto–Sivashinsky system is detailed in Chapter 3 by comparing bifurcation diagrams on coarse grids to the accurate solution. The holistic models constructed with non-local IBCs outperformed those constructed with the local IBCs in §3.4. The holistic models outperform traditional centered difference approximations of comparable stencil width in §3.4.3. The bifurcation diagrams of §3.4 show that more accuracy is gained by taking higher order holistic models in γ, the interelement coupling parameter than by taking higher order models in the nonlinearity α. The performance of the holistic models on coarse grids are compared to the approximate inertial manifold methods of [25] in §3.5. The $\mathcal{O}\left(\gamma^5, \alpha^2\right)$ holistic models perform well in comparison to these Galerkin approximations on a coarse grid of just 8 elements on $[0, \pi]$. In §3.6 we see the $\mathcal{O}\left(\gamma^5, \alpha^2\right)$ holistic model achieves similar accuracy to a second order centered difference approximation on a grid of roughly twice the resolution. This increased accuracy on a coarse grid allows larger time steps of approximately an order of magnitude greater for explicit time integration schemes.

Good performance for the holistic models for accurately reproducing the time dependent phenomena of the Kuramoto–Sivashinsky equation is de-

tailed in Chapter 4. The holistic models more accurately model the eigenvalues near the steady states of the Kuramoto–Sivashinsky system compared to explicit centered difference approximations of equal stencil widths as detailed in §4.1. The coarse grid holistic models also more accurately model the first Hopf bifurcation and the resulting period doubling sequence in §4.2. By comparing time averaged power spectrums we find that the $\mathcal{O}(\gamma^5, \alpha^2)$ holistic model achieves similar accuracy to the 2nd order and 6th order centered difference approximations on approximately $\frac{1}{3}$ and $\frac{3}{4}$ of the grid resolutions respectively. Again, this increased accuracy on coarse grids allow larger time steps for explicit time integration schemes.

Holistic discretisation provides a direct link between the two-dimensional advection-diffusion dynamics (5.1) for shear dispersion in a $2D$ channel and the one-dimensional numerical holistic model (5.15), without first deriving a $1D$ continuum model such as the Taylor model, detailed in Chapter 5. The shear dispersion term is calculated in the $\mathcal{O}(\gamma^3, \mathcal{P}^3)$ holistic model (5.15), listed in §5.4. The holistic technique also provides a natural incorporation of physical boundary conditions, detailed in §5.5 for symmetric Dirichlet and Neumann boundary conditions at the inlet and outlet. The $\mathcal{O}(\gamma^3, \mathcal{P}^3)$ holistic model for the evolution of grid values near the physical boundaries is listed in §5.5. Using the holistic technique to directly derive one-dimensional numerical models opens enormous possibilities: such as deriving numerical models of thin fluid film dynamics direct from the Navier-Stokes equations, and similarly for beam and shell models, and shallow water models.

The holistic method is applied to discretising the second order RGL (6.1) in Chapter 6. The RGL is an example of a reaction diffusion equation. The

performance of the holistic models of the RGL is explored by comparing bifurcation digrams on coarse grids to an accurate solution. The excellent performance of the holistic models on coarse grids seen for the Kuramoto–Sivashinsky equation was not found for the RGL in §6.4. However, improvement in performance for holistic models of higher orders in the inter-element coupling parameter γ was observed.

The holistic method is extended to PDEs of two spatial dimensions for discretising the $2D$ RGL (7.1) in Chapter 7. In particular, a natural extension of the non-local IBCs (6.4–6.5) is used. The $\mathcal{O}(\gamma^2, \alpha^2)$ holistic model is listed in §7.3.1 and is an extension of the $1D$ $\mathcal{O}(\gamma^2, \alpha^2)$ holistic model of the $1D$ RGL. The $\mathcal{O}(\gamma^2, \alpha^2)$ holistic model performs more poorly than an explicit second order centered difference approximation in §7.5. The $\mathcal{O}(\gamma^2, \alpha^2)$ holistic model in $2D$ is $\mathcal{O}(h^2)$ consistent as shown in §7.3.2, confirming that the dual justification property highlighted by Roberts [46] extends to $2D$ PDEs for this low order holistic model. While the excellent performance of the holistic models has not been observed for the RGL in either $1D$ or $2D$, it has served as a proof of principle for applying the holistic method to PDEs of two spatial dimensions.

I have detailed an algorithm for the numerical construction of the subgrid field and the subsequent macroscale model in Chapter 8. The algorithm iterates with a discrete linear operator to solve for updates to the subgrid field and the macroscale model using LU factorisation with a symbolic RHS. This is significant for developing holistic models in two or more spatial dimensions since in general they cannot be constructed analytically, as discussed in §7.6. As a result of this work, higher order holistic models in $2D$ may now be

constructed as in the RGL example of §8.5.1.

Good results in 1D for the RGL (6.1) and Kuramoto–Sivashinsky (2.1) equation provide evidence that the numerically constructed holistic models are useful even when constructed on subgrids of relatively low resolution. By considering a macroscale grid of 8 elements on $[0, \pi]$ in $1D$ and comparing bifurcation diagrams for the holistic models of the RGL and Kuramoto–Sivashinsky equation in §8.3 to the bifurcation diagrams for the analytical models, we find subgrid resolutions of 6 and 8 points give indiscernible differences over a large range of the nonlinearity parameter. Similarly for the $\mathcal{O}(\gamma^2, \alpha^2)$ holistic model of the $2D$ RGL, a subgrid resolution of just 8×8 points is sufficient to reproduce the bifurcation diagram of the analytic model. Evidently the numerical construction of the holistic models, even for low subgrid resolutions, accurately reproduces the analytical holistic models.

Richardson extrapolation improves the order of accuracy of the numerical construction of the subgrid problem, detailed in §8.2. Using Richardson extrapolation, an $\mathcal{O}(\gamma^3, \alpha^2)$ holistic model of the $2D$ RGL is constructed. Improvement in performance for the $\mathcal{O}(\gamma^3, \alpha^2)$ holistic model over the $\mathcal{O}(\gamma^2, \alpha^2)$ model in $2D$ is similar in §8.5.3 to the improvement in $1D$ for the RGL §6.4 on coarse grids. This demonstrates the improvement in accuracy gained by higher order holistic models in the inter-element coupling parameter extends to PDEs of two spatial dimensions.

9.2 Future directions

Chapters 5–8 of this dissertation are largely proof of principle that the holistic discretisation method can be extended to higher spatial dimensions. For a

complete three dimensional application of the holistic method for discretising dynamical systems of fluid flow and convection, the algorithm for numerical construction of the subgrid field detailed in Chapter 8 will play a vital role.

For shear dispersion in a $2D$ channel the numerical construction of the subgrid field allows holistic models for more general advection velocity and cross-channel diffusion profiles than specifically considered in Chapter 5. Non-symmetric inlet and outlet boundary conditions are also possible with the numerically constructed subgrid models. Numerical experiments for these cases should show advantages using the holistic technique to directly create the one dimensional numerical model.

Since the performance of the holistic models of the RGL reaction-diffusion equation in one and two spatial dimensions (Chapter 6 and 7) did not show the same excellent performance as the holistic models of the Kuramoto–Sivashinsky equation, it is possible that a different form of the IBCs may work better for this class of PDEs. Roberts and Kevrekidis [55] suggest using IBCs formulated in terms of the flux of the field u and it is possible that other formulations or modifications of these IBCs may give improved results for reaction-diffusion equations. The complex Ginzburg Landau CGL equation [31, 21, 8] exhibits more complex time-dependent behaviour and would be a good test case for the holistic technique for modelling the time-dependent phenomena of reaction-diffusion equations.

Improvements to the numerical algorithm presented in Chapter 8 are still required for a full application of the holistic method in three spatial dimensions. An iteration scheme employing iterative multigrid methods [38, 3] or incomplete LU factorisation and Krylov subspace methods [28, 64] should

give a more efficient solution. A parallel implementation of the algorithm in REDUCE would also be beneficial for three dimensional problems.

The performance of the holistic models of the Kuramoto–Sivashinsky equation seen in Chapters 3 and 4 suggest that that holistic models of the Kuramoto–Sivashinsky equation in two spatial dimensions may also exhibit excellent performance. The holistic method needs to be extended to the Kuramoto–Sivashinsky equation in $2D$. A two dimensional version of the IBCs (2.7–2.8) should be sufficient to construct the holistic models. However the computational task of creating the holistic models of the two dimensional Kuramoto–Sivashinsky equation will increase because to apply the IBCs the subgrid field must be extended not only to neighbouring elements, but also their neighbours as well .

The holistic method also needs to be extended to discretise the two-dimensional Navier-Stokes equations. The complexity of the Navier-Stokes in $2D$ is greater than the $2D$ RGL since the equations are coupled and the velocity and pressure components evolve in time. The algorithm for numerical construction of the subgrid field should assist in constructing holistic discretisations of the Navier-Stokes equations in two and ultimately three spatial dimensions.

Appendix A

REDUCE programs to construct holistic models

A.1 1D Analytical subgrid fields

A.1.1 Second order dissipative PDEs

```
1   %% Reduce code to generate holistic models of
2   %% second order PDEs. Higher order models are
3   %% constructed by changing the order of
4   %% neglected terms. Different PDEs are defined
5   %% by changing the nonlinear term nonlin.
6
7   %% Improve printing
8   on div; off allfac; on revpri;
9   factor gamma,h;
10
11  %% Make function of xi=(x-x_j)/h
12  depend xi,x; let df(xi,x)=>1/h;
13
14  operator uu;
15  depend uu,x;
16  discof:=1;
17  nonlin:=a*(uu-uu^3);
18  operator u;
```

```
19
20  %% Solvability condition
21  operator solg; linear solg;
22  let { solg(xi^~p,xi)=>(1+(-1)^p)/(p+2)/(p+1)
23      , solg(xi,xi)=>0, solg(1,xi)=>1 };
24
25  %% Define solving operator
26  operator solv; linear solv;
27  %% Solves v''=RHS s.t. v(0)=0 and v(+1)=v(-1)
28  let { solv(xi^~p,xi) =>
29            ( xi^(p+2)-(1-(-1)^p)*xi/2 )/(p+1)/(p+2)
30      , solv(xi,xi) => (xi^3-xi)/6
31      , solv(1,xi) => (xi^2)/2 };
32
33  %% Parametrise with evolving u(j)
34  depend u,t; let df(u(~k),t)=>sub(j=k,gj);
35
36  %% Linear solution in jth element
37  uu:=u(j)+udash;
38  udash:=0;
39  gj:=0;
40
41  %% Order of terms to neglect
42  let {gamma^2=>0,a^2=>0};
43
44  %% Iterate until residuals are zero
45  iteration:=0$
46  repeat begin
47     iteration:=iteration+1;
48     deq:=-df(uu,t)+discof*df(uu,x,2)+nonlin;
49     rbc:=-(sub(xi=+1,uu)-sub(xi=0,uu))
50        +gamma*(u(j+1)-u(j));
51     lbc:=-(sub(xi=0,uu)-sub(xi=-1,uu))
52        +gamma*(u(j)-u(j-1));
53     ok:= if (deq=0)and(rbc=0)and(lbc=0) then 1 else 0;
54     gd:=solg(deq,xi) +discof/h^2*(rbc-lbc);
55     gj:=gj+gd;
56     udash:=udash+h^2*solv(-deq+gd,xi)/discof
57        +xi/2*(rbc+lbc);
58  end until ok or(iteration>25);
```

A.1.2 Fourth order dissipative PDEs

```
%% Reduce code to generate holistic models of
%% fourth order PDEs. Higher order models are
%% constructed by changing the order of
%% neglected terms. Different PDEs are defined
%% by changing the nonlinear term nonlin.

%% Improve printing
on div; off allfac; on revpri;
factor gamma,h;

%% Make function of xi=(x-x_j)/h
depend xi,x; let df(xi,x)=>1/h;

operator uu;
depend uu,x;

dissipate:=df(uu,x,4);
discof:=-4;
nonlin:=-a*(uu*df(uu,x)+df(uu,x,2));

% Solvability condition
operator solg; linear solg;
let { solg(xi^~p,xi)=>(1+(-1)^p)/(p+2)/(p+1)
    , solg(xi,xi)=>0, solg(1,xi)=>1 };

% Define solving operator depending upon the dissipation
operator solv; linear solv;

% Solves v''''=RHS s.t. v(0)=v(+1)=v(-1)=0 and v(+2)=v(-2)
let { solv(xi^~p,xi) =>
          ( xi^(p+4)-(1+(-1)^p)/2*xi^2
             -(1-(-1)^p)/6*((2^(p+3)-1)*xi^3+(4-2^(p+3))*xi)
             )/(p+1)/(p+2)/(p+3)/(p+4)
    , solv(xi,xi) => (xi^5-(15*xi^3-12*xi)/3)/120
    , solv(1,xi) => (xi^4-xi^2)/24 };

% Parametrise with evolving uu(j)
operator u;
depend u,t;
```

```
let df(u(~k),t)=>sub(j=k,gj);

% Linear solution in jth element
uu:=u(j)+udash;
udash:=0;
gj:=0;

%% Order of terms to neglect
let {gamma^5=>0,a^2=>0};

%% Iterate until residuals are zero
iteration:=0$
repeat begin
   write iteration:=iteration+1;
   deq:=-df(uu,t)+discof*dissipate+nonlin;
   rbc:=-(sub(xi=+1,uu)-sub(xi=0,uu))+gamma*(u(j+1)-u(j));
   lbc:=-(sub(xi=0,uu)-sub(xi=-1,uu))+gamma*(u(j)-u(j-1));
   ok:= if (deq=0)and(rbc=0)and(lbc=0) then 1 else 0;
   rrbc:=-(sub(xi=+2,uu)-3*sub(xi=+1,uu)
            +3*sub(xi=0,uu)-sub(xi=-1,uu))
            +gamma^2*(u(j+2)-3*u(j+1)+3*u(j)-u(j-1));
   llbc:=-(sub(xi=+1,uu)-3*sub(xi=0,uu)
            +3*sub(xi=-1,uu)-sub(xi=-2,uu))
            +gamma^2*(u(j+1)-3*u(j)+3*u(j-1)-u(j-2));
   ok:=if ok and(rrbc=0)and(llbc=0) then 1 else 0;
   gd:=solg(deq,xi) +discof/h^4*(rrbc-llbc);
   gj:=gj+gd;
   udash:=udash+h^4*solv(-deq+gd,xi)/discof
      +xi/2*(rbc+lbc)+xi^2/2*(rbc-lbc)
      -(xi-xi^3)/12*(rrbc+llbc);
   showtime;
end until ok or(iteration>25);
```

A.2 2D Analytical subgrid fields

A.2.1 Second order dissipative PDEs

```
%% Reduce code to generate holistic models of
%% second order PDEs in 2D. Higher order models are
%% constructed by changing the order of
```

```
4   %% neglected terms. Different PDEs are defined
5   %% by changing the nonlinear term nonlin.
6
7   %% Improve printing
8   on div; off allfac; on revpri;
9   factor gam,h,x,y;
10
11  operator u;
12  operator cc;
13
14  %% Make function of xi=(x-x_j)/h and yi
15  depend xi,x;
16  let df(xi,x)=>1/h;
17  depend yi,y;
18  let df(yi,y)=>1/h;
19
20
21  %% Parametrise with evolving u(i,j)
22  depend u,t;
23  let df(u(~k,~m),t)=>sub(i=k,j=m,g);
24
25  %% Linear solution in i,jth element
26  v:=u(i,j);
27  g:=0;
28
29  %% Order of terms to neglect
30  let {gam^2=>0, a^2=>0};
31
32  %% Construct multinomical for method of
33  %% undetermined coefficients
34  o:=6;
35  vv:=for m:=0:o sum for n:=0:o-m sum cc(m,n)*xi^m*yi^n$
36  cs:=for m:=0:o join for n:=0:o-m collect cc(m,n)$
37  operator ugh;
38  linear ugh;
39  depend xi,xy;
40  depend yi,xy;
41  let ugh(xi^~m*yi^~n,xy)=>z^(n-2+(m+n-4)*(m+n-3)/2);
42
43  %% Iterate until residuals are zero
44  it:=0;
```

```
repeat begin
   write it:=it+1;
   %% PDE residual
   de:=df(v,t)-df(v,x,2)-df(v,y,2)-a*(v-v^3);
   %% IBC residuals
   bcr:=sub(xi=1,v)-sub(xi=0,v)
      -gam*(sub({xi=0,i=i+1},v)-sub(xi=0,v));
   bcl:=sub(xi=-1,v)-sub(xi=0,v)
      -gam*(sub({xi=0,i=i-1},v)-sub(xi=0,v));
   bct:=sub(yi=1,v)-sub(yi=0,v)
      -gam*(sub({yi=0,j=j+1},v)-sub(yi=0,v));
   bcb:=sub(yi=-1,v)-sub(yi=0,v)
      -gam*(sub({yi=0,j=j-1},v)-sub(yi=0,v));
   %% Create equations in terms of the multinomial vv
   deq:=de+gd-df(vv,x,2)-df(vv,y,2);
   rbcr:=bcr+sub(xi=1,vv)-sub(xi=0,vv);
   lbcl:=bcl+sub(xi=-1,vv)-sub(xi=0,vv);
   tbct:=bct+sub(yi=1,vv)-sub(yi=0,vv);
   bbcb:=bcb+sub(yi=-1,vv)-sub(yi=0,vv);
   %% Check if residuals are all 0
   ok:=if (de=0)and(bcr=0)and(bcl=0)and(bct=0)and(bcb=0)
      then 1 else 0;
   %% Update subgrid field and evolution
   eqns:=ugh(xi^2*yi^2*deq,xy);
   eqns:=append(coeff(eqns,z),cc(0,0).
      append(coeff(rbcr,yi),append(coeff(lbcl,yi),
      append(coeff(tbct,xi),coeff(bbcb,xi)))));
   sol:=solve(eqns,gd.cs);
   sol:=(sol where arbcomplex(~p)=>0);
   v:=v+sub(sol,vv);
   g:=g+sub(sol,gd);
end until ok or(it>25);

write g:=sub({gam=1},g);
```

A.2.2 Shear dispersion in a 2D channel

```
%% Reduce code to generate holistic models of
%% shear dispersionn in a 2D channel. Higher order models
%% are constructed by changing the order of neglected terms.
%% Dirichlet boundary condition defined by setting
```

```
5   %% dirichlet=1.
6   %% Neumann boudary condition defined by setting
7   %% midpoint=1.
8
9   %% Improve printing
10  on div; off allfac; on revpri; factor gam,h,xi,y,p;
11
12  dirichlet:=0;
13  midpoint:=1;
14
15  % Order of polynomials for subgrid field.
16  o:=10;
17
18  %% Make function of xi=(x-x_j)/h
19  depend xi,x;
20  let df(xi,x)=>1/h;
21
22  % Number grid points near the boundaries affected by
23  % the inlet and outlet boundary conditions
24  oo:=2;
25
26  % Parametrise with evolving u(j)
27  operator u;
28  depend u,t;
29  let {df(u(~k),t)=>sub(j=k,gj) when
30                      (not fixp(k))or(fixp(k) and k>oo)
31         ,df(u(~k),t)=>g(k) when fixp(k) and k<=oo and k>0};
32
33  operator a;
34  depend a,t;
35
36  let df(a(~p),t)=>a(p+1);
37
38  % Arrays for BC near the boundaries
39  array g(oo),v(oo),vo(oo),soln(oo);
40
41  % Linear solution in jth element
42  vj:=u(j);
43  gj:=0;
44  for j:=1:oo do v(j):=u(j);
45
```

```
% Solve using method of undetermined coefficients
operator c;
vd:=for m:=0:o sum for n:=0:o-m sum c(m,n)*xi^m*y^n$
cs:=for m:=0:o join for n:=0:o-m collect c(m,n)$
operator ugh;
linear ugh;
depend xi,xy;
depend y,xy;
let ugh(xi^^m*y^^n,xy)=>z^(n-2+(m+n-4)*(m+n-3)/2);

% Choice of advection and diffusion profile for
% analytical solution
ka:=(1-y^2);
uu:=p*3/2*(1-y^2);

% Order of terms to neglect
let {gam^3=>0,p^3=>0,a(1)=>0};

%% Iterate until residuals are zero
it:=0;
repeat begin
   write it:=it+1;
   if it=1 then let ma^2=>0 else
   if it=2 then let ma^3=>0 else
   if it=3 then let ma^4=>0 else
   if it=4 then let ma^5=>0 else
   if it=5 then let ma^6=>0 else
   if it=6 then let ma^7=>0 else
   if it=7 then let ma^8=>0 else
   if it=8 then let ma^9=>0;
   de:=-df(vj,t)-ma*uu*df(vj,x)+ka*df(vj,x,2)
      +df(ka*df(vj,y),y);
   rb:=-(sub(xi=+1,vj)-sub(xi=0,vj))
      +gam*ma*(sub({xi=0,j=j+1},vj)-sub(xi=0,vj));
   lb:=-(sub(xi=0,vj)-sub(xi=-1,vj))
      +gam*ma*(sub(xi=0,vj)-sub({xi=0,j=j-1},vj));
   ok:=if(de=0)and(rbj=0)and(lb=0)then 1 else 0;
   deq:=de-gd+ka*df(vd,x,2)+df(ka*df(vd,y),y);
   rbc:=rb-(sub(xi=+1,vd)-sub(xi=0,vd));
   lbc:=lb-(sub(xi=0,vd)-sub(xi=-1,vd));
   eqns:=ugh(xi^2*y^2*deq,xy);
```

```
87      eqns:=append(coeff(eqns,z),
88         c(0,0).append(coeff(rbc,y),coeff(lbc,y)));
89      solnj:=solve(eqns,gd.cs);
90      solnj:=(solnj where arbcomplex(~p)=>0);
91      ok:=if (de=0)and(rb=0)and(lb=0) then 1 else 0;
92      for jj:=1:oo do begin
93         de:=-df(v(jj),t)-ma*uu*df(v(jj),x)+ka*df(v(jj),x,2)
94            +df(ka*df(v(jj),y),y);
95         rb:=-(sub(xi=+1,v(jj))-sub(xi=0,v(jj)))+gam*ma*(
96         sub(xi=0,if jj<oo then v(jj+1) else
97            sub(j=oo+1,vj))-sub(xi=0,v(jj)));
98         if jj>1 then
99            lb:=-(sub(xi=0,v(jj))-sub(xi=-1,v(jj)))
100              +gam*ma*(sub(xi=0,v(jj))-sub(xi=0,v(jj-1)))
101        else if dirichlet then
102           lb:=-(sub(xi=0,v(1))-sub(xi=-1,v(1)))
103              +gam*ma*(sub(xi=0,v(1))-a(0))
104        else if midpoint then
105           lb:=-sub(xi=-1/2,h*df(v(1),x))+gam*ma*a(0)
106        else begin
107           ab:=-sub(xi=0,h*df(v(1),x))+gam*ma*a(0);
108           lb:=2*ab-rb;
109        end;
110        deq:=de-gd+ka*df(vd,x,2)+df(ka*df(vd,y),y);
111        rbc:=rb-(sub(xi=+1,vd)-sub(xi=0,vd));
112        lbc:=lb-(if (jj>1)or(dirichlet) then
113              (sub(xi=0,vd)-sub(xi=-1,vd))
114           else if midpoint then sub(xi=-1/2,h*df(vd,x))
115           else sub(xi=0,2*h*df(vd,x))
116              -(sub(xi=1,vd)-sub(xi=0,vd)));
117        eqns:=ugh(xi^2*y^2*deq,xy);
118        eqns:=append(coeff(eqns,z),
119           c(0,0).append(coeff(rbc,y),coeff(lbc,y)));
120        soln(jj):=solve(eqns,gd.cs);
121        soln(jj):=(soln(jj) where arbcomplex(~p)=>0);
122        ok:=if(de=0)and(rb=0)and(lb=0) then ok else 0;
123     end;
124     for jj:=1:oo do begin
125        v(jj):=v(jj)+sub(soln(jj),vd);
126        g(jj):=g(jj)+sub(soln(jj),gd);
127     end;
```

```
128      vj:=vj+sub(solnj,vd);
129      gj:=gj+sub(solnj,gd);
130      showtime;
131   end until ok or(length(solnj)=0);
132
133   % Write evolution of grid points
134   ma:=1;
135   write g(1):=sub(gam=1,g(1));
136   write g(2):=sub(gam=1,g(2));
137   write ggj:=sub(gam=1,gj);
```

A.3 1D Numerical subgrid fields

A.3.1 Second order dissipative PDEs

```
1   %% Holistic models of 2nd ord PDEs with numerical
2   %% construction of the subgrid field. This program
3   %% requires LU decomposition routines lu_decomp, lu_backsub.
4
5   on roundbf; on div; off allfac; on revpri; factor h;
6
7   %% Routines for eqn solve with LU decomp
8   in lu_decomp$ in lu_backsub$
9
10  %% Subgrid resolution defined by n
11  n:=8$ dx:=h/n$ nn:=2*n+2$
12
13  %% Matrix declarations (Matrix scope is global in REDUCE)
14  matrix eqns(nn,1);
15  matrix indx(nn,1);
16  matrix vv(nn,1);
17  matrix lu(nn,nn);
18  matrix uu(nn-1,1)$
19
20  %% Parametrise with evolving u(j)
21  operator u; depend u,t;
22  g:=0$
23  let df(u(~k),t)=>sub(j=k,(g+gd)/h^2);
24
25  %% Setup initial subgrid field uu
```

```
26  operator ud;
27  matrix vd(nn-1,1)$
28  for ii:=1:nn-1 do uu(ii,1):=u(j)$
29  for ii:=1:nn-1 do vd(ii,1):=ud(ii)$
30  uu:=uu+vd$
31
32  %% Pattern matching. Ignores higher order terms
33  let { gam^2=>0, ud(~j)*gam=>0, a^2=>0, a*ud(~j)=>0 };
34  iter:=0$
35  showtime;
36  %% Loop for to find updates to uu and g
37  repeat begin
38     iter:=iter+1;
39     uur:=sub(j=j+1,uu);
40     uul:=sub(j=j-1,uu);
41
42     %% amplitude condition
43     if iter=1 then eqns(1,1):=ud(nn/2) else eqns(1,1):=0$
44
45     %% boundary conditions
46     eqns(2,1):=uu(2*n+1,1)-uu(n+1,1)
47        -gam*(uur(n+1,1)-uu(n+1,1));
48     eqns(3,1):=uu(1,1)-uu(n+1,1)
49        -gam*(uul(n+1,1)-uu(n+1,1));
50
51     %% interior equations
52     for ii:=2:nn-2 do begin
53        eqns((2+ii),1):=h^2*(-df(uu(ii,1),t)
54           +(uu(ii+1,1)+uu(ii-1,1)-2*uu(ii,1))/(dx^2)
55           %% This is the nonlinear term for the PDE
56           +(a*uu(ii,1)-a*uu(ii,1)^3));
57     end;
58
59     %% Setup linear problem for first iteration
60     if iter=1 then begin
61        for ii:=1:nn do begin
62           temp:=coeff((-eqns(ii,1)+art*xx^nn where {ud(~k)=>
63              xx^k, gd=>xx^nn,u(~k)=>0 }),xx);
64           for jj:=1:nn do begin
65              lu(ii,jj):=part(temp,jj+1);
66           end;
```

```
67          end;
68          lu:=(lu where art=>0);
69          lu_decomp();
70          eqns:=(eqns where ud(~k)=>0);
71          gd:=0;
72          uu:=(uu where ud(~k)=>0);
73       end;
74
75       %% Check if all residuals are 0
76       iter_flag:=1;
77       for i:=1:nn do if not(eqns(i,1)=0) then iter_flag:=0;
78
79       %% LU back solve and update g and uu
80       lu_backsub();
81       g:=g+eqns(nn,1);
82       for ii:=1:(nn-1) do uu(ii,1):=uu(ii,1)+eqns(ii,1);
83    end until iter_flag;
84    showtime;
85    gam:=1;
86    gj:=g/h^2;
```

A.3.2 Fourth order dissipative PDEs

```
1   %% Holistic models of 4th ord PDEs with numerical
2   %% construction of the subgrid field. This program
3   %% requires LU decomposition routines lu_decomp, lu_backsub.
4
5   on roundbf; on div; off allfac; on revpri; factor h;
6
7   %% Routines for eqn solve with LU decomp
8   in lu_decomp$ in lu_backsub$
9
10  %% Subgrid resolution defined by n
11  n:=8$ dx:=h/n$ nn:=4*n+2$
12
13  %% Matrix declarations (Matrix scope is global in REDUCE)
14  matrix eqns(nn,1);
15  matrix indx(nn,1);
16  matrix vv(nn,1);
17  matrix lu(nn,nn);
18  matrix uu(nn-1,1)$
```

```
19
20  %% Parametrise with evolving u(j)
21  operator u; depend u,t;
22  g:=0$
23  let df(u(~k),t)=>sub(j=k,(g+gd)/h^4);
24
25  %% Setup initial subgrid field uu
26  operator ud;
27  matrix vd(nn-1,1)$
28  for ii:=1:nn-1 do uu(ii,1):=u(j)$
29  for ii:=1:nn-1 do vd(ii,1):=ud(ii)$
30  uu:=uu+vd$
31
32  %% Pattern matching. Ignores higher order terms
33  let { gam^3=>0, ud(~j)*gam=>0, a^2=>0, a*ud(~j)=>0 };
34  iter:=0$
35
36  %% Loop for to find updates to uu and g
37  repeat begin
38     iter:=iter+1;
39     uur:=sub(j=j+1,uu);
40     uul:=sub(j=j-1,uu);
41     uurr:=sub(j=j+2,uu);
42     uull:=sub(j=j-2,uu);
43
44     %% amplitude condition
45     if iter=1 then eqns(1,1):=ud(nn/2) else eqns(1,1):=0$
46
47     %% boundary conditions
48     eqns(2,1):=uu(3*n+1,1)-uu(2*n+1,1)
49        -gam*(uur(2*n+1,1)-uu(2*n+1,1));
50     eqns(3,1):=uu(n+1,1)-uu(2*n+1,1)
51        -gam*(uul(2*n+1,1)-uu(2*n+1,1));
52     eqns(4,1):=uu(4*n+1,1)-3*uu(3*n+1,1)
53        +3*uu(2*n+1,1)-uu(n+1,1)
54        -gam^2*(uurr(2*n+1,1)-3*uur(2*n+1,1)
55           +3*uu(2*n+1,1)-uul(2*n+1,1));
56     eqns(5,1):=uu(3*n+1,1)-3*uu(2*n+1,1)
57        +3*uu(n+1,1)-uu(1,1)
58        -gam^2*(uur(2*n+1,1)-3*uu(2*n+1,1)
59           +3*uul(2*n+1,1)-uull(2*n+1,1));
```

```
60
61      %% interior equations
62      for ii:=3:nn-3 do begin
63         eqns((3+ii),1):=h^4*(-df(uu(ii,1),t)
64            -4*(uu(ii+2,1)-4*uu(ii+1,1)+6*uu(ii,1)
65               -4*uu(ii-1,1)+uu(ii-2,1))/(dx^4)
66            -a*(uu(ii+1,1)-2*uu(ii,1)+uu(ii-1,1))/(dx^2)
67            -a*uu(ii,1)*(uu(ii+1,1)-uu(ii-1,1))/(2*dx)
68         );
69      end;
70
71      %% Setup linear problem for first iteration
72      if iter=1 then begin
73         for ii:=1:nn do begin
74            temp:=coeff((-eqns(ii,1)+art*xx^nn where {ud(~k)=>
75               xx^k, gd=>xx^nn,u(~k)=>0}),xx);
76            for jj:=1:nn do begin
77               lu(ii,jj):=part(temp,jj+1);
78            end;
79         end;
80         lu:=(lu where art=>0);
81         lu_decomp();
82         eqns:=(eqns where ud(~k)=>0);
83         gd:=0;
84         uu:=(uu where ud(~k)=>0);
85      end;
86
87      %% Check if all residuals are 0
88      iter_flag:=1;
89      for i:=1:nn do if not(eqns(i,1)=0) then iter_flag:=0;
90
91      %% LU back solve and update g and uu
92      lu_backsub();
93      g:=g+eqns(nn,1);
94      for ii:=1:(nn-1) do uu(ii,1):=uu(ii,1)+eqns(ii,1);
95   end until iter_flag;
96   gam:=1;
97   gj:=g/h^4;
```

A.3.3 MATHEMATICA code for second order PDEs

```
(** Holistic models of 2nd ord PDEs with numerical
construction of the subgrid field. **)

(** subgrid resolution **)
n=8;
NN=2*n+2;
ClearAll[i,zd,g,vd,uu,LL,Linv,eqns];
dx=h/n;

(** Define Replacement Rules. Ignore higher order terms **)
ClearAll[gam,a];
gam^n_ ^:=0 /; n> 1;
a^n_ ^:=0 /; n> 1;
gam*ud[i_] ^:=0;
a*ud[i_] ^:=0 ;
ud[i_] ^n_^:=0;
u/:D[u[m_],t,NonConstants->{u}]:= (((g/.{i->m})+zd)/h^2);

(** Setup matrices **)
uu=u[i]*Table[1,{i,(2*n+1)},{j,1}];
vd=Table[ud[i],{i,(2*n+1)},{j,1}];
eqns=Table[0,{i,NN},{j,1}];
uu=uu+vd;
g=0;
iterflag=0;
iter=0;

While[iterflag!=1,
   iter=iter+1;
   uur=uu/.{i->(i+1)};
   uul=uu/.{i->(i-1)};

   (** Amplitude condition **)
   If[iter==1 , eqns[[1,1]]=ud[NN/2],eqns[[1,1]]=0];

   (** Boundary conditions **)
   eqns[[2,1]]=Expand[uu[[2*n+1,1]]-uu[[n+1,1]]
      -gam*(uur[[n+1,1]]-uu[[n+1,1]])];
   eqns[[3,1]]=Expand[uu[[1,1]]-uu[[n+1,1]]
```

```
40          -gam*(uul[[n+1,1]]-uu[[n+1,1]])];
41
42       (** Interior equations **)
43       Do[eqns[[k+2,1]]=
44          Expand[h^2*(-D[uu[[k,1]],t,NonConstants->{u}]
45             +(uu[[k+1,1]]+uu[[k-1,1]]-2*uu[[k,1]])/(dx^2))
46             +a*h^2*(uu[[k,1]]-uu[[k,1]]^3)],
47             {k,2,NN-2}];
48       eqns=Chop[eqns];
49
50       (** Setup linear problem for first iteration **)
51       If[iter==1,
52          LL={};
53          For[ii=1,ii<(NN+1),ii++,
54             tt=-eqns[[ii,1]]/.{ud[i_]->X^i,zd->X^NN,u[i_]->0};
55             LL=Append[ LL,Take[CoefficientList[tt+aa*X^NN,X]
56                /.aa->0,-NN]];
57          ];
58          Linv=Chop[Inverse[N[LL,16]]];
59          eqns=eqns/.{ud[i_]->0};
60          uu=uu/.{ud[i_]->0};
61          zd=0;
62       ];
63
64       (** Solve for update **)
65       eqns=Chop[Expand[Linv.N[eqns,16]]];
66       g=g+eqns[[NN,1]];
67       uu=uu+Transpose[Chop[Expand[Partition[Flatten[
68          Take[eqns,(NN-1)]],NN-1]]]];
69
70       (** Check if residuals are all 0 **)
71       iterflag=1;
72       For[ii=1,ii<(NN+1),ii++,
73          If[N[eqns[[ii,1]],16]=!=0,
74             iterflag=0;
75             ii=NN+1;
76          ];
77       ];
78    ];
79    Expand[g/(h^2)/.gam->1]
```

A.4 2D Numerical subgrid fields

A.4.1 Second order dissipative PDEs

```
%% Holistic models of 2nd ord PDEs in 2D with numerical
%% construction of the subgrid field. This program
%% requires LU decomposition routines lu_decomp, lu_backsub.

on roundbf; on div; off allfac; on revpri; factor h;

%% Routines for eqn solve with LU decomp
in lu_decomp$ in lu_backsub$

%% Subgrid resolution defined by n
n:=4$ dx:=h/n$
nn:=(2*n+1)^2+1$

%% Matrix declarations (Matrix scope is global in REDUCE)
matrix eqns(nn,1);
matrix indx(nn,1);
matrix vv(nn,1);
matrix lu(nn,nn);
matrix uu(2*n+1,2*n+1)$

%% Parametrise with evolving u(j)
operator u;
depend u,t;
g:=0$
let df(u(~k,~m),t)=>sub({i=k,j=m},(g+gd)/h^2);

%% Setup initial subgrid field uu
operator ud;
matrix vd(2*n+1,2*n+1)$
for ii:=1:(2*n+1) do for jj:=1:(2*n+1)
   do uu(ii,jj):=u(i,j)$
for ii:=1:(2*n+1) do for jj:=1:(2*n+1)
   do vd(ii,jj):=ud(ii,jj)$
uu:=uu+vd$

% Pattern matching. Ignores higher order terms
let { gam^2=>0, ud(~i,~j)*gam=>0, a^2=>0, a*ud(~i,~j)=>0 };
```

```
iter:=0;

%% Loop for to find updates to uu and g
repeat begin
   iter:=iter+1;

   % Amplitude condition
   if iter=1 then eqns(1,1):=ud(n+1,n+1) else eqns(1,1):=0;

   % Corner conditions
   if iter=1 then
   << eqns(2,1):=ud(1,1); eqns(3,1):=ud(1,2*n+1);
   eqns(4,1):=ud(2*n+1,1); eqns(5,1):=ud(2*n+1,2*n+1) >>
   else << eqns(2,1):=0; eqns(3,1):=0;
   eqns(4,1):=0; eqns(5,1):=0 >>;

   uur:=sub(i=i+1,uu);
   uul:=sub(i=i-1,uu);
   uut:=sub(j=j+1,uu);
   uub:=sub(j=j-1,uu);
   eq_count:=6;

   %% Boundary conditions
   for ll:=2:(2*n) do begin
      eqns(eq_count,1):=uu(2*n+1,ll)-uu(n+1,ll)
         -gam*(uur(n+1,ll)-uu(n+1,ll));
      eq_count:=eq_count+1;
      eqns(eq_count,1):=uu(1,ll)-uu(n+1,ll)
         -gam*(uul(n+1,ll)-uu(n+1,ll));
      eq_count:=eq_count+1;
      eqns(eq_count,1):=uu(ll,2*n+1)-uu(ll,n+1)
         -gam*(uut(ll,n+1)-uu(ll,n+1));
      eq_count:=eq_count+1;
      eqns(eq_count,1):=uu(ll,1)-uu(ll,n+1)
         -gam*(uub(ll,n+1)-uu(ll,n+1));
      eq_count:=eq_count+1;
   end;

   %% Interior equations
   for ii:=2:(2*n) do begin
      for jj:=2:(2*n) do begin
```

```
79            eqns(eq_count,1):=h^2*(df(uu(ii,jj),t)
80               -(uu(ii+1,jj)+uu(ii-1,jj)+uu(ii,jj+1)
81               +uu(ii,jj-1)-4*uu(ii,jj))/(dx^2)
82               %% Nonlinear term
83               -a*uu(ii,jj)+a*uu(ii,jj)^3);
84               eq_count:=eq_count+1;
85         end;
86      end;
87
88      %% Setup linear problem for first iteration
89      if iter=1 then begin
90         for ii:=1:nn do begin
91            temp:=coeff((-eqns(ii,1)+art*xx^nn where
92               {ud(~k,~m)=>xx^(k+(m-1)*(2*n+1)),
93               gd=>xx^nn,u(~k,~m)=>0}),xx);
94            for jj:=1:nn do begin
95               lu(ii,jj):=part(temp,jj+1);
96            end;
97         end;
98         lu:=(lu where art=>0);
99         lu_decomp();
100        eqns:=(eqns where {ud(~i,~j)=>0});
101        gd:=0;
102        uu:=(uu where ud(~i,~j)=>0);
103     end;
104
105     % Check if all residuals are 0
106     iter_flag:=1;
107     for ii:=1:nn do if not(eqns(ii,1)=0) then iter_flag:=0;
108
109     % lu back solve and update g and v
110     lu_backsub();
111     g:=g+eqns(nn,1);
112     for ii:=1:(2*n+1) do begin
113        for jj:=1:(2*n+1) do begin
114           uu(ii,jj):=uu(ii,jj)+eqns((jj-1)*(2*n+1)+ii,1);
115        end;
116     end;
117
118  end until iter_flag;
119
```

```
120  factor h;
121  write sub(gam=1,g/h^2);
```

A.5 LU factorisation routines

```
1   %% LU decomposition (Numerical recipes in Fortran 77).
2   %% Requires lu(n,1), indx(n,1) and vv(n,1) to be predefined.
3   %% Matrices are global in scope in REDUCE.
4
5   procedure lu_decomp;
6   begin scalar n,np,i,j,k,imax,dd,aamax,dum,sum,tiny;
7      tiny:=1.0e-20;
8      n:=first(length(lu));
9      dd:=1;
10     for i:=1:n do begin
11        aamax:=0;
12        for j:=1:n do begin
13           if(abs(lu(i,j))>aamax) then aamax:=abs(lu(i,j));
14        end;
15        vv(i,1):=1/aamax;
16     end;
17     for j:=1:n do begin
18        for i:=1:(j-1) do begin
19           sum:=lu(i,j);
20           for k:=1:(i-1) do sum:=sum-lu(i,k)*lu(k,j);
21           lu(i,j):=sum;
22        end;
23        aamax:=0;
24        for i:=j:n do begin
25           sum:=lu(i,j);
26           for k:=1:(j-1) do sum:=sum-lu(i,k)*lu(k,j);
27           lu(i,j):=sum;
28           dum:=vv(i,1)*abs(sum);
29           if dum>=aamax then begin
30              imax:=i;
31              aamax:=dum;
32           end;
33        end;
34        if not(j=imax) then begin
35           for k:=1:n do begin
```

```
36              dum:=lu(imax,k);
37              lu(imax,k):=lu(j,k);
38              lu(j,k):=dum;
39           end;
40           dd:=-dd;
41           vv(imax,1):=vv(j,1);
42        end;
43        indx(j,1):=imax;
44        if lu(j,j)=0 then lu(j,j):=tiny;
45        if not(j=n) then begin
46           dum:=1/lu(j,j);
47           for i:=(j+1):n do lu(i,j):=lu(i,j)*dum;
48        end;
49     end;
50  end;
```

```
1   %% LU back substitution (Numerical recipes in Fortran 77).
2   %% Requires lu(n,1), indx(n,1) and eqns(n,1) to be
3   %% predefined and lu and indx must be allocated by
4   %% lu_decomp. Matrices are global in scope in REDUCE.
5
6   procedure lu_backsub;
7   begin scalar n,i,j,ii,ll,sum;
8      n:=first(length(lu));
9      ii:=0;
10     for i:=1:n do begin
11        ll:=indx(i,1);
12        sum:=eqns(ll,1);
13        eqns(ll,1):=eqns(i,1);
14        if not(ii=0) then
15        << for j:=ii:(i-1) do sum:=sum-lu(i,j)*eqns(j,1) >>
16        else if   not(sum=0) then ii:=i;
17        eqns(i,1):=sum;
18     end;
19     for i:=n step -1 until 1 do begin
20     sum:=eqns(i,1);
21        for j:=(i+1):n do begin
22           sum:=sum-lu(i,j)*eqns(j,1);
23        end;
24        eqns(i,1):=sum/lu(i,i);
25     end;
```

```
26    end;
```

Bibliography

[1] D. Armbruster, J. Guckenheimer, and P. Holmes. Kuramoto sivashinsky dynamics on the centre-unstable manifold. *Siam J Appl Math*, 49:676–691, 1989.

[2] G. Berkooz, P. Holmes, and J.L. Lumley. On the relation between low dimensional models and the dynamics of coherent structures in the turbulent wall layer. *Theoret. Comput. Fluid Dynamics*, 4:255–269, 1993.

[3] W.L. Brigg, V.E. Hanson, and S.F. McCormick. *A multigrid tutorial*. Society for Industrial and Applied Mathematics (SIAM), Philadelphia, 2000.

[4] J. Carr. *Applications of centre manifold theory*, volume 35 of *Applied Math Sci*. Springer-Verlag, 1981.

[5] J. Carr and R.G. Muncaster. The application of centre manifold theory to amplitude expansions. II. infinite dimensional problems. *J. Diff. Eqns*, 50:280–288, 1983.

[6] Jaime Cisternas, C. William Gear, Simon Levin, and Ioannis G. Kevrekidis. Equation-free modeling of evolving diseases: Coarse-grained computations with individual-based models. Technical report, [http://arXiv.org/abs/nlin.AO/0310011], 2003.

[7] P.H. Coullet and E.A. Spiegel. Amplitude euqations for systems with competing instabilities. *SIAM J. Appl. Math.*, 43:776–821, 1983.

[8] M.C. Cross and P.C.Hohenberg. Pattern formation outside of equilibrium. *Reviews of Modern Physics*, 65:851–1089, 1993.

[9] H. Dankowicz, P. Holmes, G. Berkooz, and J. Elezgaray. Local models of spatio-temporally complex fields. *Physica D*, 90:387–407, 1996.

[10] B. Derrida. Non-trivial exponents in coarsening phenomena. *Physica D*, 103:466–477, 1997.

[11] E.J. Doedel, R.C. Paffenroth, A.R. Champneys, T.F. Fairgrieve, Yu.A. Kuznetsov, B. Sandstede, and X. Wang. Auto 2000: Continuation and bifurcation software for ordinary differential equations (with HomCont). Technical report, Caltech, 2001.

[12] B. Ermentrout. XPPAUT 5.0 - the differential equations tool. Technical report, [http://www.math.pitt.edu/~bard/bardware/xpp_doc.pdf], 2001.

[13] C. Foias, M.S. Jolly, I.G. Kevrekidis, G.R. Sell, and E.S. Titi. On the computation of inertial manifolds. *Phys. Lett. A*, 131:433–436, 1988.

[14] C. Foias, M.S. Jolly, I.G. Kevrekidis, and E.S. Titi. On some dissipative fully discrete nonlinear galerkin schemes for the kuramoto–sivashinsky equation. *Phys Lett A*, 186(1):87, 1994.

[15] C. Foias, B. Nicolaenko, G.R. Sell, and R. Teman. Inertial manifolds for the kuramoto-sivashinsky equation. *Comptes Rendus, Serie I*, 301:285–288, 1985. French.

[16] B. Fornberg. On the stability of the leap-frog and Crank-Nicolson approximations of a nonlinear partial differential equation. *Maths of Comput.*, 27:45–57, 1973.

[17] J. Fujimura. Methods of centre manifold multiple scales in the theory of nonlinear stability for fluid motions. *Proc. Roy. Soc. Lond. A*, 434:719–733, 1991.

[18] T. Gallay and A. Mielke. Convergence results for a coarsening model using global linearization. *J. Nonlinear Sci.*, 13:311–346, 2003.

[19] C. William Gear, Ioannis G. Kevrekidis, and Constantinos Theodoropoulos. 'Coarse' integration/bifurcaton analysis via microscopic simulators: micro-galerkin methods. *Computers and Chemical Engineering*, 26:941–963, 2002.

[20] C. William Gear, Ju Li, and Ioannis G. Kevrekidis. The gap-tooth method in particle simulations. *Phys. Lett. A*, 316:190–195, 2003.

[21] J.D. Gibbon. Weak and strong turbulence in the complex Ginzburg-Landau equation. In G.R. Sell, C. Foais, and R. Temam, editors, *Turbulence in fluid flows–A dynamical systems approach*, volume 55 of *The IMA volumes in mathematics and its applications*, pages 33–48. Springer-Verlag, 1993.

[22] A.C. Hearn. [http://www.reduce-algebra.com]. 2004.

[23] P. Holmes, J.L. Lumley, and G. Berkooz. *Turbulence, Coherent Structures, Dynamical Systems and Symmetry*. Cambridge University Press, 1996.

[24] J.M. Hyman and B. Nicolaenko. The kuramoto-sivashinsky equation: A bridge between pdes and dynamical systems. *Physica D*, 18:113–126, 1986.

[25] M.S. Jolly, I.G. Kevrekidis, and E.S. Titi. Approximate inertial manifolds for the kuramoto-sivashinsky equation: analysis and computations. *Physica D*, 44:38–60, 1990.

[26] D.A. Jones, L.G. Margolin, and E.S. Titi. On the effectiveness of the approximate inertial manifold– a computational study. *Theoret. Comput. Fluid Dynamics*, 7:243–260, 1995.

[27] D.A. Jones and A.M. Stuart. Attractive invariant manifolds under approximation. *Inertial manifolds*, 123:588–637, 1995.

[28] C.T. Kelley. *Iterative methods for linear and nonlinear equations*, volume 16 of *Frontiers in applied mathematics*. Society for Industrial and Applied Mathematics SIAM, 1995.

[29] I.G. Kevrekidis, B. Nicolaenko, and J.C. Scovel. Back in the saddle again: A computer assisted study of the Kuramoto–Sivashinsky equation. *SIAM J. Appl. Math.*, 50:760–790, 1990.

[30] Y. Kuramoto. Diffusion induced chaos in reactions systems. *Progr. Theoret. Phys. Suppl.*, 64:346–367, 1978.

[31] C.D. Levermore and M. Oliver. The complex Ginzburg-Landau equation as a model problem. In P. Deift, C.D. Levermore, and C.E. Wayne, editors, *Dynamical systems and probabilistic methods in partial differ-*

ential equations, volume 35 of *Lectures in Applied Mathematics*, pages 141–190. American Mathematical Society, 1996.

[32] S.J. Liao. The quite general BEM for strongly nonlinear problems. In Brebbia, Kim, Osswald, and Power, editors, *Boundary Elements XII*, pages 67–74. Computational Mechanics Publications, 1995.

[33] S.J. Liao and S.P. Zhu. Solving the Liouville equation with the general boundary element method approach. In C.S. Chen, C.A. Brebbia, and D.W. Pepper, editors, *Boundary Element Technology XIII*, pages 407–416. WIT Press, 1998.

[34] T. MacKenzie and A. J. Roberts. Holistic finite differences accurately model the dynamics of the Kuramoto-Sivashinsky equation. In ANZIAM J., volume 42(E), pages C918–C935. 2000. [Online] http://anziamj.austms.org.au/V42/CTAC99/Mack.

[35] T. MacKenzie and A. J. Roberts. Holistic discretisation of shear dispersion in a 2D channel. In ANZIAM J., volume 44(E), pages C512–C530. 2003. [Online] http://anziamj.austms.org.au/V44/CTAC2001/Mack.

[36] T. MacKenzie and A.J. Roberts. The dynamics of reaction diffusion equations lead to a holistic approximation. In R. L. May, G. F. Fitz-Gerald, and I. H. Grundy, editors, *EMAC 2000 Proceedings. Proceedings of the fourth biennial Engineering Mathematics and Applications Conference*, pages 199–202. 2000.

[37] M. Marion and R. Temam. Nonlinear Galerkin methods. *SIAM J. Numer. Anal.*, 26(5):1139–1157, 1989.

[38] S.F. McCormick. *Multilevel projection methods for partial differential equations*. Society for Industrial and Applied Mathematics (SIAM), Philadelphia, 1992.

[39] G.N. Mercer and A.J. Roberts. A centre manifold description of contaminant dispersion in channels with varying flow properties. *SIAM J. Appl. Math.*, 50:1547–1565, 1990.

[40] G.N. Mercer and A.J. Roberts. A complete model of shear dispersion in pipes. *Jap. J. Indust. Appl. Math.*, 11:499–521, 1994.

[41] E. Meron and I. Procaccia. Theory of chaos in surface waves: The reduction from hydrodynamics to few-dimensional dynamics. *Phys. Rev. Lett.*, 56:1323–1326, 1986.

[42] A. Mielke. The Ginzburg–Landau equation in its role as a modulation equation. In B. Fiedler, editor, *Handbook of dynamical systems*, volume 2, pages 759–834. Elsevier Science, 2002.

[43] A.C. Newell, T. Passot, and J.Lega. Order parameter equations for patterns. *Annual Rev. Fluid Mech.*, 25:399–453, 1993.

[44] Y. Pomeau and S. Zaleski. The kuramoto-sivashinsky equation: A caricature of hydrodynamic turbulence? *Lecture Notes In Physics*, 230, 1984.

[45] W. H. Press, S. A. Teukolsky, W. T. Vetterling, and B. P. Flannery. *Numerical recipes in FORTRAN. The art of scientific computing*. CUP, 2nd edition, 1992.

[46] A. J. Roberts. A holistic finite difference approach models linear dynamics consistently. *Mathematics of Computation*, 72:247–262, 2002. http://www.ams.org/mcom/2003-72-241/S0025-5718-02-01448-5.

[47] A.J. Roberts. The utility of an invariant manifold description of the evolution of a dynamical system. *SIAM J. Math. Anal.*, 20:1447–1458, 1989.

[48] A.J. Roberts. Boundary conditions for approximate differential equations. *J. Austral. Math. Soc. B*, 34:54–80, 1992.

[49] A.J. Roberts. The invariant manifold of beam deformations, Part 1: the simple circular rod. *J. Elas.*, 30:1–54, 1993.

[50] A.J. Roberts. Low-dimensional models of thin film fluid dynamics. *Phys. Letts. A*, 212:63–72, 1996.

[51] A.J. Roberts. Low-dimensional modelling of dynamical systems. Technical report, [http://xxx.lanl.gov/abs/chao-dyn/9705010], 1997.

[52] A.J. Roberts. Low-dimensional modelling of dynamics via computer algebra. *Comput. Phys. Comm.*, 100:215–230, 1997.

[53] A.J. Roberts. Derive boundary conditions for holistic discretisations of Burgers' equation. Technical report, [http://arXiv.org/abs/math.NA/0106224], 2001.

[54] A.J. Roberts. Holistic discretisation ensures fidelity to Burgers' equation. *Applied Numerical Mathematics*, 37:371–396, 2001.

[55] A.J. Roberts and I.G. Kevrekidis. Higher order accuracy in the gap-tooth scheme for large-scale solutions using microscopic simulators. Technical report, [http://arXiv.org/abs/math.NA/0410310], 2004.

[56] S. Rosencrans. Taylor dispersion in curved channels. *SIAM J. Appl. Math.*, 57:1216–1241, 1997.

[57] R. Valery Roy, A. J. Roberts, and M. E. Simpson. A lubrication model of coating flows over a curved substrate in space. *J. Fluid Mech.*, 454:235–261, 2002.

[58] R.J. Schilling and S.L. Harris. *Applied numerical methods for engineers using Matlab and C.* Brooks/Cole, 1996.

[59] C. Scovel, I.G. Kevrekidis, and B. Nicolaenko. Scaling laws and the prediction of bifurcations in systems modeling pattern formation. *Phys. Lett. A.*, 130:73–80, 1988.

[60] G.I. Sivashinsky. Nonlinear analysis of hydrodynamic instabiliy in laminar flames, part i: Derivation of the basic equations. *Acta Astronauica*, 4:1176–1206, 1977.

[61] R. Smith. Entry and exit conditions for flow reactors. *IMA J. Appl. Math.*, 41:1–20, 1988.

[62] G.I. Taylor. Conditions under which dispersion of a solute in a stream of solvent can be used to measure molecular diffusion. *IMA J. Appl. Math.*, 225:473–477, 1954.

[63] R. Temam. Inertial manifolds. *Mathematical Intelligencer*, 12:68–74, 1990.

[64] H.A. van der Vorst. *Iterative Krylov methods for large linear systems*, volume 13 of *Cambridge monographs on applied and computational mathematics*. Cambridge University Press, 2003.

[65] A. Vanderbauwhede. Centre manifolds. *Dynamics Reported*, pages 89–169, 1989.

[66] S.D. Watt and A.J. Roberts. The accurate dynamic modelling of contaminant dispersion in channels. *SIAM J. Appl. Math.*, 55(4):1016–1038, 1995.

[67] S. Wolfram. *The Mathematica Book, 3rd ed.* Wolfram Media/Cambridge University Press, 1996.